

CHIRAL OXAZOLINE AND BIS(OXAZOLINE) LIGANDS – NEW BIOMIMETIC MODELS FOR IRON CONTAINING NONHEME PROTEINS AND THEIR APPLICATION IN CATALYSIS

Dissertation

zur Erlangung des Doktorgrades der Naturwissenschaften

Dr. rer. nat.

an der Fakultät für Chemie und Pharmazie
der Universität Regensburg



vorgelegt von

Caroline Anja Schall

aus

Schwandorf

Regensburg 2007

Die Arbeit wurde angeleitet von: Prof. Dr. O. Reiser

Promotionsgesuch eingereicht am: 05. November 2007

Promotionskolloquium am: 30. November 2007

Prüfungsausschuss:

Vorsitz:	Prof. Dr. J. Heilmann
1. Gutachter:	Prof. Dr. O. Reiser
2. Gutachter:	Prof. Dr. R. Gschwind
3. Prüfer:	Prof. Dr. R. Winter

Der experimentelle Teil der vorliegenden Arbeit wurde unter der Leitung von Herrn Prof. Dr. Oliver Reiser in der Zeit von August 2004 bis September 2007 am Institut für Organische Chemie der Universität Regensburg sowie in der Arbeitsgruppe von Prof. Dr. A. Borovik, University of Kansas, angefertigt.

Herrn Prof. Dr. Oliver Reiser möchte ich für die Überlassung des äußerst interessanten Themas, die fortwährenden Diskussionen und seine Unterstützung während der Durchführung dieser Arbeit danken.

for my family...

**“Raise new questions,
explore new possibilities,
regard old problems from a new angle.”**

Albert Einstein

Table of Content

TABLE OF CONTENT	6
A. INTRODUCTION	8
A.1 Do we need biomimetic models?	8
A.2 Models for nonheme iron enzymes	16
A.3 Aim of this work.....	20
B. MAIN PART – SYNTHESIS.....	23
B.1 Ligand Synthesis	23
B.1.1 General Retrosynthesis of Oxazoline, Bis(oxazoline) Ligands and their Derivatives	23
B.1.2 Route to Oxazoline Ligands and their Derivatives	24
B.1.3 Route to Bis(oxazoline) Ligands	28
C. MAIN PART – OXAZOLINE COMPLEX ANALYSIS.....	37
C.1 Determination of Stoichiometry and Equilibrium Constant.....	37
C.1.1 Siderophores – A General Introduction	37
C.1.2 Stoichiometry Determination by Job's Plot Analysis	40
C.1.3 Determination of Equilibrium-Constants	42
C.2 Characterization of Oxazoline-Metal-Complexes	47
C.2.1 Formation of Iron(III) Complexes using $\text{Fe}(\text{ClO}_4)_2 \cdot 6(\text{H}_2\text{O})$	47
C.2.2 Solid-State-Analysis of Iron(III) Complexes – $[\text{Fe}^{\text{III}}(7a-9)_2] \cdot (\text{ClO}_4)$	48
C.2.3 Liquid-State-Analysis of Iron(III) Complexes – $[\text{Fe}^{\text{III}}(7a-9)_2] \cdot (\text{ClO}_4)$	50
C.2.4 Formation of Iron(III) Complexes using $\text{Fe}(\text{OAc})_2$	55
C.2.5 Solid-State-Analysis of Iron(III) Complexes – $[\text{Fe}^{\text{III}}(7a-9)_2(\text{OAc})]$	56
C.2.6 Liquid-State-Analysis of Iron(III) Complexes – $[\text{Fe}^{\text{III}}(7a-9)_2(\text{OAc})]$	63
C.2.7 Formation of Iron(III) Complexes using $\text{Fe}(\text{acac})_3$	66
C.2.8 Liquid-State-Analysis of Iron(III) Complexes – $[\text{Fe}^{\text{III}}(7a-9)_2(\text{acac})]$	67
C.2.9 Formation of Ruthenium(III) Complexes using $[\text{RuCl}_2(\text{benzene})]_2$	70
C.2.10 Liquid-State-Analysis of Ruthenium(III) Complexes – $[\text{Ru}^{\text{III}}(7a-9)_3]$	71
C.2.11 Formation of Zinc(II) Complexes using $\text{Zn}(\text{ClO}_4)_2 \cdot 6\text{H}_2\text{O}$	74
C.2.12 Solid-State-Analysis of Zinc(II) Complexes – $[\text{Zn}^{\text{II}}(7a-9)_2]_2 \cdot (\text{ClO}_4)_2$	75
C.2.13 Liquid-State-Analysis of Zinc(II) Complexes – $[\text{Zn}^{\text{II}}(7a-9)_2]_2 \cdot (\text{ClO}_4)_2$	81
C.2.14 Formation of a Manganese(III) Complex using $\text{Mn}(\text{ClO}_4)_2 \cdot 6\text{H}_2\text{O}^{28}$	83
C.2.15 Solid-State-Analysis of a Manganese(III) Complex – $[\text{Mn}^{\text{III}}(7a)_2(\text{THF})_2] \cdot (\text{ClO}_4)$	83
C.2.16 Liquid-State-Analysis of a Manganese(III) Complex – $[\text{Mn}^{\text{III}}(7a)_2(\text{THF})_2] \cdot (\text{ClO}_4)$	87
C.2.17 Summary	89
D. MAIN PART – BIS(OXAZOLINE) COMPLEX ANALYSIS	90
D.1 Characterization of Bis(oxazoline)-Metal-Complexes	90
D.1.1 Formation of Iron(III) Complexes using $\text{Fe}(\text{ClO}_4)_2 \cdot 6(\text{H}_2\text{O})$	90
D.1.2 Solid-State-Analysis of Iron(III) Complexes – $\text{Fe}^{\text{III}}((\text{meso})-4)_{\text{ox}}(\text{H}_2\text{O}) \cdot (\text{ClO}_4)$	92
D.1.3 Liquid-State-Analysis of Iron(III) Complexes – $[\text{Fe}^{\text{III}}(1/2)(\text{H}_2\text{O})_2] \cdot (\text{ClO}_4)_2$ and $[\text{Fe}^{\text{III}}((\pm)-4/(\text{meso})-4/5)_{\text{ox}}(\text{H}_2\text{O})] \cdot (\text{ClO}_4)$	95
D.1.4 Formation of Ruthenium(II) and Ruthenium(III) Complexes using $[\text{RuCl}_2(\text{benzene})]_2$	97
D.1.5 Liquid-State-Analysis of Ruthenium(II) and Ruthenium(III) Complexes – $[\text{Ru}^{\text{III}}(1/2)(\text{Cl})(\text{solvent})]$ and $[\text{Ru}^{\text{II}}((\pm)-4/(\text{meso})-4/5)(\text{Cl})_2]$	100
D.1.6 Formation of Zinc(II) Complexes using $\text{Zn}(\text{ClO}_4)_2 \cdot 6\text{H}_2\text{O}$	103

Table of Content

D.1.7	Solid-State-Analysis of Zinc(II) Complexes – $[\text{Zn}^{\text{II}}(1/2)]\cdot(\text{ClO}_4)_2$ and $[\text{Zn}^{\text{II}}((S,S)-4/5)]\cdot(\text{ClO}_4)_2$	104
D.1.8	Liquid-State-Analysis of Zinc(II) Complexes – $[\text{Zn}^{\text{II}}(1/2)]\cdot(\text{ClO}_4)_2$ and $[\text{Zn}^{\text{II}}((\pm)-4/(\text{meso})-4/5)]\cdot(\text{ClO}_4)_2$	107
D.1.9	Summary	110
E. MAIN PART – CATALYSIS		111
E.1	Catalysis.....	111
E.1.1	Functionalization of Alkanes by C-H Bond Activation	111
E.1.2	Oxidation of Ethylbenzene by Oxazoline / Bis(oxazoline) Complexes	114
E.1.3	Preparation of Optical Active Sulfoxides	119
E.1.4	Asymmetric Sulfide Oxidation	120
F. EXPERIMENTAL PART.....		123
F.1	General.....	123
F.2	Abbreviations	125
F.3	Oxazoline and Thiazoline Ligands	126
F.5	Bis(oxazoline) ligands	134
F.5	Precursor for Oxazoline and Bis(oxazoline) Ligands	142
F.6	General precursor	154
F.7	Synthesized Complexes of Oxazoline Ligands.....	159
F.7.1	Iron Complexes	159
F.7.2	Ruthenium Complexes	168
F.7.3	Zinc Complexes	171
F.7.4	Manganese Complex	174
F.8	Synthesized Complexes of Bis(oxazoline) Ligands	175
F.8.1	Iron Complexes	175
F.8.2	Ruthenium Complexes	179
F.8.3	Zinc Complexes	183
F.9	UV/Vis-Titrations.....	187
F.9.1	UV/Vis-Job's Plot Titration	187
F.9.2	UV/Vis-Equilibrium Constant Titration	188
F.9.2	General UV/Vis- and CD-Measurements	190
F.10	Catalysis Reactions	193
F.10.1	Oxidation of ethylbenzene	193
F.10.2	Oxidation of methyl phenyl sulfide	194
F.11	X-Ray Structure Data.....	195
G. REFERENCES		223
H. CURRICULUM VITAE		228
I. ACKNOWLEDGEMENT.....		231

A. Introduction

A.1 *Do we need biomimetic models?*

Trace elements are essential for living individuals but their availability in the biomass is limited.¹ This fact depends not on a low distribution of such metal elements on earth, rather on their restricted solubility at ambient aqueous conditions (1 atm, 0-30 °C). Particularly, variable pH values and redox potentials in the environment govern the formation of soluble salts. Therefore only a few elements are able to be taken up by cells at reasonably low energy cost. Some transition metal ions, when placed in a framework of carbon, hydrogen, oxygen, nitrogen, and sulphur atoms in the cell, form highly functionalized complexes, which are able to manage a broad variety of demanding tasks in the metabolism of the body. But without intake of these metals, no life may exist and this clearly indicates how indispensable trace elements are.

Current investigations focus on the function of transition metals with respect to their environment set by their coordination with ligands. The main questions here are not locating the active site in an enzyme or investigating the secondary and tertiary structure; it is rather the oxidation state of the metal as well as the catalytic cycle they are able to perform. As early as 30 years ago, J. M. Wood realized this fact and made a provocative statement for the definition of biochemistry:

*“The concept of biological cycles for the elements is logical because organic life on this planet evolved on an inorganic matrix. From this inorganic matrix certain metals have been selected to catalyze important reactions in living systems. Biochemistry is the **coordination chemistry** of living systems!”*

J. M. Wood, 1975²

Wood’s view was a venture in a direction of science which pointed to coordination chemistry as a cornerstone between interactions of transition metal ions and biological systems. Today, this statement is broadly accepted, but it was revolutionary in 1975!

Iron is one of the most widespread metals in nature and due to that it is precisely tuned and regulated in its properties. This has given it the capability of catalyzing a wide array of

chemical transformations (e. g. electron transfer, dioxygen transport, and redox transformations). Thus, a broad spectrum of biological processes involves iron-containing enzymes. The diversity of these molecules has resulted in their sub-classifications into heme, iron-sulphur, and nonheme proteins:

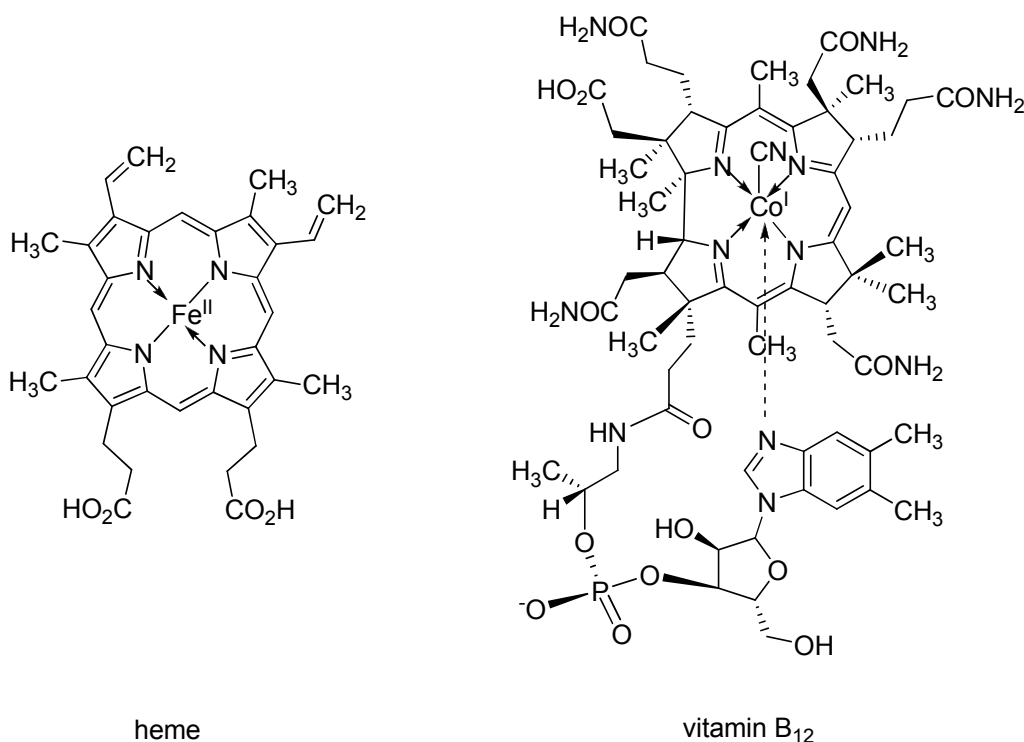


Figure 1. Metalloporphyrinoids: heme and vitamin B₁₂.³

Metalloporphyrinoids (Figure 1) are intensely coloured molecules and are therefore sometimes referred to as “*pigments of life*”.^{4,5,6} The typical porphyrin core contains four pyrroles and four methylene groups as bridges between them. Iron or some other metals, such as magnesium, zinc, nickel, or cobalt are found in the centre. The heme unit (Figure 1, left) plays an essential role as a cofactor in the mode of action in multiple protein structures, e.g. haemoglobin (dioxygen transport), myoglobin (dioxygen storage), and cytochromes (electron transport).^{7,8,9} Vitamin B₁₂, also named cyanocobalamin (Figure 1, right), is based on a corrin ring, which has a cobalt ion in the centre. The relationship to the porphyrin core can be clearly seen, but in the corrin ligand system, two oppositely positioned methylene bridges contain an additional CH₃ group and another methylene bridging group between a pair of pyrroles is missing. Vitamin B₁₂ is involved in the methylmalonyl-coenzyme A mutase pathway (MUT) as well as in the methionine synthase cycle (MTR, 5-methyltetrahydrofolate-homocysteine methyltransferase). A reduced availability of vitamin B₁₂ has a negative effect on the DNA / RNA synthesis and on the blood cell proliferation.¹⁰⁻¹²

Iron-sulphur clusters, Fe_2S_2 and Fe_4S_4 , represent the second iron-species. They are one of the oldest metal-containing cofactors and are widely distributed in nature, found in anaerobic, aerobic, and photosynthetic bacteria, as well as in mammals, plants, and fungi.¹³ These clusters are nonheme prosthetic groups, consisting of iron atoms bonded both to inorganic sulphur atoms and to four sulphur atoms located on cysteine residues on the protein. Their catalytic activity is used for electron transport and structure-directing tasks. Iron-sulphur clusters accept and release electrons one at a time. Typical structural motifs are shown in simple Fe-S moieties (Figure 2).¹⁴⁻¹⁶

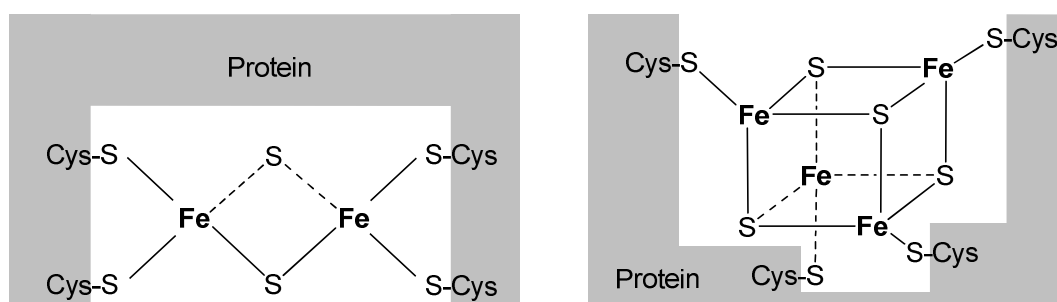


Figure 2. Three-dimensional structures of some iron-sulphur clusters in electron-transporting proteins: (left) a dimeric Fe_2S_2 cluster; (right) a tetrameric Fe_4S_4 cluster.

Finally, the last and for this thesis the most important class of iron-containing enzymes is predominately based on O- and N-containing ligands. They allow the oxidative utilization of dioxygen under ambient conditions when coordinating activated iron ions in their centres. These so-called nonheme iron proteins are able to catalyze oxidation reactions of non-activated C-H bonds, detoxification of biologically harmful radicals and reversible O_2 -binding reactions. Nonheme metalloproteins consist of two different types of active sites, the mononuclear and the dinuclear forms.

Many mononuclear iron enzymes feature in their octahedral geometry two coordinated histidines and a carboxylate (glutamate or aspartate) residue. On the opposite face, three readily displaceable water molecules are bound. This structural formation is typical for an enzyme superfamily named 2-His-1-carboxylate facial triad (e.g. deacetoxycephalosporin C synthase, Figure 3 a).¹⁷

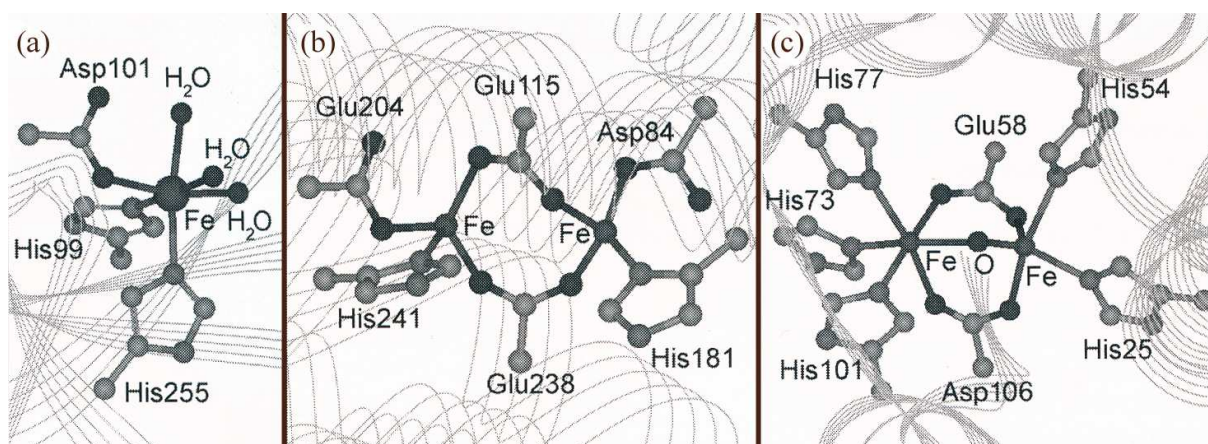
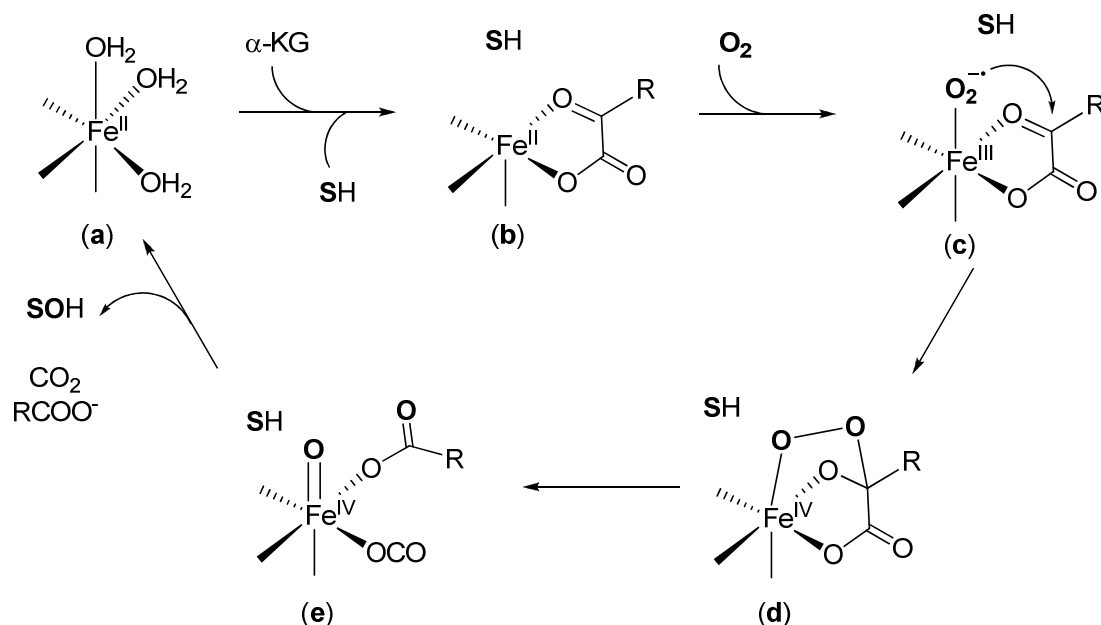


Figure 3. Common active-site structures for nonheme iron enzymes; (a) deacetoxycephalosporin C synthase, (b) reduced ribonucleotide reductase (RNR R2), (c) methemerythrin (merHr).³

The resulting flexibility around the iron metal permits binding of exogenous ligands such as solvent, substrate, cofactors, and / or O_2 at three available coordination sites.¹⁸ As a general example, the mononuclear nonheme iron family that requires an α -keto acid (α -KA) for activation was chosen to describe the proposed reaction mechanism between the iron centre and the substrate, cofactor, and O_2 (Scheme 1):^{19,20,21,22}

- (a) resting state of a 2-His-1-carboxylate facial triad fashion enzyme;
- (b) coordination of an α -keto acid (α -KA) to the Fe^{II} centre by displacing two water ligands and subsequent binding of a substrate (SH) in the outer sphere of the active site; this substrate binding leads to a dissociation of the third water molecule and results in a penta-coordinated and unsaturated Fe^{II} centre;
- (c) addition of O_2 creates a Fe^{III} -superoxo species ($Fe^{III}-O_2^-$) which undergoes a nucleophilic attack on the carbonyl-C of the bound α -KA;
- (d) a new metal-peroxo species with a $Fe^{IV}-O_2$ oxidation state is formed, and O-O bond cleavage in combination with decarboxylation occurs;
- (e) a formation of a $Fe^{IV}=O$ intermediate (oxo-iron(IV) species) leads to substrate oxidation and after the catalytic step, product, succinate ($RCOO^-$) and CO_2 dissociate from the active site, releasing the resting enzyme.



Scheme 1. Proposed reaction mechanism for α -keto acid-dependent enzymes.^{3,23}

X-ray structures for these activated intermediates have been reported and show clearly the ligation of an α -keto acid to the iron centre (Figure 4 a) and the dissociation of the third water ligand (Figure 4 b). The activated enzyme can then come into contact with an oxygen molecule and perform the oxidation reaction at the substrate as described above.

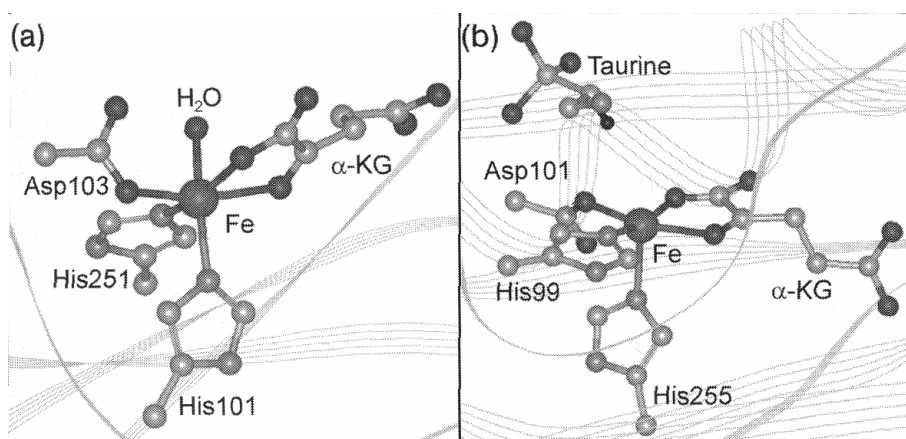
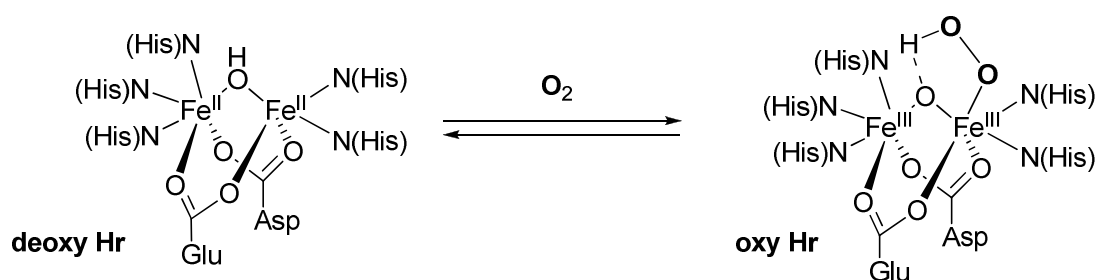


Figure 4. Active-site structures of various states of α -KA-dependent enzymes based on X-ray crystallographic data: (a) the α -KA is already coordinated on the iron centre, and (b) the third water ligand is dissociated and a unsaturated iron(II) centre is exposed.³

In dinuclear nonheme proteins usually two histidine- and four carboxylate-moieties are involved in the redox processes of the iron ions and their resulting oxygen-activation (e.g. reduced ribonucleotide reductase (RNR R2), Figure 3 b). Histidine residues represent

permanent terminal ligands, whereas carboxylates are capable of acting as terminal ligands as well as bridging ones between both metal centres.²⁴ These kinds of enzyme belong to a subclass of diiron proteins which are called carboxylate-rich, in comparison to histidine-rich active site proteins. The latter retain five histidines and only two carboxylates (e.g. methemerythrin, another form of hemerythrin, Figure 3 c).²⁵

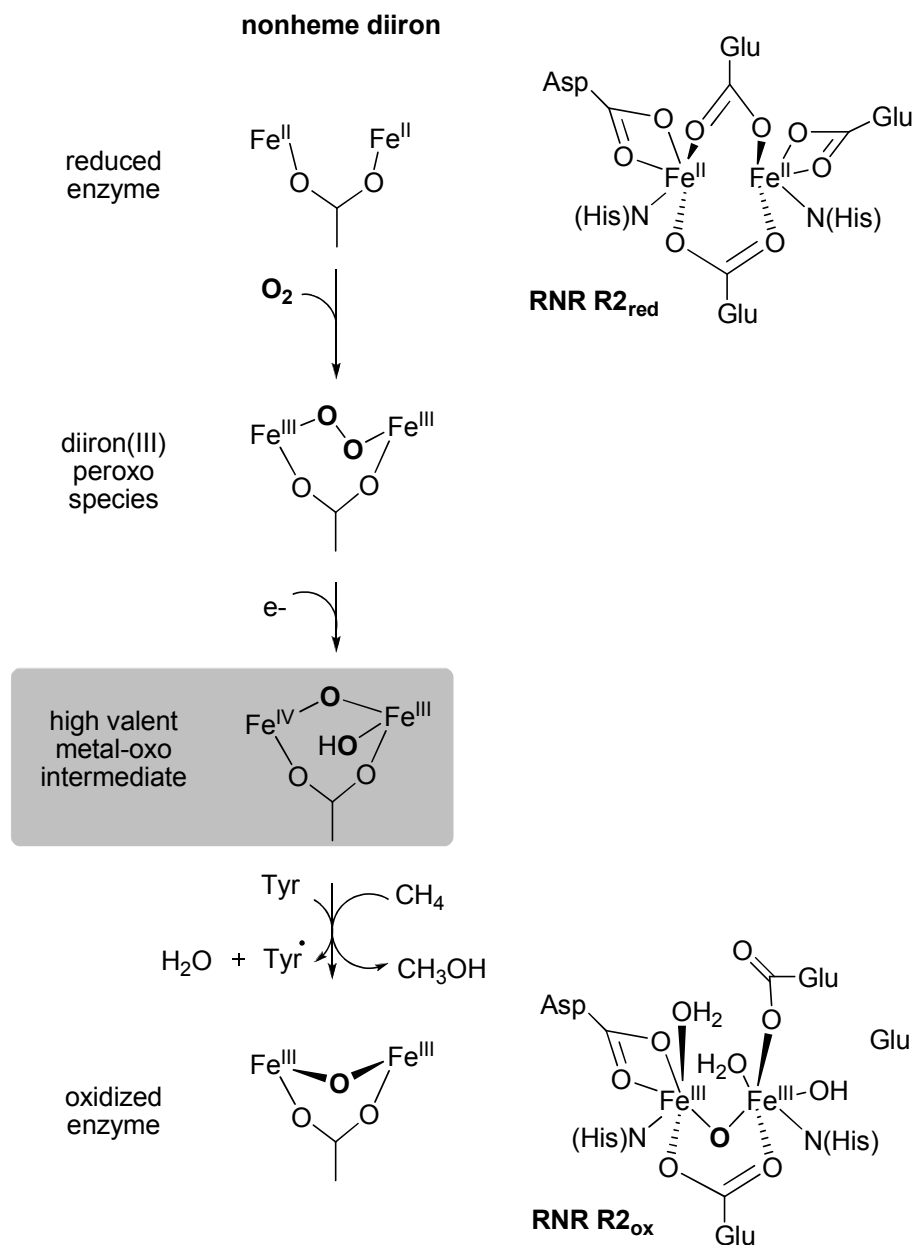
Hemerythrin (Hr) is a dioxygen carrier (Scheme 2) and therefore displays a completely different function in comparison to other diiron nonheme proteins.^{22,26} This enzyme was only found in a limited number of marine invertebrates and it was assumed that it is probably a evolutionary dead end because of its low abundance. Nevertheless, the chemistry of hemerythrin has been investigated in depth in the past, identifying it as the first diiron nonheme enzyme. Today, the knowledge in this field often serves as a platform for other diiron protein research.



Scheme 2. Dioxygen binding at the hemerythrin (Hr) active site.²²

Deoxy Hr consists of a (μ -hydroxo)bis(μ -carboxylato)diiron(II) core and binds O_2 end-on at one of the coordinatively unsaturated iron centres (Scheme 2). The activated oxy Hr is formed as a (μ -oxo)bis(μ -carboxylato)diiron(III) complex with a terminal η^1 -hydroperoxo ligand. This oxidized form was for a long time suspected to be the key for all diiron protein motifs. Oxo bridges and carboxylato ligands are quite important for building activated intermediates and lead to an impressive flexibility in diiron core structures.³

The primary function of nonheme diiron enzymes, i.e. the oxygen activation, is discussed in detail for each oxidation state of ribonucleotide reductase (RNR R2), starting from its reduced form (Scheme 3).



Scheme 3. Dioxygen activation mechanism for nonheme diiron enzymes, e.g. type I ribonucleotide reductase (RNR R2).^{19,27-29}

The diiron(II) centres of RNR R2_{red} react with O₂ and afford a diiron(III) peroxo species. This peroxo form undergoes electron transfer and is partly oxidized into a high-valent iron-oxo intermediate, resulting in a Fe^{III}(μ-O)Fe^{IV} core.³⁰ The activated enzyme is able to oxidize a phenol group from a closely placed tyrosine residue to generate a catalytically important tyrosyl radical. Both the high-valent centres and the radical are responsible for further

substrate oxidations (e.g. of methane to methanol). Subsequently, the activated core is reduced to a diiron(III) state and can easily be returned to the starting form of the catalytic cycle by the cellular machinery. In related protein systems similar mechanisms for oxygen activation were observed, differing in the high valent iron-oxo intermediate, which is changed from $\text{Fe}^{\text{III}}(\mu\text{-O})\text{Fe}^{\text{IV}}$ to $\text{Fe}^{\text{IV}}(\mu\text{-O})\text{Fe}^{\text{IV}}$. The formation of radical species was also not observed in other enzyme mechanisms.^{22,3}

Studying enzyme active sites is challenging with regard to the high complexity of their bio-frameworks (Figure 5). Thus, it is desirable to scale down the size of protein systems, while retaining their functionality.

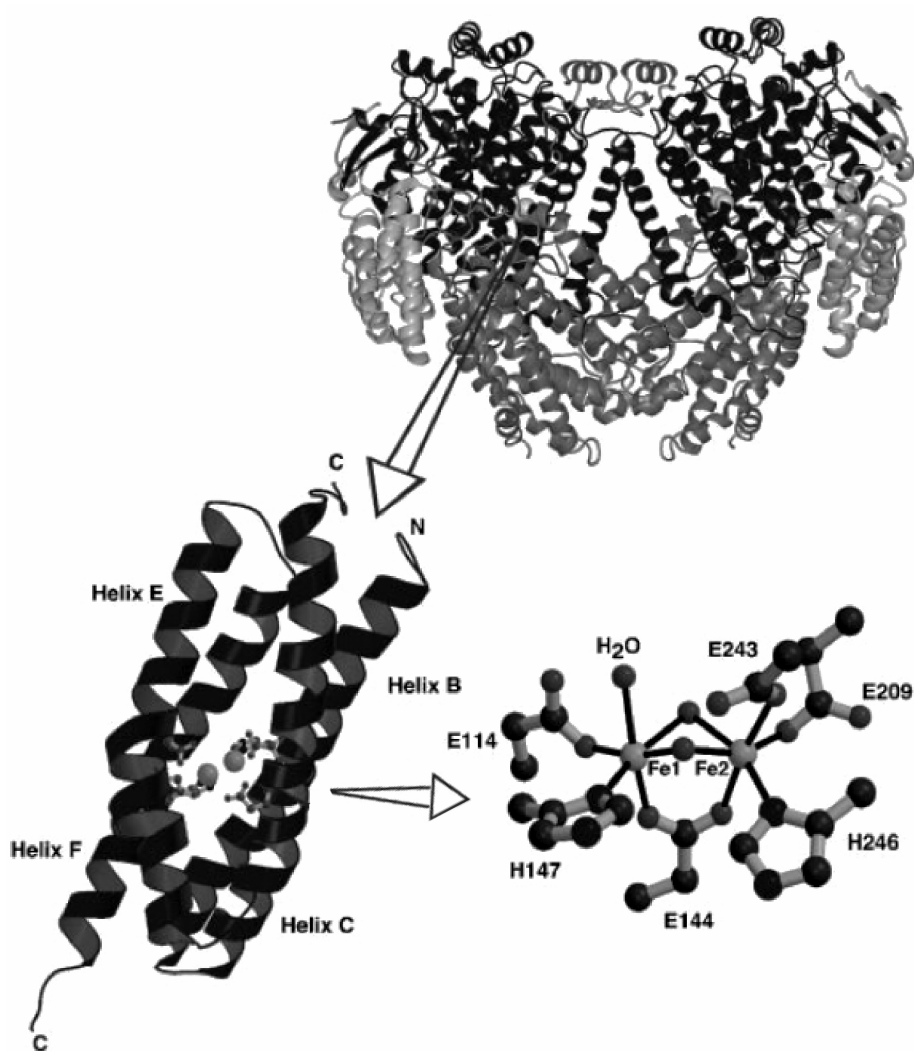
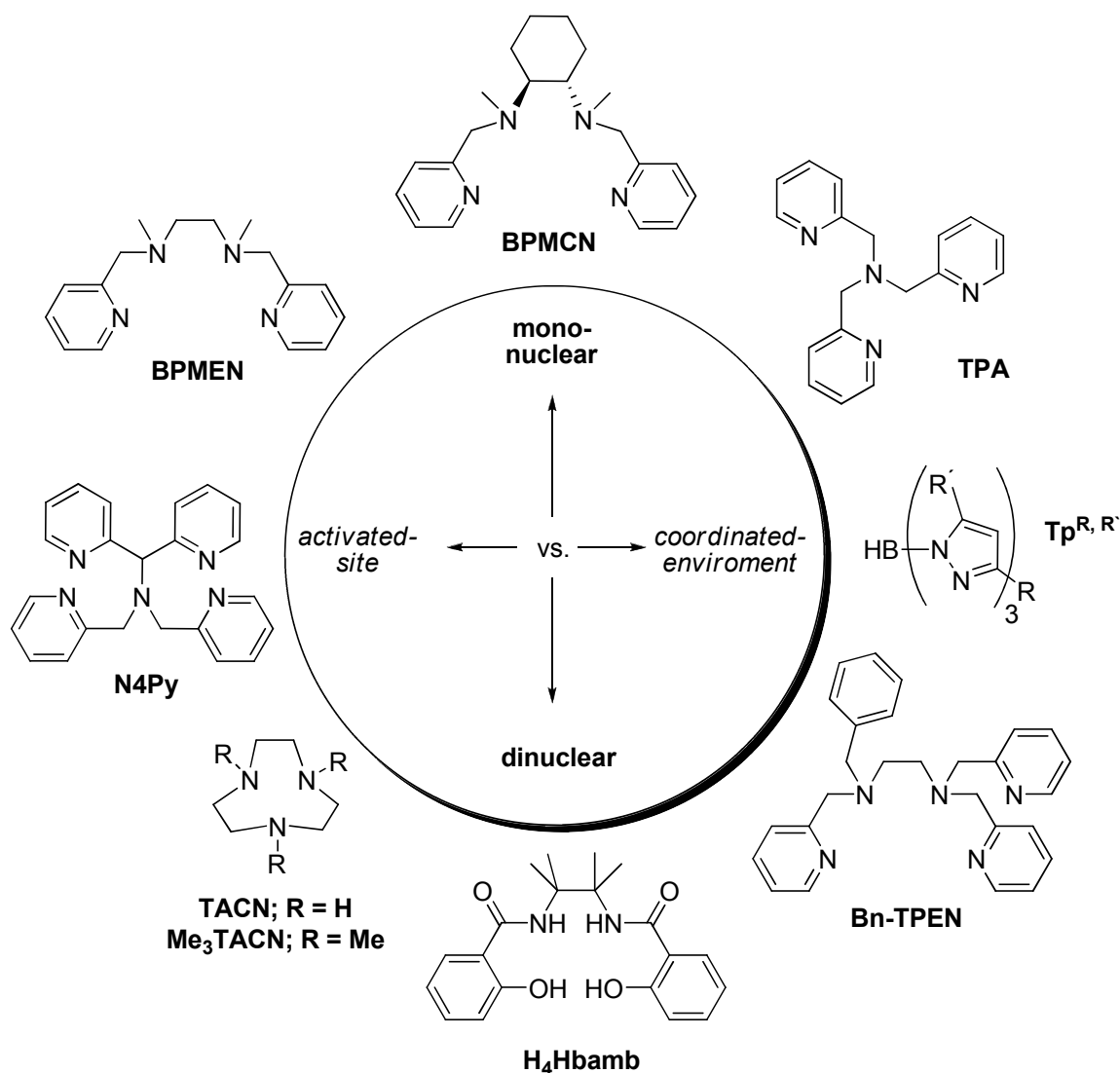


Figure 5. Three structural levels in MMOM (methane monooxygenase) from *M. capsulatus* (Bath).²⁴

Investigations in enzyme catalysis are frequently obscured by their complexity and herein lies the answer to the title question: yes, biomimetic models are definitely necessary to get a better view of activated intermediates and their coordination environment.

A.2 Models for nonheme iron enzymes

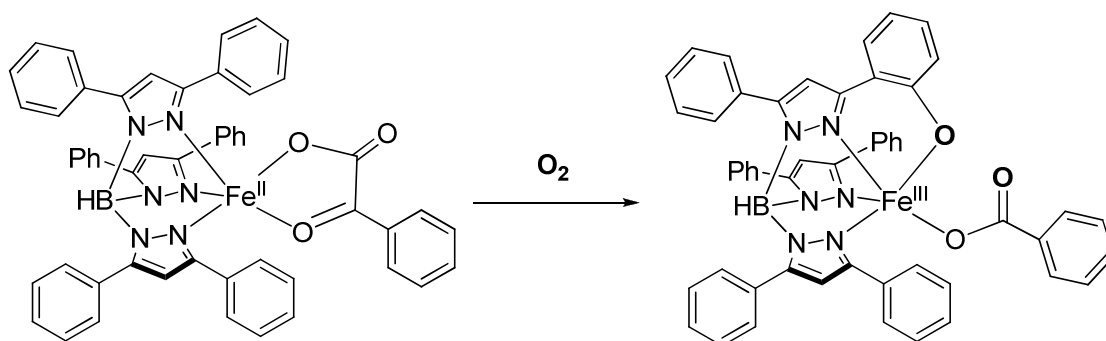
The ultimate goal in bioinorganic chemistry will be achieved by mimicking structural and physical characteristics of complex protein systems with small organic molecules. Based on a deeper understanding of these fields, the basic catalytical processes can be investigated in more detail. In both mononuclear and dinuclear nonheme iron enzymes the major synthetic targets are very similar. The construction of iron(II)- and iron(III)-centres, peroxo intermediates, and high-valent oxoiron intermediates are the predominant aims in biomimetic science. To achieve this, a variety of polydentate ligands are synthesized to model enzymes and their special environments (Scheme 4):²¹



Scheme 4. Collection of biomimetic ligand systems.

The following examples are representative for the achievements in biomimetic modelling of enzyme properties:

To mimic the 2-His-1-carboxylate facial triad of an α -KA-dependent enzyme, a polydentate ligand like Tp^{Ph_2} (Scheme 4, Tp = tris(pyrazolyl)borate) was found to be suitable. The peripheral phenyl groups of the tridentate ligand hinder access to the metal centre in such a way that the α -keto carboxylate (benzoylformate) binds as shown in (Scheme 5, left).²³ The enzyme-cofactor-model contains a coordinatively unsaturated iron centre, which is suitable for O_2 binding. With this model, structural as well as spectroscopic features were investigated and led to more information about 2-His-1-carboxylate facial triad proteins.



Scheme 5. Structures of $[\text{Fe}^{\text{II}}(\text{Tp}^{\text{Ph}_2})(\text{bf})]$ (Tp = tris(pyrazolyl)borate, bf = benzoylformate) (left) and its oxygenated product (right) based on X-ray crystallographic data.²³

The most important high-valent oxoiron intermediates in mononuclear enzymes can be modelled by a topology of polydentate N4 and N5 ligands. Figure 6 shows two different ligand systems, Bn-TPEN (= *N*-benzyl-*N,N',N'*-tris(2-pyridylmethyl)ethane-1,2-diamine) and N4Py (= *N,N*-bis(2-pyridylmethyl)-*N*-bis(2-pyridyl)methylamine) (Scheme 4), which are utilized to stabilize the oxoiron(IV) unit in a nonheme environment. These models allow a deeper view into the characteristics of highly reactive intermediates by spectroscopic investigations, revealing their relevance in catalytic cycles.

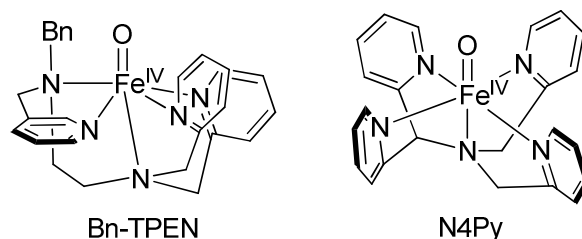


Figure 6. Structures of nonheme oxoiron(IV) complexes based on X-ray crystallographic and spectroscopic data.³¹⁻³⁵

Another aim in the biomimetic chemistry of nonheme diiron proteins is the development of a $(\mu\text{-oxo})\text{bis}(\mu\text{-carboxylato})\text{diiron(III)}$ core (Figure 7), which can be observed in hemerythrin. Mimicking a histidine-rich active site molecule, tridentate ligands such as tris(pyrazolyl)borate (Tp) (Scheme 4) and 1,4,7-triazacyclononane (TACN)³⁶ are successful candidates to generate self-assembling $[\text{L}_2\text{Fe}^{\text{II}}_2(\mu\text{-O})(\mu\text{-O}_2\text{CR})_2]$ complexes with the desired structure. These Fe^{II} -complexes are starting points to investigate the stability and oxidation potential of histidine-rich diiron proteins in different oxidation states.

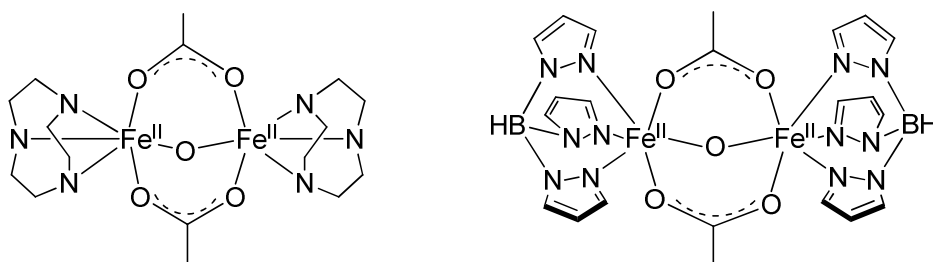


Figure 7. Structures of $[\text{Fe}^{\text{II}}_2(\mu\text{-O})(\mu\text{-O}_2\text{CCH}_3)_2(\text{TACN})_2]$ (left) and $[\text{Fe}^{\text{II}}_2(\mu\text{-O})(\mu\text{-O}_2\text{CR})_2(\text{Tp})_2]$ (right) based on X-ray crystallographic data.^{37,38}

Carboxylate-rich models with a structural motif like $[\text{Fe}_2\text{L}_2(\text{ArCO}_2)_4]$ (L = nitrogen base) mimic an active site common to methane monooxygenase (MMOH) or RNR R2 and are realized by bulky terphenyl carboxylates and related benzyl-substituted benzoates.³⁰ Figure 8 shows an example of such a carboxylate ligand with this sterically demanding functionality.

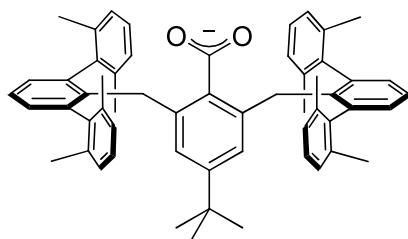


Figure 8. Structure of a bulky terphenyl carboxylate.³⁰

Oxygen-activating diiron enzymes can be modelled very well by $[\text{Fe}^{\text{II}}(\text{Tp}^{\text{iPr}_2})(\text{O}_2\text{CR})]$ (R = benzyl) (Figure 9) and their synthetic analogues. These complexes bind O_2 reversibly and exhibit a 1,2-peroxo-bridged diiron(III) unit. Spectroscopic analysis assigns a high similarity to nonheme diiron proteins, permitting study of dioxygen binding.

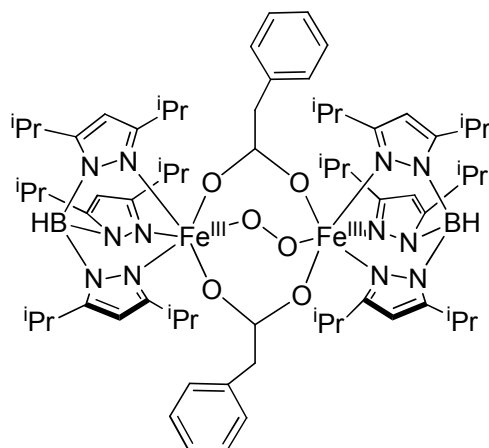


Figure 9. Structure of $[\text{Fe}^{\text{III}}_2(\mu\text{-}1,2\text{-O}_2)(\mu\text{-O}_2\text{CCH}_2\text{Ph})_2(\text{Tp}^{\text{iPr}_2})]$ based on X-ray crystallographic data.³⁹

High-valent iron-oxo intermediates are the ultimate oxidative form in nonheme iron chemistry. MMOH and RNR R2 are typical enzymes which fulfil their catalytic activity by a diiron(IV) core. Diiron(IV) species, however, remain elusive, while a number of iron(III)iron(IV) intermediates are easily accessible to study. A member of this group of special oxidation-state-molecules with a $\text{Fe}_2(\mu\text{-O})_2$ diamond unit is shown in Figure 10. Here a modified tris(2-pyridylmethyl)amine (TPA) ligand serves as a suitable metal environment.⁴⁰

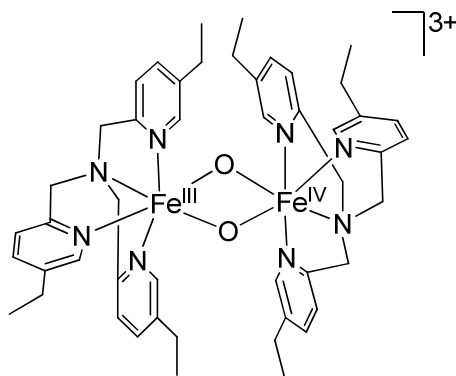


Figure 10. Structure of $[\text{Fe}^{\text{III}}\text{Fe}^{\text{IV}}(\mu\text{-O})_2(5\text{-Et}_3\text{-TPA})_2]^{3+}$ based on X-ray crystallographic data.⁴¹

All of these examples of models and many more are necessary to complete the “puzzle” in bioinorganic chemistry. There are still many open fields which have to be investigated, e. g. mononuclear oxoiron(IV) model complexes catalyze oxidation reactions less impressively than their biological counterparts and need therefore more investigation and development.

A.3 Aim of this work

The exciting chemistry of oxazolines and bis(oxazolines) has long represented a fruitful field for investigations, initiated already many years ago. Also in our group the knowledge about bis(oxazolines), in catalysis as well as in structure analysis, was continuously increased. Within this work, a former explored ligand model^{42,43} with excellent binding properties was used as a basis to introduce certain functional groups with the aim to improve its structural and catalytical behaviour:

The first goal of this thesis was to find a selective way for the synthesis of these promising modified bis(oxazolines) (Figure 11) and to obtain important structural data of complexes formed by these ligands in combination with iron, ruthenium and zinc salts. The investigations in solid state and in solution should make further contributions to mimic mononuclear nonheme iron proteins with an octahedral geometry around the metal centre.

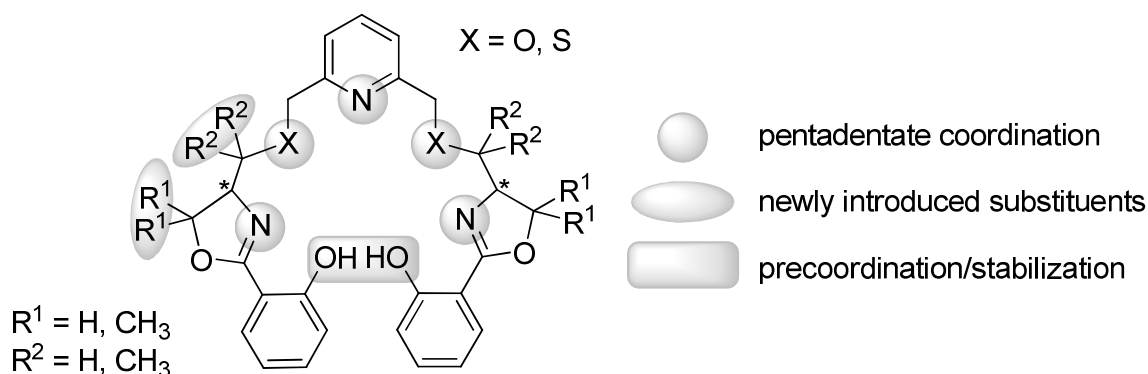


Figure 11. Pentadentate bis(oxazoline) ligand system.

The therefore necessary ligand will be obtained by an asymmetric synthesis, which allows to access both stereo isomers (*R,R* and *S,S*) by minimal variations in the synthetic strategy and affords the C_2 -symmetric bis(oxazoline) systems. The use of flexible donor-sets (N/O or N/S) results in a pentadentate ligand, with the possibility to introduce two sterical demanding alkyl groups, placed on two different positions at the ligand, which are assumed to influence the space near the stereo centres. Different chromophores (pyridine and phenols) are available for liquid-state analysis by using electronic absorption methods (UV/Vis and CD). Newly introduced *ortho*-OH groups on the phenyl rings are envisioned to interact with either an iron(III)-peroxo-intermediate or a substrate by pre-coordination, utilizing additional hydrogen-bridges (Figure 12).

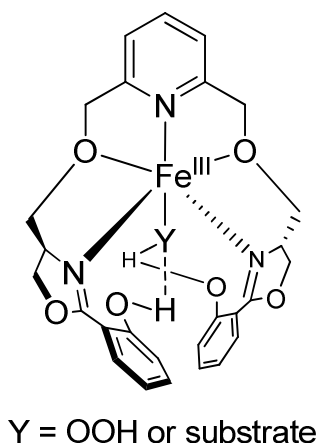


Figure 12. Proposed pentadentate binding model, stabilizing either an iron(III)-peroxo-intermediate or substrate – shown on the unsubstituted ether bridged ligand **1**.

The second goal for this thesis is directly derived from the synthesis of the bis(oxazoline) ligands. The whole oxazoline side chain, which was used as an advanced precursor for the bis(oxazoline) synthesis, resembles already the basic structure of desferrithiocin (DFT), a very important biological active siderophore (Figure 13).

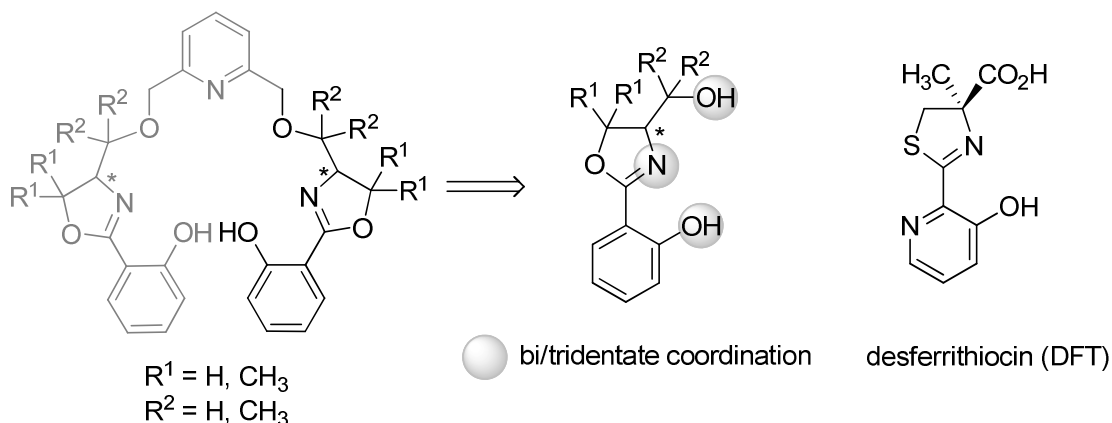


Figure 13. Oxazoline moieties as model for a siderophore (DFT) – derived from the bis(oxazoline) synthesis as precursor.

This natural product is known to be an excellent iron chelator, and just recently Bouwman and co-workers⁴⁴ reported new data on its binding behaviour by using a similar oxazoline model, only in racemic form (see discussion in *main part – oxazoline complex analysis C.2.3*, Figure 13). Realizing the close structural relationship of these chiral oxazoline derivatives (Figure 13) to the siderophore DFT and the model of Bouwman, it was of certain interest to investigate in detail their chelating properties with different iron salts and other related and interesting metals in solid state and especially in solution.

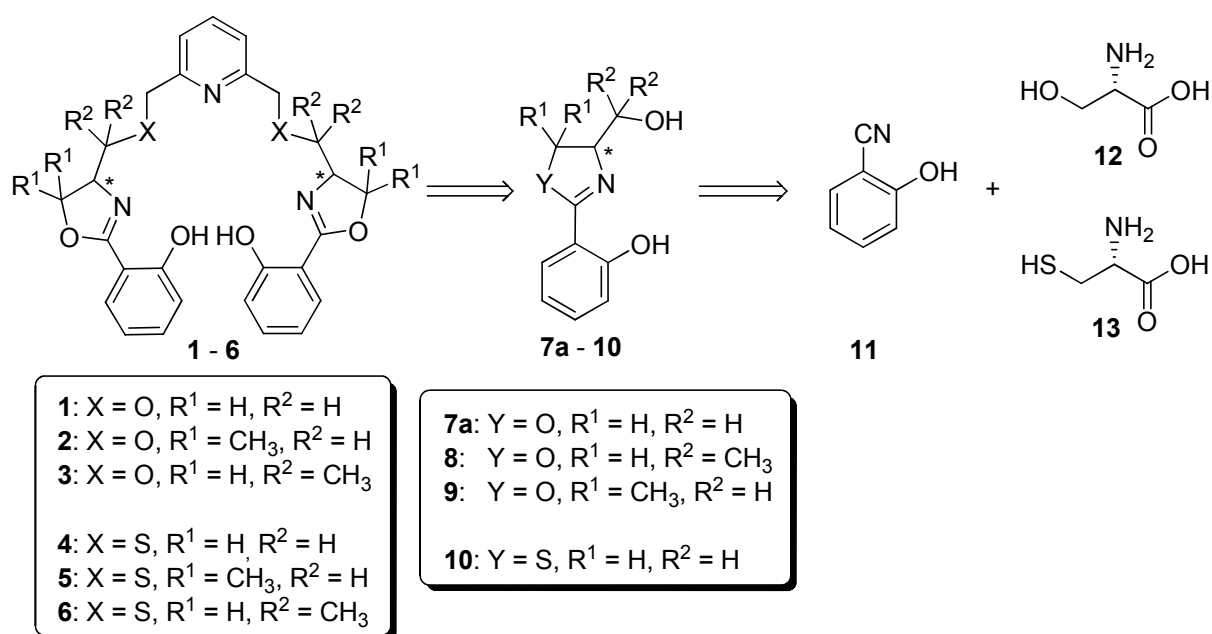
After the successful synthesis and in combination with the obtained structural data, the formed oxazoline and bis(oxazoline) complexes were screened in asymmetric oxidation catalysis reactions of non-activated C-H bonds, a still challenging field in organic chemistry with high importance not only for industrial applications.

B. Main Part – Synthesis

B.1 Ligand Synthesis

B.1.1 General Retrosynthesis of Oxazoline, Bis(oxazoline) Ligands and their Derivatives

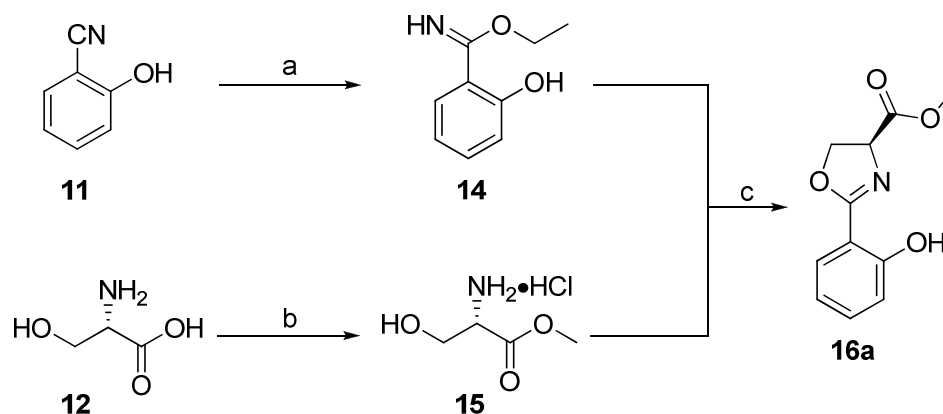
The retrosynthesis of the desired ligand systems aimed at a flexible entry into a variety of derivatives in oxazoline and bis(oxazoline) chemistry. Starting from simple and commercially available building blocks like chiral amino acids (*L*-serine (**12**), *L*-cysteine (**13**)) and an aromatic nitrile (2-hydroxybenzonitrile (**11**)), oxazoline ligands **7a-9** and their thio derivative **10** can be synthesized in a few steps (Scheme 1). To access bis(oxazolines) **1-6**, an additional pyridine linker is utilized to combine both oxazoline moieties to a C₂-symmetric molecule. Via this flexible synthetic route a number of promising ligands for mimicking biological active enzymes may be produced.



Scheme 1. Retrosynthesis of oxazoline, bis(oxazoline) ligands and their derivatives.

B.1.2 Route to Oxazoline Ligands and their Derivatives

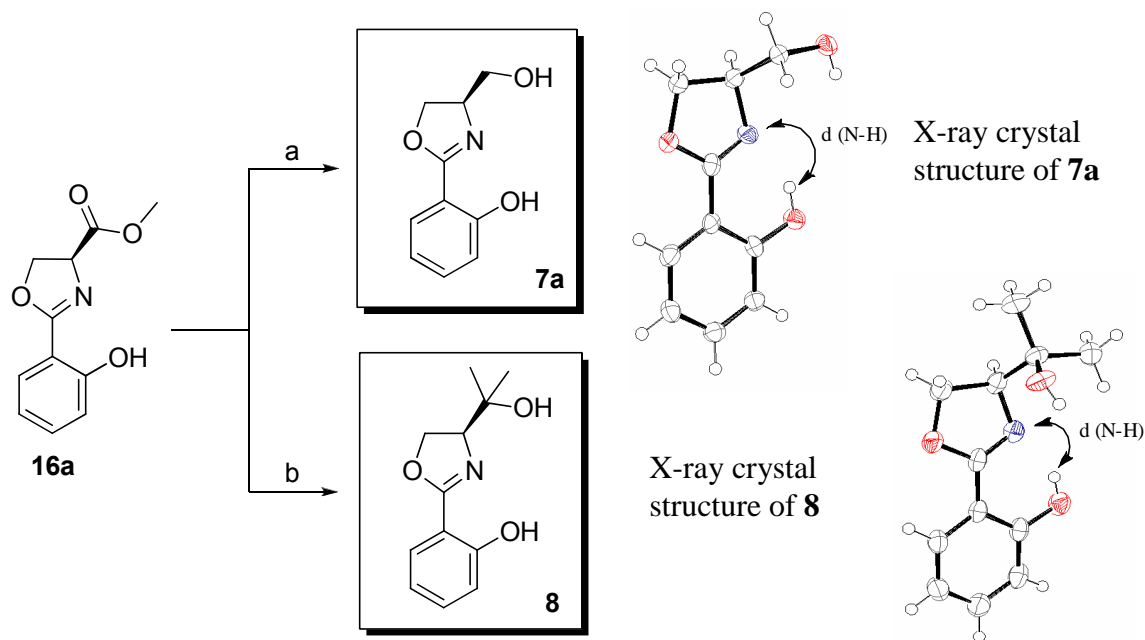
The synthesis follows standard procedures, developed in our group, using nitriles and amino alcohols as building blocks to form five-membered oxazoline-ring systems.⁴⁵ The success of these reactions depends on the reactivity of the nitriles used; in some cases they have to be activated by transformation to the corresponding imidate, in order to perform the desired ring closing reaction. To achieve this, an anhydrous stream of HCl was passed through a solution of 2-hydroxybenzonitrile (**11**) in ethanol/benzene and the imidate hydrochloride was formed, which precipitated from the solution over approximately two weeks. The hydrochloride was transformed into the free imidate **14** by addition of NaHCO₃. A subsequent liquid-liquid extraction for 24 h increased the reported yield from 45%⁴³ now up to 96% (Scheme 2, top). An esterification of *L*-serine (**12**) was the next step on the way to the oxazoline ligands. Under conventional conditions (SOCl₂, MeOH), the serine methyl ester **15** was obtained quantitatively (Scheme 2, bottom). The reaction between the imidate **14** and the chiral amino alcohol **15** resulted in the first precursor **16a** in a yield of 90%.



Scheme 2. Synthesis of oxazoline precursor **16a**: a) HCl gas (> 2.0 eq.),⁴⁶ benzene/EtOH, 0 °C, crystallization: 14 d, 96%; b) SOCl₂ (3.5 eq.), MeOH, rt, 36 h, 99%; c) **14** (1.0 eq.), **15** (1.2 eq.), C₂H₄Cl₂, reflux, 60 h, 90%.

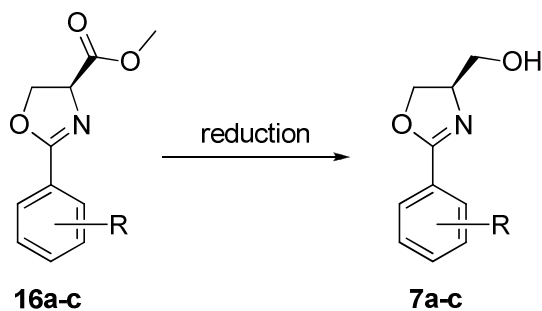
With the ester **16a** in hand, two potential oxazoline ligands could be synthesized in the next step (Scheme 3). Reduction with LAH at -30 °C formed the oxazoline **7a**, which was accessible in only 32% in enantiomerically pure form (Table 1, entry 1). Different reagents and procedures were tested to improve the reaction without loss of the chiral information, but only the more expensive DIBAL-H afforded the corresponding alcohol in 44% while retaining the same purity of the product (Table 1, entry 2). The reason for this low yield may be the presence of the *ortho*-OH substitution of the aromatic ring.

In contrast to this, reductions using LAH on similar substrates, e. g. oxazoline **16b** with the OH-group in *para*-position, resulted in 93% of the corresponding alcohol and an optical active form (Table 1, entry 3). Furthermore, the completely unsubstituted oxazoline ester **16c** was reduced as described in literature⁴⁷ and the yield was increased to 74% in comparison with earlier results reported in our group⁴² (Table 1, entry 4).



Scheme 3. Synthesis of oxazoline ligands **7a** and **8**: a) LAH (1.3 eq.), THF, -30 °C / 3.5 h – rt, 32%; b) 3.0 M MeMgBr (3.0 eq.), Et₂O, 0 °C, 5 h, 70% - ORTEP plot at the 50% probability level of ligand **7a** and **8**.

Table 1. Selected results of reductions of ester **16a-c** and similar substrates.

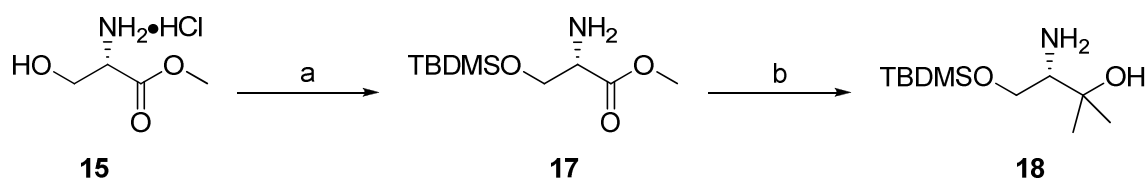


Entry	Substrate	Reaction Conditions	Yield [%]
1	R = <i>ortho</i> -OH 16a	LAH (1.3 eq.), -30 °C / 3.5 h	32
2	R = <i>ortho</i> -OH 16a	1 M DIBAL-H (3.5 eq.), 0 °C / 5 h	44 ^a
3	R = <i>para</i> -OH 16b	LAH (2.5 eq.), -30 °C - 0 °C, 100 min	93 ^a
4	R = H 16c	LAH (0.55 eq.), -30 °C - 0 °C, 75 min	74

^a optimized conditions; pH values were adjusted (pH~7).

The second oxazoline ligand **8** was synthesized by a nucleophilic attack of a Grignard reagent on the ester **16a** (Scheme 3). A commercially available MeMgBr-solution gave good yields (70%) of the tertiary alcohol **8** in this reaction. Both oxazolines provided crystals, which were suitable for X-ray structure determination (Scheme 3, right). They feature an almost planar structure between the aromatic- and the oxazoline-ring, indicating a conjugation across both systems. The proton of the phenolic OH-group remains in close proximity to the nitrogen ($d(\text{N-H})$ 1.9 Å), and it can be presumed that a long distance hydrogen bond may exist.

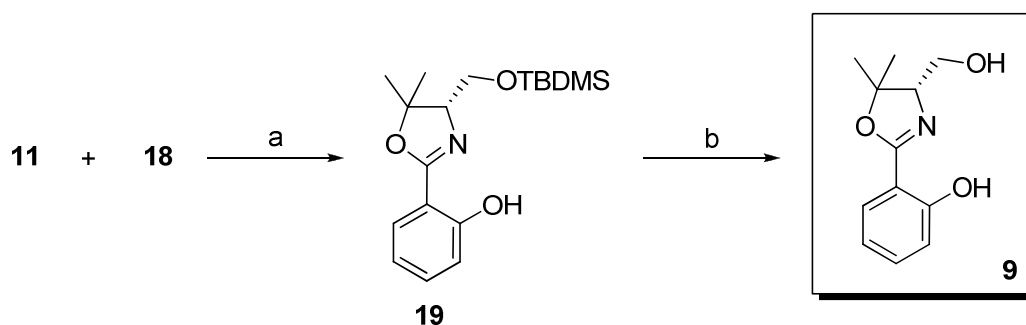
The last oxazoline ligand **9** that was synthesized in this series exhibits similar structural characteristics as the ligands **7a** and **8**, but in this case the two methyl groups are located directly on the oxazoline ring and not in the side chain. To achieve this, a change in the synthetic strategy was required:



Scheme 4. Synthesis of oxazoline precursors: a) TBDMSO (1.5 eq.), NEt₃ (3.0 eq.), DMAP (0.1 eq.), DCM, rt, 72 h, 71%; b) 3.0 M MeMgBr (3.0 eq.), Et₂O, 0 °C, 2 h, 89%.

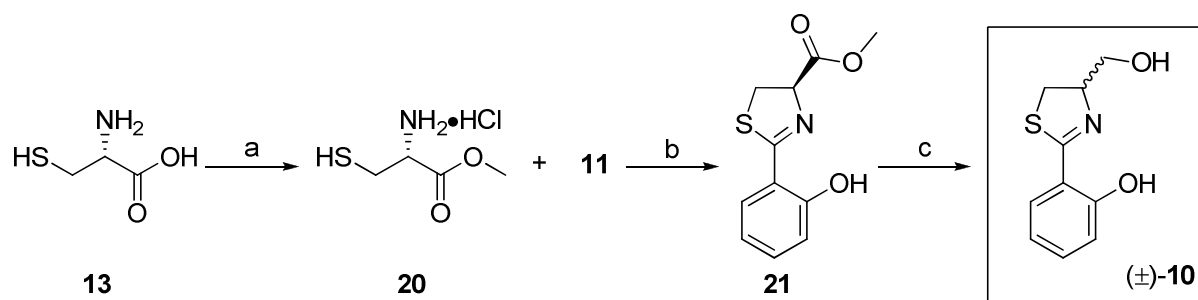
Starting again from serine methyl ester hydrochloride **15** (Scheme 4), the free alcohol is protected with TBDMSO under standard conditions, leading to ester **17** in acceptable yields. The subsequent nucleophilic attack of a Grignard reagent (MeMgBr) gave the dimethylated amino alcohol **18** in excellent yield.⁴⁸

In order to access the ligand precursor **19** (Scheme 5), the imidate **11** and the amino alcohol **18** were successfully combined in moderate yield. After deprotection with TBAF, the desired ligand **9** was isolated in an optical active form in 73% yield. Notably, the modified synthetic route offers access to the opposite stereochemistry for the oxazoline **9** (and later on of two further bis(oxazolines) **2/5**), with the configuration of the stereocentre at the oxazoline ring inverted in comparison to ligands **7a** and **8**.



Scheme 5. Synthesis of oxazoline precursor **19** and ligand **9**: a) **11** (1.0 eq.), **18** (1.5 eq.), C₂H₄Cl₂, reflux, 4 d, 62%; b) NEt₃ (0.1 eq.), TBAF (1.02 eq.), THF, rt, 20 h, 73%.

The thiazoline (±)-**10** is a known natural compound in the class of siderophores.⁴⁹ Its similarity to the oxazoline ligands provides a good base for a further derivatization. Starting from *L*-cysteine **13** instead of *L*-serine **12** the synthesis of thiazoline (±)-**10** follows a similar strategy as described above (Scheme 6).



Scheme 6. Synthesis of thiazoline ligand (±)-**10**: a) SOCl₂ (3.5 eq.), MeOH, rt, 4 d, 94%; b) **11** (1.0 eq.), C₂H₄Cl₂, reflux, 48 h, 16%; c) NaBH₄ (2.6 eq.), THF, reflux, 10 min, 61%.

The acid **13** was transformed into the cysteine methyl ester hydrochloride **20**. Coupling of the imidate **11** with the cysteine ester **20** gave a poor yield of 16% of the thiazoline ester **21**. The last step, a reduction of the ester **21** to the thiazoline alcohol (±)-**10**, also proved to be difficult. Three different procedures were investigated: NaBH₄ (Table 2, entry 1) was used as described in the literature.^{50,51} This afforded just a moderate yield of 61% thiazoline (±)-**10** in racemic form. To improve this result the starting material **21** was also treated with LAH (Table 2, entry 2) at -30 °C, but no reaction was observed. Use of DIBAL-H (Table 2, entry 3) at -30 °C, 0 °C and rt also did not provide the reduced product.

Table 2. Reduction methods of thiazoline methyl ester **21**.

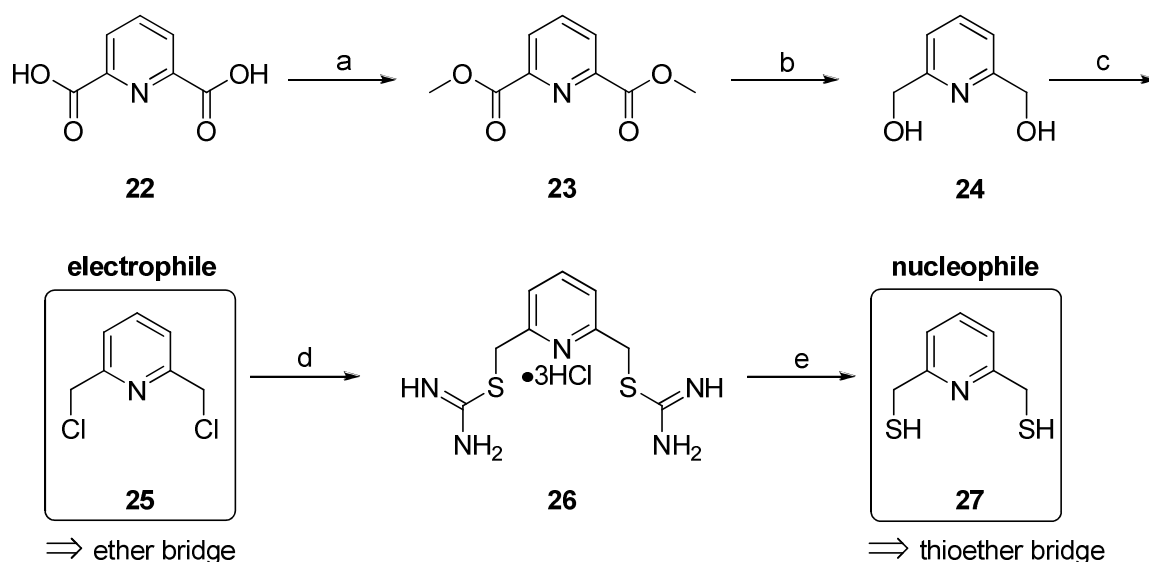
Entry	Substrate	Reaction Conditions	Yield [%]
1	21	NaBH ₄ (2.6 eq.), reflux / 10 min	61 / 60 ⁵⁰ / 41 ⁵¹
2	21	LAH (0.8 eq.), -30 °C / 3.5 h	0 ^a
3	21	DIBAL-H (3.5 eq.), -30 °C / 3.5 h, 0 °C / 2 h, rt / 12 h	0 ^a

^a only unreacted starting material recovered.

B.1.3 Route to Bis(oxazoline) Ligands

B.1.3.1 Synthesis of Pyridine Linkers

The bis(oxazoline) ligands **1-6** consist of two oxazoline units which are linked by a pyridine bridge. This bridge was synthesized starting from 2,6-pyridinedicarboxylic acid **22**, which was first transformed into the dimethylester **23** (Scheme 7). **23** was then reduced with NaBH₄ to the diol **24**, followed by dichlorination to **25** using SOCl₂. The resulting dichloride **25** was further treated with thiourea to afford diisothiurea **26**. All reactions, starting from **22** to **26** are of high yields (> 90%) and afforded very pure compounds.

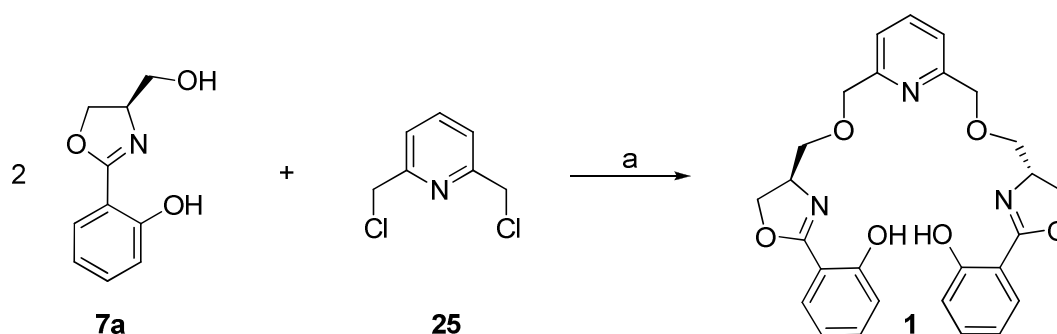


Scheme 7. Synthesis of pyridine linker moieties: a) conc. H₂SO₄, MeOH, reflux, 5 h, 90%; b) NaBH₄ (4.7 eq.), EtOH, 0 °C, 1 h, 96%; c) SOCl₂ (2.2 eq.), Et₂O, 0 °C / 1 h, rt/20 h, 90%; d) thiourea (2.4 eq.), EtOH, reflux, 30 min, 96%; e) NaOH (5.5 eq.), H₂O, reflux, 2 h, 78%.

For the preparation of dithiol **27**, a nitrogen or argon atmosphere was necessary and all solvents were degassed before use. The diisothiourea **26** was treated with NaOH and was converted into the air-sensitive dithiol **27** in an improved yield of 78% in comparison with earlier results obtained in our group.^{42,43} The resulting unpleasant-smelling product **27** was stable to storage under inert gas at -20 °C for month.

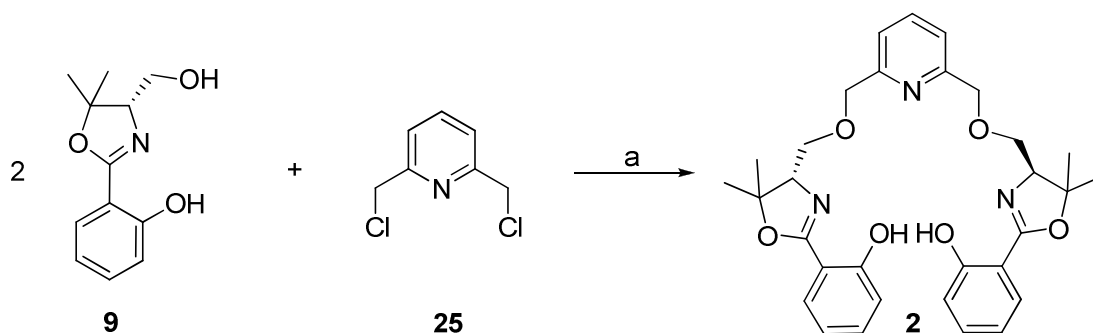
B.1.3.2 Coupling of ether-bridged Bis(oxazolines)

Bis(oxazolines) linked by an ether moiety were prepared by a S_N-type reaction of two nucleophilic oxazoline units and a dichloride pyridine linker **25** as the electrophile. NaH deprotonated both OH-groups of the oxazolines **7a**, but only the attack of the primary alcoholate at the methylene carbon of **25** was observed, leading to the desired chiral bis(oxazoline) ligand **1** in 48% yield (Scheme 8).



Scheme 8. Synthesis of bis(oxazoline) ligand **1**: a) **7a** (2.2 eq.), **25** (1.0 eq.), NaH 60% (4.1 eq.), DMF, 0 °C / 70 °C, 24 h, 48%.

A similar reaction of the dimethylated oxazoline derivative **9** resulted in a bis(oxazoline) comparable to **1** in moderate yield. This ligand **2** (Scheme 9) has the additional sterically demanding methyl groups on the oxazoline ring, and the stereocentres show an opposite configuration because of the changed synthetic strategy for the precursor **9** (Scheme 5). Furthermore, this ligand crystallized in colourless plates, which enabled X-ray crystal structure analysis, providing the final proof for the desired structure (Figure 1).



Scheme 9. Synthesis of bis(oxazoline) ligand **2**: a) **9** (2.2 eq.), **25** (1.0 eq.), NaH 60% (4.1 eq.), DMF, 0 °C / 70 °C, 72 h, 40%.

The X-ray structure of **2** is characteristically stretched⁴² and shows the pyridine moiety in the centre of the molecule, which is flanked by two ether bridges and the linked oxazoline units (Figure 1).

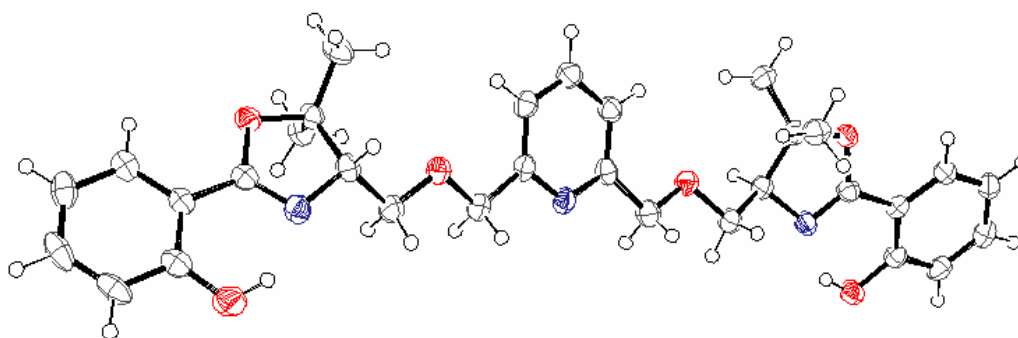
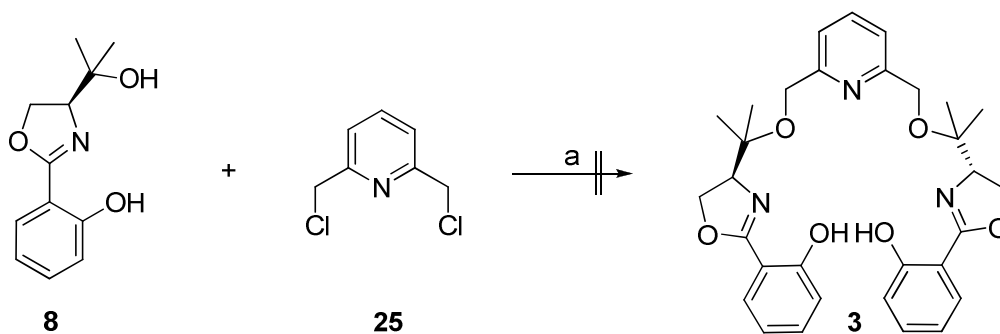


Figure 1. ORTEP plot at the 50% probability level of bis(oxazoline) **2**.

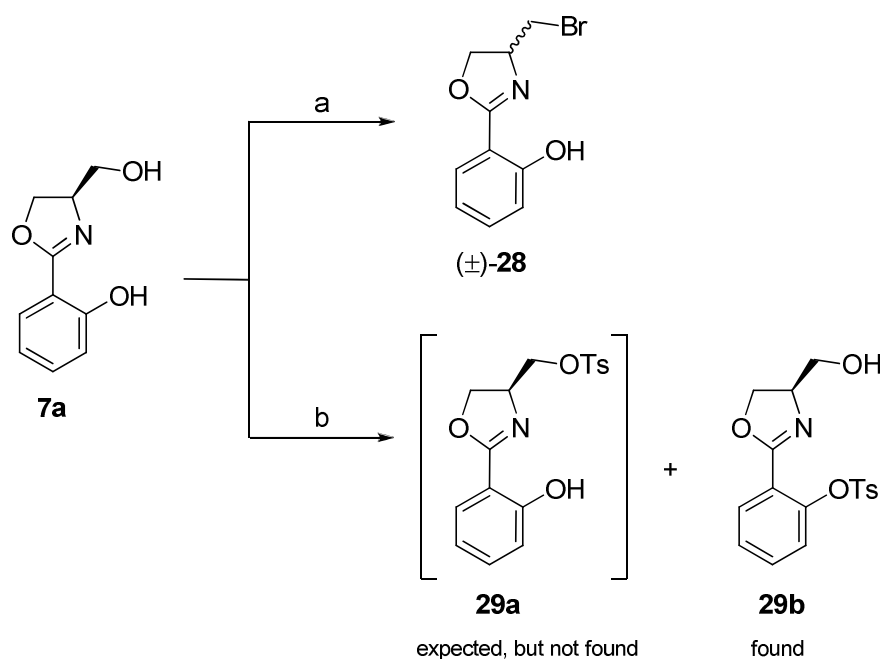
Attempts were made to couple the third oxazoline building block **8**, which contains a sterically hindered tertiary alcohol, with the pyridine linker **25**, but unfortunately this reaction failed to afford bis(oxazoline) **3** (Scheme 10). It is assumed that the methyl groups in the side chain prevent the bond formation due to an increased steric demand at the reaction centre.



Scheme 10. Attempt towards the synthesis of bis(oxazoline) ligand **3**: a) **8** (2.2 eq.), **25** (1.0 eq.), NaH 60% (4.1 eq.), DMF, 0 °C / 70 °C, 72 h, 0%.

B.1.3.3 Coupling of thioether-bridged Bis(oxazolines)

To create a related bis(oxazoline) scaffold, which contains a thioether-bridge instead of an ether-bridge, further modification needed to be done before the coupling reaction. The conversion of the alcohol in the side chain of the oxazoline units to a leaving group was therefore envisioned. The oxazoline alcohol moieties were transformed into an electrophile (Scheme 11-14) and the dithiol **27** (pyridine-linker) was used as the corresponding nucleophile. Differentiation between the aliphatic hydroxy functionality in the side chain and a phenolic one at the aromatic ring was necessary: A selective bromination of the primary alcohol under *Appel*-conditions should displace the nucleophilic OH to a good leaving group while leaving the phenolic hydroxyl group intact.^{43,52} PPh₃ and CBr₄ were used to modify oxazoline **7a** (Scheme 11, top) and the resulting bromide (±)-**28** was isolated in 67% yield, but all attempts afforded only a racemic mixture.

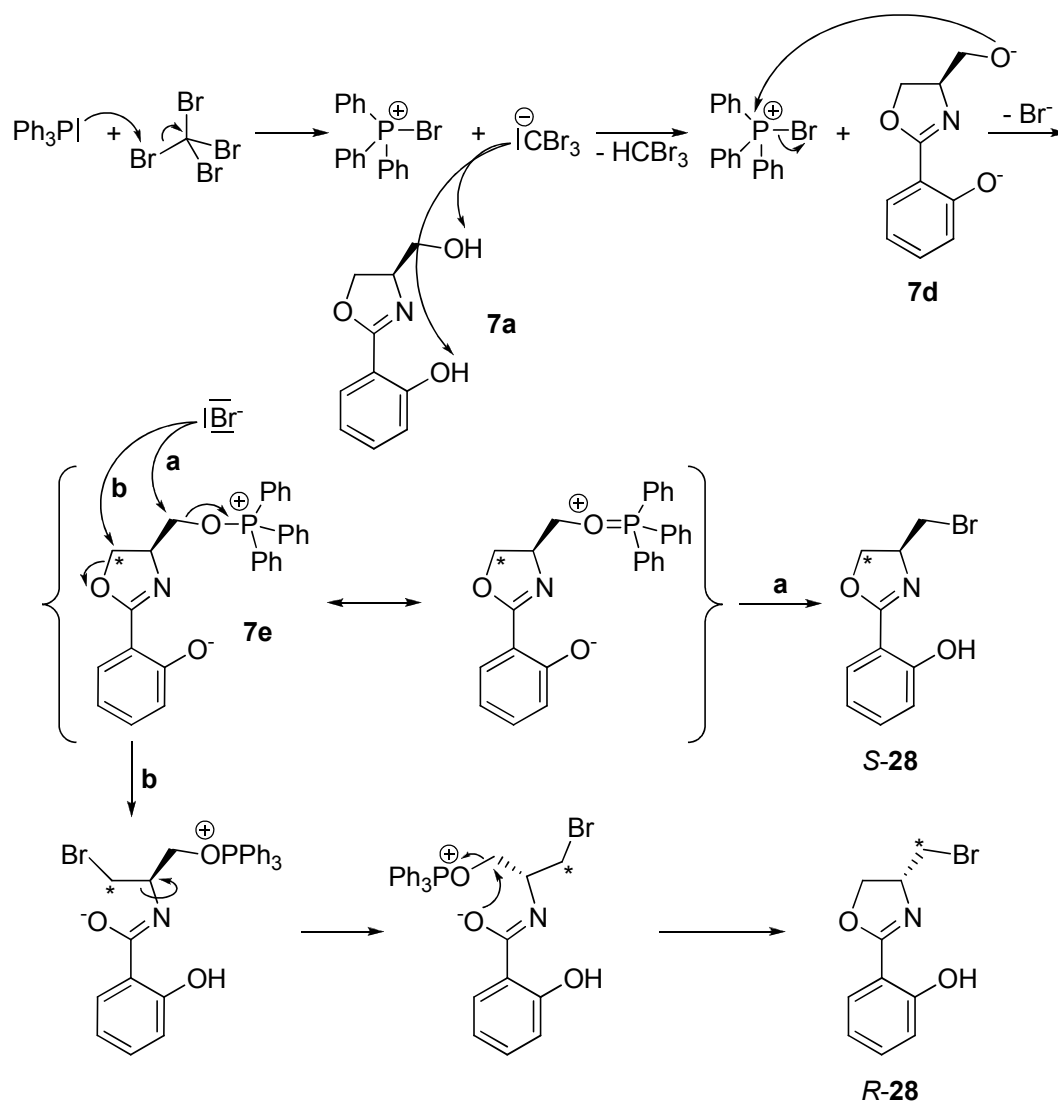


Scheme 11. Synthesis of bis(oxazoline) precursors (±)-**28** and **29a/b**: a) CBr₄ (1.2 eq.), PPh₃ (1.2 eq.), DCM, 0 °C-rt, 20 h, 67%; b) NEt₃ (2.5 eq.), TsCl (1.1 eq.), DCM, 0 °C-rt, 20 h, 67%.

To overcome this problem, a tosylation reaction was tested to prevent loss of the chiral information. This reaction tends to show no selectivity between both aliphatic and phenolic alcohols, but it was assumed that the influence of the sterical hindrance on the *ortho*-OH group would result primarily in the desired isomer **29a** (Scheme 11, bottom), if a sterical demanding reagent as tosyl is used instead of mesyl. However, the outcome of this reaction

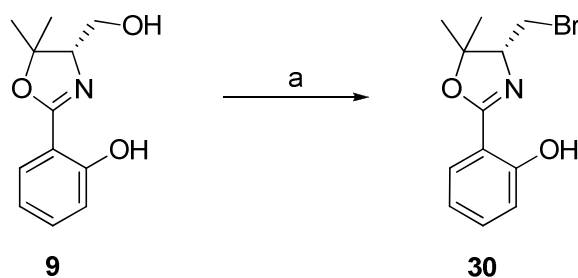
was initially unclear. ^1H NMR spectra indicated that only the phenolic alcohol **29b** was tosylated (the phenolic OH-peak at 12 ppm disappeared and the aliphatic OH-peak around 3 ppm was still present) and therefore the subsequent attempt at the coupling reaction failed. The use of a sterical hindered reagent was unfortunately not convenient. A possible explanation for the preferential formation of substituted phenol-OH **29b** can be found in the pK_s -values. The pK_s -value of a primary alcohol lies around 17, whereas a phenolic alcohol has a pK_s of approximately 10.⁵³ The base therefore deprotonated the more acidic phenolic-OH preferentially and this reacted although being sterically more hindered.

A proposed mechanism of the racemization during the *Appel*-bromination is outlined in Scheme 12: Initiated by an attack of PPh_3 on CBr_4 , a $\text{Ph}_3\text{PBr}^+\text{CBr}_3^-$ salt is formed. CBr_3^- deprotonates oxazoline **7a** to oxazoline **7d**, and in a nucleophilic substitution reaction the primary alcoholate of **7d** binds to the phosphane of the salt and forms **7e**. The final step in the *Appel*-mechanism (Scheme 12, route **a**) is fulfilled by a free bromide attack on the electrophilic methylene carbon bearing the oxygen in **7e**, resulting in the corresponding oxazoline bromide *S*-**28**. The driving force of this reaction results from the high stability of leaving group O=PPh_3 . However, this final step faces a competing reaction: The free bromide is also able to attack the electrophilic carbon (Scheme 12, route **b**) of the oxazoline ring in **7e** and initiates a ring opening reaction,⁵⁴ the bond between the nitrogen and the stereocentre is thus free to rotate. The new created oxygen nucleophile from the oxazoline ring subsequently reacts with the methylene carbon of the former side chain in a ring closing reaction to *R*-**28**, releasing O=PPh_3 . This proposed mechanism shows the generation of both enantiomers of bromide **28**, therefore explaining why the synthesis results in a racemic mixture.



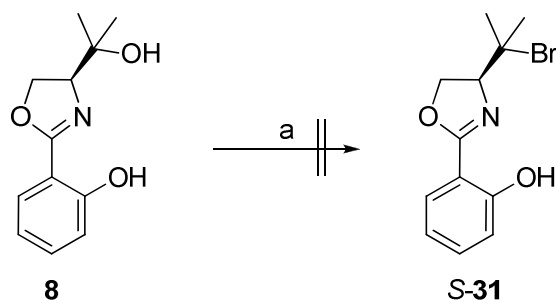
Scheme 12. Proposed mechanism for the racemization during the Appel-reaction.

To avoid the competing reaction, the electrophilic carbon in the oxazoline ring has to be made less accessible.⁴³ This property is present in oxazoline **9** with its two sterical demanding methyl groups, which also decrease the electrophilic character of this carbon (Scheme 13). Under the same reaction conditions, 90% yield of the bromide **30** was isolated in an optically active form.



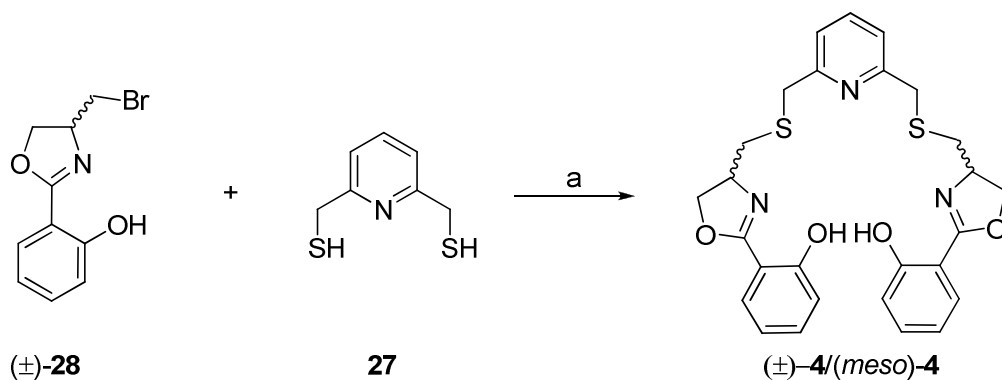
Scheme 13. Synthesis of bis(oxazoline) precursor **30**: a) CBr_4 (1.2 eq.), PPh_3 (1.2 eq.), DCM, 0 °C-rt, 24 h, 90%.

Also the conversion of oxazoline **8** into its bromide **31** was attempted (Scheme 14). In this case, the methylene carbon in the side chain contains two methyl groups, which provide steric hindrance. Unfortunately this reaction resulted in no product formation and only starting material was recovered. It is presumed that the methyl groups prohibit the initial attack of the phosphane of the salt (Scheme 14), and therefore the necessary leaving group was not formed.



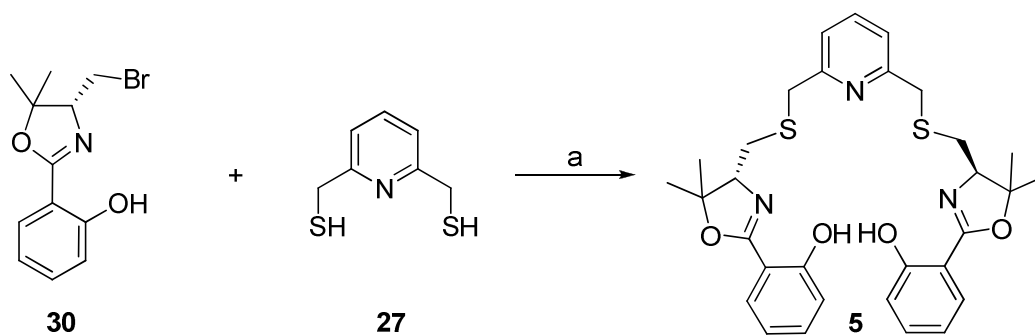
Scheme 14. Attempt towards the synthesis of bis(oxazoline) precursor **31**: a) CBr_4 (1.2 eq.), PPh_3 (1.2 eq.), DCM, 0 °C-rt, 24 h, 0%.

The racemic bromide (\pm)-**28** was successfully used in the coupling reaction with the dithiol pyridine linker **27** (Scheme 15). The S_N -reaction generated the bis(oxazoline) ligand mixture (\pm)-**4**/*meso*-**4** in 78% yield, but due to the use of the racemate of (\pm)-**28**, the bis(oxazoline) (\pm)-**4**/*meso*-**4** was not optical active.



Scheme 15. Synthesis of bis(oxazoline) ligand (\pm)-**4**/*meso*-**4**: a) (\pm)-**28** (2.2 eq.), **27** (1.0 eq.), NaH 60% (2.5 eq.), DMF, 0 °C / 70 °C, 24 h, 78%.

The successfully synthesized precursor **30** was also coupled to the dithiol pyridine linker **27**, and the chiral bis(oxazoline) ligand **5** was formed in 78% yield. Notably, bis(oxazoline) ligand **5** possesses two inverted stereo centres compared to ligands **1** and **2**, and additional sterically demanding methyl groups at the oxazoline-rings, which have their origin in the different synthesis.



Scheme 16. Synthesis of bis(oxazoline) ligand **5**: a) **30** (2.2 eq.), **27** (1.0 eq.), NaH 60% (2.5 eq.), DMF, 0 °C / 75 °C, 90 h, 78%.

In summary, three chiral oxazoline ligands **7a-9** and one racemic thiazoline ligand (\pm)-**10** were synthesized. Furthermore, two optical active ether-bridge bis(oxazoline) ligands (**1**, **2**) as well as two thioether-bridge bis(oxazoline) ligands ((\pm)-**4**/(*meso*)-**4**, **5**) were also generated. An overview of all the ligands synthesized is presented in Figure 2:

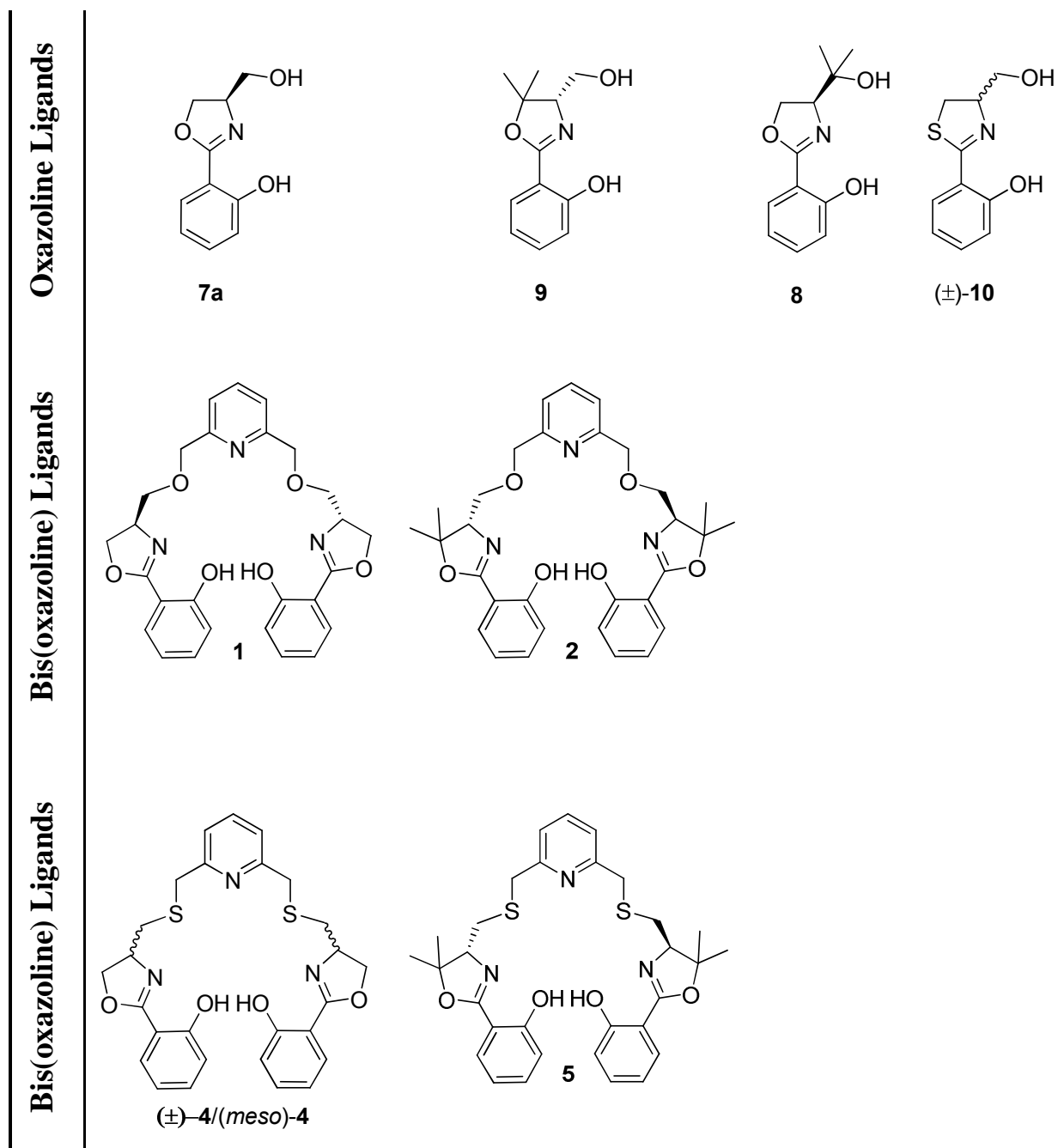


Figure 2. Ligand collection.

C. Main part – Oxazoline Complex Analysis

C.1 Determination of Stoichiometry and Equilibrium Constant

C.1.1 Siderophores – A General Introduction

The transition metal iron plays an important role in biological systems. This is based on its distribution on earth (approximately 5%) as well as its redox potential $\text{Fe}^{2+}/\text{Fe}^{3+}$ (+0.77 V / pH 0 and -0.69 V / pH 14) adequate for biological processes. The continuous access to iron over millions of years allowed its broad integration by evolution. In spite of its high deposition (second most metal abundant), its natural concentration in solution is disappearingly low under today's aerobic conditions (e.g. metal ion Fe^{3+} in the sea 10^{-17} M).^{3,55} This is caused by a restricted solubility of most iron species, which usually consist of insoluble oxides and sulfides. Furthermore, the bioavailability of iron is also limited by the solubility of Fe^{3+} ions ($<10^{-17}$ M) under physiological conditions (pH 7-8). Nevertheless, prokaryotic and eukaryotic cells need an iron concentration of 10^{-7} M for a well working metabolism.^{1,56} To handle this deficit, nature developed iron-specific chelators to supply cells with sufficient amounts of this metal. These chelators are named siderophores and are synthesized by microorganisms, e. g. bacteria and fungi, but not from higher developed species. The iron transport system in higher eukaryotes is rather based on transfer- and storage-proteins (e. g. transferrin and ferritin, respectively).^{57,58}

Around 200 different species of natural siderophores are known and they can be found in high concentrations in the ground and in the sea. Siderophores are usually secreted into the cell environment to absorb the metal, transport it into the cell, metabolize or store it and finally excrete iron out of the cells. Because of the restricted solubility of iron-species, a successful binding of iron requires a high binding constant of the formed chelat (iron-siderophore complexes, $\log K = 15-50$; in comparison: iron(III)-EDTA complex, $\log K = 25$).⁵⁹ They prefer hexadentate binding motifs and can therefore form octahedral complexes, a geometry favoured by iron. Furthermore, siderophores highly prefer Fe^{3+} in comparison to transition metals similar in size and charge. Even Fe^{2+} possesses a noticeable lower binding constant. Indeed, this allows the siderophores to bind Fe^{3+} and to release the metal again by reduction. Microorganisms produce low-molecular-weight siderophores (~300-2000 Da), which can be classified into three different types of ligands:

- (1) catecholamides (e. g. parabactin **32**),
- (2) hydroxamates (e. g. desferrioxamine DFO **33**) and
- (3) α -hydroxy/keto-carboxylates (e. g. desferrithiocin DFT **34**) (Figure 1).⁶⁰

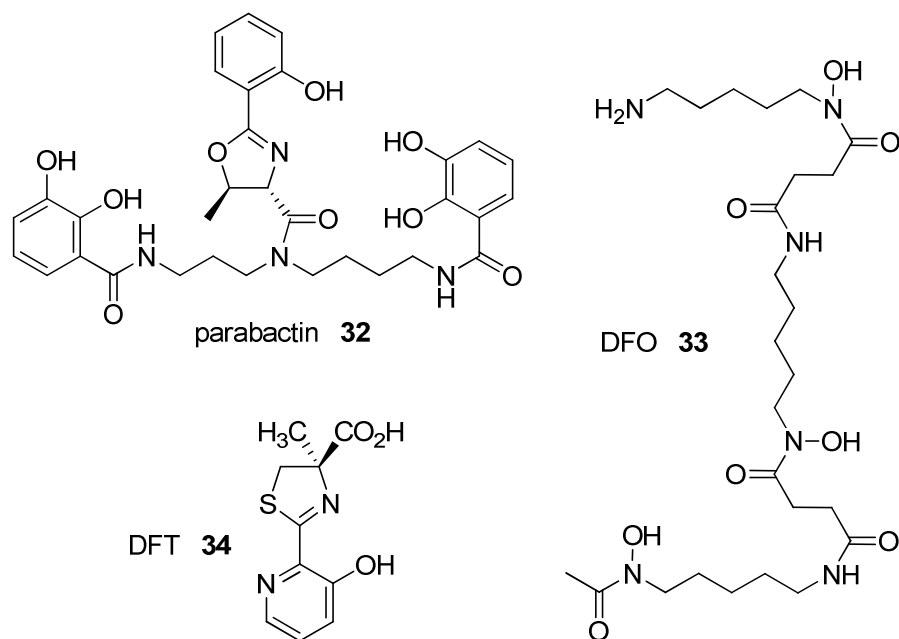
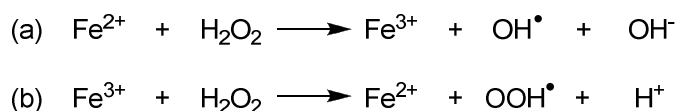


Figure 1. Different types of siderophores.

The necessity of siderophores as potential agents in medicine also becomes clear by the fact that in humans just 1 mg of iron can be absorbed and excreted per day. Iron excess leads to deposition of the transition metal in heart, liver, pancreas, and other tissues. The enhanced risk for iron-overload disease is caused by genetic defects (e. g. hemochromatosis – increased absorption of iron through nutrition; or β -thalassemia major and other refractory anemias – treatment needs continual blood transfusions and consequently a higher accumulation of iron takes place as usual). The harmful build-up of iron in the human body leads directly to other diseases like cirrhoses, diabetes, and heart dysfunction.^{57,58}

Furthermore, iron-overloading is also directly associated with significant oxidative damage to tissues. The Fenton reaction results here in serious consequences (Scheme 1). Ferrous Fe^{2+} is oxidized by an oxidant (e. g. H_2O_2) to ferric Fe^{3+} , and a free hydroxyl radical is released. Fe^{3+} is then reduced back to Fe^{2+} (e. g. by H_2O_2 or other biological reductants, e. g. ascorbate cycle) and produces a further hydrogen peroxide radical.⁶¹⁻⁶³



Scheme 1. Fenton reaction.

Free radicals are known as very harmful species in living tissues. After their formation, they are able to start radical-mediated chain processes and therefore they can attack membranes, DNA, and many other important biological components. Hence, radical reactions cause mutations in different phases of the cell, destroy the proliferation and apoptosis rhythm and lead finally to a variety of cancer.

The limited physiological mechanisms to excrete iron and the complete lack of efficient mechanisms to excrete excess iron require effective therapies.^{64,65} One of the first iron chelators that was shown to be orally active is desferrithiocin (DFT **34**, Figure 1). It belongs to a unique class of iron-complexing natural compounds and was originally observed as a metabolite in the micro-organism of *Streptomyces antibioticus*.⁶⁶ DFT is known as a tridentate siderophore that forms a stable 1:2 complex with Fe^{3+} ($\log K = 29.6$).^{67,68} In biological tests, DFT **34** proved to be a successful chelator and showed good iron-clearing efficiency values (ICE-value).⁶⁹⁻⁷¹ The enormous disadvantage of desferrithiocin **34** lies in its high nephrotoxic character.⁷¹ Therefore, the medicinal research is strongly interested in finding analogues of DFT which possess high ICEs as well as higher compatibility with the kidney.^{72,73} In addition to the medical aspects, the analysis of the binding geometry of siderophores and their electronic properties are a current area of research.

C.1.2 Stoichiometry Determination by Job`s Plot Analysis

The complex of oxazoline ligand **7a** and $\text{Fe}(\text{ClO}_4)_2 \cdot 6(\text{H}_2\text{O})$ was used as a representative oxazoline-iron complex and the stoichiometry was determined by spectrophotometric UV/Vis-titration. The typical low-energy absorption maximum around 500 nm served to detect the newly formed complex. This spectroscopic feature describes the charge-transfer transition (LMCT) from the p_π orbitals of the phenolic oxygens to the half-filled d_π^* orbitals of the ferric iron(III) ion (Figure 2).⁷⁴⁻⁷⁶

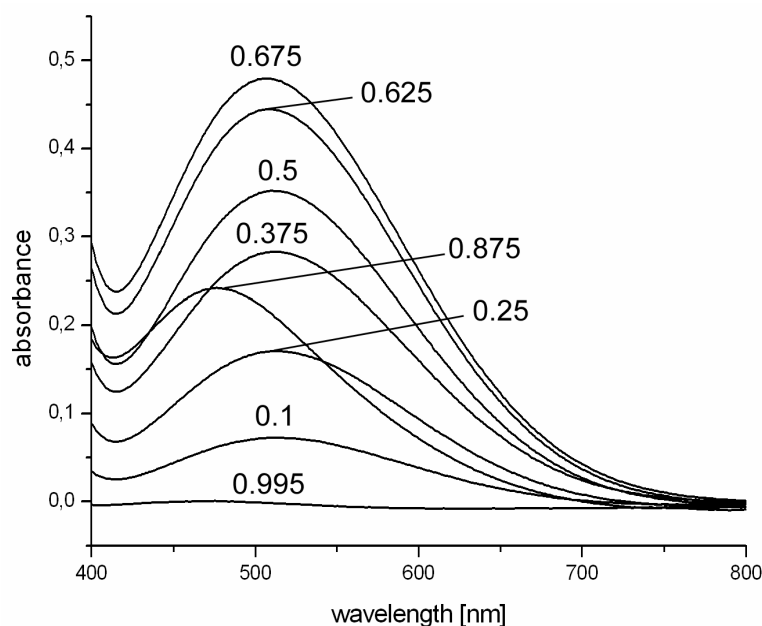


Figure 2. UV/Vis-titration for ligand **7a** and $\text{Fe}(\text{ClO}_4)_2 \cdot 6\text{H}_2\text{O}$ – mole fractions for ligand **7** are shown.

Bergeron and co-workers explored similar ligands (**35** and **36**, Figure 3), which in analogy to the oxazolines **7a-9** form 1:2 complexes with iron.^{60,77,78} It was assumed that ligand **7a**, due to its close structural relationship, would exhibit the same stoichiometry.

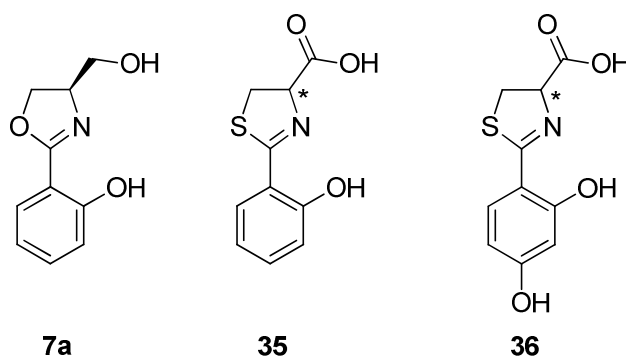


Figure 3. Oxazoline ligand **7a** and desazadesmethyldesferrithiocin analogues **35** and **36**.

Theoretically, a 1:2 complex shows a significant maximum in the Job's Plot at 0.667 for the mole fraction of the ligand. To confirm this for the case of ligand **7a**, all absorptions at the maximum of 506 nm for each concentration were plotted against the corresponding mole fraction of the ligand (Figure 4).

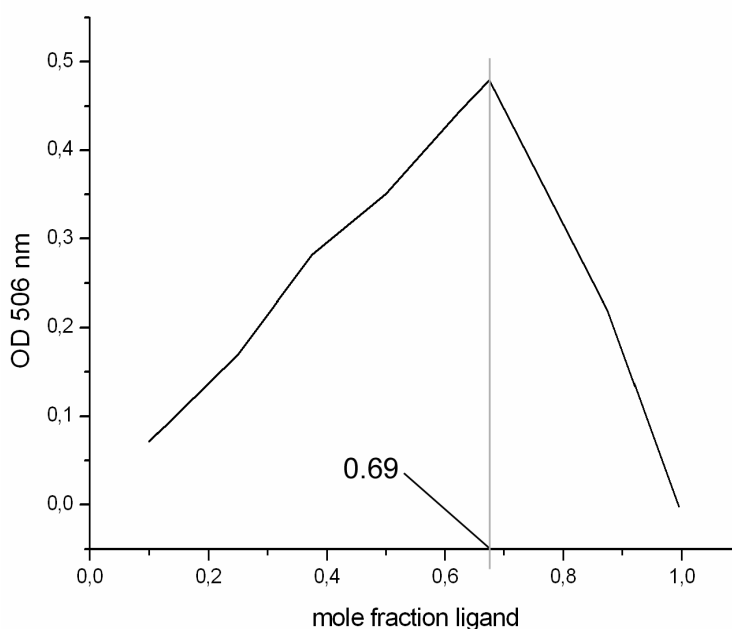


Figure 4. Job's Plot for ligand **7a** and $\text{Fe}(\text{ClO}_4)_2 \cdot 6\text{H}_2\text{O}$.^{60,78}

Indeed, the Job's Plot of ligand **7a** gave the evidence for a 1:2 complex by showing a maximum at 0.69. Due to the high structural similarity within oxazoline ligands (**7a-9**) and thiazoline ((\pm)-**10**), it is reasonable to assume that all these ligands will also form a complex with 1:2 stoichiometry, which was later confirmed by X-ray structure analysis (see *main part - oxazoline complex analysis C.2.1–C.2.8*).

C.1.3 Determination of Equilibrium-Constants

The defining characteristic of siderophores is their high affinity towards iron. Therefore, it is of highest interest to compare the affinity of typical siderophores to iron with different new model structures. Abdallah and co-workers⁷⁹ published a UV/Vis-titration experiment to determine the equilibrium constant of pyochelin **37** and its analogues (Figure 5). This experimental protocol can be used for investigations on the equilibrium constant for the complex formation using oxazoline ligand **7a**. To obtain a better understanding of the binding properties, the closely related thiazoline ligand (\pm)-**10** was also synthesized. With its thiazole moiety, (\pm)-**10** serves as a bridge between the oxazoline ligand **7a** and the siderophore pyochelin **37** and its analogues **38** / **39**, which also include a thiazole ring system.

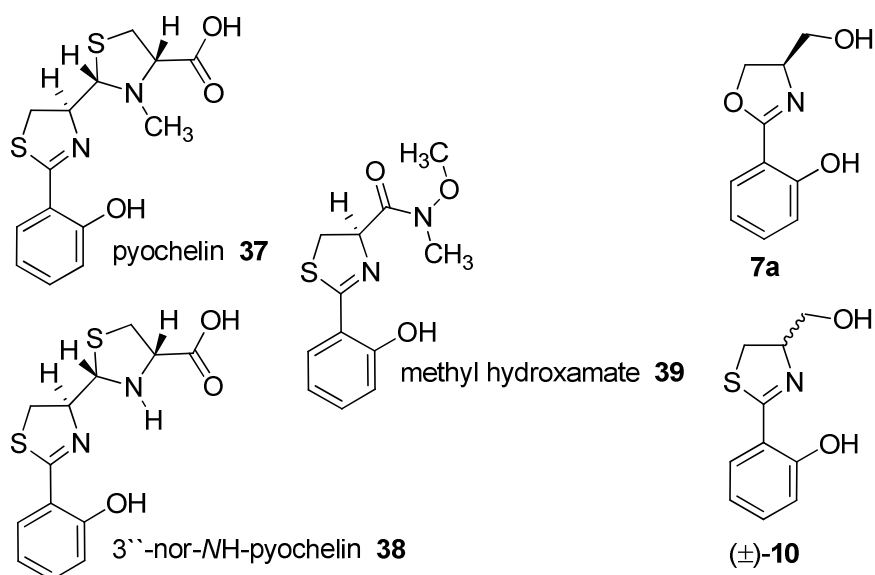
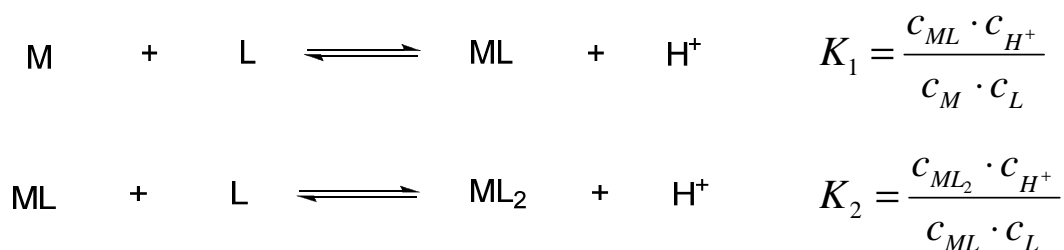


Figure 5. Bacterial siderophores **37-39** in comparison to oxazoline **7a** and thiazoline (\pm)-**10**.⁷⁹

For the investigated ligand **7a** it was already shown that the stoichiometry of binding to the metal is a 1:2 ratio (Figure 4). In theory, a ligand L is always in equilibrium with the metal M and the feasible complexes ML (1:1) and ML₂ (1:2). The equilibrium reactions of both complexes as well as their equilibrium constant equations (K_1 and K_2) are outlined in Scheme 2. For each ligand attachment, the phenol moiety of the ligand has to be deprotonated first and release one proton. To simplify this situation an acetonitrile/H₂O (1:1) system, buffered with 0.053 M formic acid, was chosen. This gives rise to the assumption that the concentration of the protons is constant while the reactions run at the same pH of ~2.



Scheme 2. Equilibrium reaction of a ML- and a ML₂- complex and the corresponding conditional equilibrium constant equations of K₁ and K₂.

The overall equilibrium constant K₃, which is given by the product of K₁ and K₂, is shown in Scheme 3 and points out the tendency of a ligand to build a 1:2 complex.

$$K_3 = K_1 \cdot K_2 = \frac{c_{\text{ML}_2} \cdot c_{\text{H}^+}^2}{c_{\text{M}} \cdot c_{\text{L}}^2}$$

Scheme 3. Overall equilibrium constant equation of K₃.

Abdallah and co-workers⁷⁹ calculated the conditional equilibrium constants for **37–39** (Table 1) using these known equations. In the case of pyochelin **37** and its derivative **38**, the equilibrium constants K₁ was found to be much higher than K₂. However, methyl hydroxamate **39** results in similar K₁ and K₂ values. The value of the overall formation constant K₃ for all 1:2 complexes is very high and confirms a strong binding to the iron ion.

Table 1. Conditional equilibrium constants (pH~2) determined for the formation of Fe(III) complexes of pyochelin and its analogs.⁷⁹

Entry	Ligand	K ₁ [M ⁻¹]	K ₂ [M ⁻¹]	K ₃ [M ⁻²]
1	pyochelin 37	6740 (±4640 69%)	274 (±178 65%)	1.85 • 10 ⁶
2	3''-nor-NH-pyochelin 38	33300 (±4940 15%)	2630 (±1070 41%)	87.6 • 10 ⁶
3	methyl hydroxamate 39	3010 (±520 17%)	2790 (±779 28%)	8.40 • 10 ⁶

As already used in for the construction of the Job's Plot (Figure 4), the same charge-transfer transition served here also as the detectable absorption band. The titration experiments are based on the Lambert-Beers law:

$$\text{absorbance } (\lambda) = \text{OD} = \varepsilon_{\text{ML}} (\lambda) \cdot c_{\text{ML}} + \varepsilon_{\text{ML}_2} (\lambda) \cdot c_{\text{ML}_2}$$

The optical density (OD) consists of the absorptions resulting from the ML (1:1) and the ML₂ (1:2) complexes formed. To obtain the extinction coefficients ε_{ML} and $\varepsilon_{\text{ML}_2}$, different titrations were done. In the forward titration a constant concentration of the metal M was used and the concentrations of the ligand L were continuously increasing (see experimental part). The complex formed at high ligand-to-metal concentration ratios was therefore assumed to have a 1:2 complex character. In the reverse titration with a constant concentration of the ligand L the concentration of the metal M was increased (see experimental part), and a complex at a high metal-to-ligand concentration ratio was expected to form a 1:1 stoichiometry.

Figure 6 and 7 show the outcome of the forward and reverse titrations of oxazoline ligand **7a** and the thiazoline ligand (\pm)-**10**, respectively, using FeCl₃•6H₂O as the iron source. On the left hand side the ligand-to-metal ratios (L/M) and on the right hand side the metal-to-ligand ratios (M/L) are given:

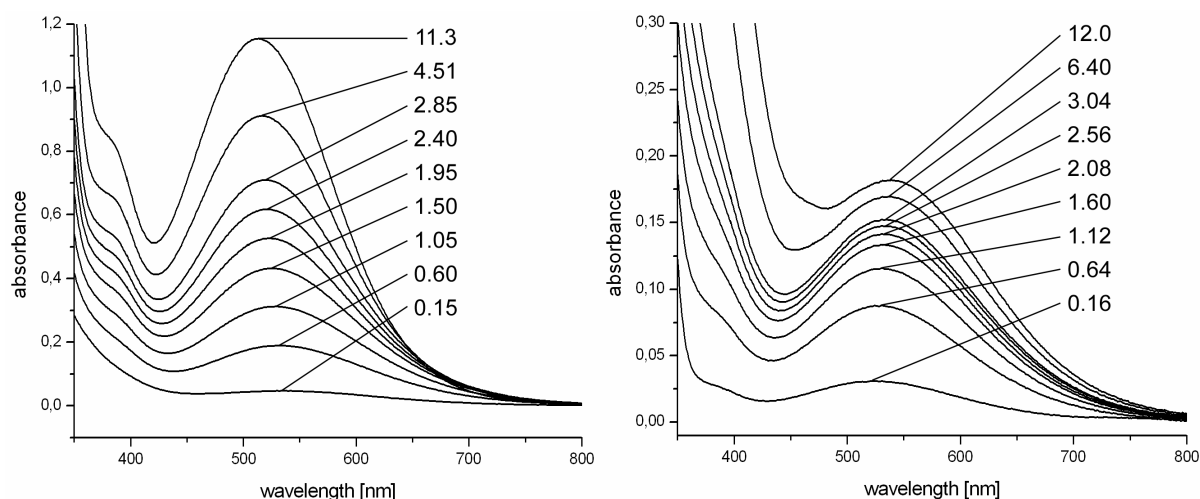


Figure 6. UV/Vis-titration for ligand **7a** and FeCl₃•6H₂O – **forward titration:** ratios of ligand **7a** / FeCl₃•6H₂O (ligand/salt) (left) and **reverse titration:** ratios of FeCl₃•6H₂O / ligand **7a** (salt/ligand) (right).

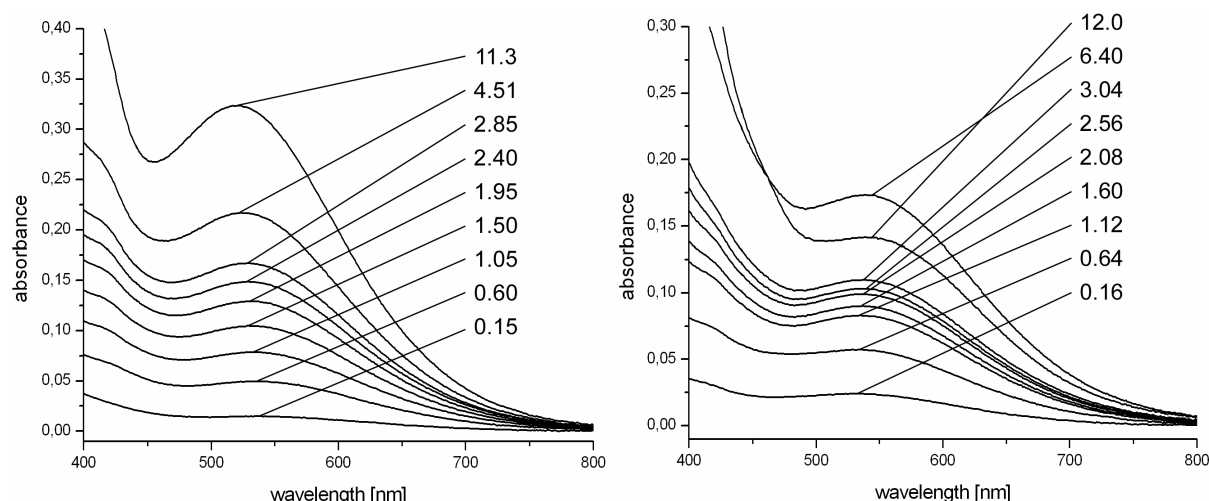


Figure 7. UV/Vis-titration for ligand (±)-**10** and $\text{FeCl}_3 \cdot 6\text{H}_2\text{O}$ – **forward titration**: ratios of ligand (±)-**10** / $\text{FeCl}_3 \cdot 6\text{H}_2\text{O}$ (ligand/salt) (left) and **reverse titration**: ratios of $\text{FeCl}_3 \cdot 6\text{H}_2\text{O}$ / ligand (±)-**10** (salt/ligand) (right).

The extinction coefficients for oxazoline **7a** and thiazoline (±)-**10** were calculated by Lambert-Beers law under the described conditions and are outlined in Table 2. The wavelengths used were chosen around the given maximum. With the extinction coefficients in hand, the conditional equilibrium constants for both ligands were accessed and point to an eight to eighteen times higher K_1 value in comparison to K_2 (Table 3, entry 1 and 3). The calculated errors of 61% and 38% of oxazoline **7a** (Table 3, entry 1) are comparable to the results obtained by Abdallah and co-workers (Table 1), but indicate a high variance in the calculated data. An attempt to optimize the equilibrium constant calculation for oxazoline ligand **7a** (Table 3, entry 2) by decreasing the dispersion of the data (excluding data points with highest variance) resulted in a K_3 value of $0.99 \cdot 10^6 \text{ M}^{-2}$ and decreased errors of 15% and 8% for K_1 and K_2 . Nevertheless, both equilibrium constants K_3 (Table 3, entry 1-2) are much smaller in comparison to the natural siderophore pyochelin **37** and its analogs **38** and **39** (Table 1).

Table 2. Extinction coefficients of the ML as well as the ML_2 complex of oxazoline **7a** and thiazoline **10**.

Entry	Ligand	Wavelength [nm]	ϵ_{ML}	ϵ_{ML_2}
1	oxazoline 7a	530	1448	4465
		580	1287	2762
2	thiazoline 10	535	1315	2506
		580	1386	2541

Table 3. Conditional equilibrium constants (pH~2) determined for the formation of Fe(III) complexes of oxazoline **7a** and thiazoline **10**.

Entry	Ligand	$K_1 [M^{-1}]$	$K_2 [M^{-1}]$	$K_3 [M^{-2}]$
1	oxazoline 7a	1134 (±690 61%)	144 (±55 38%)	$0.158 \cdot 10^6$ (±0.899 57%)
2	oxazoline 7a ^a	748 (±111 15%)	131 (±8 6%)	$0.989 \cdot 10^6$ (±0.208 21%)
3	thiazoline (±)- 10	1855 (±1996 108%)	100 (±103 102%)	$0.116 \cdot 10^6$ (±0.125 108%)

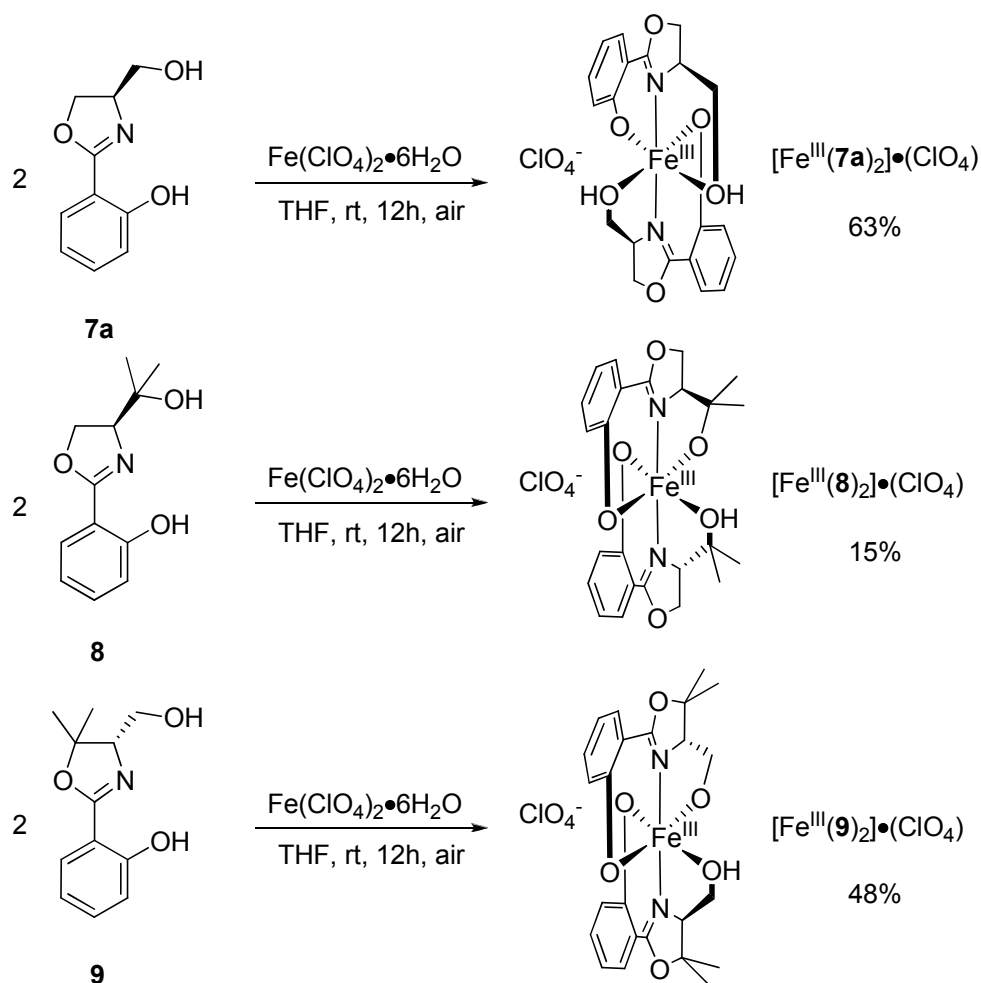
^a decreasing the dispersion of the data by excluding data points with highest variance.

With regard to the thiazoline (±)-**10** titration, the calculated errors indicate that the attempt to obtain the equilibrium constants by UV/Vis-titration completely failed (Table 3, entry 3). Even an optimization was not feasible and the reason for the unsuccessful approach is probably found in the simplified nature of the experiment. Because a racemic ligand was used, at least two complex species (*R,R* / *S,S* and *R,S*) might form and this was not paid attention to in the calculation. An improvement might be possible by a more sophisticated and multivariable data analysis program for modelling and fitting chemical kinetics, as well as expanding the theory of the complex formation kinetics.

C.2 Characterization of Oxazoline-Metal-Complexes

C.2.1 Formation of Iron(III) Complexes using $\text{Fe}(\text{ClO}_4)_2 \cdot 6(\text{H}_2\text{O})$

The series of oxazoline derivatives **7a-9** were utilized to form complexes with $\text{Fe}(\text{ClO}_4)_2 \cdot 6(\text{H}_2\text{O})$ as an iron source (Scheme 4). As already demonstrated above (see *main part - oxazoline complex analysis C.1.2*, Figure 4), this type of ligands will form 1:2 complexes. Therefore, two equivalents of ligand **7a-9** were dissolved in THF and were transferred into a solution of one equivalent $\text{Fe}(\text{ClO}_4)_2 \cdot 6(\text{H}_2\text{O})$ in THF. The colour immediately changed from slightly yellow to dark purple, indicating a rapid complex formation. In addition to that, the iron(II) complexes formed seem to be highly sensitive to air and get immediately oxidized from Fe^{2+} to Fe^{3+} (the dark purple colour originates from a charge-transfer transition from the phenolic oxygen to a iron(III) ion).⁷⁴



Scheme 4. Synthesis of iron(III) complexes $[\text{Fe}^{\text{III}}(\mathbf{7a-9})_2] \cdot (\text{ClO}_4)$ using $\text{Fe}(\text{ClO}_4)_2 \cdot 6\text{H}_2\text{O}$.

The non-coordinating nature of the counterpart anion, ClO_4^- , leads to the assumption that the hydroxymethylene alcohols also coordinate to the iron(III) centre, to form the preferred octahedral geometry, which was later proven by X-ray analysis (Figure 8).

C.2.2 Solid-State-Analysis of Iron(III) Complexes – $[\text{Fe}^{\text{III}}(\mathbf{7a-9})_2] \cdot (\text{ClO}_4)$

Typical features of the complexes $[\text{Fe}^{\text{III}}(\mathbf{7a-9})_2] \cdot (\text{ClO}_4)$ were identified by investigating the IR spectra. A broad alcohol stretch at $3250 - 3400 \text{ cm}^{-1}$ and the shift of an attributed strong band from 1644 cm^{-1} (uncoordinated and unsaturated $\text{C}=\text{N}$ stretch) to 1612 cm^{-1} for a coordinating ligand $\text{C}=\text{N}$ vibration are seen. Furthermore, a characteristic broad and very strong band at 1080 cm^{-1} as well as a sharp band at 619 cm^{-1} indicated the presence of a perchlorate.⁸⁰

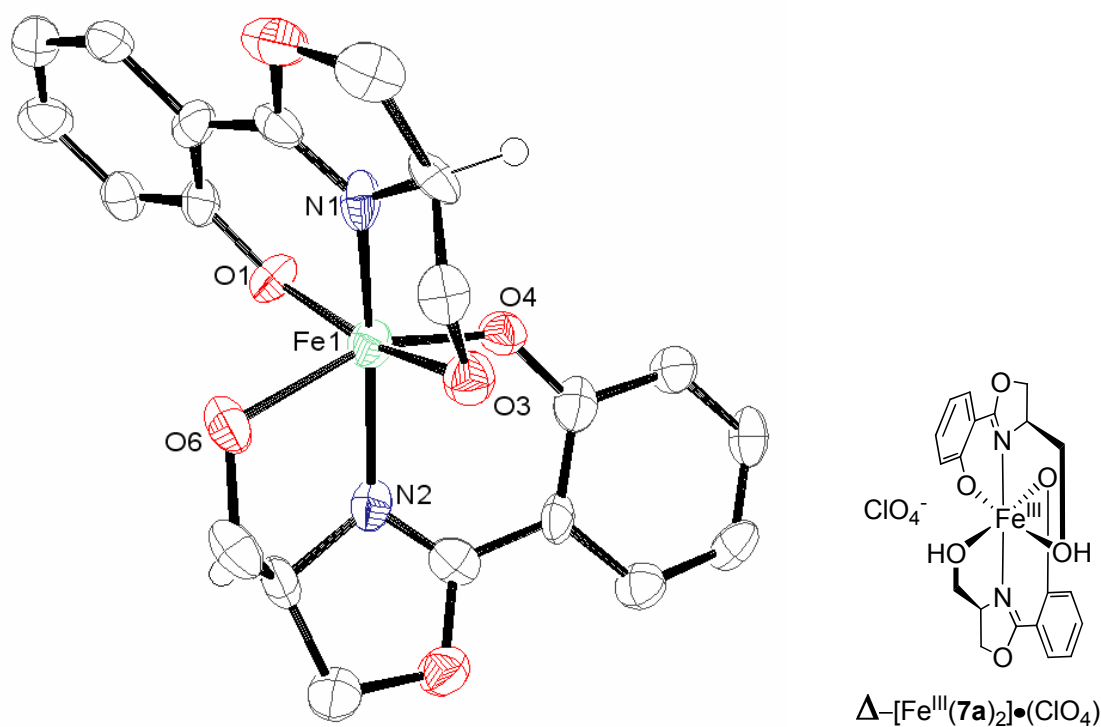


Figure 8. ORTEP plot at the 50% probability level of $[\text{Fe}^{\text{III}}(\mathbf{7a})_2] \cdot (\text{ClO}_4)$ – (not important hydrogen atoms and ClO_4^- are omitted for clarity).

In the crystallographic measurement of $[\text{Fe}^{\text{III}}(\mathbf{7a})_2] \cdot (\text{ClO}_4)$ the two ligands are bound meridionally to the metal centre (Figure 8). This class of oxazoline-phenolates chelates iron with their nitrogen atoms of the oxazoline-ring systems, the deprotonated phenolates and the protonated hydroxymethylene groups of the side chain. In the resulting bis(tridentate) iron(III) complex $[\text{Fe}^{\text{III}}(\mathbf{7a})_2] \cdot (\text{ClO}_4)$, the iron(III) ion equalizes two negative charges on the phenolates and one perchlorate in the outer environment of the complex to give a neutral compound. The

distance of the two oppositely placed nitrogen atoms to the octahedral chelated metal has the typical length of 2.00 to 2.03 Å (Table 4), which was also observed in a similar crystal structure (Figure 13) obtained by Bouwman and co-workers,⁴⁴ who used a comparable ligand system ((±)-**46**, see *main part - catalysis* **E.1.1**, Figure 1). The bond lengths between the iron centre and the phenolate oxygen atoms (Fe(1)-O(1), Fe(1)-O(4)) of 1.88 Å and the hydroxymethylene group (Fe(1)-O(3), Fe(1)-O(6)) of 2.23 / 2.26 Å to the metal centre fit also to these published data.⁴⁴ A *trans*-oriented alignment of N(1)-Fe(1)-N(2) was confirmed by an angle of 159°, leading to a slightly distorted octahedral geometry. Characteristic for a meridional ligand is also the angle between both oxygen binding sites (O(1)-Fe(1)-O(3)), spanning 159°, which indicates a nearly opposite position. The orientation of both ligands is described by the angle between O(1)-Fe(1)-O(6) with 92°, showing the ligands in a nearly perpendicular alignment (Table 4). The complex [Fe^{III}(**7a**)₂](ClO₄) was identified as a *mer*-(O,N,O-Δ) isomer (Figure 9).

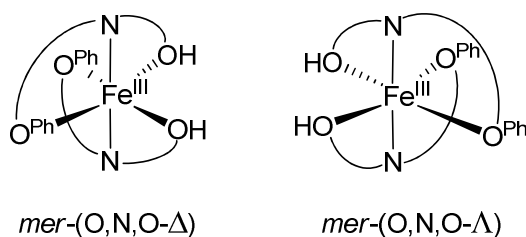


Figure 9. Meridional octahedral binding models Δ and Λ for two tridentate ligands.⁸¹

An overview of all obtained iron(III) oxazoline X-ray structures is given in *experimental part* – **F.11**, Figure 8.

Table 4. Selected bond distances (Å) and angles (°) of $[\text{Fe}^{\text{III}}(\mathbf{7a})_2]\cdot(\text{ClO}_4)$.

Bond Distances [Å]		Angles [°]	
Fe(1)-O(1)	1.881(7)	O(1)-Fe(1)-O(3)	158.7(3)
Fe(1)-O(3)	2.255(9)	O(1)-Fe(1)-O(4)	103.2(3)
Fe(1)-O(4)	1.881(8)	O(1)-Fe(1)-O(6)	91.8(3)
Fe(1)-O(6)	2.227(8)	O(1)-Fe(1)-N(1)	87.0(4)
Fe(1)-N(1)	2.003(10)	O(1)-Fe(1)-N(2)	106.7(4)
Fe(1)-N(2)	2.023(9)	O(3)-Fe(1)-O(4)	89.2(3)
		O(3)-Fe(1)-O(6)	82.0(3)
		O(3)-Fe(1)-N(1)	72.9(3)
		O(3)-Fe(1)-N(2)	91.0(3)
		O(4)-Fe(1)-O(6)	158.1(3)
		O(4)-Fe(1)-N(1)	104.9(4)
		O(4)-Fe(1)-N(2)	87.3(3)
		O(6)-Fe(1)-N(1)	91.6(3)
		O(6)-Fe(1)-N(2)	73.0(3)
		N(1)-Fe(1)-N(2)	159.3(4)

Furthermore, the mass spectrometry (ESI) shows for all complexes $[\text{Fe}^{\text{III}}(\mathbf{7a-9})_2]\cdot(\text{ClO}_4)$ a significant mass peak corresponding to the 1:2-iron(III) complex $([\text{Fe}^{\text{III}}(\text{L})_2]^+)$ of the specific ligand. Additionally in two spectra the mass for the free ligand (L) was detected. The elemental analysis confirmed for all three compounds the proposed complex system, including two ligands with deprotonated phenols, one iron metal and one perchorate ion (Scheme 4).

C.2.3 Liquid-State-Analysis of Iron(III) Complexes – $[\text{Fe}^{\text{III}}(\mathbf{7a-9})_2]\cdot(\text{ClO}_4)$

The UV/Vis spectra of the complexes $[\text{Fe}^{\text{III}}(\mathbf{7a-9})_2]\cdot(\text{ClO}_4)$ were measured between 200 and 750 nm in acetonitrile at room temperature (Figure 10). All three iron(III) compounds show the same absorption bands indicating the same structure in solution, which was also strengthened by comparing the UV/Vis spectra of further iron(III) complexes with a different binding motive (see *experimental part F.9.2*, Figure 7). To differentiate which absorption maximum belongs to the metal, the ligand or to the complex, each of them was explored

separately under the same conditions (see *experimental part F.9.2*, Figure 1 and 4) and so an assignment of the high energy maxima at 240 nm and 300 nm was possible. They characterize ligand based transitions ($n \rightarrow \pi^*$ or $\pi \rightarrow \pi^*$) and are probably caused by the chromophore of the conjugated system in the ligand. The shoulder between 350 and 400 nm as well as the absorption at 475 nm are identified as complex specific. These features in the electronic spectra are the relatively intense charge-transfer (CT) bands responsible for the dark purple colour and they can be assigned to a transition from the p_π orbital on the phenolate oxygen to the half-filled d_π^* orbitals on the ferric iron(III) ion.⁷⁴⁻⁷⁶

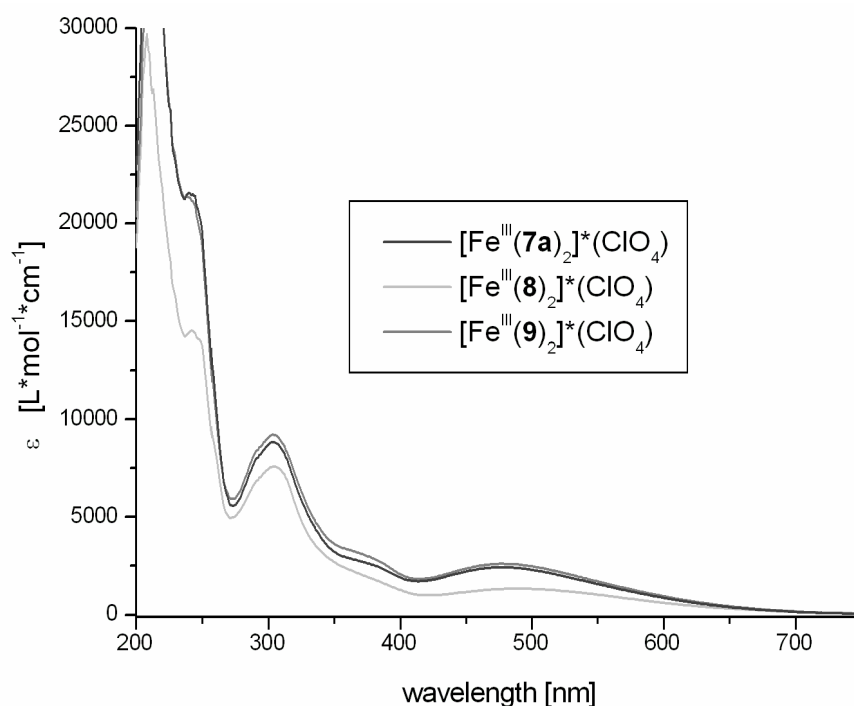


Figure 10. UV/Vis spectra for the $[\text{Fe}^{\text{III}}(\mathbf{7a-9})_2] \cdot (\text{ClO}_4)$ series.

The circular dichroism spectra (CD) of the $[\text{Fe}^{\text{III}}(\mathbf{7a-9})_2] \cdot (\text{ClO}_4)$ series exhibit a high similarity in behaviour under the influence of circularly polarized light (Figure 11), and are not comparable to the CD spectra of further iron(III) complexes. An example for this, including ligand **7a** is shown in *experimental part F.9.2*, Figure 7.

The specific features of this class of iron(III) complexes reach from 200 to 750 nm, measured in acetonitrile at room temperature. Complex $[\text{Fe}^{\text{III}}(\mathbf{7a})_2] \cdot (\text{ClO}_4)$ (Figure 11, black line), for which the crystallographic data are known, was identified as an octahedral Δ -isomer with two tridentate meridional ligands, and it is presumed that $[\text{Fe}^{\text{III}}(\mathbf{7a})_2] \cdot (\text{ClO}_4)$ has the same conformation in solution. Following this assumption, the CD spectra of the complexes $[\text{Fe}^{\text{III}}(\mathbf{8/9})_2] \cdot (\text{ClO}_4)$ (Figure 11, light and dark grey line), can be interpreted as their mirror

imaged curves in comparison to $[\text{Fe}^{\text{III}}(\mathbf{7a})_2] \cdot (\text{ClO}_4)$, what leads to the reasonable assumption that $[\text{Fe}^{\text{III}}(\mathbf{8/9})_2] \cdot (\text{ClO}_4)$ will form the opposite meridional Λ -isomer. However, this conclusion, obtained from the CD, means that two stereo chemical analogue ligands **7a** and **8**, differing only in the substituted methylene alcohols, are able to control both complex geometry formations. Within this thesis, this effect was observed only by using $\text{Fe}(\text{ClO}_4)_2 \cdot 6(\text{H}_2\text{O})$ and might be caused by its unique meridional complex binding ability.

The CD spectra of the ligands **7a-9** (see *experimental part F.9.2*, Figure 4) are still in agreement with their stereo chemical information.

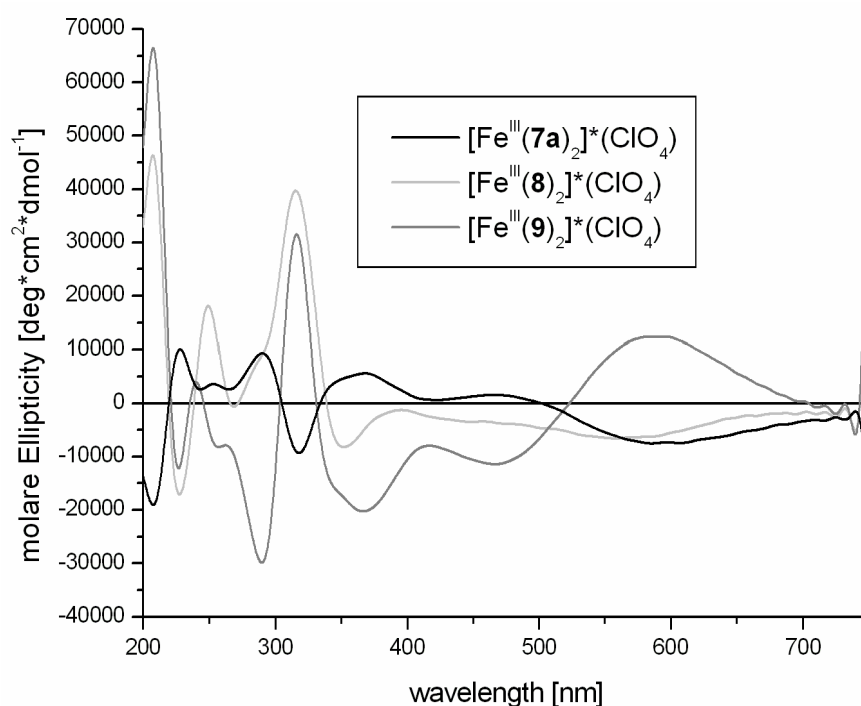


Figure 11. CD spectra for the $[\text{Fe}^{\text{III}}(\mathbf{7a-9})_2] \cdot (\text{ClO}_4)$ series.

The observation that ligands with identical absolute configuration of the chiral carbon atom are able to form both enantiomeric metal coordination geometries was already reported by Hahn and co-workers.⁶⁸ In the anionic chromium(III) complex including ligand **34** (DFT, desferrithiocin) the counter cation controls the meridional isomer formation. The Λ -isomer was crystallized as the tetramethylammonium salt, and the Δ -isomer was obtained as the potassium salt (Figure 12).

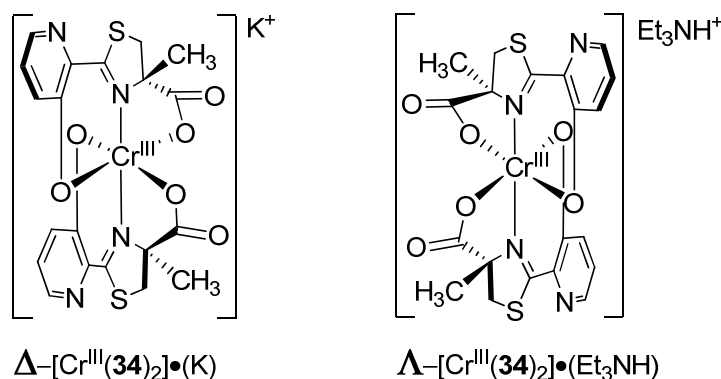


Figure 12. Two chromium(III) complexes, including the *S*-configured ligand **34** and different counter cations, are able to form different metal geometries.⁶⁸

The proposed structure model of the siderophore desferrithiocin (DFT), chelating an Fe³⁺ ion, predicted a meridional octahedral iron(III) complex formation (Figure 13, top).⁷⁷ Bouwman and co-workers⁴⁴ reported recently a structurally-characterized analog for an iron(III) siderophore complex, using a very similar ligand structure to DFT, which contains instead of a chiral thiazoline system a racemic oxazoline moiety (\pm)-**46** (Figure 13, bottom, right). The crystallized complex consists only of the (*S*)-configured ligand and shows an anionic isomer of (HNEt₃)₂•[Fe^{III}((*S*)-**46**)₂](ClO₄).

The comparability of the proposed structure formation as well as the model of Bouwman to the X-ray structure of complex [Fe^{III}(**7a**)₂](ClO₄) (Figure 13, bottom, left), which resulted from a DFT related enantiopure ligand **7a**, provides a further suitable model system to mimic the binding characteristic of this important siderophore. Both obtained crystal structures for (HNEt₃)₂•[Fe^{III}((*S*)-**46**)₂](ClO₄) and [Fe^{III}(**7a**)₂](ClO₄) show the same metal geometry (Figure 13, bottom). Due to the enantiopure ligands **7a-9**, the CD spectroscopy of the corresponding iron(III) complexes offers further information on the complex behaviour in solution.

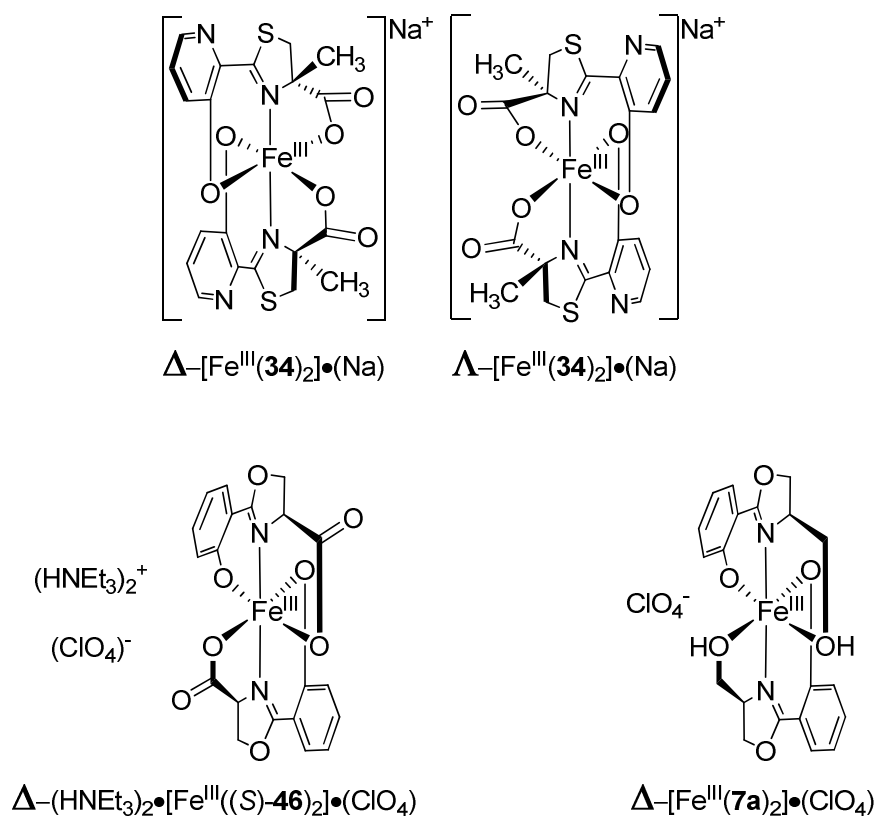
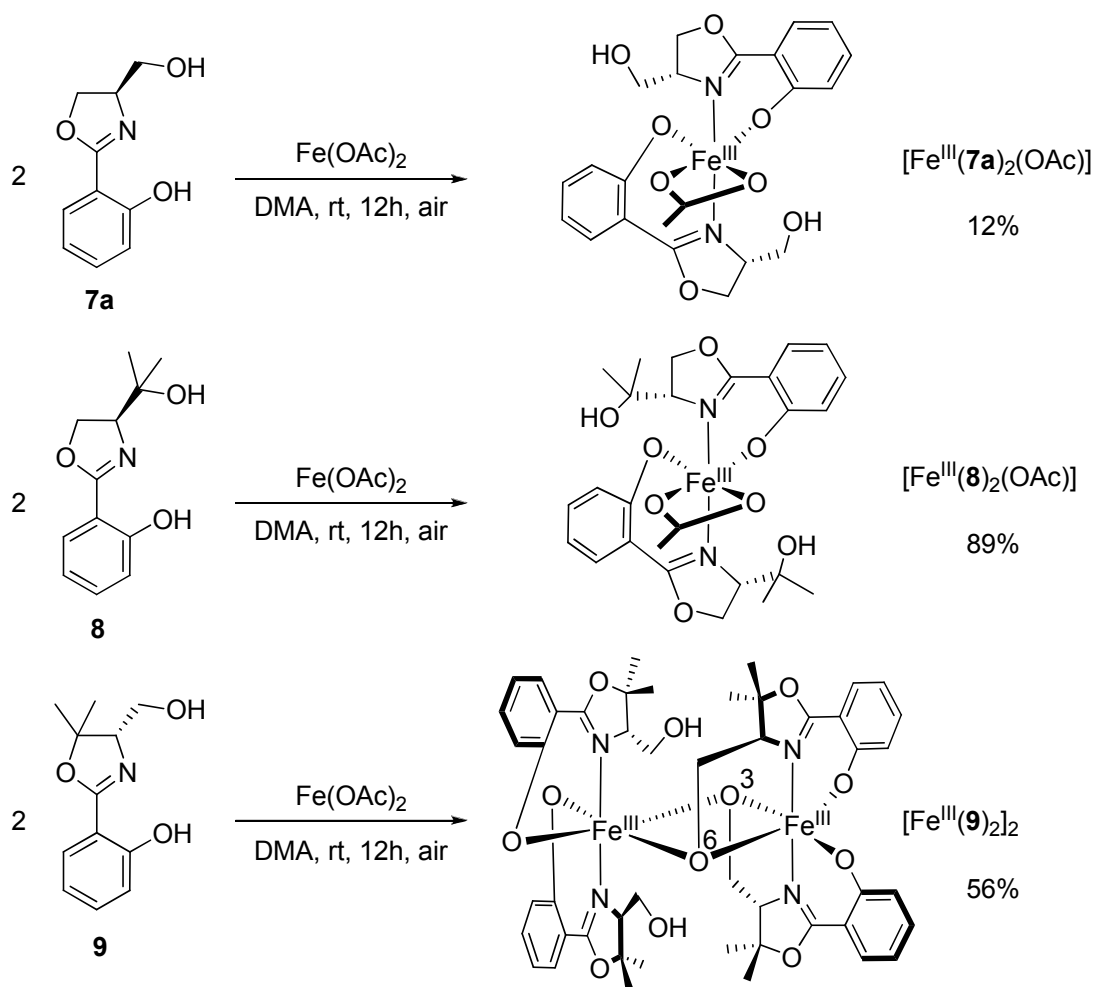


Figure 13. Proposed structure of desferrithiocin diastereomeric 1:2 complexes with Fe^{3+} (top); X-ray structure of the anionic isomer $\text{mer-}[\text{Fe}^{\text{III}}(S)\text{-}\mathbf{46}]_2^-$ (bottom, left) and determined structure of $[\text{Fe}^{\text{III}}(\mathbf{7a})_2]\bullet(\text{ClO}_4)$ (bottom, right).^{68,77}

C.2.4 Formation of Iron(III) Complexes using $\text{Fe}(\text{OAc})_2$

Many nonheme iron enzymes are based on N- and O-containing ligands, and therefore carbonic acids plays an important role as oxygen source. To investigate this on the oxazoline ligand systems, $\text{Fe}(\text{OAc})_2$ was chosen to test the effect of an acetate residue on the metal centre. The preparation of the $[\text{Fe}^{\text{III}}(\mathbf{7a-9})_2(\text{OAc})]$ complex series required a change of the solvent. $\text{Fe}(\text{OAc})_2$ proved to be highly insoluble in THF and only the use of a very polar solvent led to a homogenous solution, which is necessary for a successful complex formation. Two equivalents of ligand **7a-9** were therefore dissolved in N,N-dimethylacetamide (DMA) and transferred into a solution of $\text{Fe}(\text{OAc})_2$ in DMA (Scheme 5), which was accompanied by an immediate colour change from slightly yellow into a dark orange-red complex. This intensive colour is significant for these complex formations and it is assumed that the iron(II) complex initially formed is not stable on air and is oxidized.⁷⁴



Scheme 5. Synthesis of iron(III) complexes $[\text{Fe}^{\text{III}}(\mathbf{7a-9})_2(\text{OAc})]$ using $\text{Fe}(\text{OAc})_2$.

C.2.5 Solid-State-Analysis of Iron(III) Complexes – $[\text{Fe}^{\text{III}}(\mathbf{7a-9})_2(\text{OAc})]$

IR analysis of all three $[\text{Fe}^{\text{III}}(\mathbf{7a-9})_2(\text{OAc})]$ complexes revealed a typical stretch of the free alcohols at $3340 - 3410 \text{ cm}^{-1}$ and the shifted strong stretch from 1644 cm^{-1} (uncoordinated and unsaturated C=N stretch) to 1604 cm^{-1} for a coordinating ligand C=N vibration. The bound acetate is detected by two characteristic bands at 1580 cm^{-1} and at 1240 cm^{-1} .

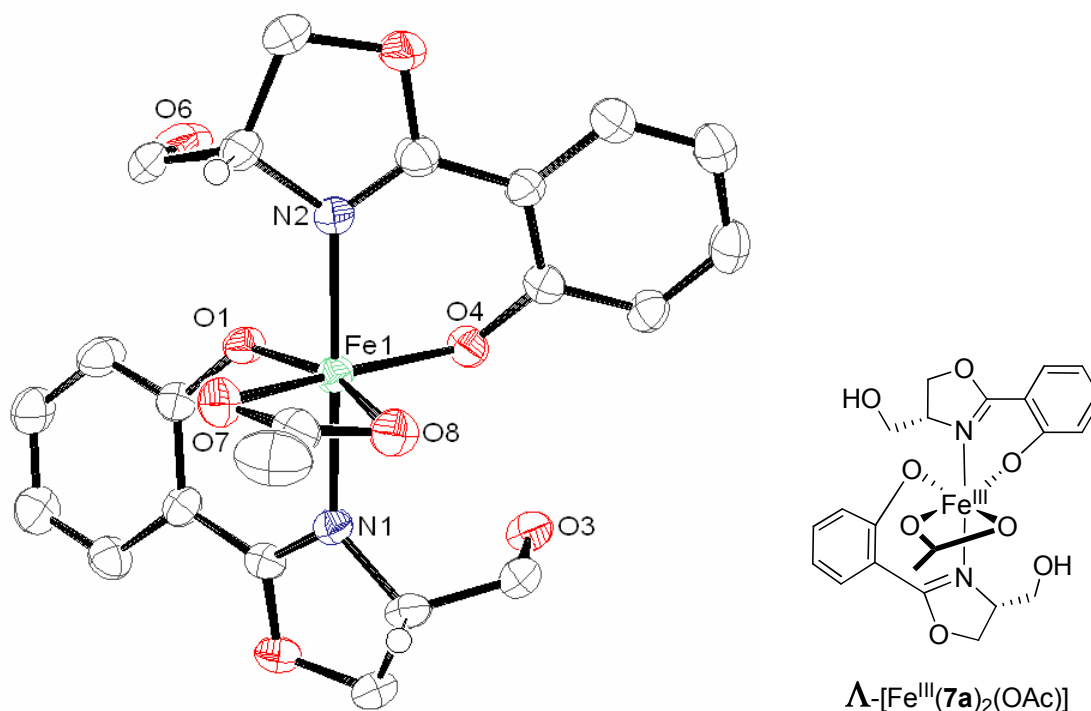


Figure 14. ORTEP plot at the 50% probability level of $[\text{Fe}^{\text{III}}(\mathbf{7a})_2(\text{OAc})]$ – (not important hydrogen atoms are omitted for clarity).

For complex $[\text{Fe}^{\text{III}}(\mathbf{7a})_2(\text{OAc})]$ a crystal structure was obtained (Figure 14). The iron(III) centre is chelated by two bidentate oxazoline ligands **7a** and one bidentate acetate. The positive charge of the metal is in balance with two deprotonated phenolates as well as with the negative charge of the acetate. The distorted octahedral binding structure is given by the *trans*-oriented nitrogen atoms with an angle of 179° (N(1)-Fe(1)-N(2)) and a bond distance of 2.09 \AA (Fe(1)-N(1)/(2)) (Table 5). Furthermore, the nearly planar orientation of the four oxygens of the phenolates and the acetate around the iron are in agreement with this geometry. The bond lengths of O(1) and O(4) to the metal Fe(1) are shorter (1.92 \AA) as compared to the distance of O(7) and O(8) to Fe(1) (2.11 \AA). The angles between O(1)-Fe(1)-O(4) and O(7)-Fe(1)-O(8) span 104° and 62° , respectively, resulting in a strong distortion of the octahedral geometry. Nevertheless, the complex $[\text{Fe}^{\text{III}}(\mathbf{7a})_2(\text{OAc})]$ can be identified as the Λ -isomer (Figure 15).

Based on the strong counter anion acetate, the meridional bis(tridentate) structure formation, found for the perchlorat complex $[\text{Fe}^{\text{III}}(\mathbf{7a})_2] \cdot (\text{ClO}_4)$, was not able to form in this case. Because of this, the unbound hydroxymethylene groups are both aligned to be anti to the acetate ligand and the distances between Fe(1)-O(3)/O(6) are measured as 3.82 / 3.80 Å (values not given in Table 5).

Table 5. Selected bond distances (Å) and angles (°) of $[\text{Fe}^{\text{III}}(\mathbf{7a})_2(\text{OAc})]$.

Bond Distances [Å]			Angles [°]
Fe(1)-O(1)	1.927(2)	O(1)-Fe(1)-O(4)	103.86(11)
Fe(1)-O(4)	1.914(3)	O(1)-Fe(1)-O(7)	99.63(11)
Fe(1)-O(7)	2.122(3)	O(1)-Fe(1)-O(8)	160.24(11)
Fe(1)-O(8)	2.106(3)	O(1)-Fe(1)-N(1)	86.47(11)
Fe(1)-N(1)	2.091(3)	O(1)-Fe(1)-N(2)	92.19(12)
Fe(1)-N(2)	2.095(3)	O(4)-Fe(1)-O(7)	155.56(11)
		O(4)-Fe(1)-O(8)	95.48(11)
		O(4)-Fe(1)-N(1)	93.80(12)
		O(4)-Fe(1)-N(2)	86.78(12)
		O(7)-Fe(1)-O(8)	61.78(11)
		O(7)-Fe(1)-N(1)	94.28(12)
		O(7)-Fe(1)-N(2)	85.67(12)
		O(8)-Fe(1)-N(1)	88.28(12)
		O(8)-Fe(1)-N(2)	92.89(12)
		N(1)-Fe(1)-N(2)	178.64(12)

An overview of all obtained iron(III) oxazoline X-ray structures is given in *experimental part* – **F.11**, Figure 8.

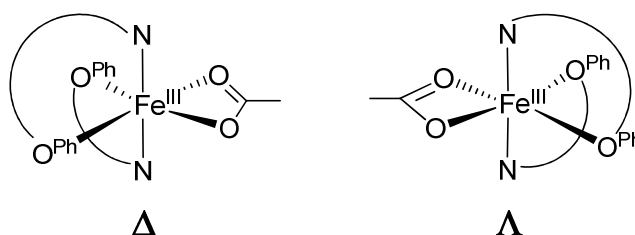


Figure 15. Octahedral binding models Δ and Λ for three bidentate ligands.

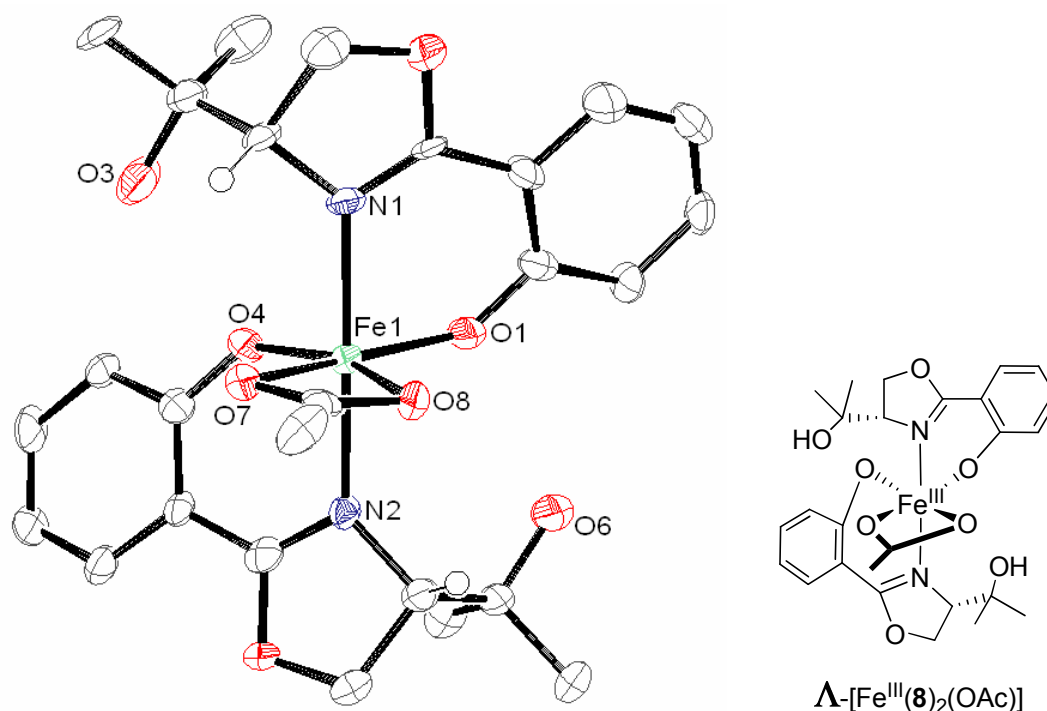


Figure 16. ORTEP plot at the 50% probability level of $[\text{Fe}^{\text{III}}(\mathbf{8})_2(\text{OAc})]$ – (not important hydrogen atoms are omitted for clarity).

The crystallographic results of complex $[\text{Fe}^{\text{III}}(\mathbf{8})_2(\text{OAc})]$ show two bidentate oxazolines around the iron centre and an additional third bidentate acetyl ligand (Figure 16). Both phenolates as well as the acetate compensate the charge of the Fe^{3+} centre, forming a neutral complex. Both nitrogen atoms are placed in a *trans*-position (178°) with a bond length to the metal of 2.12 \AA (Table 6).^{44,82} The deprotonated oxygens of the phenolate groups also bind with the typical length of 1.98 \AA , comparable to the other crystal structures obtained in this series. The angle between these oxygen atoms (O(1)/O(4)) and iron is stretched (106°) as usual by the planar coordinating bidentate acetyl ligand (61° for O(7)-Fe(1)-O(8)), to a highly distorted octahedral structure. The average bond length of an acetate oxygen to the metal was found to be 2.13 \AA . The two substituted hydroxymethylene side chains are not involved in the complexation and point away from the metal centre, resulting in an average distance for the hydroxymethylene oxygen to the iron of 3.73 \AA (value not given in Table 6). The complex structure could be identified as the Λ -isomer (Figure 15).

The oxazoline ligands **7a** and **8**, which are equipped with a simple hydroxymethylene group as well as with a dimethylated hydroxymethylene group, caused a similar binding motif in both structures. The substitution on the side chain of ligand **8** leads to no sterical hindrance, while the use of the strong coordinating counter anion OAc^- prevents the formation of the third bond of the ligand to the metal.

Table 6. Selected bond distances (Å) and angles (°) of [Fe^{III}(**8**)₂(OAc)].

Bond Distances [Å]		Angles [°]	
Fe(1)-O(1)	1.892(4)	O(1)-Fe(1)-O(4)	105.92(15)
Fe(1)-O(4)	1.902(4)	O(1)-Fe(1)-O(7)	157.31(15)
Fe(1)-O(7)	2.117(4)	O(1)-Fe(1)-O(8)	97.28(15)
Fe(1)-O(8)	2.135(4)	O(1)-Fe(1)-N(1)	86.36(17)
Fe(1)-N(1)	2.117(5)	O(1)-Fe(1)-N(2)	95.17(17)
Fe(1)-N(2)	2.085(5)	O(4)-Fe(1)-O(7)	96.08(14)
		O(4)-Fe(1)-O(8)	156.49(15)
		O(4)-Fe(1)-N(1)	94.18(17)
		O(4)-Fe(1)-N(2)	86.78(17)
		O(7)-Fe(1)-O(8)	61.32(14)
		O(7)-Fe(1)-N(1)	86.57(16)
		O(1)-Fe(1)-O(8)	91.49(16)
		O(8)-Fe(1)-N(1)	90.99(16)
		O(8)-Fe(1)-N(2)	87.41(16)
		N(1)-Fe(1)-N(2)	177.92(17)

An overview of all obtained iron(III) oxazoline X-ray structures is given in *experimental part* – **F.11**, Figure 8.

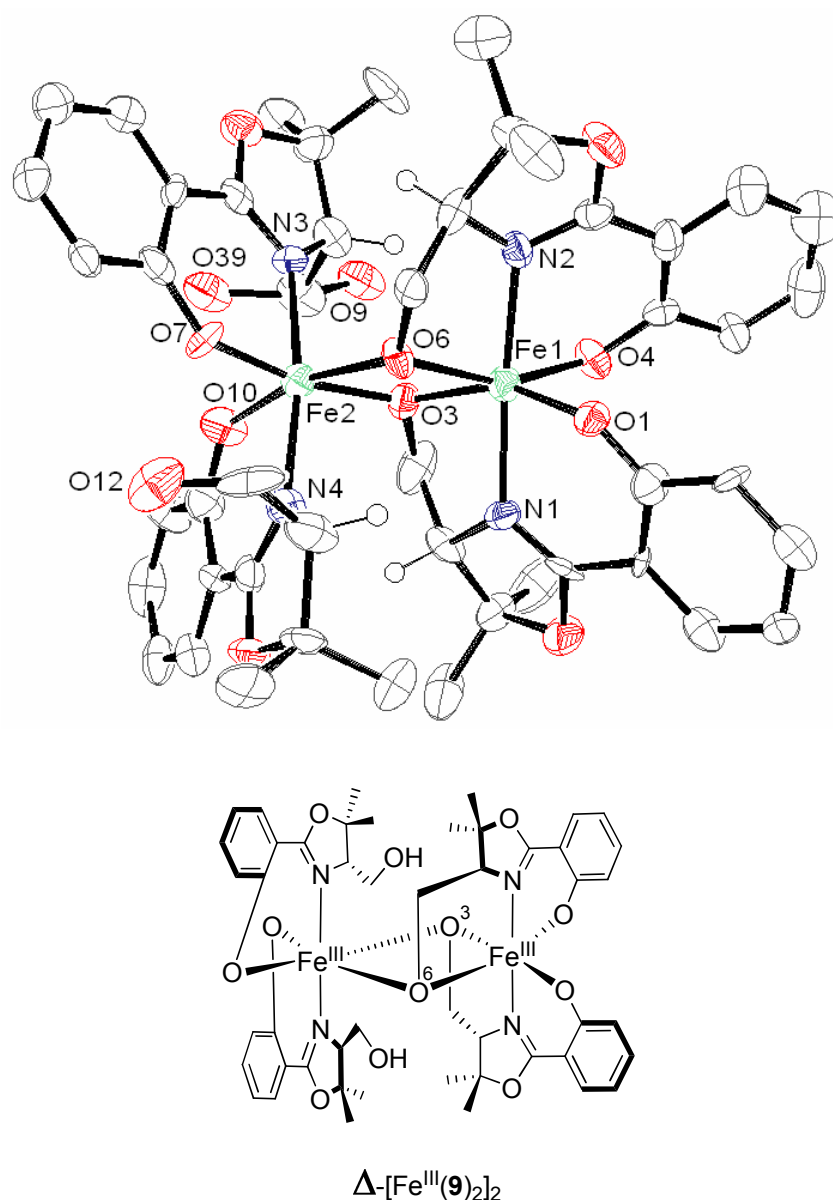


Figure 17. ORTEP plot at the 50% probability level of $[\text{Fe}^{\text{III}}(\mathbf{9})_2]_2$ – (not important hydrogen atoms are omitted for clarity).

A further iron(III) complex $[\text{Fe}^{\text{III}}(\mathbf{9})_2]_2$ with an unexpected diiron core in the solid state (Figure 17) was obtained by complexation of **9** with $\text{Fe}(\text{OAc})_2$. Characteristic features of this complex include an involvement of four ligands as well as a two-iron cluster containing two oxo bridges. In this complex the charge is balanced without the necessity of counter anions. In both metal centres, the iron is chelated in an octahedral binding geometry and shows a C_2 axis along the Fe-Fe vector.⁸³ The metal core is bridged by two oxygen atoms coming from two hydroxymethylene groups of two separate ligands. Two hydroxymethylene groups of two further ligands do not coordinate to the iron centres in this structure. Starting from the right hand side metal centre (Figure 17), the phenolate oxygen atoms bind to the iron with an

average bond length of 1.96 Å and span an angle of 93° (O(1)-Fe(1)-O(4)) (Table 7). Meridional coordination on this iron is indicated by an 156° angle of both phenolate oxygens over the iron centre to the hydroxymethylene oxygens (O(1)-Fe(1)-O(3) and O(4)-Fe(1)-O(6)). These hydroxymethylene oxygens bridge both iron metals with unequal bond distances. Fe(1)-O(6) and Fe(1)-O(3) show an average bond length of 2.03 Å. However, Fe(2) is bound with a bond of length 2.01 Å to O(6) and 2.04 Å to O(3). The corresponding nitrogen atoms around Fe(1) differ slightly from each other in their bonding with bond lengths of 2.06 Å and 2.10 Å, and are placed directly in opposite positions, spanning an angle of 175°. Switching to the second iron centre Fe(2), its octahedral environment is formed by two bidentate oxazoline ligands and both oxygen bridges. In comparison to the Fe(1) data, the phenolate oxygens bind to the left hand iron centre with similar bond distances (1.92 Å and 1.95 Å). The angle of O(7)-Fe(2)-O(10) was observed to be 97°. The two nitrogen atoms (N(3) and N(4)) are nearly aligned in *trans*-position (172°) and the distances to the Fe(2) metal centre are longer than on the Fe(1) side (2.12 Å and 2.09 Å, respectively). For both iron metals the isomer geometry is determined as the Δ -form (Figure 18).

An explanation for the favoured formation of the dinuclear iron(III) complex $[\text{Fe}^{\text{III}}(\mathbf{9})_2]_2$ is probably based on a concentration gradient during the crystallization process. As described later in detail, the liquid-state analysis was not able to answer the question of whether the dinuclear structure also exists in solution. Furthermore, it should be mentioned that the dinuclear complex (Δ) was formed with a different geometry than both mononuclear complexes (Δ), a fact, which is in agreement with the absolute configuration of the chiral carbon atom of the ligands. This might be caused by an energetically more stable dinuclear Δ -isomer compared to a mononuclear Δ -isomer, with the monomer possessing more stability in the Δ -form.

Table 7. Selected bond distances (Å) and angles (°) of [Fe^{III}(9)₂]₂.

Bond Distances [Å]		Angles [°]	
Fe(1)-O(1)	1.9687(19)	O(1)-Fe(1)-O(3)	155.49(8)
Fe(1)-O(3)	2.0281(19)	O(1)-Fe(1)-O(4)	93.15(8)
Fe(1)-O(4)	1.9527(19)	O(1)-Fe(1)-O(6)	98.38(7)
Fe(1)-O(6)	2.0295(19)	O(1)-Fe(1)-N(1)	82.90(9)
Fe(1)-N(1)	2.063(2)	O(1)-Fe(1)-N(2)	92.09(9)
Fe(1)-N(2)	2.097(2)	O(3)-Fe(1)-O(4)	100.47(8)
Fe(2)-O(3)	2.0387(19)	O(3)-Fe(1)-O(6)	76.81(7)
Fe(2)-O(6)	2.0110(18)	O(3)-Fe(1)-N(1)	75.67(9)
Fe(2)-O(7)	1.9243(19)	O(3)-Fe(1)-N(2)	109.52(9)
Fe(2)-O(10)	1.9495(19)	O(4)-Fe(1)-O(6)	156.50(9)
Fe(2)-N(3)	2.094(2)	O(4)-Fe(1)-N(1)	95.36(9)
Fe(2)-N(4)	2.120(2)	O(4)-Fe(1)-N(2)	83.49(9)
		O(6)-Fe(1)-N(1)	106.31(9)
		O(6)-Fe(1)-N(2)	75.72(8)
		N(1)-Fe(1)-N(2)	174.80(9)
		O(3)-Fe(2)-O(6)	76.98(7)
		O(3)-Fe(2)-O(7)	168.66(8)
		O(3)-Fe(2)-O(10)	92.67(8)
		O(3)-Fe(2)-N(3)	87.62(8)
		O(3)-Fe(2)-N(4)	99.56(9)
		O(6)-Fe(2)-O(7)	94.96(8)
		O(6)-Fe(2)-O(10)	165.34(8)
		O(6)-Fe(2)-N(3)	99.52(9)
		O(6)-Fe(2)-N(4)	86.26(8)
		O(7)-Fe(2)-O(10)	96.62(8)
		O(7)-Fe(2)-N(3)	85.86(9)
		O(7)-Fe(2)-N(4)	87.72(9)
		O(10)-Fe(2)-N(3)	90.27(9)
		O(10)-Fe(2)-N(4)	85.25(9)
		N(3)-Fe(2)-N(4)	171.70(9)
		Fe(1)-O(3)-Fe(2)	102.59(8)
		Fe(1)-O(6)-Fe(2)	103.53(8)

An overview of all obtained iron(III) oxazoline X-ray structures is given in *experimental part* – **F.11**, Figure 8.

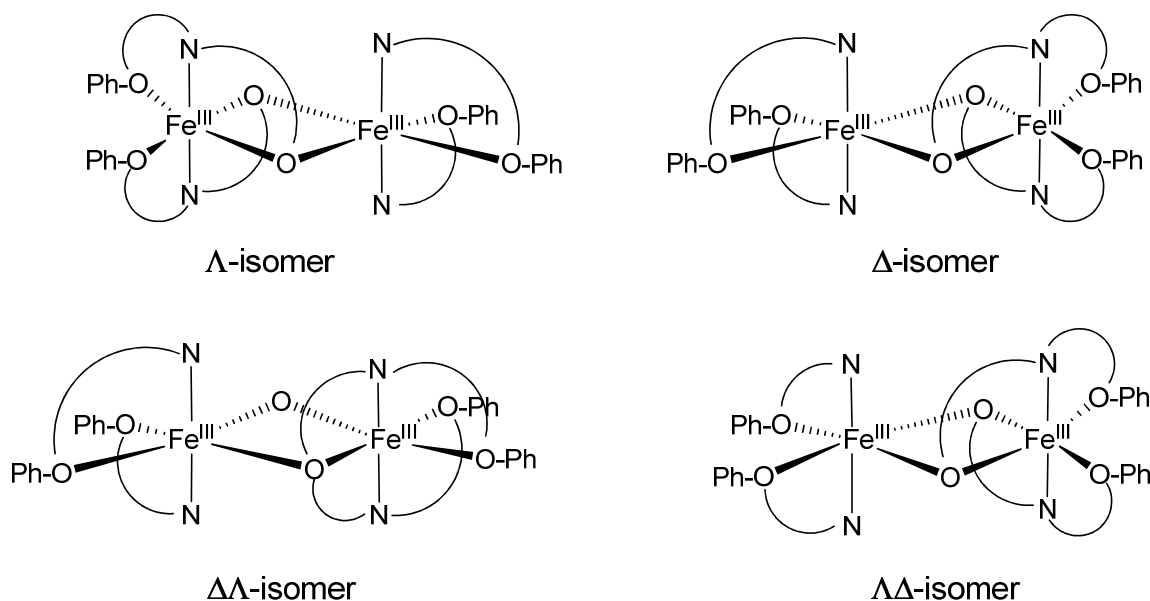


Figure 18. Dinuclear octahedral binding models Δ / Δ and $\Delta\Delta / \Delta\Delta$ for two bidentate ligands and two tridentate ligands.

Finally, all the data obtained for the three complexes were confirmed by mass analysis (ESI), having each a significant mass peak of a 1:2-iron(III) complex ($[\text{Fe}^{\text{III}}(\text{L})_2]^+$) and a peak for the corresponding ligand (L). These measurement conditions probably cause cleavage of the dimer into the mononuclear form, and it was not surprising that the dinuclear mass peak was not detectable. The elemental analysis fit very well for all three complex systems with a 1:2-iron(III) oxazoline structure including acetate as third ligand, and even for the dinuclear sample an acetate ion was calculated, whereas in the solid state structure no counter anion is seen (Scheme 5).

C.2.6 Liquid-State-Analysis of Iron(III) Complexes – $[\text{Fe}^{\text{III}}(\mathbf{7a-9})_2(\text{OAc})]$

The UV/Vis spectra of the $[\text{Fe}^{\text{III}}(\mathbf{7a-9})_2(\text{OAc})]$ series were measured between 200 and 750 nm in acetonitrile at room temperature (Figure 19). The complexes $[\text{Fe}^{\text{III}}(\mathbf{7a})_2(\text{OAc})]$ and $[\text{Fe}^{\text{III}}(\mathbf{9})_2(\text{OAc})]$ show the same absorption bands which indicate a similar structure in solution, whereas $[\text{Fe}^{\text{III}}(\mathbf{8})_2(\text{OAc})]$ differs in its absorption curve. Starting from the absorption maximum at 310 nm, which is for all complexes the same and based on ligand specific transitions ($n \rightarrow \pi^*$ or $\pi \rightarrow \pi^*$) (see *experimental part F.9.2*, Figure 1 and 4), the extraordinary width of this band for complex $[\text{Fe}^{\text{III}}(\mathbf{7a})_2(\text{OAc})]$ and $[\text{Fe}^{\text{III}}(\mathbf{9})_2(\text{OAc})]$ reach from 275 to 400 nm. In the spectra of complex $[\text{Fe}^{\text{III}}(\mathbf{8})_2(\text{OAc})]$ a shoulder is clearly

recognized between 340 and 400 nm. The complex specific and distinct maximum at 460 nm for complex $[\text{Fe}^{\text{III}}(\mathbf{7a})_2(\text{OAc})]$ and $[\text{Fe}^{\text{III}}(\mathbf{9})_2(\text{OAc})]$ was also not observed for $[\text{Fe}^{\text{III}}(\mathbf{8})_2(\text{OAc})]$, only a small increase in the band is detected around this wavelength. The width of the bands, the shoulder as well as the absorption at 460 nm led to the assumption of relatively intense charge-transfer transitions of the ligand to the metal (LMCT). The changes between the spectra of the acetate complexes and the perchlorate complexes were also reflected by a colour change from dark purple to now dark orange-red.⁷⁴⁻⁷⁶

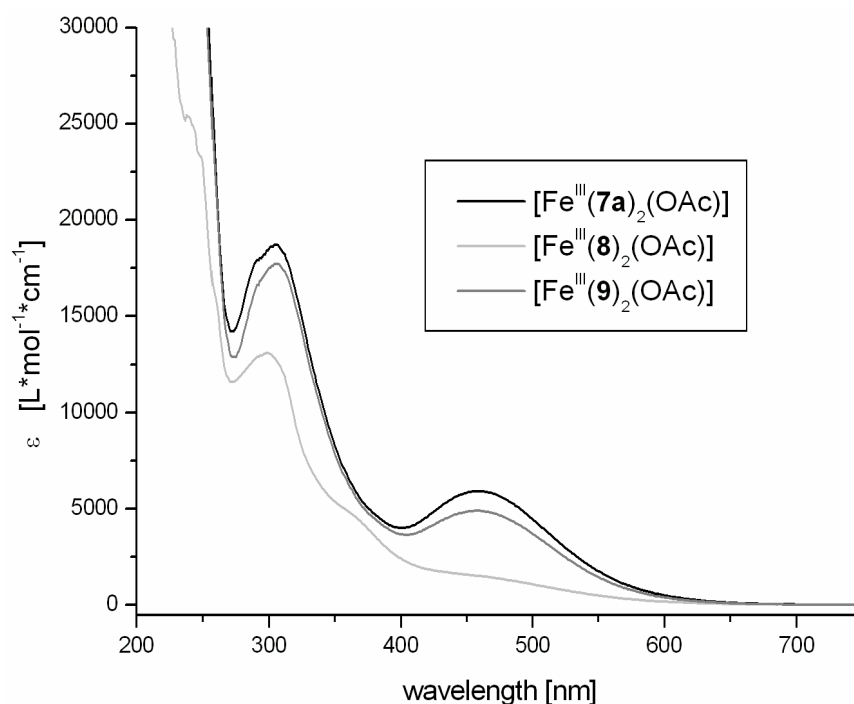


Figure 19. UV/Vis spectra for the $[\text{Fe}^{\text{III}}(\mathbf{7a-9})_2(\text{OAc})]$ series.

In the circular dichroism spectra (CD) of the $[\text{Fe}^{\text{III}}(\mathbf{7a-9})_2(\text{OAc})]$ series, slightly different results were observed under the influence of circularly polarized light (Figure 20). Complex $[\text{Fe}^{\text{III}}(\mathbf{8})_2(\text{OAc})]$ (Figure 20, light grey line), exhibit an small shift of its curve in the CD graph, but it is still comparable to the complexes $[\text{Fe}^{\text{III}}(\mathbf{7a-9})_2(\text{OAc})]$. As already indicated in the UV/Vis measurements this complex generates a non-typical electronic absorption spectra for this series. The CD curve for complex $[\text{Fe}^{\text{III}}(\mathbf{7a})_2(\text{OAc})]$ exhibits a mirror imaged behaviour to the graph of complex $[\text{Fe}^{\text{III}}(\mathbf{9})_2(\text{OAc})]$ (Figure 20, black and dark grey line), indicating a similar complex structure with opposite geometry in solution. In addition to that, the identification by crystallographic data of complex $[\text{Fe}^{\text{III}}(\mathbf{7a})_2(\text{OAc})]$ to form the Λ -isomer and for complex $[\text{Fe}^{\text{III}}(\mathbf{9})_2(\text{OAc})]$ to form the Δ -isomer (dinuclear structure in the crystallographic measurement) is in a good agreement with this. However, no evidence was found for the dinuclear nature of complex $[\text{Fe}^{\text{III}}(\mathbf{9})_2(\text{OAc})]$. Therefore, it is presumed that

$[\text{Fe}^{\text{III}}(\mathbf{9})_2(\text{OAc})]$ exists in solution only in a monomeric form. The already mentioned CD graph of complex $[\text{Fe}^{\text{III}}(\mathbf{8})_2(\text{OAc})]$ (Figure 20, light grey line) shows similar positive and negative features as complex $[\text{Fe}^{\text{III}}(\mathbf{7a})_2(\text{OAc})]$ (Figure 20, black line) and in combination with its crystal structure discussed above (Figure 16) confirms the Λ -isomer for both complexes.

Furthermore, in the $[\text{Fe}^{\text{III}}(\mathbf{7a-9})_2(\text{OAc})]$ series it is possible to infer the influence of the stereo centre within the ligand on the stereo chemical outcome of the complexes. This fact becomes very interesting, because the hydroxymethylen side chains are not directly bound on the metal and influence the metal geometry only in a secondary way. This is in direct contrast to the above statement for the perchlorate complexes. As outlined in Figure 20, the CD spectra of the complexes $[\text{Fe}^{\text{III}}(\mathbf{7a-9})_2(\text{OAc})]$ are in agreement with their stereo chemical information of their corresponding ligands **7a-9** (see *experimental part F.9.2*, Figure 4).

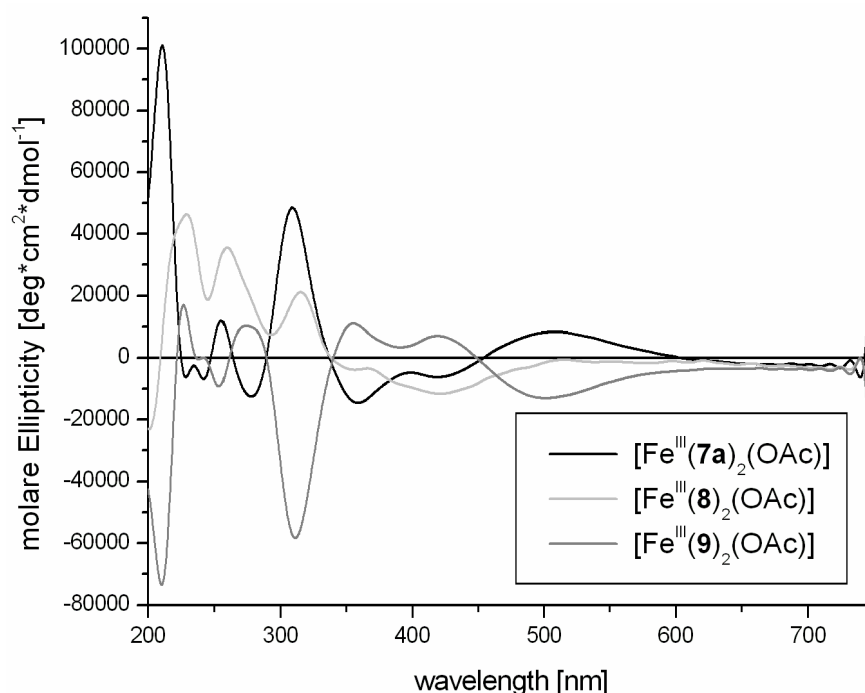
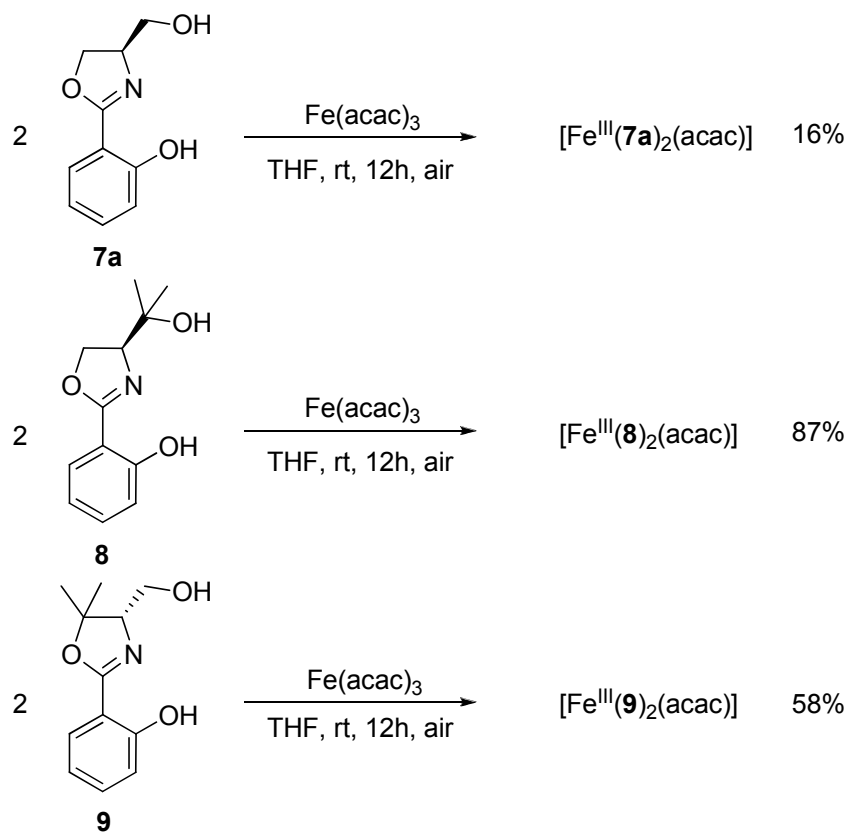


Figure 20. CD spectra for the $[\text{Fe}^{\text{III}}(\mathbf{7a-9})_2(\text{OAc})]$ series.

C.2.7 Formation of Iron(III) Complexes using Fe(acac)₃

Iron(III) acetylacetonate, Fe(acac)₃, was the third salt explored in this series. In this salt iron resides already in the +3 oxidation state, and acetylacetonate is a coordinating anion of similar strength to acetate. As before, the iron salt and the oxazoline derivatives **7a-9** were used in a ratio of 1:2 to form the desired complexes (Scheme 6). The ligands were dissolved in THF and were transferred into a solution of Fe(acac)₃ in THF. The observed colour change from a slightly yellow into a dark blood-red, indicates a successful complex formation, but took place significantly slower than observed for the Fe(OAc)₂ or Fe(ClO₄)₂•6H₂O salts (Scheme 4 and 5).⁷⁴ The newly formed iron(III) complexes appear to be stable on air.



Scheme 6. Synthesis of iron(III) complexes [Fe^{III}(**7a-9**)₂(acac)] using Fe(acac)₃.

Features typical for [Fe^{III}(**7a-9**)₂(acac)] complexes were observed by IR analysis. A broad alcohol stretch was found between 3430 and 3350 cm⁻¹, and a typical strong band around 1360 cm⁻¹ was assigned to the acetylacetonate group. The shifted strong band of an uncoordinated and unsaturated C=N stretch from 1644 cm⁻¹ to 1604 cm⁻¹ indicated a coordinating ligand C=N vibration.

In all three cases the mass spectrometry was able to detect a significant mass peak for a 1:2-iron(III) complex ($[\text{Fe}^{\text{III}}(\text{L})_2]^+$), which contained two oxazoline ligands (L) and an iron(III) metal. Furthermore, an 1:1:1-iron(III) complex ($[\text{Fe}^{\text{III}}(\text{L})(\text{acac})]^+$) with two different kinds of ligands, an oxazoline (L) and an acetylacetonate (acac), bound to an iron(III) metal was observed as well as a mass peak of the corresponding free oxazoline ligand (L) (Figure 21). These results can be interpreted that the expected $[\text{Fe}^{\text{III}}(\mathbf{7a-9})_2(\text{acac})]$ complexes were formed (Scheme 6) and under the measurement conditions used (ESI) these complexes were ionized differently by losing either an oxazoline ligand or an acetylacetonate ligand. The elemental analysis confirmed for all three complex systems the expected $[\text{Fe}^{\text{III}}(\mathbf{7a-9})_2(\text{acac})]$ formation.

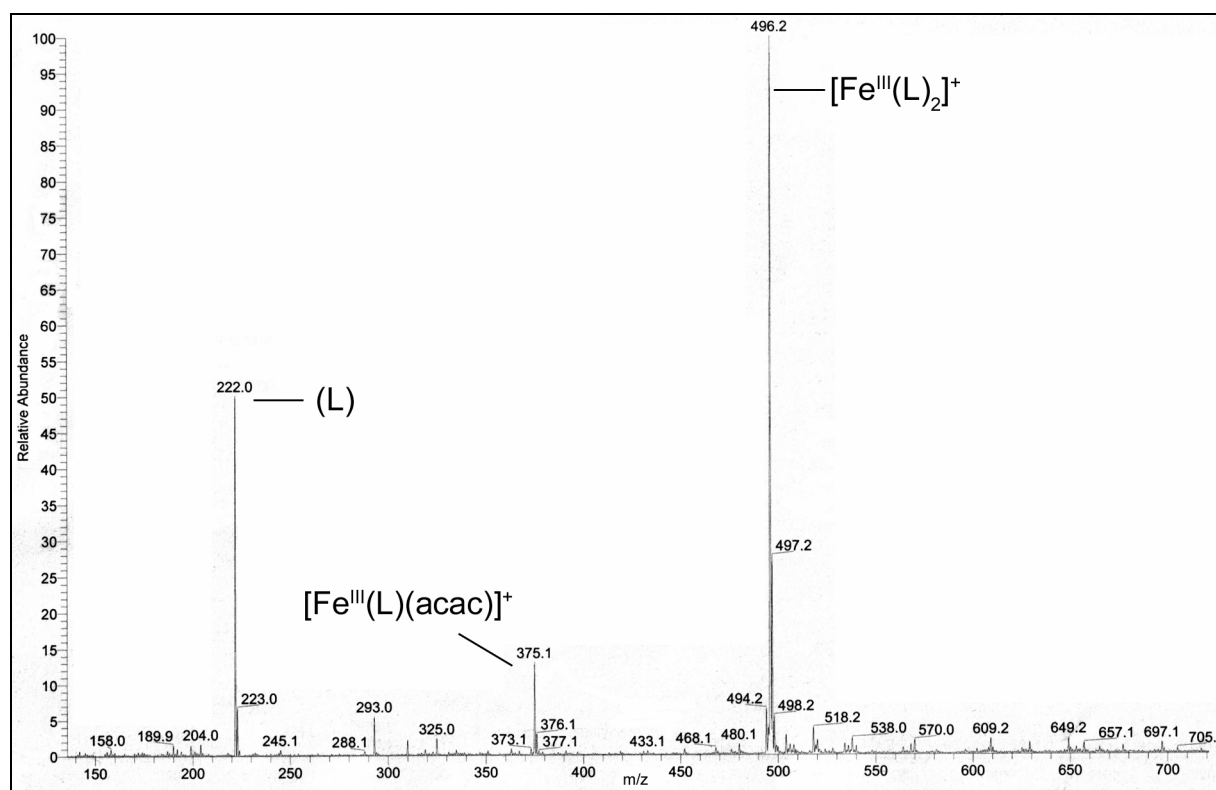


Figure 21. Mass spectrum of $[\text{Fe}^{\text{III}}(\mathbf{9})_2(\text{acac})]$, representative for all three iron(III) acetylacetonate complexes.

C.2.8 Liquid-State-Analysis of Iron(III) Complexes – $[\text{Fe}^{\text{III}}(\mathbf{7a-9})_2(\text{acac})]$

Unfortunately, all attempts to obtain crystals of this series suitable for X-ray analysis failed. The UV/Vis spectra of the $[\text{Fe}^{\text{III}}(\mathbf{7a-9})_2(\text{acac})]$ series were measured between 200 and 750 nm in acetonitrile at room temperature (Figure 22). The assignment of the absorption bands from 360 nm to higher energies was not easy to make. It is assumed that most of them are representative for the complexes, since they are not present in the spectra of the free

ligands nor of the pure salt (see *experimental part F.9.2*, Figure 2 and 4). Clear evidence for the newly formed complexes $[\text{Fe}^{\text{III}}(\mathbf{7a-9})_2(\text{acac})]$ is found in the observed maximum from 450 to 470 nm. A similar band around 430 nm is already found in the UV/Vis spectra of the pure salt, but a shift of between 20 to 50 nm to lower energies indicates a significant charge-transfer transitions of the ligand to the metal (LMCT).⁷⁴⁻⁷⁶ This small difference originates from a CT transition of the phenolic oxygen to an iron(III) ion and accompanies the darkening of the complex solution.

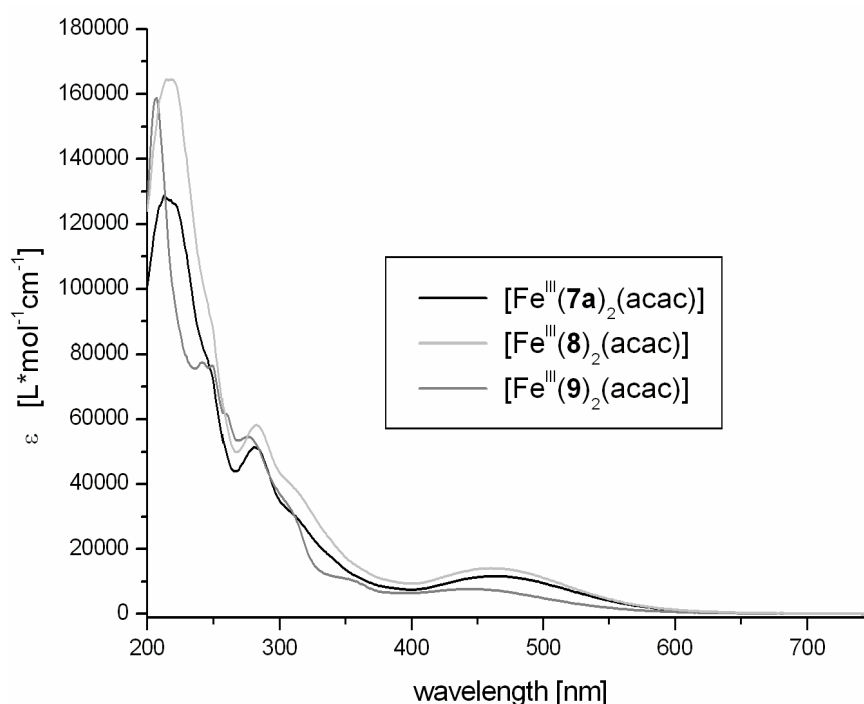


Figure 22. UV/Vis spectra for the $[\text{Fe}^{\text{III}}(\mathbf{7a-9})_2(\text{acac})]$ series.

The $[\text{Fe}^{\text{III}}(\mathbf{7a-9})_2(\text{acac})]$ series exhibit in their CD spectra a strong similarity in the progression of their curves in the circular dichroism spectra (Figure 23). The complexes $[\text{Fe}^{\text{III}}(\mathbf{7a-9})_2(\text{acac})]$ showed very distinct graphs, which are comparable in their stereochemical information to the corresponding ligand spectra (see *experimental part F.9.2*, Figure 4). This feature is in agreement with the CD results of the $[\text{Fe}^{\text{III}}(\mathbf{7a-9})_2(\text{OAc})]$ complexes (Figure 20). On the basis of this correspondence, both CD spectra of $[\text{Fe}^{\text{III}}(\mathbf{7a-9})_2(\text{OAc})]$ and $[\text{Fe}^{\text{III}}(\mathbf{7a-9})_2(\text{acac})]$ were compared: In both graphs around 300 nm and 500 nm a similar behaviour of the curves for the related complexes was recognized, because all maxima or minima on these wavelengths match together. Furthermore, the zero crossings in both complex series are seen at the same points at 340 and 450 nm. These facts and the proposed structure (Figure 24) based on the other analysis give rise to the speculation

that the $[\text{Fe}^{\text{III}}(\mathbf{7a-9})_2(\text{acac})]$ complex series might have the identical complex geometry as the corresponding $[\text{Fe}^{\text{III}}(\mathbf{7a-9})_2(\text{OAc})]$ complexes (Figure 15). This would mean that $[\text{Fe}^{\text{III}}(\mathbf{7a})_2(\text{acac})]$ and $[\text{Fe}^{\text{III}}(\mathbf{8})_2(\text{acac})]$ form the Λ -isomer similar to $[\text{Fe}^{\text{III}}(\mathbf{7a})_2(\text{OAc})]$ and $[\text{Fe}^{\text{III}}(\mathbf{8})_2(\text{OAc})]$, respectively. In contrast to this, $[\text{Fe}^{\text{III}}(\mathbf{9})_2(\text{acac})]$ forms the Δ -isomer like $[\text{Fe}^{\text{III}}(\mathbf{9})_2(\text{OAc})]$.

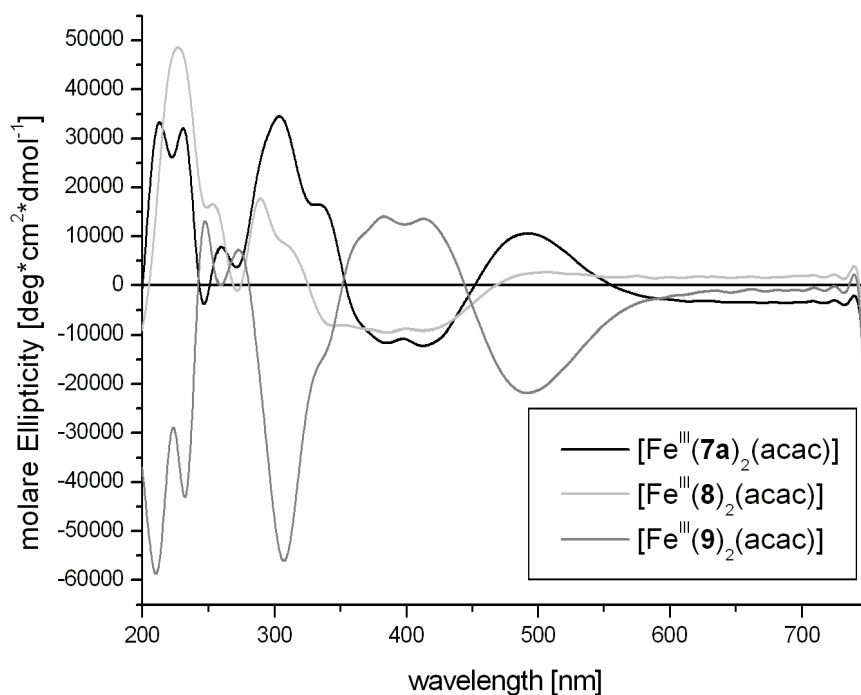


Figure 23. CD spectra for the $[\text{Fe}^{\text{III}}(\mathbf{7a-9})_2(\text{acac})]$ series.

Due to the unsuccessful crystallization experiments, resulting in the lack of structural data in the solid state, all spectroscopic results as well as the high analogy to the $[\text{Fe}^{\text{III}}(\mathbf{7a-9})_2(\text{OAc})]$ complexes (see *main part – oxazoline complex analysis C.2.4-C.2.6*) were used to propose a possible structure model, including the assumed complex geometry (Figure 24).

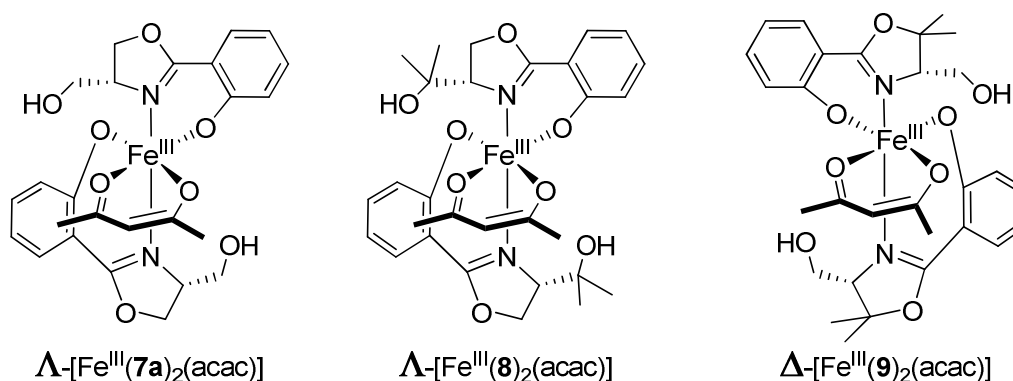
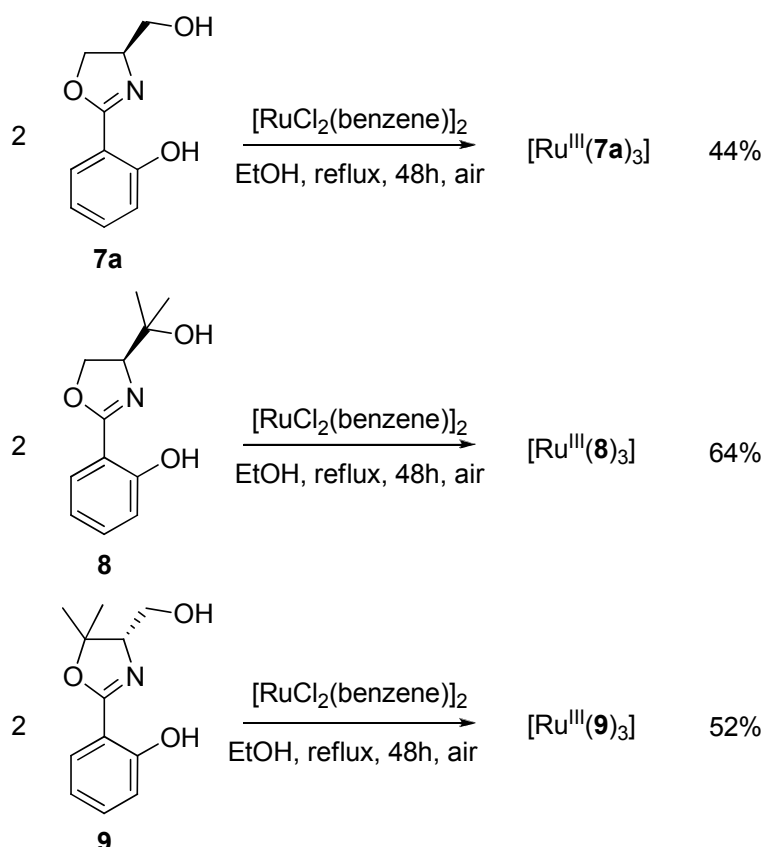


Figure 24. Proposed structures for the complexes $[\text{Fe}^{\text{III}}(\mathbf{7a-9})_2(\text{acac})]$.

C.2.9 Formation of Ruthenium(III) Complexes using $[\text{RuCl}_2(\text{benzene})]_2$

To test the effect of an iron related metal, ruthenium was chosen, because many of its chemical properties are similar and it is located in the periodic table directly under iron. The ruthenium salt, $[\text{RuCl}_2(\text{benzene})]_2$ was selected as suitable metal source.⁸⁴ One equivalent of it was suspended in ethanol and two equivalents of the dissolved ligand **7a-9** in ethanol were transferred into the suspension (Scheme 7). The reaction mixture was heated to reflux for 48 h. During this time the colour slowly changed from a green-brown ruthenium(II) complex to a dark purple ruthenium(III) complex. As already seen in the other complexation reactions, this indicates an air sensitive oxidation step of the ruthenium(II) metal into a ruthenium(III) complex and the probability of a charge-transfer transition from the phenolic oxygen to a ruthenium(III) ion.⁷⁴



Scheme 7. Synthesis of ruthenium(III) complexes $[\text{Ru}^{\text{III}}(\mathbf{7a-9})_3]$ using $[\text{RuCl}_2(\text{benzene})]_2$.

The three ruthenium(III) complexes $[\text{Ru}^{\text{III}}(\mathbf{7a-9})_3]$ feature typical IR bands: the free alcohol was detected between 3355 and 3300 cm^{-1} and the shift of the strong band of an uncoordinated and unsaturated $\text{C}=\text{N}$ stretch from 1644 cm^{-1} to 1604 cm^{-1} indicated a coordinating ligand $\text{C}=\text{N}$ vibration.

The mass spectrometry showed the same results for all three measured compounds $[\text{Ru}^{\text{III}}(\mathbf{7a-9})_3]$. A significant peak for a 1:3-ruthenium(III) complex $([\text{Ru}^{\text{III}}(\text{L})_3]^+)$, including three oxazoline ligands (L) and a ruthenium(III) metal, a 1:2-ruthenium(III) complex $([\text{Ru}^{\text{III}}(\text{L})_2]^+)$, with only two ligands (L) and one metal, and finally the mass peak of the corresponding free ligand (L) were observed (Figure 25). It is assumed that under the used measurement conditions (ESI) the complexes are partly ionized and so the third ligand was cleaved off, presenting only one species of the ruthenium(III) complexes $[\text{Ru}^{\text{III}}(\mathbf{7a-9})_3]$ (Scheme 7). For all three complex systems, also the elemental analysis fitted best for the formation of the 1:3-ruthenium(III) complexes $[\text{Ru}^{\text{III}}(\mathbf{7a-9})_3]$.

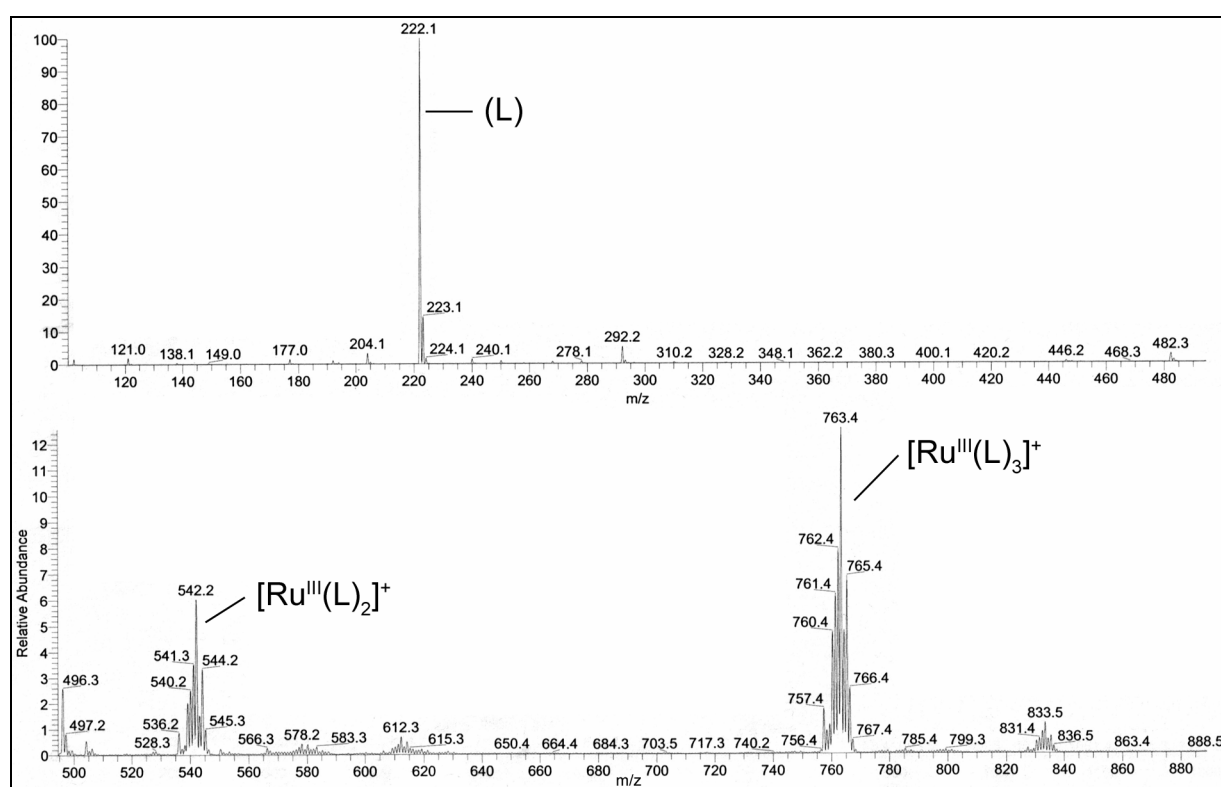


Figure 25. Mass spectrum of $[\text{Ru}^{\text{III}}(\mathbf{9})_3]$, representative for all three ruthenium(III) complexes.

C.2.10 Liquid-State-Analysis of Ruthenium(III) Complexes – $[\text{Ru}^{\text{III}}(\mathbf{7a-9})_3]$

The UV/Vis spectra of the $[\text{Ru}^{\text{III}}(\mathbf{7a-9})_3]$ series were measured between 200 and 750 nm in acetonitrile at room temperature (Figure 26). The complexes $[\text{Ru}^{\text{III}}(\mathbf{7a})_3]$ and $[\text{Ru}^{\text{III}}(\mathbf{9})_3]$, showed similar features in their absorption behaviour and indicate therefore a comparable structure for the complexes in solution (Figure 26, black and dark grey line). In spite of this, complex $[\text{Ru}^{\text{III}}(\mathbf{8})_3]$ significantly absorbed at 290 nm in a different way to the others (Figure 26, light grey line). The typical absorption properties of $[\text{Ru}^{\text{III}}(\mathbf{7a})_3]$ and $[\text{Ru}^{\text{III}}(\mathbf{9})_3]$ are comparable to the already discussed UV/Vis spectra of the iron(III) perchlorate complexes

(Figure 10). Transitions of higher energies until 270 nm usually result from the salt as well as from the ligand. The absorption maximum at 300 nm is clearly identified as ligand specific transitions ($n \rightarrow \pi^*$ or $\pi \rightarrow \pi^*$) (see *experimental part F.9.2*, Figure 2 and 4), whereas the shoulder between 340 to 400 nm and the maximum at 525 nm can be assigned as complex specific transitions. The flat curve around the last discussed maxima is dependent on the concentration used for all three complex solutions, which is reflected in a very high extinction coefficient in the spectra. All attempts to obtain a suitable UV/Vis spectra for complex $[\text{Ru}^{\text{III}}(\mathbf{8})_3]$ by changing the concentration were unsuccessful. Nevertheless, these specific complex based absorptions and the observed dark purple colour in the case of the iron(III) perchlorate complexes (see *main part – oxazoline complex analysis C.2.1-C.2.3*), lead to the assumption of there being distinct charge-transfer transitions from the ligand to the metal (LMCT).^{74-76,85}

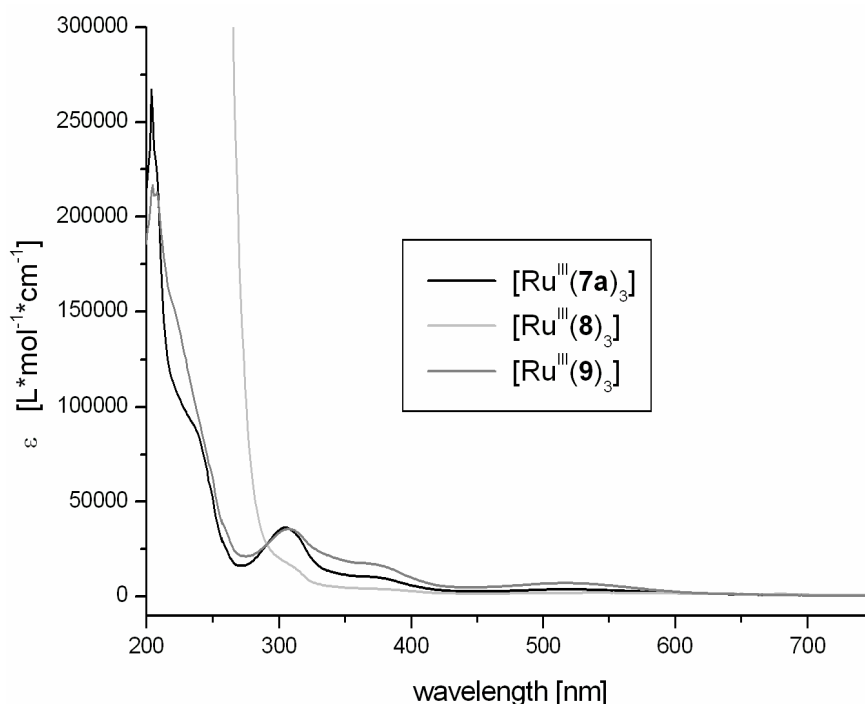


Figure 26. UV/Vis spectra for the $[\text{Ru}^{\text{III}}(\mathbf{7a-9})_3]$ series.

The failed crystallization experiments and the resulting lack of crystal structure data of this complex type demand a variety of speculations. The elemental analysis tends to a 1:3-ruthenium(III) complex system (Figure 27), which contains three oxazoline ligands, each probably bound via the nitrogen and a deprotonated phenolate.

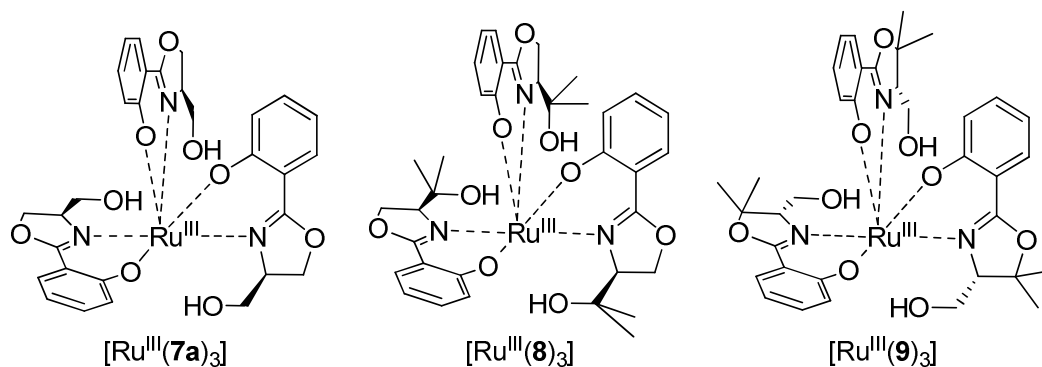


Figure 27. Proposed structure models of the complexes $[\text{Ru}^{\text{III}}(\mathbf{7a-9})_3]$.

These proposed, but unconfirmed structures allow no conclusion to be formulated from the CD spectra of the obtained ruthenium(III) complexes. It is only worth mentioning that the CD curves of the complexes (Figure 28) include the same stereo chemical information as seen for the pure ligands (see *experimental part F.9.2*, Figure 4).

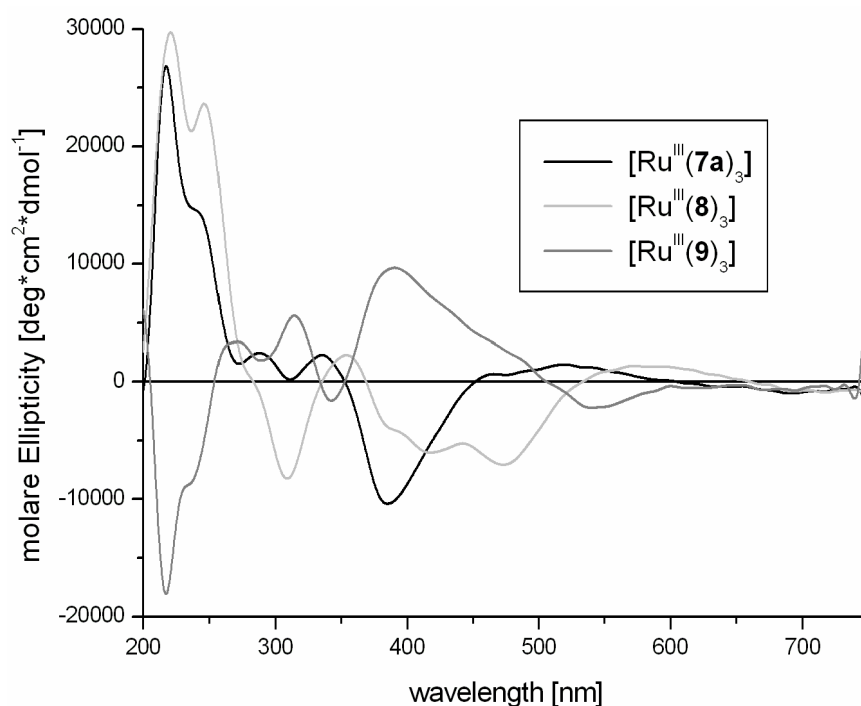
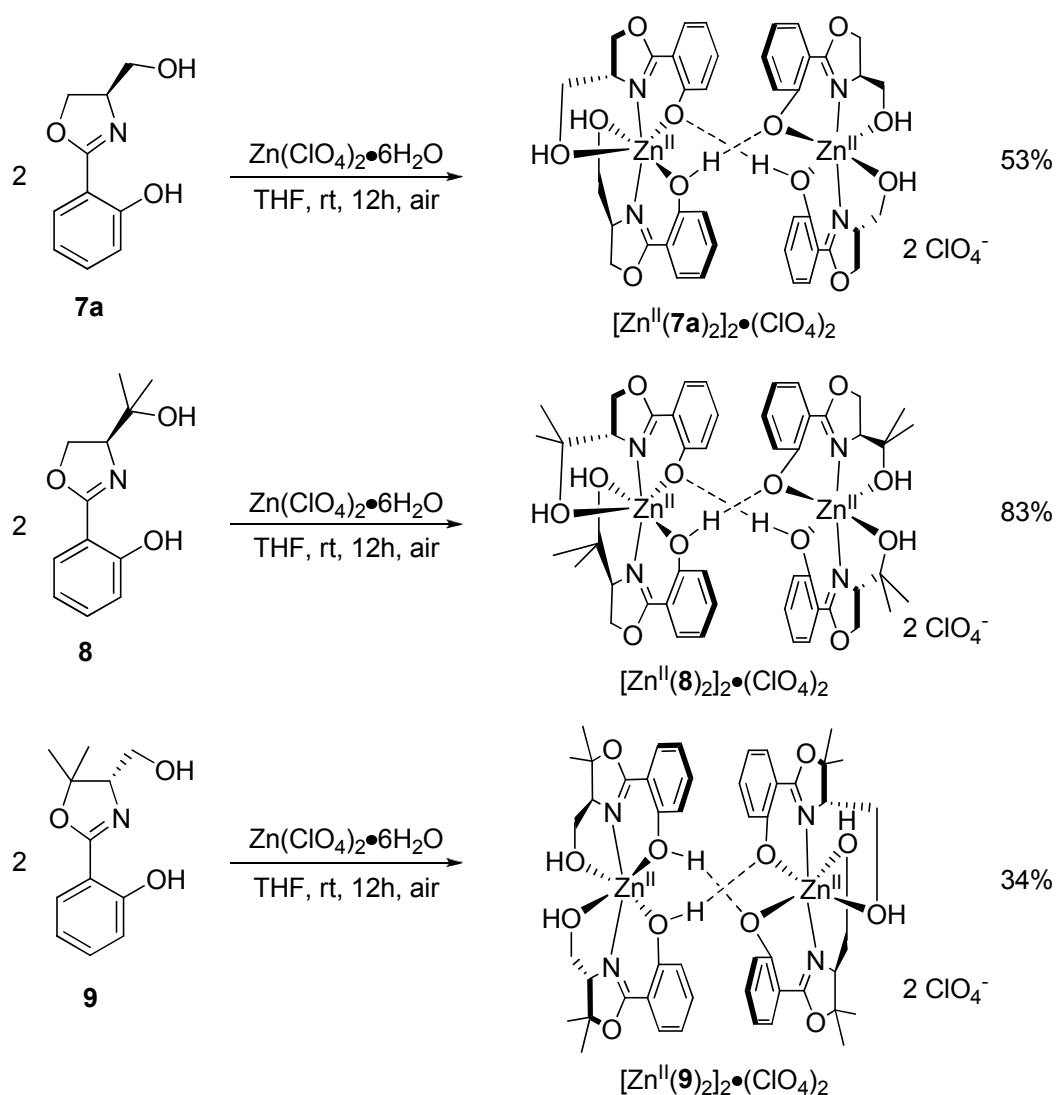


Figure 28. CD spectra for the $[\text{Ru}^{\text{III}}(\mathbf{7a-9})_3]$ series.

C.2.11 Formation of Zinc(II) Complexes using $\text{Zn}(\text{ClO}_4)_2 \cdot 6\text{H}_2\text{O}$

The $[\text{Zn}^{\text{II}}(\mathbf{7a-9})_2]_2 \cdot (\text{ClO}_4)_2$ complexes were prepared using two equivalents of ligand **7a-9** and one equivalent of $\text{Zn}(\text{ClO}_4)_2 \cdot 6\text{H}_2\text{O}$ dissolved in THF (Scheme 8). The ligands were transferred to the salt and a cloudy solution immediately formed. After a 12 h reaction time, two complexes $[\text{Zn}^{\text{II}}(\mathbf{7a/8})_2]_2 \cdot (\text{ClO}_4)_2$ were obtained as slightly orange oils and one complex $[\text{Zn}^{\text{II}}(\mathbf{9})_2]_2 \cdot (\text{ClO}_4)_2$ as a colourless solid.



Scheme 8. Synthesis of zinc(II) complexes $[\text{Zn}^{\text{II}}(\mathbf{7a-9})_2]_2 \cdot (\text{ClO}_4)_2$ using $\text{Zn}(\text{ClO}_4)_2 \cdot 6\text{H}_2\text{O}$.

C.2.12 Solid-State-Analysis of Zinc(II) Complexes – $[\text{Zn}^{\text{II}}(\mathbf{7a/9})_2]_2 \cdot (\text{ClO}_4)_2$

Typical IR features of the $[\text{Zn}^{\text{II}}(\mathbf{7a-9})_2]_2 \cdot (\text{ClO}_4)_2$ complex series are detected around 3470 cm^{-1} (weak band, identified as the alcohol stretch), at 1620 cm^{-1} (for a coordinating ligand C=N vibration), and a characteristic broad and very strong band around 1065 cm^{-1} as well as a sharp band at 620 cm^{-1} , which indicates the presence of a perchlorate anion.⁸⁰

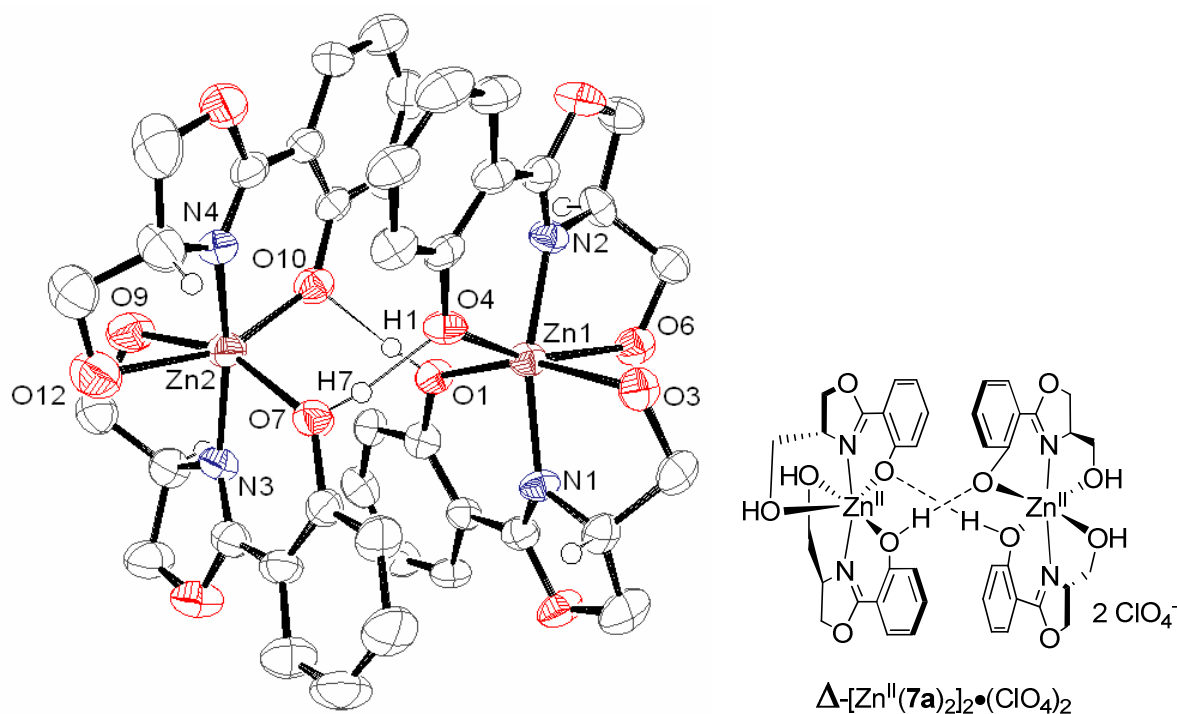


Figure 29. ORTEP plot at the 50% probability level of $[\text{Zn}^{\text{II}}(\mathbf{7a})_2]_2 \cdot (\text{ClO}_4)_2$ – (not important hydrogen atoms and ClO_4^- are omitted for clarity).

Investigations on the crystal of the zinc(II) complex $[\text{Zn}^{\text{II}}(\mathbf{7a})_2]_2 \cdot (\text{ClO}_4)_2$ exposed an extraordinary structural unit (Figure 29). Two monomeric zinc moieties are attached together by two hydrogen bonds⁸⁶ and two π -stacking interactions between two anti parallel aligned phenol-oxazoline units. The hydrogen bonds (H(1)-O(10) and H(7)-O(4)) show a very short length of 1.61 \AA and 1.62 \AA to the oppositely placed deprotonated phenolate (Figure 29 and 30) and in combination with angles around 171° (O(1)-H(1)-O(10) and O(4)-H(7)-O(7)) indicate very strong hydrogen bridges. In addition, π -stacking interactions are feasible by a distance of 3.62 \AA to 4.17 \AA between the planes of the corresponding aromatic systems (Figure 29).^{87,88} Each zinc metal is characteristically coordinated by two tridentate oxazoline ligands, and each unit includes one deprotonated phenolate and one perchlorate for its own charge balance. The strongly distorted octahedral structures feature both *trans*-oriented

nitrogen pairs, spanning angles between 162° and 165° (N(1)-Zn(1)-N(2) and N(3)-Zn(2)-N(4)) with a bond length of 1.98 \AA to Zn(1) and Zn(2) (Table 8). All four hydroxymethylene alcohole side chains point into the outer environment and are still protonated. The distances of these oxygen atoms to Zn(1) and Zn(2) are comparable and measured 2.22 \AA / 2.19 \AA (O(3)-Zn(1) / O(9)-Zn(2)) or 2.46 \AA / 2.40 \AA (O(6)-Zn(1) / O(12)-Zn(2)). The angles between them are nearly perpendicular, with 86° and 80° (O(3)-Zn(1)-O(6) and O(9)-Zn(2)-O(12)). All four phenol oxygens are oriented into the inner sphere of the whole unit and one of each zinc subunit is still protonated. The bond distances between O(1)/O(4)-Zn(1) are given with 2.12 \AA and 2.03 \AA , and for O(7)/O(10)-Zn(2) with 2.16 \AA and 2.08 \AA . It becomes obvious, that each zinc moiety possesses a significant longer Zn-O bond to the protonated oxygens (O(1) and O(7)), and a shorter one to the deprotonated oxygens (O(4) and O(10)). The four meridional coordinating ligands describe angles between 158° to 161° (O(1)-Zn(1)-O(3), O(4)-Zn(1)-O(6), O(7)-Zn(2)-O(9), O(10)-Zn(2)-O(12)). For each zinc(II) centre in complex $[\text{Zn}^{\text{II}}(\mathbf{7a})_2]_2 \cdot (\text{ClO}_4)_2$ the isomer geometry is determined as the Δ -form (Figure 31).

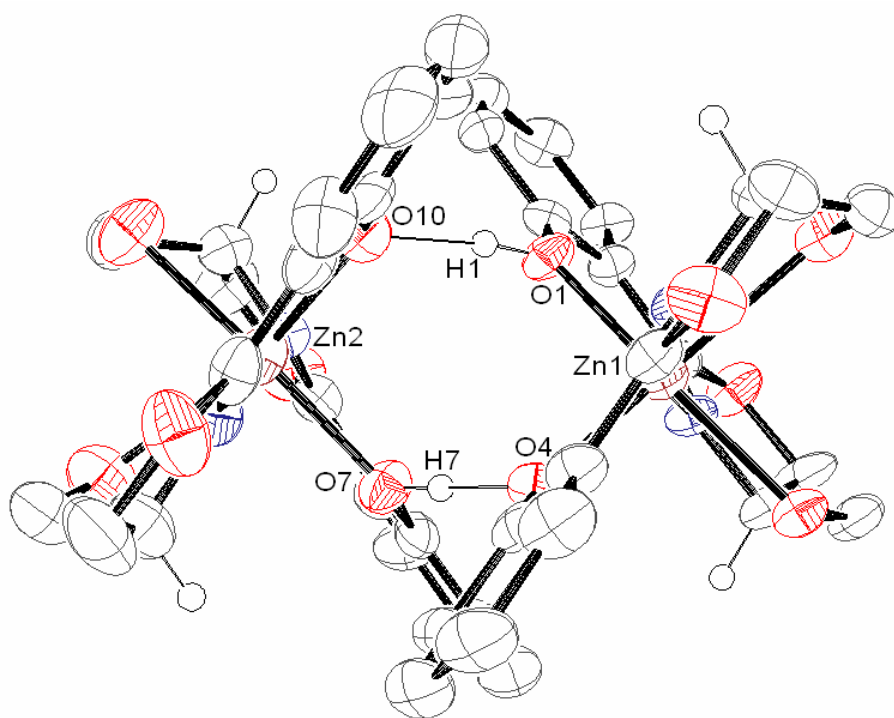


Figure 30. ORTEP plot at the 50% probability level of $[\text{Zn}^{\text{II}}(\mathbf{7a})_2]_2 \cdot (\text{ClO}_4)_2$ – (unimportant hydrogen atoms and ClO_4^- are omitted for clarity).

Table 8. Selected bond distances (Å) and angles (°) of $[\text{Zn}^{\text{II}}(\mathbf{7a})_2]_2 \cdot (\text{ClO}_4)_2$.

Bond Distances [Å]		Angles [°]	
Zn(1)-O(1)	2.122(3)	O(3)-Zn(1)-O(4)	91.93(14)
Zn(1)-O(3)	2.224(4)	O(3)-Zn(1)-O(6)	85.81(14)
Zn(1)-O(4)	2.031(4)	O(3)-Zn(1)-N(1)	76.51(16)
Zn(1)-O(6)	2.461(4)	O(3)-Zn(1)-N(2)	98.09(17)
Zn(1)-N(1)	1.978(5)	O(4)-Zn(1)-O(6)	160.05(15)
Zn(1)-N(2)	1.975(5)	O(4)-Zn(1)-N(1)	109.95(18)
Zn(2)-O(10)	2.043(4)	O(4)-Zn(1)-N(2)	87.73(18)
Zn(2)-O(12)	2.398(5)	O(6)-Zn(1)-N(1)	88.83(18)
Zn(2)-O(3)	1.988(5)	O(6)-Zn(1)-N(2)	73.02(18)
Zn(2)-O(4)	1.972(5)	O(1)-Zn(1)-N(2)	99.46(17)
Zn(2)-O(7)	2.164(4)	O(1)-Zn(1)-O(4)	97.00(14)
Zn(2)-O(9)	2.187(4)	O(1)-Zn(1)-O(6)	91.41(14)
Zn(2)-N(3)	1.988(4)	O(1)-Zn(1)-O(3)	160.58(15)
Zn(2)-N(4)	1.972(4)	O(1)-Zn(1)-N(1)	84.22(17)
		N(1)-Zn(1)-N(2)	161.5(2)
		O(7)-Zn(2)-O(9)	158.68(16)
		O(7)-Zn(2)-O(10)	98.98(16)
		O(7)-Zn(2)-O(12)	94.65(16)
		O(7)-Zn(2)-N(3)	82.01(18)
		O(7)-Zn(2)-N(4)	92.22(18)
		O(9)-Zn(2)-O(10)	93.23(17)
		O(9)-Zn(2)-O(12)	79.50(18)
		O(9)-Zn(2)-N(3)	77.74(19)
		O(9)-Zn(2)-N(4)	105.73(19)
		O(10)-Zn(2)-O(12)	158.21(16)
		O(10)-Zn(2)-N(3)	106.90(19)
		O(10)-Zn(2)-N(4)	87.79(18)
		O(12)-Zn(2)-N(3)	91.72(19)
		O(12)-Zn(2)-N(4)	74.71(19)
		N(3)-Zn(2)-N(4)	164.8(2)

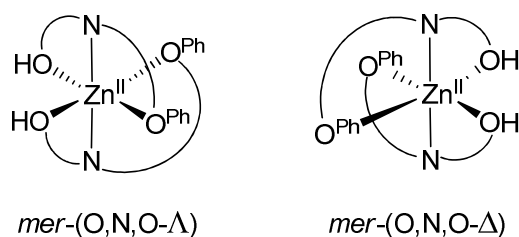


Figure 31. Meridional octahedral binding models Λ and Δ for two tridentate ligands.

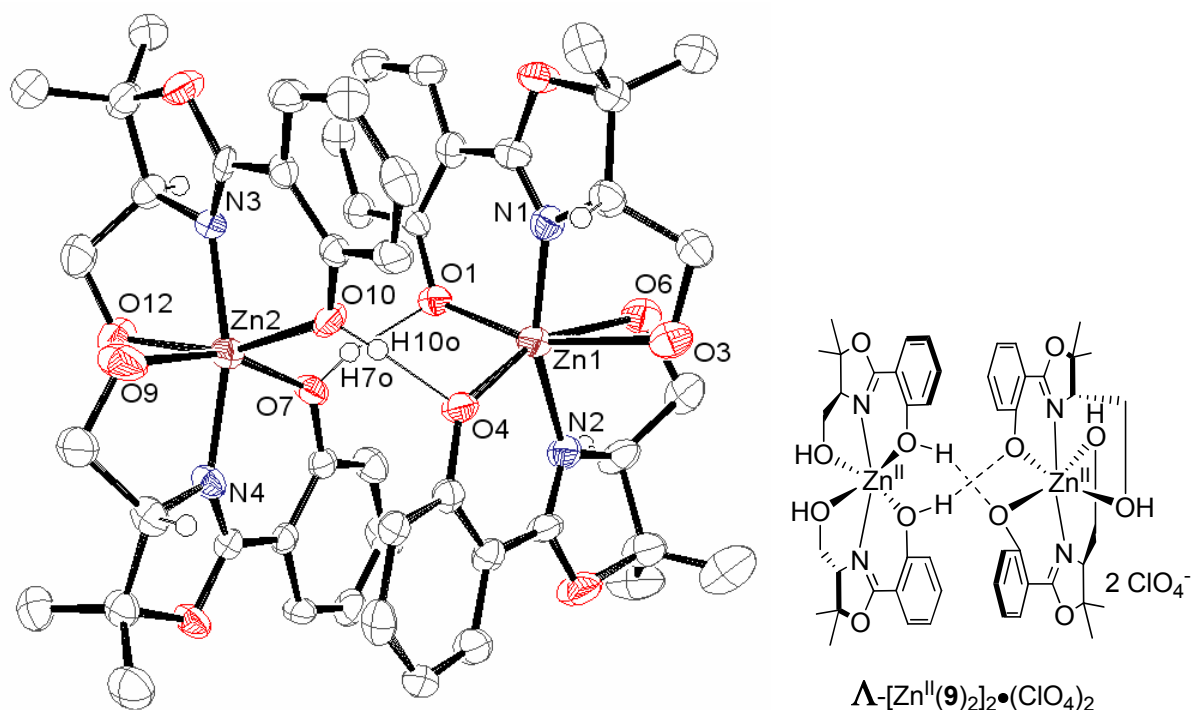


Figure 32. ORTEP plot at the 50% probability level of $[Zn^{\text{II}}(\mathbf{9})_2]_2 \cdot (\text{ClO}_4)_2$ – (not important hydrogen atoms and ClO_4^- are omitted for clarity).

Further investigations of a second zinc(II) crystal for the complex $[Zn^{\text{II}}(\mathbf{9})_2]_2 \cdot (\text{ClO}_4)_2$ revealed analogous results (Figure 32). Two monomeric zinc moieties are fixed together by two short and strong hydrogen bonds ($\text{H}(7)\text{--O}(1)$ 1.60 Å and $\text{H}(10)\text{--O}(4)$ 1.58 Å)⁸⁶ and two π -stacking interactions resulting from the anti parallel aligned phenol-oxazolines (3.96 Å - 4.27 Å) (Figure 32 and 33).^{87,88} Each zinc metal is again characteristically coordinated by two tridentate oxazoline ligands. The whole unit includes two deprotonated phenolates and two perchlorates for its charge balance. The strongly distorted octahedral structures feature both *trans*-oriented nitrogen pairs, which span angles between 160° and 164° ($\text{N}(1)\text{--Zn}(1)\text{--N}(2)$ and $\text{N}(3)\text{--Zn}(2)\text{--N}(4)$) with a bond length of 1.96 Å to Zn(1) and of 2.00 Å to Zn(2)

(Table 9). All four hydroxymethylene alcohol side chains are aligned into the outer environment and are still protonated. The distance of these oxygen atoms to Zn(1) are measured to be 2.49 Å and 2.54 Å (O(3)/O(6)-Zn(1)) and to Zn(2) to be 2.23 Å and 2.31 Å (O(9)/O(12)-Zn(2)). The angles between them are nearly perpendicular, at 81° and 87° (O(3)-Zn(1)-O(6) and O(9)-Zn(2)-O(12)). All four phenol oxygens are oriented into the inner sphere of the whole unit, but in contrast to the crystal structure of complex $[\text{Zn}^{\text{II}}(\mathbf{7a})_2]_2 \cdot (\text{ClO}_4)_2$ discussed above (Figure 29), the two bound to Zn(2) atom are still protonated, whereas on Zn(1) only deprotonated phenolates are coordinated. The bond distances between O(1)/O(4)-Zn(1) are found to be 2.06 Å long, and for O(7)/O(10)-Zn(2) to be 2.12 Å and 2.08 Å. It is clear to see, that the bonds from the Zn(2) centres to the still protonated oxygens O(7)/O(10) are slightly longer than to the unprotonated oxygens O(1)/O(4) and are probably effected by the presence of hydrogen bridges. All four meridional coordinating ligands describe comparable angles of 160° (O(1)-Zn(1)-O(3), O(4)-Zn(1)-O(6) and (O(7)-Zn(2)-O(9), O(10)-Zn(2)-O(12)). For both zinc(II) centres in complex $[\text{Zn}^{\text{II}}(\mathbf{9})_2]_2 \cdot (\text{ClO}_4)_2$ the isomer geometry is determined as the Λ -form (Figure 31).

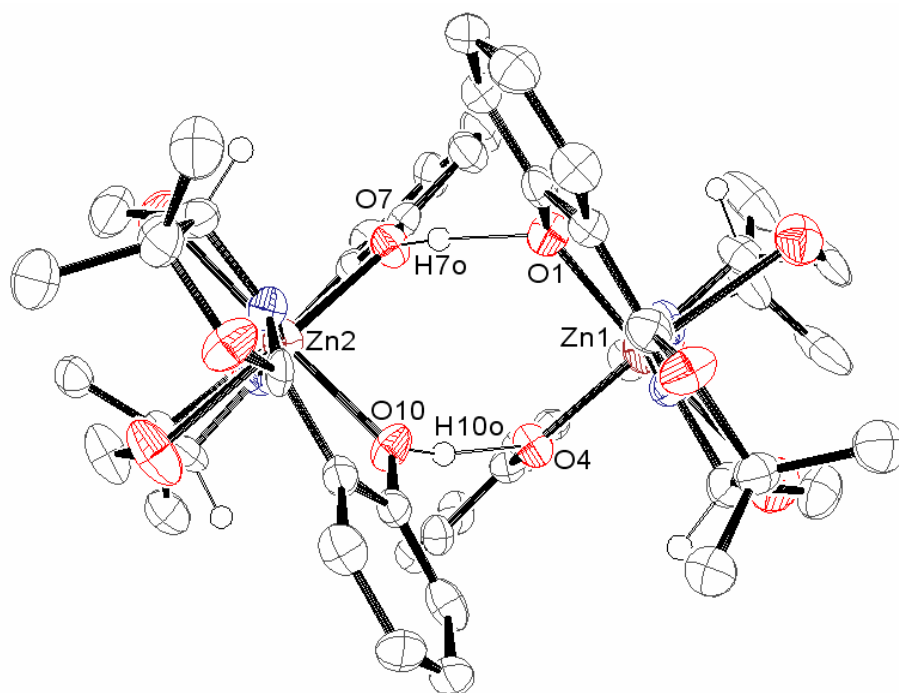


Figure 33. ORTEP plot at the 50% probability level of $[\text{Zn}^{\text{II}}(\mathbf{9})_2]_2 \cdot (\text{ClO}_4)_2$ – (not important hydrogen atoms and ClO_4^- are omitted for clarity).

Table 9. Selected bond distances (Å) and angles (°) of $[\text{Zn}^{\text{II}}(\mathbf{9})_2]_2 \cdot (\text{ClO}_4)_2$.

Bond Distances [Å]		Angles [°]	
Zn(1)-O(1)	2.056(4)	O(3)-Zn(1)-O(4)	93.41(16)
Zn(1)-O(3)	2.489(4)	O(3)-Zn(1)-O(6)	81.04(15)
Zn(1)-O(4)	2.057(4)	O(3)-Zn(1)-N(1)	72.66(16)
Zn(1)-O(6)	2.536(4)	O(3)-Zn(1)-N(2)	91.79(16)
Zn(1)-N(1)	1.956(4)	O(4)-Zn(1)-O(6)	160.05(13)
Zn(1)-N(2)	1.968(4)	O(4)-Zn(1)-N(1)	104.83(18)
Zn(2)-O(7)	2.118(4)	O(4)-Zn(1)-N(2)	88.26(16)
Zn(2)-O(9)	2.234(4)	O(6)-Zn(1)-N(1)	91.87(18)
Zn(2)-O(10)	2.083(4)	O(6)-Zn(1)-N(2)	72.88(18)
Zn(2)-O(12)	2.308(4)	O(1)-Zn(1)-N(2)	105.17(16)
Zn(2)-N(3)	2.001(4)	O(1)-Zn(1)-O(4)	96.45(15)
Zn(2)-N(4)	2.003(4)	O(1)-Zn(1)-O(6)	94.76(14)
		O(1)-Zn(1)-O(3)	160.58(13)
		O(1)-Zn(1)-N(1)	88.63(16)
		N(1)-Zn(1)-N(2)	160.0(2)
		O(7)-Zn(2)-O(9)	160.31(14)
		O(7)-Zn(2)-O(10)	93.80(15)
		O(7)-Zn(2)-O(12)	92.51(17)
		O(7)-Zn(2)-N(3)	109.05(18)
		O(7)-Zn(2)-N(4)	84.08(15)
		O(9)-Zn(2)-O(10)	93.37(15)
		O(9)-Zn(2)-O(12)	86.90(17)
		O(9)-Zn(2)-N(3)	89.99(19)
		O(9)-Zn(2)-N(4)	76.34(15)
		O(10)-Zn(2)-O(12)	160.04(14)
		O(10)-Zn(2)-N(3)	83.19(16)
		O(10)-Zn(2)-N(4)	105.44(15)
		O(12)-Zn(2)-N(3)	76.86(16)
		O(12)-Zn(2)-N(4)	94.03(16)
		N(3)-Zn(2)-N(4)	164.08(19)

The mass spectrometry (ESI) detected significant peaks of each 1:2-zinc(II) complex ($[\text{Zn}^{\text{II}}(\text{L})_2]^+$) and its corresponding free ligand (L). Furthermore, for ligand **8** an additional second complex species with a Zn_2L_3 -stoichiometry was detected, which is not surprising with regard to the crystal structures obtained and probably caused by an usual fragmentation in the ESI method. The elemental analysis also confirmed a ZnL_2 -stoichiometry, $[\text{Zn}^{\text{II}}(\text{L})_2] \cdot (\text{ClO}_4)$, which also agrees with the dimeric structure.

C.2.13 Liquid-State-Analysis of Zinc(II) Complexes – $[\text{Zn}^{\text{II}}(\mathbf{7a-9})_2]_2 \cdot (\text{ClO}_4)_2$

UV/Vis measurements of the $[\text{Zn}^{\text{II}}(\mathbf{7a-9})_2]_2 \cdot (\text{ClO}_4)_2$ complex series results in three very similar spectra (Figure 34). Absorptions before 280 nm are ligand or salt specific (see *experimental part F.9.2*, Figure 3 and 4), but the bands between 280 and 380 nm seem to be significant for the complex. It is assumed that here two different absorptions are overlapped. It is highly probable that the right hand side of this absorption, starting around 330 nm to lower energies, results from a complex-specific-transition (LMCT), whereas the left hand side of the broad band comes from a ligand-specific-transition.

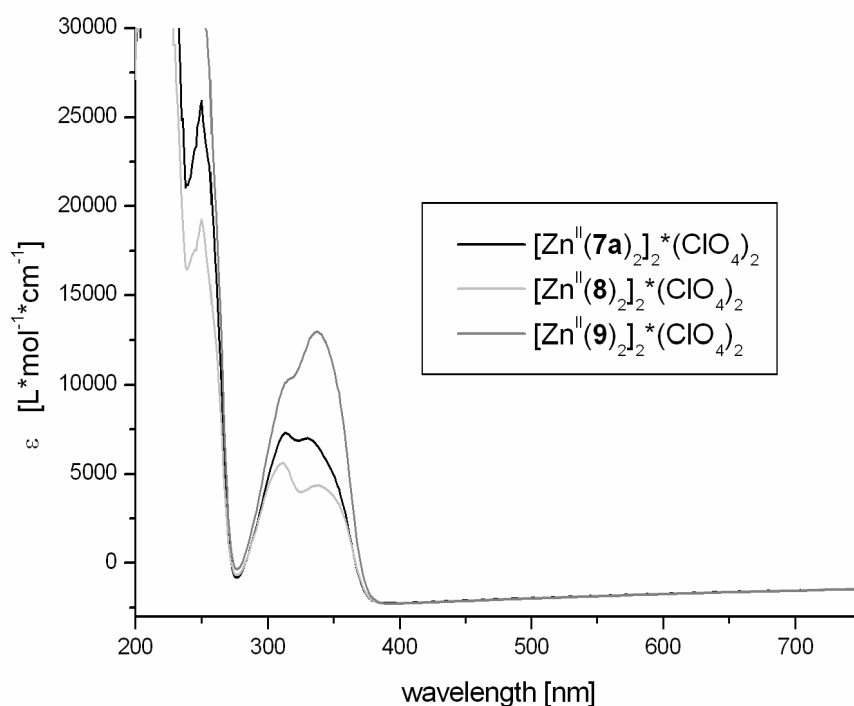


Figure 34. UV/Vis spectra for the $[\text{Zn}^{\text{II}}(\mathbf{7a-9})_2]_2 \cdot (\text{ClO}_4)_2$ series.

The circular dichroism spectra (CD) of the $[\text{Zn}^{\text{II}}(\mathbf{7a-9})_2]_2 \cdot (\text{ClO}_4)_2$ series were measured using circularly polarized light in a range of 200 to 400 nm (Figure 35) in acetonitrile at room

temperature. Complex $[\text{Zn}^{\text{II}}(\mathbf{7a})_2]_2 \cdot (\text{ClO}_4)_2$ (Figure 35, black line), which was identified to form a octahedral Δ -isomer, and complex $[\text{Zn}^{\text{II}}(\mathbf{8})_2]_2 \cdot (\text{ClO}_4)_2$ (Figure 35, light grey line), showed exactly the same CD graphs and it is reasonable to assume that $[\text{Zn}^{\text{II}}(\mathbf{8})_2]_2 \cdot (\text{ClO}_4)_2$ possesses also Δ -conformation. On the other hand, complex $[\text{Zn}^{\text{II}}(\mathbf{9})_2]_2 \cdot (\text{ClO}_4)_2$ (Figure 35, dark grey line), already known to form a Λ -isomer, shows completely different features. The CD spectra of the ligands **7a-9** (see *experimental part F.9.2*, Figure 4) are in an agreement in their stereo chemical information with the zinc(II) complexes $[\text{Zn}^{\text{II}}(\mathbf{7a-9})_2]_2 \cdot (\text{ClO}_4)_2$.

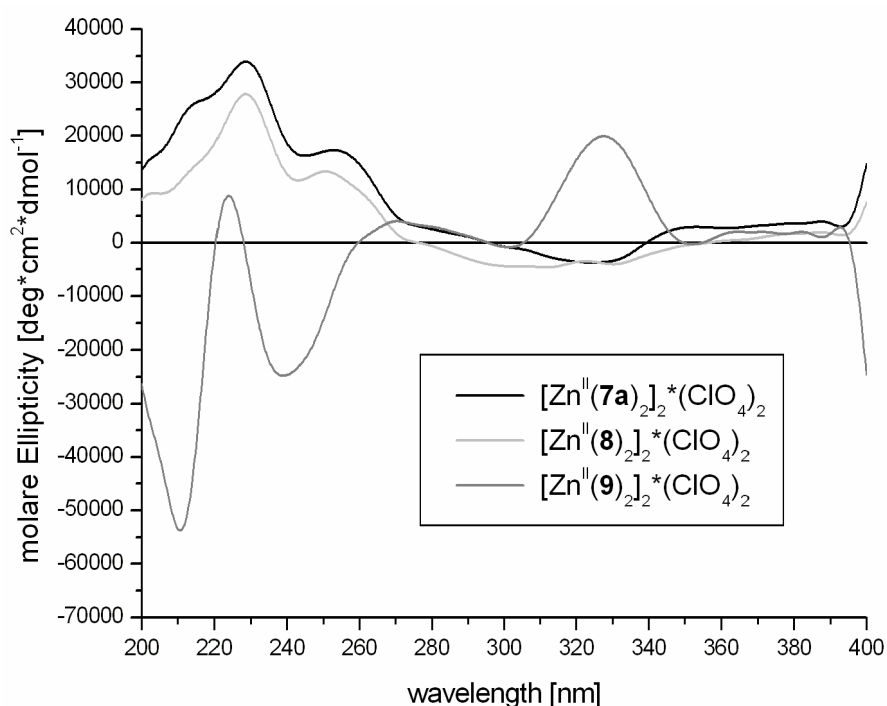
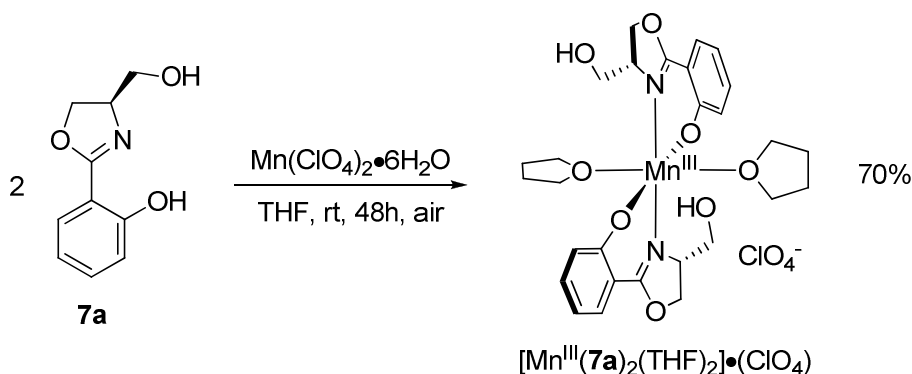


Figure 35. CD spectra for the $[\text{Zn}^{\text{II}}(\mathbf{7a-9})_2]_2 \cdot (\text{ClO}_4)_2$ series.

C.2.14 Formation of a Manganese(III) Complex using $\text{Mn}(\text{ClO}_4)_2 \cdot 6\text{H}_2\text{O}$ ²⁸

Manganese was used as the last 3d-transition metal in the complex formation reaction with ligand **7a**. Two equivalents of oxazoline ligand **7a** were dissolved in THF and were transferred into a solution of one equivalent $\text{Mn}(\text{ClO}_4)_2 \cdot 6(\text{H}_2\text{O})$ in THF (Scheme 9). The colour immediately changed without further adducts (base, e. g. NEt_3)⁸⁹ from slightly yellow into dark green. This colour change was already observed by Bouwman and co-workers and indicates the successful complex formation as well as an oxidation from Mn^{2+} to Mn^{3+} .⁸⁹ Further investigations (see below) revealed similar binding characteristics between the manganese and the iron metal. Two oxazoline ligands coordinate the metal via the nitrogen atoms as well as the deprotonated phenolate oxygen and two THF molecules complete an octahedral geometry. This is in contrast to the observed meridional structure of $[\text{Fe}^{\text{III}}(\mathbf{7a})_2] \cdot (\text{ClO}_4)$ (Figure 8), where the octahedral geometry is fulfilled by the tridentate coordinating ligands.



Scheme 9. Synthesis of the manganese(III) complex $[\text{Mn}^{\text{III}}(\mathbf{7a})_2(\text{THF})_2] \cdot (\text{ClO}_4)$ using $\text{Mn}(\text{ClO}_4)_2 \cdot 6\text{H}_2\text{O}$.

C.2.15 Solid-State-Analysis of a Manganese(III) Complex – $[\text{Mn}^{\text{III}}(\mathbf{7a})_2(\text{THF})_2] \cdot (\text{ClO}_4)$

Typical IR features of the complex $[\text{Mn}^{\text{III}}(\mathbf{7a})_2(\text{THF})_2] \cdot (\text{ClO}_4)$ are a free alcohol stretch around 3480 cm^{-1} and the shift of a strong band from 1644 cm^{-1} (uncoordinated and unsaturated C=N stretch) to 1604 cm^{-1} for a coordinating ligand C=N vibration. Furthermore, a characteristic broad and very strong band at 1086 cm^{-1} as well as a sharp band at 619 cm^{-1} indicate the presence of a perchlorate.^{80,89}

Crystallographic investigations of complex $[\text{Mn}^{\text{III}}(\mathbf{7a})_2(\text{THF})_2] \cdot (\text{ClO}_4)$ showed an octahedral coordination of the manganese(III) metal utilizing two bis(didentate) oxazoline ligands **7a** and two solvent molecules (THF) directly coordinated in a *trans*-orientation (Figure 36 and 37). The positive charge is balanced by two deprotonated phenolate oxygens of the ligands and one perchlorate molecule bound in the outer environment. Both nitrogen atoms are positioned in a typical *trans*-orientation (172°) and their distances to the manganese are between 1.95 and 1.98 Å (Table 10). The deprotonated oxygens of the phenols and the nitrogens are placed in a nearly quadratic planar manner as shown by the significant angle of O(1)-Mn(1)-O(4), spanning exactly 178° . The angles between O(1)-Mn(1)-N(1) with 90° and between O(4)-Mn(1)-N(1) with 88° complete this statement. The two THF molecules spanning an angle of 178° (O(7)-Mn(1)-O(8)) are located on the left hand and right hand side of the structure, while their orientation is almost perpendicular. The bond lengths of the two oxygens in the oxazoline ring are measured to 1.86 Å (O(1)/O(4)-Mn(1)), whereas the THF oxygens differ in their distance to the metal, from 2.21 Å (O(7)-Mn(1)) to 2.32 Å (O(8)-Mn(1)). All these features give rise to a nearly perfect octahedral complex.

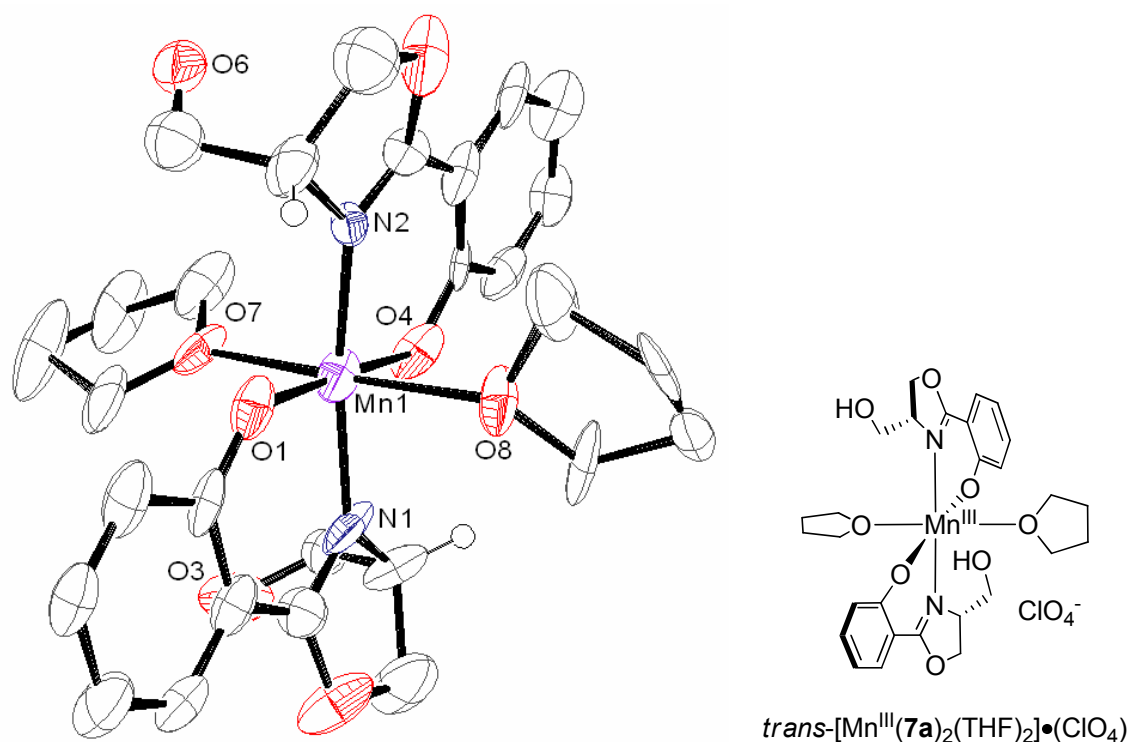


Figure 36. ORTEP plot at the 50% probability level of $[\text{Mn}^{\text{III}}(\mathbf{7a})_2(\text{THF})_2] \cdot (\text{ClO}_4)$ – (not important hydrogen atoms and ClO_4^- are omitted for clarity).

With two oxazoline ligands with the same chirality and their *trans*-orientation, both hydroxymethylen side chains are aligned in one direction (Figure 37).⁸⁹ These oxygens are

not involved in the coordination to the metal, and are found on a straight line (176° (O(3)-O(7)-O(6), not shown in Table 10) together with the THF (O(7)) oxygen. The corresponding lengths are measured as 3.83 \AA (O(6)-O(7)) and 3.66 \AA (O(3)-O(7)) (not shown in Table 10). The complex structure was identified as the *trans*-isomer (Figure 38).

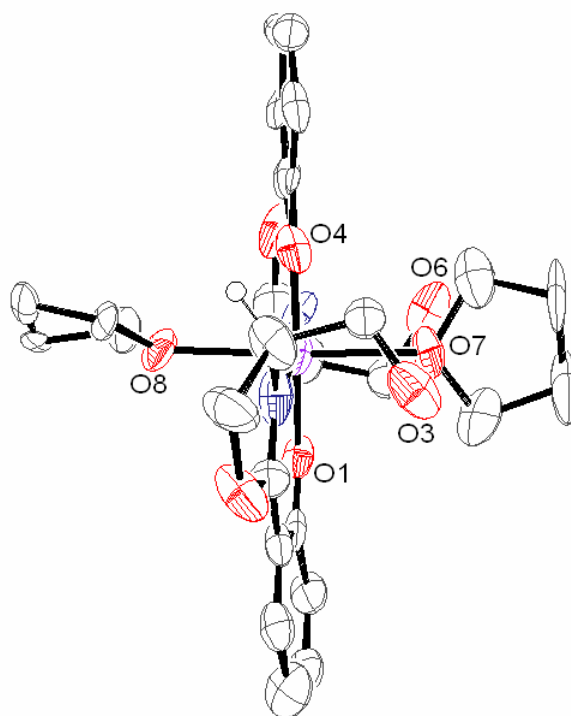


Figure 37. ORTEP plot at the 50% probability level of $[\text{Mn}^{\text{III}}(\mathbf{7a})_2(\text{THF})_2] \cdot (\text{ClO}_4)$ – (not important hydrogen atoms and ClO_4^- are omitted for clarity).

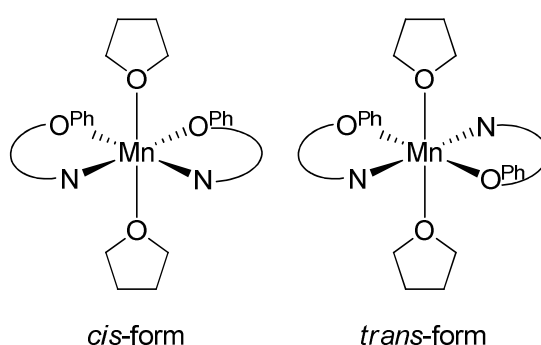


Figure 38. Octahedral binding model *cis* / *trans*-form for two didentate ligands and two solvent molecules.

Bouwman and co-workers already reported a similar complex system,⁸⁹ using the racemic ligand (\pm)-**46** and obtained the complex $(\text{HNEt}_3) \cdot \text{trans}-[\text{Mn}^{\text{III}}((R)\text{-}\mathbf{46})((S)\text{-}\mathbf{46})(\text{H}_2\text{O})_2]$ (Figure 39, left). Due to the racemic ligand (\pm)-**46** used, both carbonic acid side chains are directed in opposite half spaces, each pointing to a *trans*-oriented H_2O molecule.

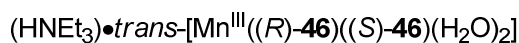
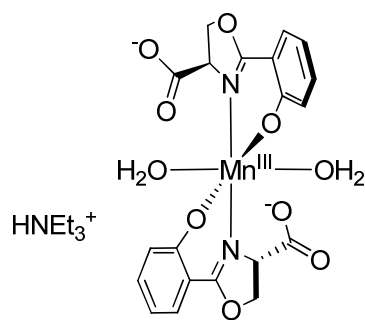


Figure 39. Manganese(III) complex, reported by Bouwman.⁸⁹

Table 10. Selected bond distances (Å) and angles (°) of $[\text{Mn}^{\text{III}}(\mathbf{7a})_2(\text{THF})_2] \cdot (\text{ClO}_4)$.

Bond Distances [Å]		Angles [°]	
Mn(1)-O(1)	1.866(5)	O(1)-Mn(1)-O(4)	178.3(2)
Mn(1)-O(4)	1.858(5)	O(1)-Mn(1)-O(7)	91.39(17)
Mn(1)-O(7)	2.211(4)	O(1)-Mn(1)-O(8)	90.54(17)
Mn(1)-O(8)	2.322(4)	O(1)-Mn(1)-N(1)	90.0(2)
Mn(1)-N(1)	1.981(6)	O(1)-Mn(1)-N(2)	91.7(2)
Mn(1)-N(2)	1.952(5)	O(4)-Mn(1)-O(7)	88.97(17)
		O(4)-Mn(1)-O(8)	89.14(17)
		O(4)-Mn(1)-N(1)	88.3(2)
		O(4)-Mn(1)-N(2)	90.0(2)
		O(7)-Mn(1)-O(8)	177.8(2)
		O(7)-Mn(1)-N(1)	95.3(2)
		O(7)-Mn(1)-N(2)	92.70(18)
		O(8)-Mn(1)-N(1)	85.9(2)
		O(8)-Mn(1)-N(2)	86.09(17)
		N(1)-Fe(1)-N(2)	171.8(2)

The mass spectrometry (ESI) shows significant mass peaks for a 1:2-manganese(III) complex ($[\text{Mn}^{\text{III}}(\text{L})_2]^+$) and for its corresponding free ligand (L). Additionally a second complex species with a Mn_2L_3 -stoichiometry was detected. This was previously seen in the mass analysis of zinc(II) complex $[\text{Zn}^{\text{II}}(\mathbf{8})_2] \cdot (\text{ClO}_4)_2$ and leads to further speculation. This

manganese-ligand-system might be also able to form dimers, if no solvent is present to stabilize the complex.⁸² Nevertheless, the elemental analysis prepared from a dried sample of the manganese(III) complex confirmed a MnL_2 -stoichiometry, which might be also in a good agreement for a dimeric structure without further stabilizations by solvent molecules.

C.2.16 Liquid-State-Analysis of a Manganese(III) Complex – $[\text{Mn}^{\text{III}}(\mathbf{7a})_2(\text{THF})_2] \cdot (\text{ClO}_4)$

The UV/Vis spectra of the manganese(III) complex shows an significant difference in comparison to the ligand as well as the pure salt spectra (see *experimental part F.9.2*, Figure 3 and 4). The shoulder between 330 and 390 nm definitely arise from a complex-specific-transition (LMCT) (Figure 40).

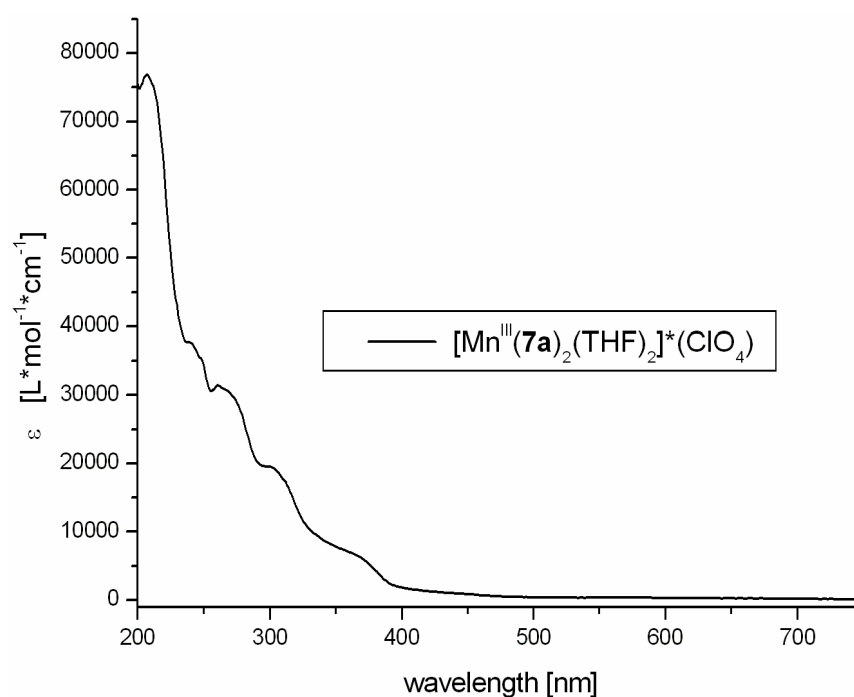


Figure 40. UV/Vis spectra of $[\text{Mn}^{\text{III}}(\mathbf{7a})_2(\text{THF})_2] \cdot (\text{ClO}_4)$.

The CD spectra of the manganese(III) complex $[\text{Mn}^{\text{III}}(\mathbf{7a})_2(\text{THF})_2] \cdot (\text{ClO}_4)$ is shown in Figure 41. As determined by X-ray crystallography the complex geometry was identified as an octahedral *trans*-isomer, and it is reasonable to assume that this is conserved in solution.

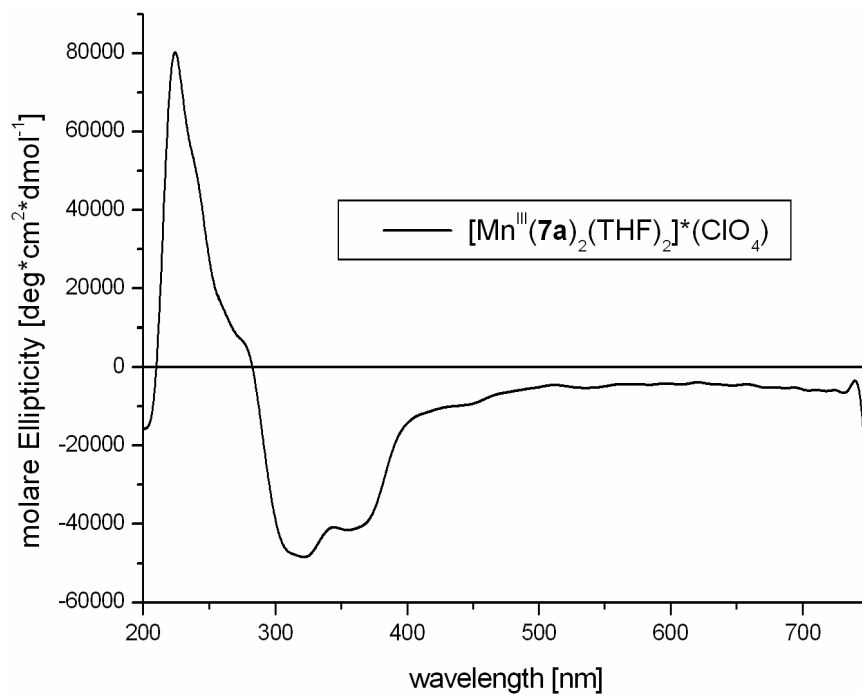


Figure 41. CD spectra of $[\text{Mn}^{\text{III}}(\mathbf{7a})_2(\text{THF})_2] \cdot (\text{ClO}_4)$.

C.2.17 Summary

In conclusion, for all three oxazoline derivatives (**7a-9**) it can be predicted that complexation reactions with salts having weak counter anions (e. g. $\text{Fe}(\text{ClO}_4)_2 \cdot 6\text{H}_2\text{O}$ and $\text{Zn}(\text{ClO}_4)_2 \cdot 6\text{H}_2\text{O}$) usually form a meridional bis(tridentate) binding structure (Table 11, entry 1/(4)/5). In counterpart to this, metals with strong counter anions (e. g. $\text{Fe}(\text{OAc})_2$ and $\text{Fe}(\text{acac})_3$) prefer a tri(didentate) structural formation (Table 11, entry 2 and 3). Furthermore, the structural geometry of the complexes is controlled by the stereo centre of the ligands as well as the nature of the counter anion.

All obtained crystallographic structures possess a distorted octahedral geometry with slightly varying angles from ideally 90° or 180° , but in spite of this fact, a C_2 -symmetric formation for all complexes can be concluded.

Table 11. Summary of all structural geometries for the salts used.

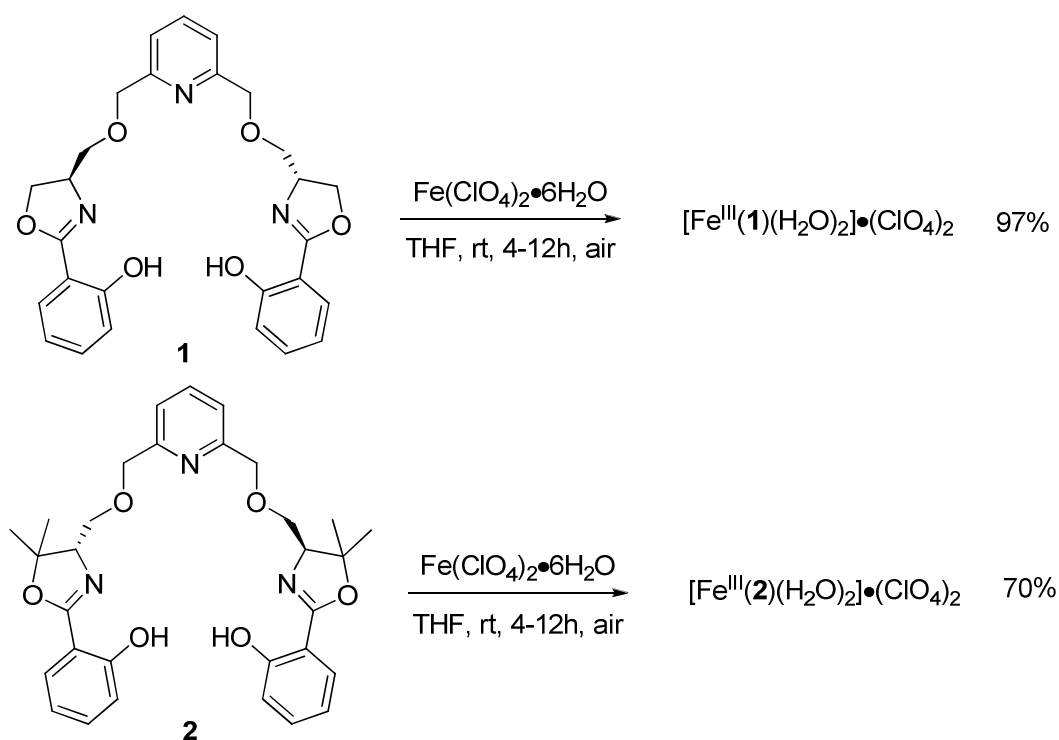
Entry	Salt	Ligand 7a		Ligand 8		Ligand 9		Ligand Coordination
1	$\text{Fe}(\text{ClO}_4)_2 \cdot 6\text{H}_2\text{O}$	Δ	(X-ray)	Δ	(CD)	Δ	(CD)	meridional - bis(tridentate)
2	$\text{Fe}(\text{OAc})_2$	Δ	(X-ray)	Δ	(X-ray)	Δ	(X-ray)	tri(didentate)
3	$\text{Fe}(\text{acac})_3$	(Δ)	(CD)	(Δ)	(CD)	(Δ)	(CD)	tri(didentate)
4	$[\text{RuCl}_2(\text{benzene})_2]_2$	-		-		-		(meridional)
5	$\text{Zn}(\text{ClO}_4)_2 \cdot 6\text{H}_2\text{O}$	Δ	(X-ray)	Δ	(CD)	Δ	(X-ray)	meridional - bis(tridentate)
6	$\text{Mn}(\text{ClO}_4)_2 \cdot 6\text{H}_2\text{O}$	<i>trans</i> -form		-		-		di(didentate)

D. Main part – Bis(oxazoline) Complex Analysis

D.1 Characterization of Bis(oxazoline)-Metal-Complexes

D.1.1 Formation of Iron(III) Complexes using $\text{Fe}(\text{ClO}_4)_2 \cdot 6(\text{H}_2\text{O})$

The bis(oxazoline) derivatives (**1**, **2**, (\pm)-**4**/(*meso*)-**4**, **5**) were utilized as a second ligand series to chelate $\text{Fe}(\text{ClO}_4)_2 \cdot 6(\text{H}_2\text{O})$ (Scheme 1 and 2). This type of ligand is known to form 1:1 complexes,^{42,43} and so one equivalent of a bis(oxazoline) ligand was dissolved in THF and was transferred into a solution of one equivalent $\text{Fe}(\text{ClO}_4)_2 \cdot 6(\text{H}_2\text{O})$ in THF. The colour immediately changed from slightly red to dark purple, indicating a rapid complex formation as well as a spontaneous oxidation of Fe^{2+} to Fe^{3+} (significant dark purple colour originates from a charge-transfer transition from the phenolic oxygen to a iron(III) ion).⁷⁴

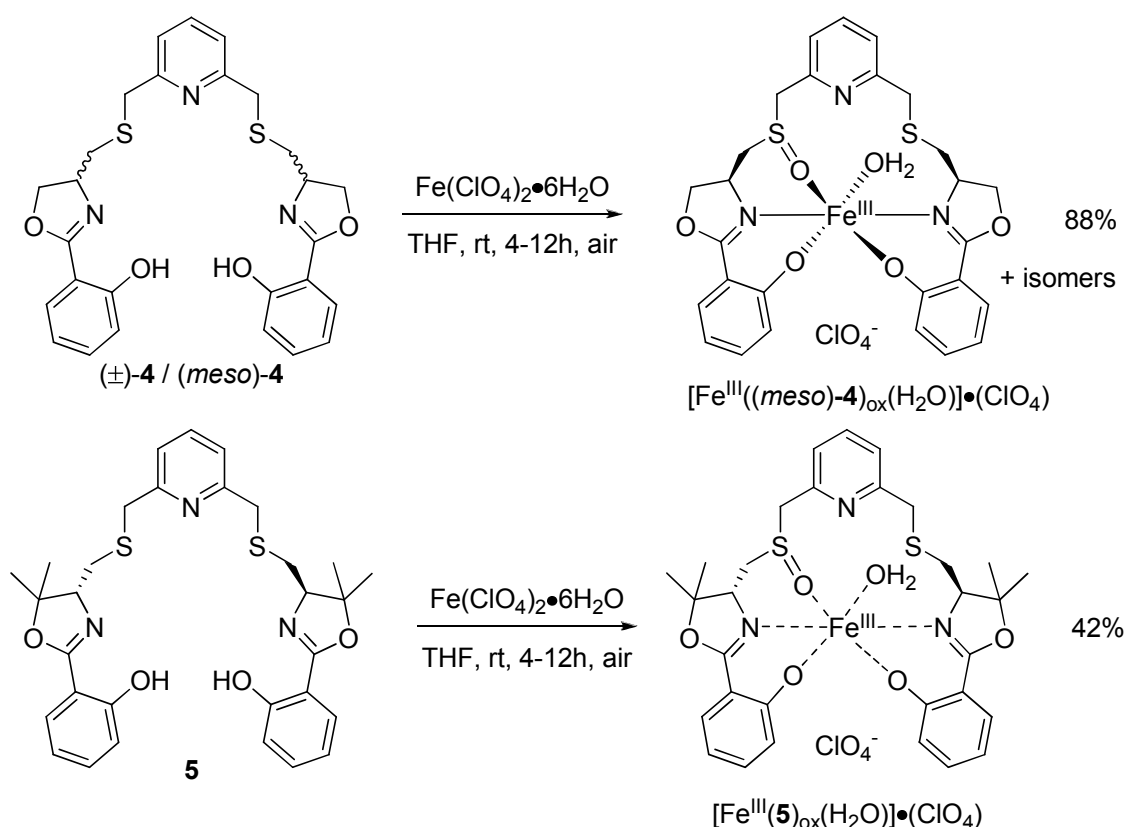


Scheme 1. Synthesis of the complexes $[\text{Fe}^{\text{III}}(\text{1})(\text{H}_2\text{O})_2] \cdot (\text{ClO}_4)_2$ and $[\text{Fe}^{\text{III}}(\text{2})(\text{H}_2\text{O})_2] \cdot (\text{ClO}_4)_2$.

Further investigations (see below) revealed a different binding characteristic than assumed from results of former investigations in our group,^{42,43} which predicted a pentadentate chelate system, using the nitrogen atom of the pyridine ring, both nitrogen atoms of the oxazoline rings and two oxygen or sulphur atoms of the ether or thioether bridges, respectively.

Instead of this, evidence was found for two further binding motifs: A tetradentate chelation, using both oxazoline nitrogen atoms and the newly introduced oxygens of the phenolates, which stabilizes the iron(III) centre (Figure 3, proposed) and a pseudo-pentadentate (Scheme 2) coordination. In the latter the tetradentate complexation is expanded by a peculiarity, which is outlined in Figure 1. The structure exhibits an unexpected sulfoxide bridge, which resulted from an oxidation of the sulphur atom, and serves as new fifth coordination position. This was only observed when using the sulphur containing ligands (\pm)-**4**/(*meso*)-**4** and **5**.

Furthermore, earlier complexation reactions between iron(II) salts and bis(oxazoline) ligands performed in our group resulted in air stable iron(II) complexes.⁴² Due to the newly introduced *ortho*-OH groups in the ligand, the changed binding motifs led to an unstable iron(II) species, which was immediately oxidized. This observation was also made for the oxazoline ligands **7a-9** (see main part – oxazoline complex analysis C.2.1-C.2.8).



Scheme 2. Synthesis of the complexes $[\text{Fe}^{\text{III}}((\text{meso})\text{-4})_{\text{ox}}(\text{H}_2\text{O})] \cdot (\text{ClO}_4)$ and $[\text{Fe}^{\text{III}}(\text{5})_{\text{ox}}(\text{H}_2\text{O})] \cdot (\text{ClO}_4)$.

D.1.2 Solid-State-Analysis of Iron(III) Complexes –

 $\text{Fe}^{\text{III}}((\text{meso})\text{-4})_{\text{ox}}(\text{H}_2\text{O})\cdot(\text{ClO}_4)$

The IR spectra of all four iron(III) bis(oxazoline) complexes showed the same typical features. A broad alcohol stretch around 3300 cm^{-1} , a strong band at 1603 cm^{-1} indicating a coordinating ligand C=N vibration, and a characteristic broad and very strong band around 1070 cm^{-1} as well as a sharp band at 619 cm^{-1} for the perchlorate, were detected.⁸⁰

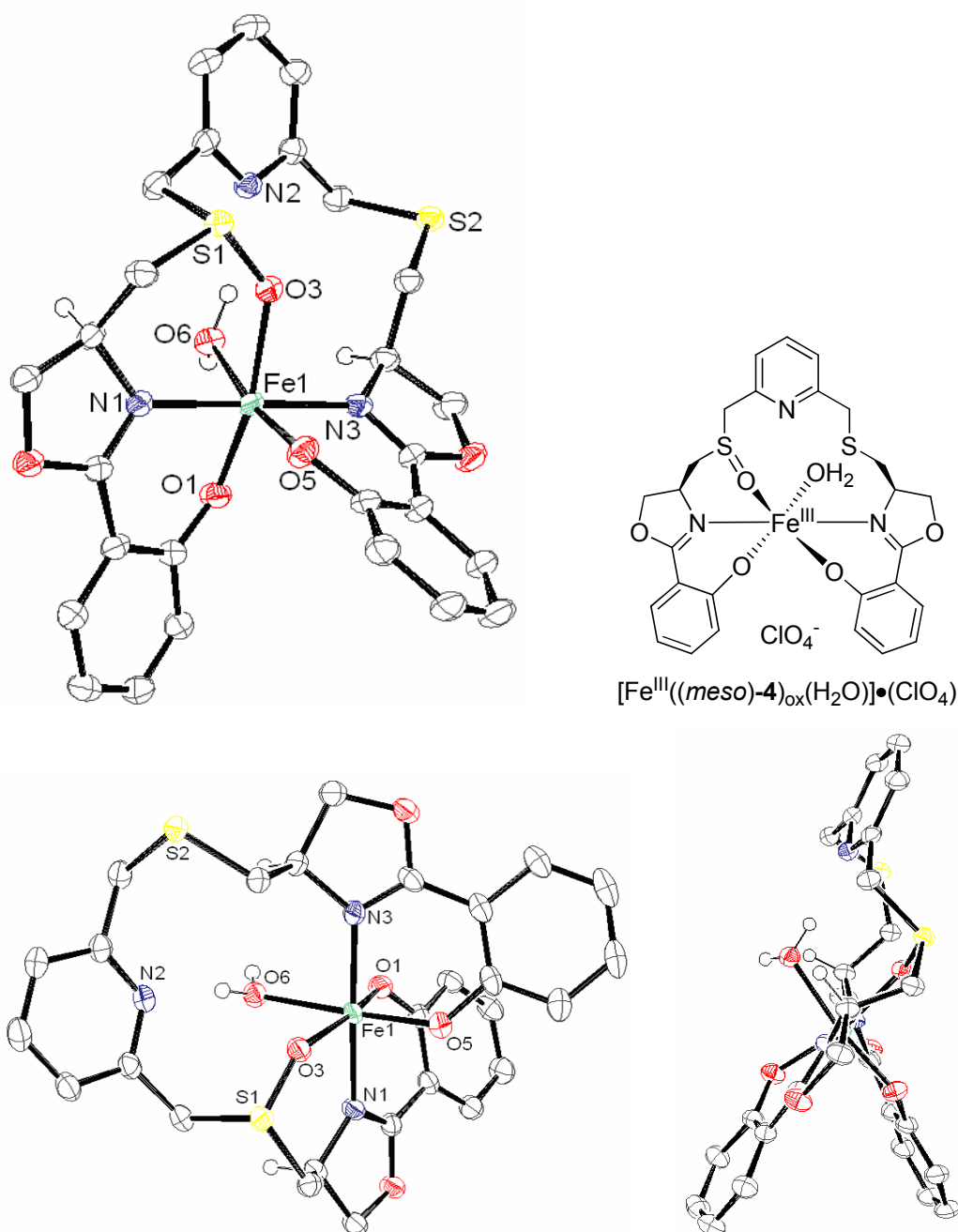


Figure 1. ORTEP plot at the 50% probability level of $[\text{Fe}^{\text{III}}((\text{meso})\text{-4})_{\text{ox}}(\text{H}_2\text{O})]\cdot(\text{ClO}_4)$ – (not important hydrogen atoms and ClO_4^- are omitted for clarity).

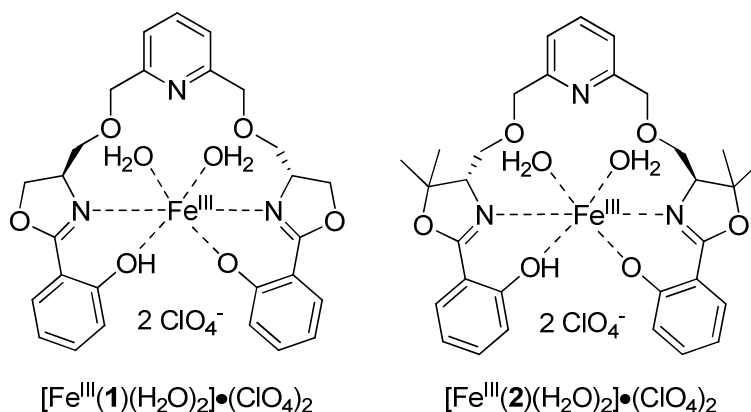
In this series, suitable crystals for X-ray crystallography were obtained only for complex $[\text{Fe}^{\text{III}}((\text{meso})\text{-4})_{\text{ox}}(\text{H}_2\text{O})]\cdot(\text{ClO}_4)$, formed by the (*meso*)-**4** ligand with mixed configured stereo centres (*R,S*). Here, the bis(oxazoline) (*R,S*)-**4** chelates an iron metal in a pseudo-pentadentate fashion and forms with a sixth coordination (H_2O) an octahedral geometry (Figure 1). As already mentioned above, both deprotonated oxygens of the phenolates and two oxazoline nitrogens are involved in the binding structure. Furthermore, the oxygen of the sulfoxide and a H_2O molecule complete the octahedral geometry around the metal, while the pyridine nitrogen does not take part in the complexation. The positive charges of the Fe^{3+} are neutralized by two deprotonated phenolates and one perchlorate that is not coordinated at the metal. The distance of the two opposite placed nitrogen atoms (N(1) and N(3)) have the typical length of 2.11 Å (Table 1), which is comparable to the distances in the di-/tridentate oxazoline iron(III) complexes (see *main part – oxazoline complex analysis* **C.2.1-C.2.8**). The bond lengths of the phenolate oxygen atoms (Fe(1)-O(1) and Fe(1)-O(5)) were determined to be 1.92 Å and are significantly shorter than the distance of the sulfoxide oxygen (Fe(1)-O(3) with 2.08 Å) and the oxygen of the water molecule (Fe(1)-O(6) with 2.13 Å) to the metal centre. A *trans*-alignment of N(1)-Fe(1)-N(3) was confirmed by an angle of 179°, leading to a slightly distorted octahedral geometry. This was also characterized by the nearly square-planar location of the coordinated oxygen atoms, which span angles between 87° and 100° (O(1)-Fe(1)-O(5), O(3)-Fe(1)-O(5), O(3)-Fe(1)-O(6), O(1)-Fe(1)-O(6)). In keeping the preferred octahedral geometry around the metal, the ligand system becomes strongly distorted by the bond interaction between the sulfoxide oxygen and the iron ion (Figure 1). Due to this unexpected complex formation, the determination of the complex isomer was not possible.

The expected formation of the complexes $[\text{Fe}^{\text{III}}(\mathbf{1}/\mathbf{2})(\text{H}_2\text{O})_2]\cdot(\text{ClO}_4)_2$ was confirmed by mass analysis (ESI and LSIMS), having each a significant mass peak corresponding to a 1:1-iron(III) complex. Furthermore, the elemental analysis fit very well for a complex system containing one bis(oxazoline) ligand, an iron(III) metal, two H_2O molecules and finally two perchlorates. Based on the X-ray structure of complex $[\text{Fe}^{\text{III}}((\text{meso})\text{-4})_{\text{ox}}(\text{H}_2\text{O})]\cdot(\text{ClO}_4)$ and the information collected for $[\text{Fe}^{\text{III}}(\mathbf{1}/\mathbf{2})(\text{H}_2\text{O})_2]\cdot(\text{ClO}_4)_2$, the complex formation as outlined in Figure 2 was proposed.

Table 1. Selected bond distances (Å) and angles (°) of $[\text{Fe}^{\text{III}}(\text{meso-4})_{\text{ox}}(\text{H}_2\text{O})]\cdot(\text{ClO}_4)$.

Bond Distances [Å]		Angles [°]	
Fe(1)-O(1)	1.920(2)	O(1)-Fe(1)-O(3)	166.37(9)
Fe(1)-O(3)	2.079(2)	O(1)-Fe(1)-O(5)	99.77(9)
Fe(1)-O(5)	1.915(2)	O(1)-Fe(1)-O(6)	87.35(10)
Fe(1)-O(6)	2.132(2)	O(1)-Fe(1)-N(1)	86.16(10)
Fe(1)-N(1)	2.110(2)	O(1)-Fe(1)-N(3)	93.85(10)
Fe(1)-N(3)	2.105(3)	O(3)-Fe(1)-O(5)	92.91(9)
S(1)-O(3)	1.523(2)	O(3)-Fe(1)-O(6)	80.47(9)
		O(3)-Fe(1)-N(1)	88.45(9)
		O(3)-Fe(1)-N(3)	91.77(9)
		O(5)-Fe(1)-O(6)	171.42(10)
		O(5)-Fe(1)-N(1)	91.96(9)
		O(5)-Fe(1)-N(3)	86.98(9)
		O(6)-Fe(1)-N(1)	93.30(10)
		O(6)-Fe(1)-N(3)	87.78(10)
		N(1)-Fe(1)-N(3)	178.93(10)

The mass analysis of the complexes $[\text{Fe}^{\text{III}}((\pm)\text{-4}/(\text{meso})\text{-4/5})_{\text{ox}}(\text{H}_2\text{O})]\cdot(\text{ClO}_4)$ showed a significant mass peak for a 1:1-iron(III) complex as well as its oxidized species, but the elemental analysis indicated only the presence of the oxidized 1:1-iron(III) complex (Scheme 2).

**Figure 2.** Proposed binding structure of the complexes $[\text{Fe}^{\text{III}}(\mathbf{1/2})(\text{H}_2\text{O})_2]\cdot(\text{ClO}_4)_2$.

D.1.3 Liquid-State-Analysis of Iron(III) Complexes –

 $[\text{Fe}^{\text{III}}(\mathbf{1}/\mathbf{2})(\text{H}_2\text{O})_2] \cdot (\text{ClO}_4)_2$ and $[\text{Fe}^{\text{III}}((\pm)\text{-}\mathbf{4}/(\text{meso})\text{-}\mathbf{4}/\mathbf{5})_{\text{ox}}(\text{H}_2\text{O})] \cdot (\text{ClO}_4)$

The UV/Vis spectra were measured between 200 and 750 nm in acetonitrile at room temperature for the $[\text{Fe}^{\text{III}}(\mathbf{1}/\mathbf{2})(\text{H}_2\text{O})_2] \cdot (\text{ClO}_4)_2$ and $[\text{Fe}^{\text{III}}((\pm)\text{-}\mathbf{4}/(\text{meso})\text{-}\mathbf{4}/\mathbf{5})_{\text{ox}}(\text{H}_2\text{O})] \cdot (\text{ClO}_4)$ complexes (Figure 3). All iron(III) compounds exhibited the same features in their absorption spectra, indicating similar structures in solution. To differentiate which absorption maximum belongs to the specific compounds (ligand, salt, complex), each of them was explored separately under the same conditions (see *experimental part F.9.2*, Figure 1 and 5). With this knowledge in hand, an assignment of the maxima at 290 nm and 340 nm was possible. They characterize ligand-based transitions ($n \rightarrow \pi^*$ or $\pi \rightarrow \pi^*$), which are probable caused by the chromophores of the conjugated system in the ligand. The shoulder between 340 and 420 nm as well as the absorption at 525 nm for $[\text{Fe}^{\text{III}}(\mathbf{1}/\mathbf{2})(\text{H}_2\text{O})_2] \cdot (\text{ClO}_4)_2$ or at 540 nm for $[\text{Fe}^{\text{III}}((\pm)\text{-}\mathbf{4}/(\text{meso})\text{-}\mathbf{4}/\mathbf{5})_{\text{ox}}(\text{H}_2\text{O})] \cdot (\text{ClO}_4)$ are identified as complex specific. These transitions detected in the electronic spectra are the relatively intense charge-transfer (CT) bands responsible for the dark purple colour. They can be assigned to a transition from the p_π orbital on the phenolate oxygen to the half-filled d_π^* orbitals on the ferric iron(III) ion.⁷⁴⁻⁷⁶

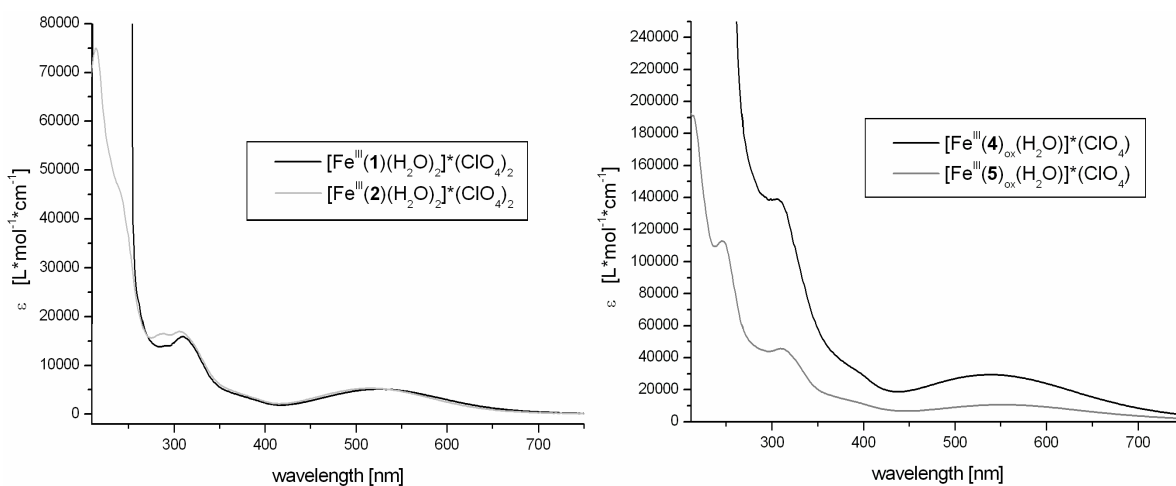


Figure 3. UV/Vis spectra of $[\text{Fe}^{\text{III}}(\mathbf{1}/\mathbf{2})(\text{H}_2\text{O})_2] \cdot (\text{ClO}_4)_2$ (left) and $[\text{Fe}^{\text{III}}((\pm)\text{-}\mathbf{4}/(\text{meso})\text{-}\mathbf{4}/\mathbf{5})_{\text{ox}}(\text{H}_2\text{O})] \cdot (\text{ClO}_4)$ (right) complexes.

The circular dichroism spectra (CD) of the $[\text{Fe}^{\text{III}}((\pm)\text{-}\mathbf{4}/(\text{meso})\text{-}\mathbf{4})_{\text{ox}}(\text{H}_2\text{O})] \cdot (\text{ClO}_4)$ complex was not detectable, because of the use of the $(\pm)\text{-}\mathbf{4}/(\text{meso})\text{-}\mathbf{4}$ ligand mixture. The resulting multiple complex geometries were not CD active in mixture. The enantiopure $[\text{Fe}^{\text{III}}(\mathbf{1}/\mathbf{2})(\text{H}_2\text{O})_2] \cdot (\text{ClO}_4)_2$ and the $[\text{Fe}^{\text{III}}(\mathbf{5})_{\text{ox}}(\text{H}_2\text{O})] \cdot (\text{ClO}_4)$ complexes exhibit a high similarity in their behaviour under the influence of circularly polarized light (Figure 4). The

samples were dissolved in acetonitrile and the measurements were made from 200 to 750 nm at room temperature. The graphs of complex $[\text{Fe}^{\text{III}}(\mathbf{2})(\text{H}_2\text{O})_2] \cdot (\text{ClO}_4)_2$ and $[\text{Fe}^{\text{III}}(\mathbf{5})_{\text{ox}}(\text{H}_2\text{O})] \cdot (\text{ClO}_4)$ (Figure 4, light grey line and dark grey line), which both contain the same methylated oxazoline rings and stereochemistry, but differ in their ether/thioether bridges, show a very similar curve progression and are comparable in their stereochemical information to the pure ligand spectra (see *experimental part F.9.2*, Figure 6). Only small features are seen, which indicate no structural homology between $[\text{Fe}^{\text{III}}(\mathbf{2})(\text{H}_2\text{O})_2] \cdot (\text{ClO}_4)_2$ and $[\text{Fe}^{\text{III}}(\mathbf{5})_{\text{ox}}(\text{H}_2\text{O})] \cdot (\text{ClO}_4)$. At 220 nm the ether bridged iron(III) complex $[\text{Fe}^{\text{III}}(\mathbf{2})(\text{H}_2\text{O})_2] \cdot (\text{ClO}_4)_2$ shows a significant maximum which was not observed in the graph of $[\text{Fe}^{\text{III}}(\mathbf{5})_{\text{ox}}(\text{H}_2\text{O})] \cdot (\text{ClO}_4)$ (thioether bridged). Furthermore, the positive curve at 330 nm of complex $[\text{Fe}^{\text{III}}(\mathbf{2})(\text{H}_2\text{O})_2] \cdot (\text{ClO}_4)_2$ was slightly shifted to 380 nm for complex $[\text{Fe}^{\text{III}}(\mathbf{5})_{\text{ox}}(\text{H}_2\text{O})] \cdot (\text{ClO}_4)$. The CD graph of the unmethylated complex $[\text{Fe}^{\text{III}}(\mathbf{1})(\text{H}_2\text{O})_2] \cdot (\text{ClO}_4)_2$ (ether bridged) (Figure 4, black line) exhibits an mirror image progression in comparison to the complexes $[\text{Fe}^{\text{III}}(\mathbf{2})(\text{H}_2\text{O})_2] \cdot (\text{ClO}_4)_2$ and $[\text{Fe}^{\text{III}}(\mathbf{5})_{\text{ox}}(\text{H}_2\text{O})] \cdot (\text{ClO}_4)$, and therefore confirms the different stereochemistry obtained in the complex as well as in the pure ligand. Unfortunately, the geometric information from the crystal of $[\text{Fe}^{\text{III}}(\textit{meso}\text{-}\mathbf{4})_{\text{ox}}(\text{H}_2\text{O})] \cdot (\text{ClO}_4)$ was not useful, because of the *meso*-character of the ligand. The complex geometry of the complexes $[\text{Fe}^{\text{III}}(\mathbf{1}/\mathbf{2})(\text{H}_2\text{O})_2] \cdot (\text{ClO}_4)_2$ and $[\text{Fe}^{\text{III}}(\mathbf{5})_{\text{ox}}(\text{H}_2\text{O})] \cdot (\text{ClO}_4)$ could not be assigned based on their CD spectra (Figure 4).

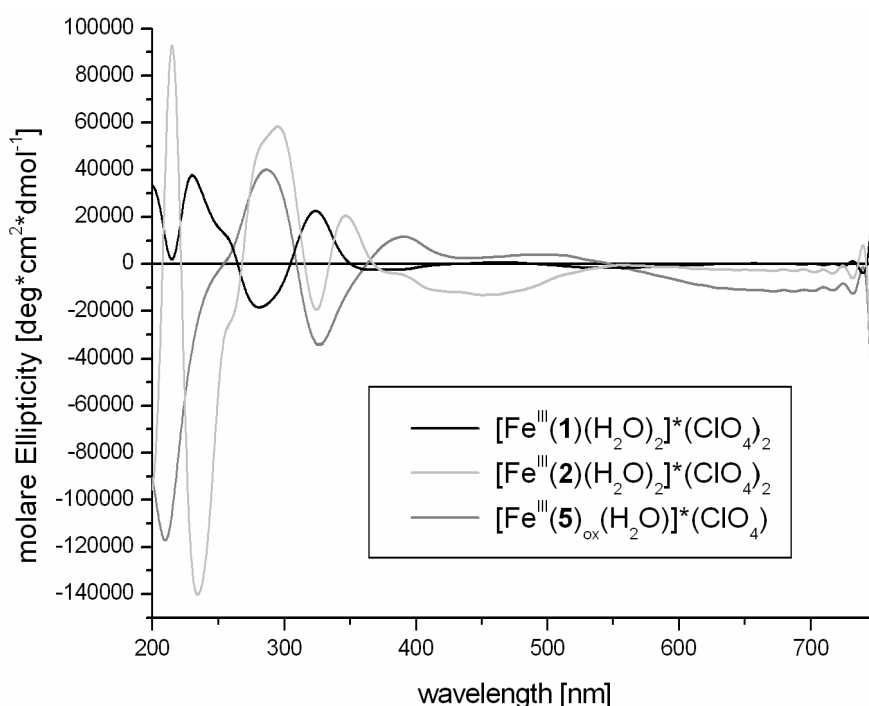
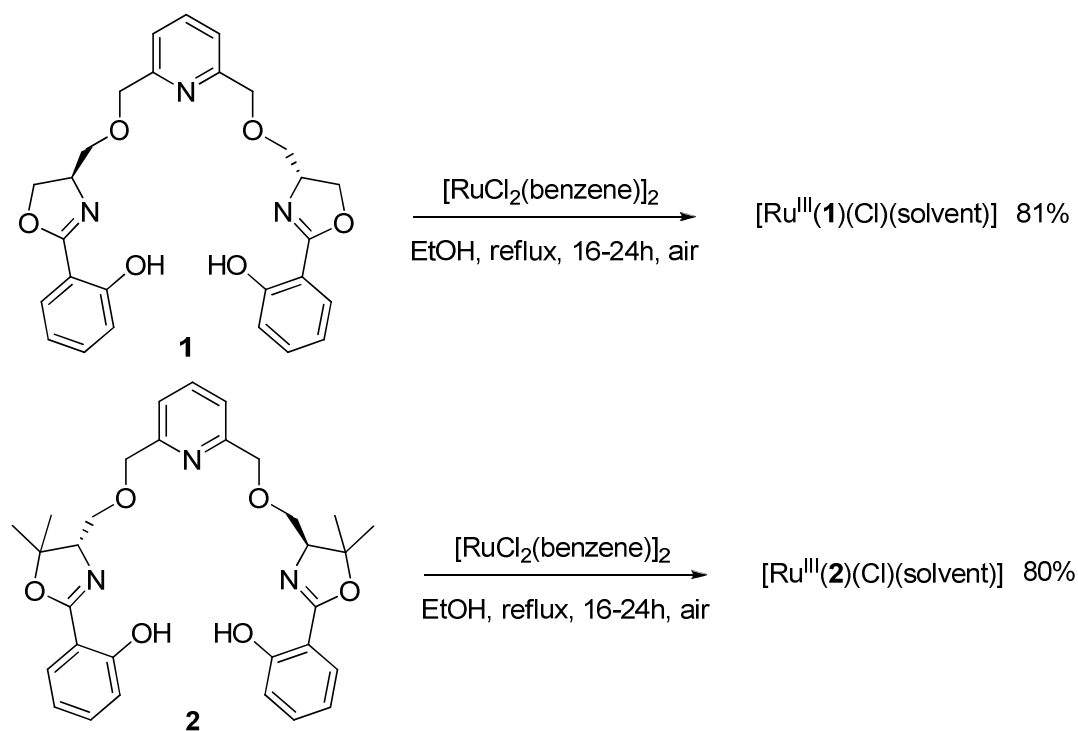


Figure 4. CD spectra of $[\text{Fe}^{\text{III}}(\mathbf{1}/\mathbf{2})(\text{H}_2\text{O})_2] \cdot (\text{ClO}_4)_2$ and $[\text{Fe}^{\text{III}}(\mathbf{5})_{\text{ox}}(\text{H}_2\text{O})] \cdot (\text{ClO}_4)$ complexes.

D.1.4 Formation of Ruthenium(II) and Ruthenium(III) Complexes using $[\text{RuCl}_2(\text{benzene})]_2$

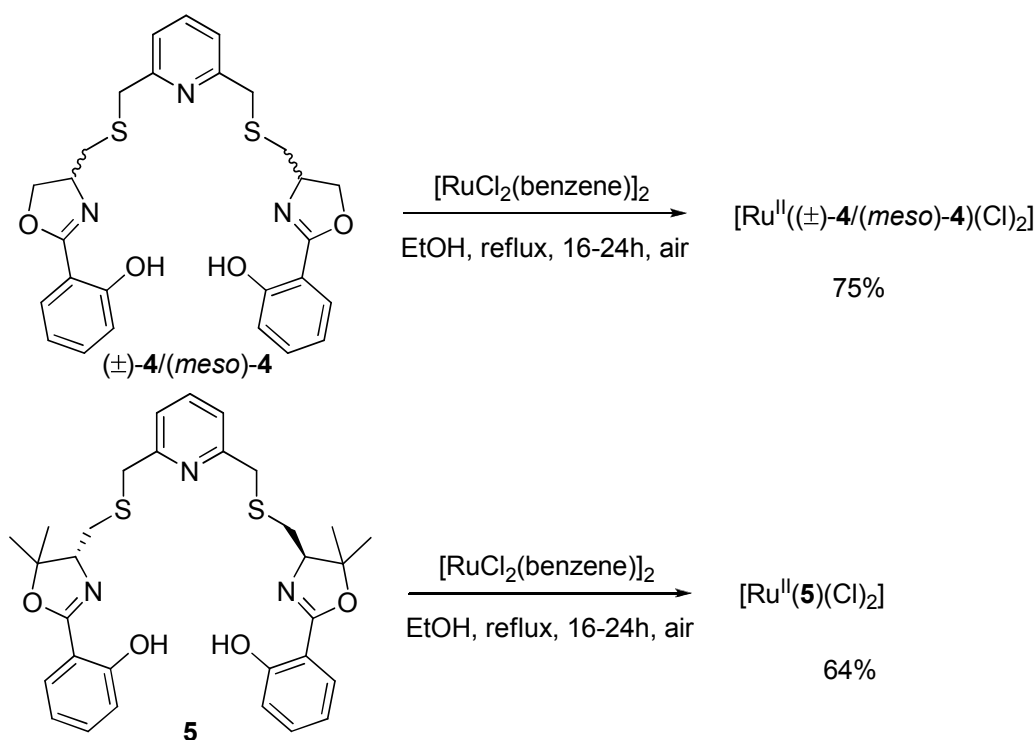
The effect on the complex formation of an iron-related metal was already described (see *main part - oxazoline complex analysis C.2.9-C.2.10*). The ruthenium salt $[\text{RuCl}_2(\text{benzene})]_2$ was selected and also serves here as a suitable metal source for the complexation experiments of the bis(oxazoline) ligands (**1**, **2**, (\pm)-**4**/(*meso*)-**4**, **5**).⁸⁴ One equivalent of the ligand (**1**, **2**, (\pm)-**4**/(*meso*)-**4**, **5**), dissolved in ethanol, was transferred into an ethanol suspension of one equivalent ruthenium salt (Scheme 3 and 4) and the reaction mixture was heated to reflux for 16-24 h. For the ether bridged ligands **1** and **2** (Scheme 3) the colour slowly changed from a green-brown ruthenium(II) salt to a dark purple ruthenium(III) complex, and for the thioether bridged ligands (\pm)-**4**/(*meso*)-**4** and **5** (Scheme 4) only the dark green colour of a ruthenium(II) complex became visible.



Scheme 3. Synthesis of the complexes $[\text{Ru}^{\text{III}}(\text{1})(\text{Cl})(\text{solvent})]$ and $[\text{Ru}^{\text{III}}(\text{2})(\text{Cl})(\text{solvent})]$.

The colour indicates that in the case of the complexes $[\text{Ru}^{\text{III}}(\text{1/2})(\text{Cl})(\text{solvent})]$ (Scheme 3) an oxidation of the ruthenium(II) salt into a ruthenium(III) complex, presumably by air, occurred. In contrast to this, the complexes $[\text{Ru}^{\text{II}}((\pm)\text{-4}/(\textit{meso})\text{-4/5})(\text{Cl})_2]$ (Scheme 4) proved to be stable on air and so a ruthenium(II) complex was isolated. It is assumed that a charge-

transfer transition from the phenolic oxygen to a ruthenium(III) ion is responsible for the dark purple colour of the complexes $[\text{Ru}^{\text{III}}(\mathbf{1}/\mathbf{2})(\text{Cl})(\text{solvent})]^{74}$ and the therefore observed colour variation indicates different product formation by using either an ether (**1**, **2**) or thioether ((\pm)-**4**/(*meso*)-**4**, **5**) bridged ligand.



Scheme 4. Synthesis of the complexes $[\text{Ru}^{\text{II}}((\pm)\text{-}\mathbf{4}/(\textit{meso})\text{-}\mathbf{4})(\text{Cl})_2]$ and $[\text{Ru}^{\text{II}}(\mathbf{5})(\text{Cl})_2]$.

The broad alcohol stretch around 3200 cm^{-1} was detected for the ruthenium(III) complexes $[\text{Ru}^{\text{III}}(\mathbf{1}/\mathbf{2})(\text{Cl})(\text{solvent})]$ as well as for the ruthenium(II) complexes $[\text{Ru}^{\text{II}}((\pm)\text{-}\mathbf{4}/(\textit{meso})\text{-}\mathbf{4}/\mathbf{5})(\text{Cl})_2]$ using IR spectroscopy. However, the IR features strongly differ in the significant strong band at 1600 cm^{-1} , which is characterized as a coordinating ligand C=N vibration. For $[\text{Ru}^{\text{III}}(\mathbf{1}/\mathbf{2})(\text{Cl})(\text{solvent})]$ the band was still sharp and intensive at 1617 cm^{-1} , but for $[\text{Ru}^{\text{II}}((\pm)\text{-}\mathbf{4}/(\textit{meso})\text{-}\mathbf{4}/\mathbf{5})(\text{Cl})_2]$, the extra broad band was divided into two signals at 1633 and 1600 cm^{-1} . This might also indicate a different complex formation.

The mass spectrometry (ESI or LSIMS) of the complexes $[\text{Ru}^{\text{III}}(\mathbf{1}/\mathbf{2})(\text{Cl})(\text{solvent})]$ (ether bridged ligands) both showed a significant peak for a 1:1-ruthenium(III) complex, and in addition the spectra of complex $[\text{Ru}^{\text{III}}(\mathbf{1})(\text{Cl})(\text{solvent})]$ showed a second mass for the same complex, binding one chloride. The elemental analysis confirmed the 1:1 complex formation and also suggested one bound chloride and one solvent molecule. This information led to the

proposed binding motif for the complexes $[\text{Ru}^{\text{III}}(\mathbf{1}/\mathbf{2})(\text{Cl})(\text{solvent})]$, including a tetradentate ligand system (Figure 5, top). The complexes $[\text{Ru}^{\text{II}}((\pm)\text{-}\mathbf{4}/(\text{meso})\text{-}\mathbf{4}/\mathbf{5})(\text{Cl})_2]$ (thioether bridged ligands) were also detected in the mass analysis (ESI) as a 1:1-ruthenium(II) compound and a corresponding complex binding one additional chloride. In the elemental analysis of $[\text{Ru}^{\text{II}}((\pm)\text{-}\mathbf{4}/(\text{meso})\text{-}\mathbf{4}/\mathbf{5})(\text{Cl})_2]$ a 1:1 complex with two bound chlorides was also confirmed. The resulting binding motif contains a pentadentate ligand system, which is shown in Figure 5 (bottom).

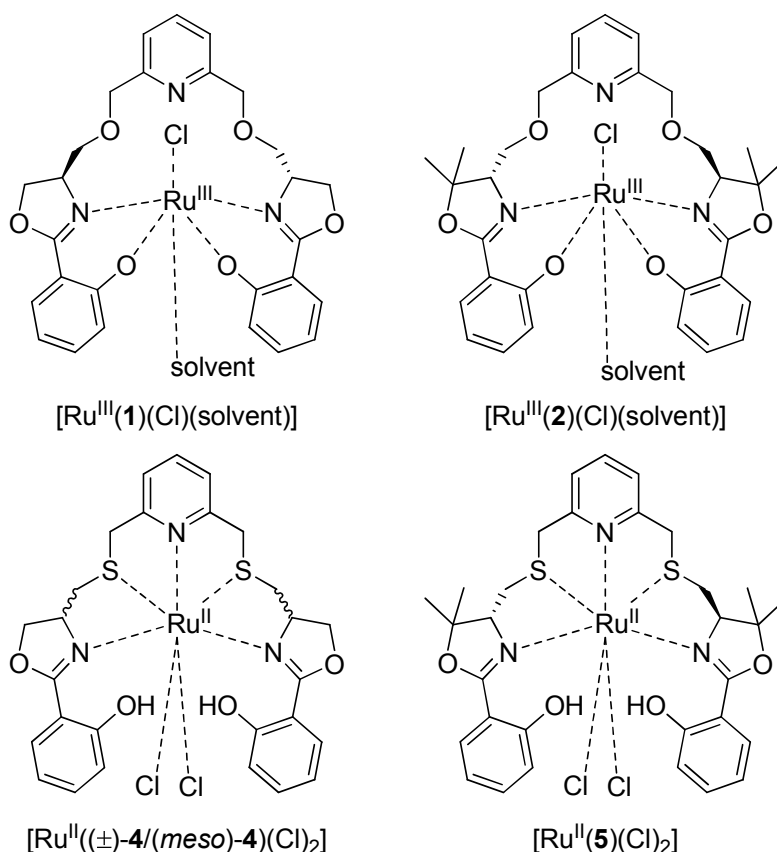


Figure 5. Two proposed binding motifs (tetradentate and pentadentate) of the complexes $[\text{Ru}^{\text{III}}(\mathbf{1}/\mathbf{2})(\text{Cl})(\text{solvent})]$ and $[\text{Ru}^{\text{II}}((\pm)\text{-}\mathbf{4}/(\text{meso})\text{-}\mathbf{4}/\mathbf{5})(\text{Cl})_2]$.

D.1.5 Liquid-State-Analysis of Ruthenium(II) and Ruthenium(III)

Complexes – $[\text{Ru}^{\text{III}}(\mathbf{1}/\mathbf{2})(\text{Cl})(\text{solvent})]$ and $[\text{Ru}^{\text{II}}((\pm)\text{-}\mathbf{4}/(\text{meso})\text{-}\mathbf{4}/\mathbf{5})(\text{Cl})_2]$

It is not surprising that the assumed binding motifs of the complexes $[\text{Ru}^{\text{III}}(\mathbf{1}/\mathbf{2})(\text{Cl})(\text{solvent})]$ and $[\text{Ru}^{\text{II}}((\pm)\text{-}\mathbf{4}/(\text{meso})\text{-}\mathbf{4}/\mathbf{5})(\text{Cl})_2]$ are distinguishable by their different UV/Vis spectra (Figure 6 and 7). Measured in acetonitrile at room temperature between 200 and 750 nm, complexes $[\text{Ru}^{\text{III}}(\mathbf{1})(\text{Cl})(\text{solvent})]$ (Figure 6, black line) and $[\text{Ru}^{\text{III}}(\mathbf{2})(\text{Cl})(\text{solvent})]$ (Figure 6, light grey line) showed similar features in their absorption behaviour and indicate therefore a comparable structure of the complexes in solution. The lower concentration used for complex $[\text{Ru}^{\text{III}}(\mathbf{2})(\text{Cl})(\text{solvent})]$ caused a very weak absorption band. The section between 450 nm to 700 nm was enlarged and exhibits also a noticeable maximum at 560 nm in both graphs (Figure 6, right). These absorptions as well as the shoulders between 350 to 430 nm of the complexes $[\text{Ru}^{\text{III}}(\mathbf{1}/\mathbf{2})(\text{Cl})(\text{solvent})]$ are assigned as complex-specific transitions and can be interpreted in combination with the observed dark purple colour as a distinct charge-transfer transition from the p_π orbital on the phenolate oxygen of the ligand to the half-filled d_π^* orbitals of the ruthenium(III) ion (LMCT).^{74-76,85} The absorption maximum around 300 nm is clearly identified as due to ligand-specific transitions ($n \rightarrow \pi^*$ or $\pi \rightarrow \pi^*$) (see *experimental part F.9.2*, Figure 2 and 5).

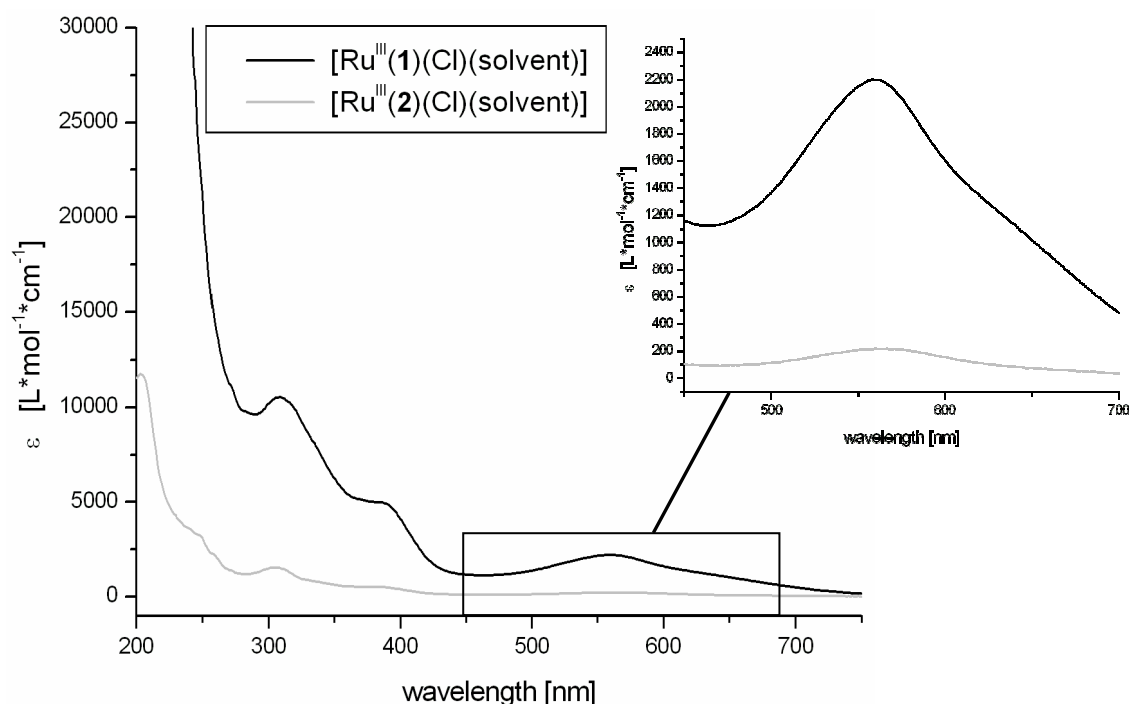


Figure 6. UV/Vis spectra of $[\text{Ru}^{\text{III}}(\mathbf{1}/\mathbf{2})(\text{Cl})(\text{solvent})]$ complexes (left) and offset 450 to 700 nm (right).

Compared to the ruthenium(III) species, the $[\text{Ru}^{\text{II}}((\pm)\text{-4}/(\text{meso})\text{-4/5})(\text{Cl})_2]$ complexes showed also ligand specific absorptions around 300 nm and complex-based transitions between 350 nm and 475 nm (Figure 7). In contrast to this, the significant absorption maximum at 560 nm was not detectable and confirmed again a different binding motif of the ruthenium(II) species without interaction of a phenolate oxygen to the metal (Figure 5).

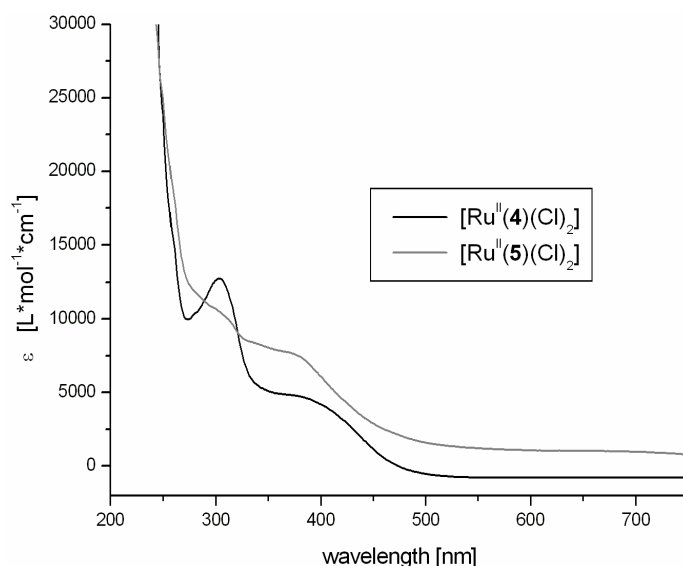


Figure 7. UV/Vis spectra of the $[\text{Ru}^{\text{II}}((\pm)\text{-4}/(\text{meso})\text{-4/5})(\text{Cl})_2]$ complexes.

The circular dichroism (CD) spectra of the complexes $[\text{Ru}^{\text{III}}(\text{1/2})(\text{Cl})(\text{solvent})]$ and $[\text{Ru}^{\text{II}}(\text{5})(\text{Cl})_2]$ were measured between 200 to 750 nm in acetonitrile at room temperature (Figure 8). Both ruthenium(III) species $[\text{Ru}^{\text{III}}(\text{1/2})(\text{Cl})(\text{solvent})]$, which are formed by ether bridged ligands with a different stereochemistry, exhibit curves with an opposite progression (Figure 8, black and light grey line). They possess a minimum or maximum at 240 nm and 325 nm and the behaviour is comparable to the CD spectra of their corresponding ligands, including their stereo chemical information (see *experimental part F.9.2*, Figure 6). The ruthenium(II) complex $[\text{Ru}^{\text{II}}(\text{5})(\text{Cl})_2]$ (Figure 8, dark grey line) behaved differently under the influence of circularly polarized light than the ruthenium(III) complexes and this indicates a significant change in the metal coordination, e. g. from an assumed tetradentate into a pentadentate chelation.

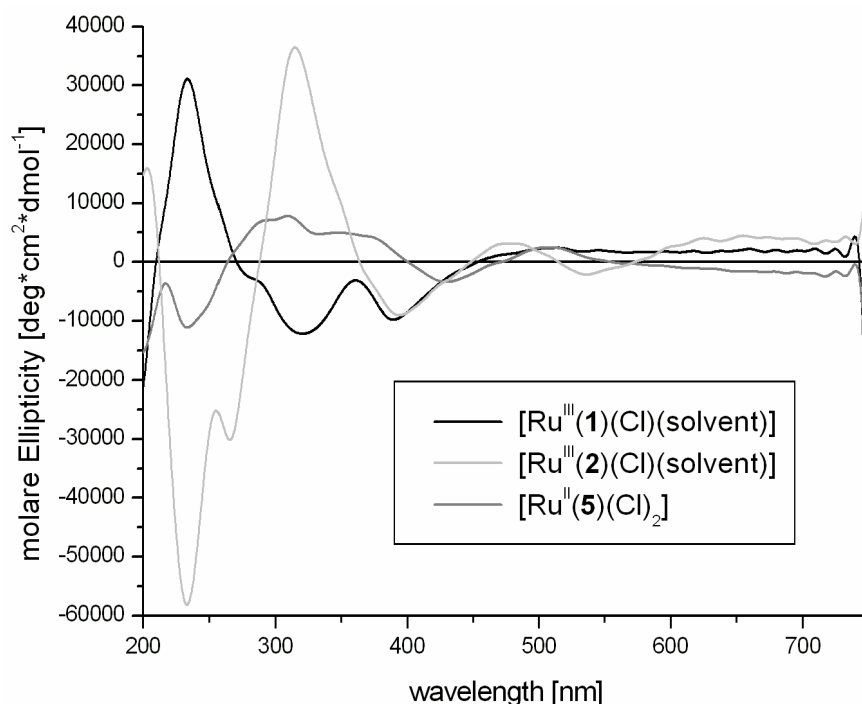


Figure 8. CD spectra of the $[\text{Ru}^{\text{III}}(\mathbf{1})(\text{Cl})(\text{solvent})]$ and $[\text{Ru}^{\text{II}}(\mathbf{5})(\text{Cl})_2]$ complexes.

The attempt to compare these newly obtained results with a similar ruthenium(II) complex **40**, synthesized by *M. Seitz* (Figure 9)^{42,90} is difficult, because of the lack of X-ray data of this complex. **40** contains a bis(oxazoline) ligand, without *ortho*-positioned hydroxyl groups and without methylated oxazoline rings. The CD spectra of **40** was measured only from 200 to 300 nm (see *experimental part F.9.2*, Figure 8). Nevertheless, in this short wavelength range both complexes also exhibit different features. The curve progression of **40** is detected only on the positive side, whereas the comparable complex $[\text{Ru}^{\text{II}}(\mathbf{5})(\text{Cl})_2]$ (Figure 8) shows a negative one in this area.

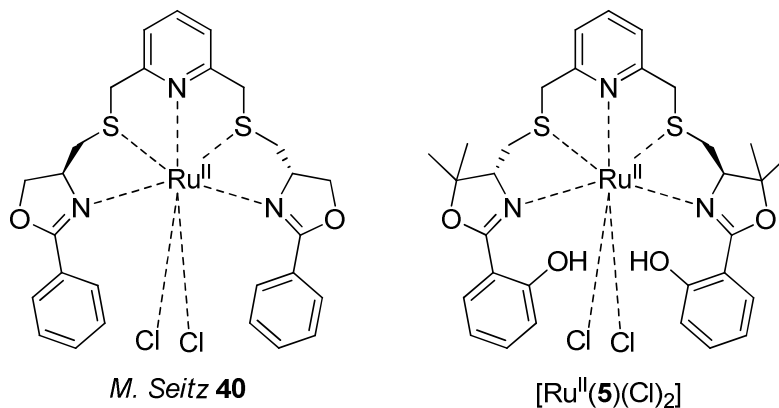
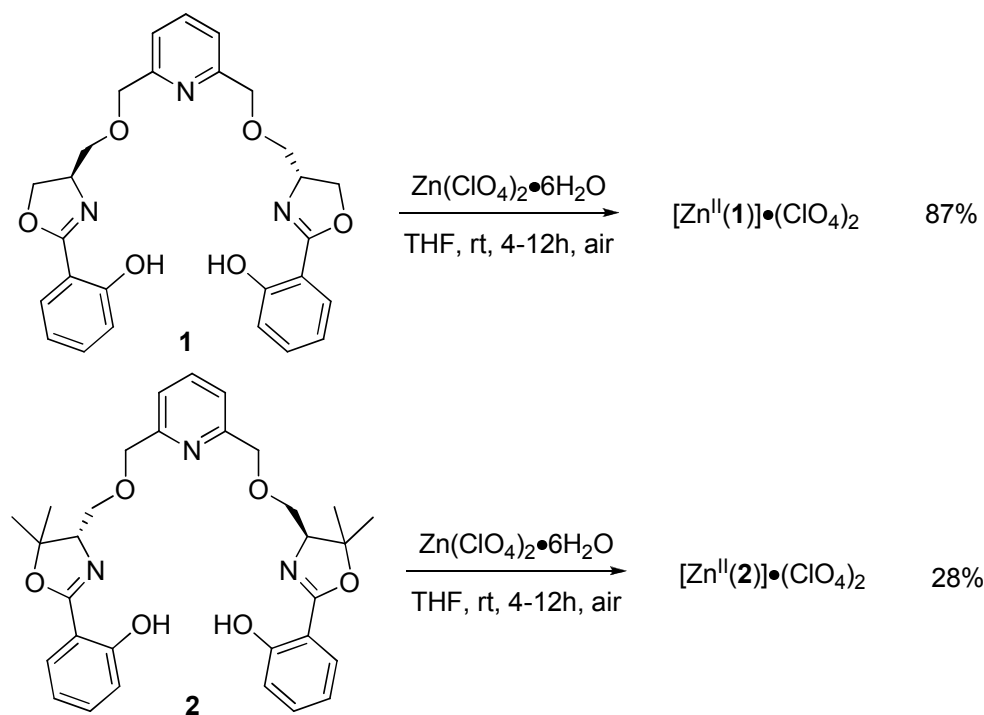


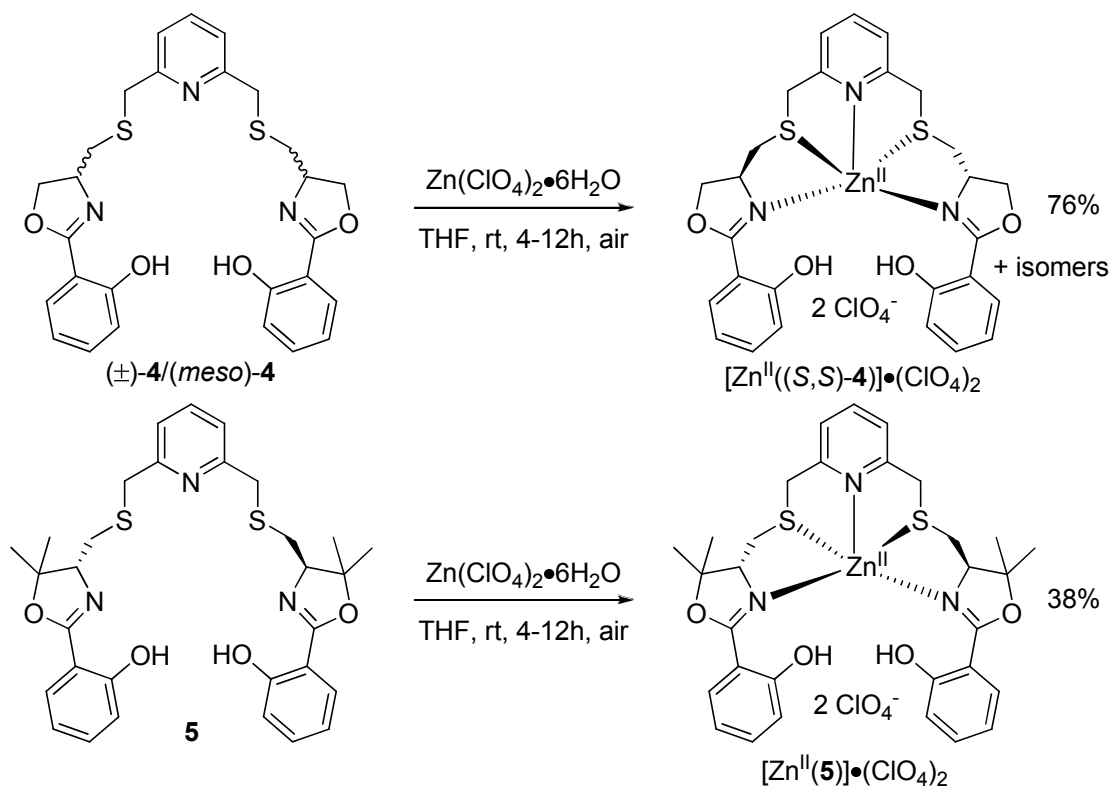
Figure 9. Proposed binding motifs of two ruthenium(II) complexes – *M. Seitz* **40** (left) and complex $[\text{Ru}^{\text{II}}(\mathbf{5})(\text{Cl})_2]$ (right).

D.1.6 Formation of Zinc(II) Complexes using $\text{Zn}(\text{ClO}_4)_2 \cdot 6\text{H}_2\text{O}$

The $[\text{Zn}^{\text{II}}(\mathbf{1}, \mathbf{2}, (\pm)\text{-}\mathbf{4}/(\text{meso})\text{-}\mathbf{4}, \mathbf{5})] \cdot (\text{ClO}_4)_2$ complexes were prepared using one equivalent of the bis(oxazoline) ligand ($\mathbf{1}, \mathbf{2}, (\pm)\text{-}\mathbf{4}/(\text{meso})\text{-}\mathbf{4}, \mathbf{5}$) and one equivalent of $\text{Zn}(\text{ClO}_4)_2 \cdot 6\text{H}_2\text{O}$ dissolved in THF (Scheme 5 and 6).



Scheme 5. Synthesis of the complexes $[\text{Zn}^{\text{II}}(\mathbf{1})] \cdot (\text{ClO}_4)_2$ and $[\text{Zn}^{\text{II}}(\mathbf{2})] \cdot (\text{ClO}_4)_2$.



Scheme 6. Synthesis of the complexes $[\text{Zn}^{\text{II}}((S,S)\text{-}\mathbf{4})] \cdot (\text{ClO}_4)_2$ and $[\text{Zn}^{\text{II}}(\mathbf{5})] \cdot (\text{ClO}_4)_2$.

The ligands were transferred to the salt and a precipitate immediately formed in each reaction. After a 4-12 h reaction time, the ether bridged complexes $[\text{Zn}^{\text{II}}(\mathbf{1})]\cdot(\text{ClO}_4)_2$ and $[\text{Zn}^{\text{II}}(\mathbf{2})]\cdot(\text{ClO}_4)_2$ were obtained as a slightly pink or a colourless solid, respectively. Both thioether bridged complexes $[\text{Zn}^{\text{II}}((\pm)\text{-}\mathbf{4}/(\text{meso})\text{-}\mathbf{4}, \mathbf{5})]\cdot(\text{ClO}_4)_2$ gave yellow solid complexes. Previous investigations⁴² predicted a pentadendate 1:1-zinc(II) complex formation, including two non-coordinated perchlorates, which was confirmed by the following observed data.

D.1.7 Solid-State-Analysis of Zinc(II) Complexes – $[\text{Zn}^{\text{II}}(\mathbf{1}/\mathbf{2})]\cdot(\text{ClO}_4)_2$ and $[\text{Zn}^{\text{II}}((S,S)\text{-}\mathbf{4}/\mathbf{5})]\cdot(\text{ClO}_4)_2$

The IR spectra of all four bis(oxazoline) zinc(II) complexes featured the same typical properties: a weak alcohol stretch around 3300 cm^{-1} , a strong band at 1620 cm^{-1} indicating a coordinating ligand $\text{C}=\text{N}$ vibration, and a characteristic broad and very strong band around 1070 cm^{-1} as well as a sharp band at 620 cm^{-1} for the perchlorate.⁸⁰

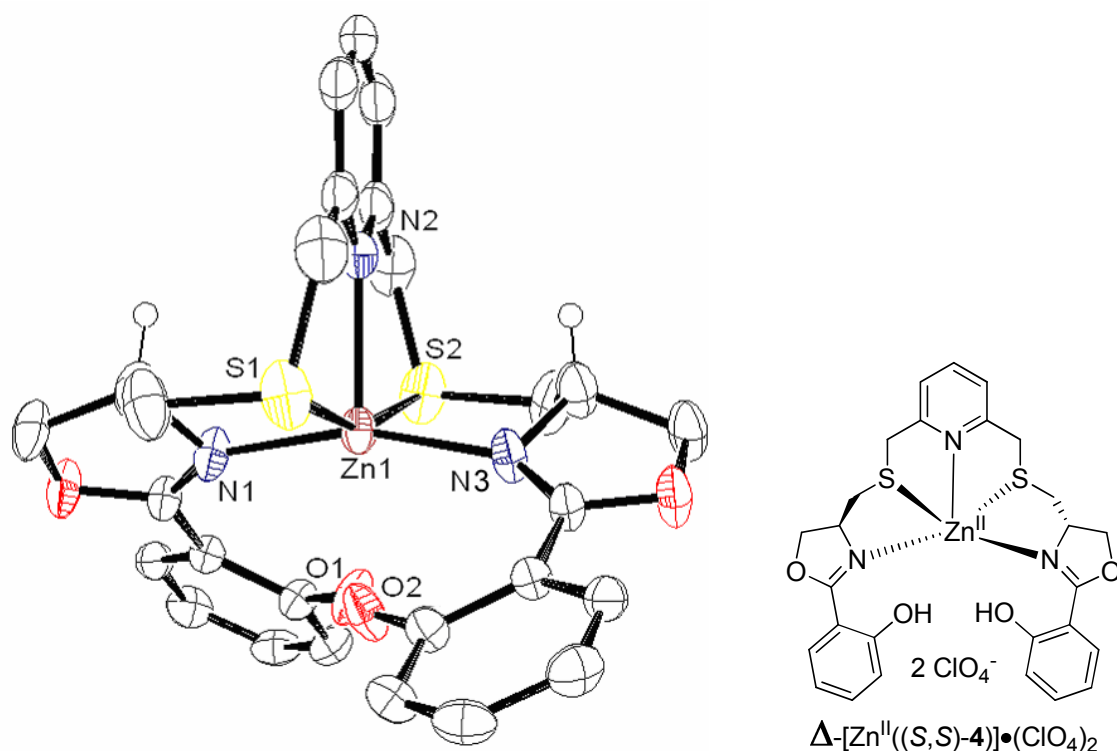


Figure 10. ORTEP plot at the 50% probability level of $[\text{Zn}^{\text{II}}((S,S)\text{-}\mathbf{4})]\cdot(\text{ClO}_4)_2$ – (not important hydrogen atoms and ClO_4^- are omitted for clarity).

From the complex mixture $[\text{Zn}^{\text{II}}((\pm)\text{-}\mathbf{4}/(\text{meso})\text{-}\mathbf{4})]\cdot(\text{ClO}_4)_2$ a crystal was obtained with two stereo centres of the ligand in the same configuration (S,S). The crystallographic data of

$[\text{Zn}^{\text{II}}((S,S)\text{-4})]\cdot(\text{ClO}_4)_2$ shows a pentadentate coordinated Zn^{2+} ion surrounded by an (*S,S*)-isomer of the bis(oxazoline) ligand (Figure 10 and 11) and neutralized by two non-coordinated perchlorates. The crystal structure is C_2 -symmetric and exhibits a strongly distorted square-pyramidal geometry. The nitrogens N(1) and N(3) of the oxazoline ring and both sulphurs S(1)/(2) of the thioether bridges form a nearly planar square at the bottom of this structure. The distance of the two almost oppositely placed nitrogen atoms (161°) has the typical length of 2.00 Å to the metal ($\text{Zn}(1)\text{-N}(1)/(3)$) (Table 3), which is comparable to the distances in the dimeric oxazoline zinc(II) complexes (see *main part – oxazoline complex analysis C.2.11-C.2.13*). The bond between the pyridine nitrogen N(2) on the top of the pyramid and the zinc centre is significantly longer and measured to 2.25 Å. The bond lengths of the sulphur atoms to the metal are 2.56 Å and the nearly *trans*-oriented alignment of S(1)-Zn(1)-S(2) was confirmed by an angle of 159° .

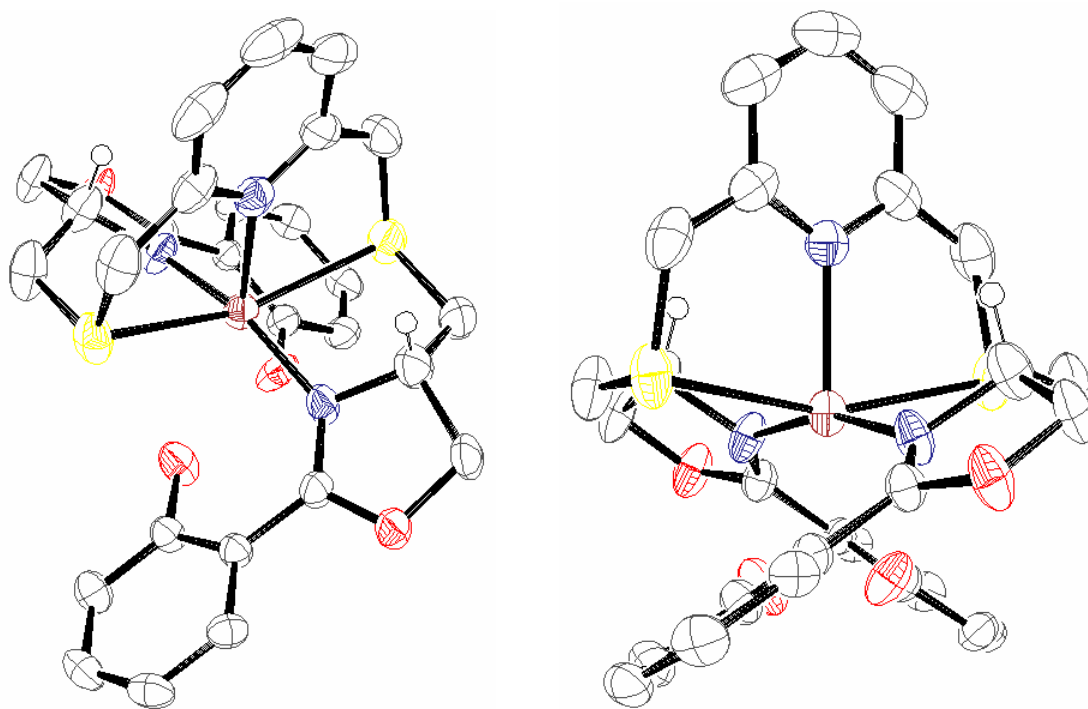


Figure 11. ORTEP plot at the 50% probability level of $[\text{Zn}^{\text{II}}((S,S)\text{-4})]\cdot(\text{ClO}_4)_2$ – (not important hydrogen atoms and ClO_4^- are omitted for clarity).

A special feature that should be mentioned is that both phenolates are still protonated and point into the complex centre (Figure 11). Their distances to zinc measure exactly 2.60 Å (not shown in Table 3) and confirm a weak interaction between the hydroxyl group and the metal. The complex geometry of $[\text{Zn}^{\text{II}}((S,S)\text{-4})]\cdot(\text{ClO}_4)_2$ was identified as the Δ -isomer (Figure 12).

The mass spectrometry (ESI, LSIMS) as well as the elemental analysis of all four zinc(II) complexes confirmed a 1:1 stoichiometry, in which two positive charges from the zinc are equilized by two perchlorate anions (Scheme 5 and 6).

Table 3. Selected bond distances (Å) and angles (°) of $[\text{Zn}^{\text{II}}((S,S)\text{-4})] \cdot (\text{ClO}_4)_2$.

Bond Distances [Å]			Angles [°]
Zn(1)-S(1)	2.5588(12)	S(1)-Zn(1)-N(1)	83.61(10)
Zn(1)-S(2)	2.5588(12)	S(1)-Zn(1)-N(2)	79.61(4)
Zn(1)-N(1)	1.997(4)	S(1)-Zn(1)-S(2)	159.22(6)
Zn(1)-N(2)	2.250(5)	S(1)-Zn(1)-N(3)	99.78(10)
Zn(1)-N(3)	1.997(4)	N(1)-Zn(1)-N(2)	99.36(11)
		S(2)-Zn(1)-N(1)	99.78(10)
		N(1)-Zn(1)-N(3)	161.29(16)
		S(2)-Zn(1)-N(2)	79.61(4)
		N(3)-Zn(1)-N(2)	99.36(11)
		S(2)-Zn(1)-N(1)	83.61(10)

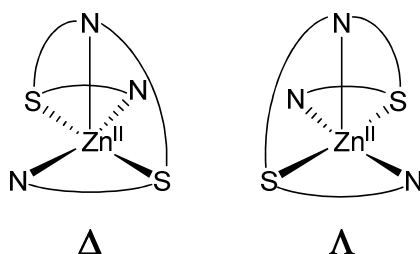


Figure 12. Pentadentate binding model for a square pyramidal geometry.

D.1.8 Liquid-State-Analysis of Zinc(II) Complexes – $[\text{Zn}^{\text{II}}(1/2)]\cdot(\text{ClO}_4)_2$ and $[\text{Zn}^{\text{II}}((\pm)\text{-4}/(\text{meso})\text{-4/5})]\cdot(\text{ClO}_4)_2$

Although two different ligand systems were used, the UV/Vis measurements of the $[\text{Zn}^{\text{II}}(1/2)(\pm)\text{-4}/(\text{meso})\text{-4/5}]\cdot(\text{ClO}_4)_2$ complex series resulted in similar electronic spectra (Figure 13). Absorptions with energy higher than 280 nm are ligand or salt specific (see *experimental part F.9.2*, Figure 3 and 5), whereas the bands between 280 and 380 nm are identified as overlapping transitions of the ligand and the newly formed zinc(II) complex. It is assumed that the right hand side of this broad absorption, starting around 330 nm to lower energies, results from a complex-specific transition (LMCT), and the left hand side indicates a ligand-specific transition.

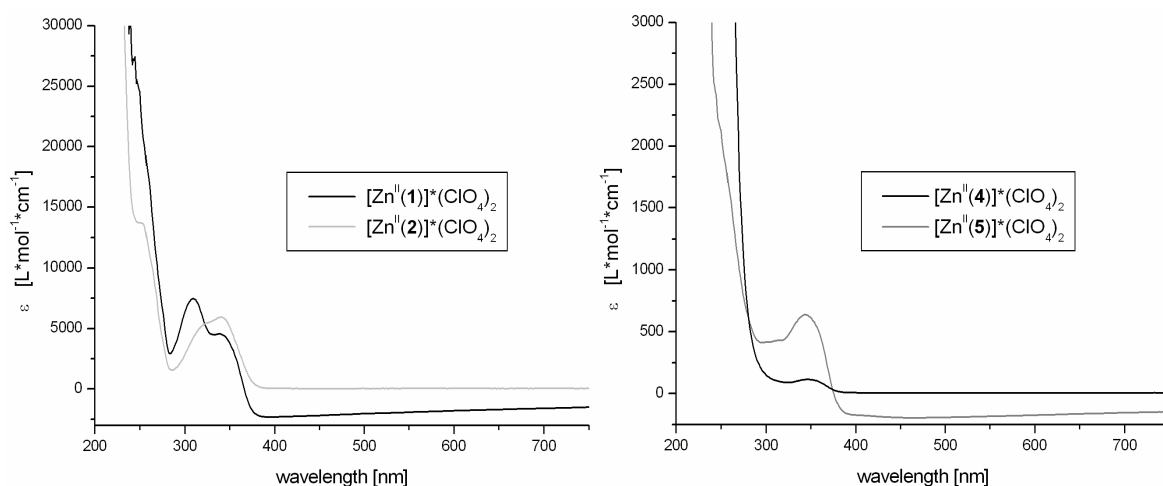


Figure 13. UV/Vis spectra of the complexes $[\text{Zn}^{\text{II}}(1/2)]\cdot(\text{ClO}_4)_2$ and $[\text{Zn}^{\text{II}}((\pm)\text{-4}/(\text{meso})\text{-4/5})]\cdot(\text{ClO}_4)_2$.

The circular dichroism spectra (CD) of the $[\text{Zn}^{\text{II}}(1/2/5)]\cdot(\text{ClO}_4)_2$ complex series were measured using circularly polarized light in a range of 200 to 750 nm in acetonitrile at room temperature (Figure 15), but only in the range between 200 to 450 nm complex specific curves are seen. The complexes $[\text{Zn}^{\text{II}}((\pm)\text{-4}/(\text{meso})\text{-4})]\cdot(\text{ClO}_4)_2$ were only obtained in a mixture of multiple geometries and was therefore not CD active. Starting from the methylated complexes, $[\text{Zn}^{\text{II}}(2)]\cdot(\text{ClO}_4)_2$ (Figure 15, light grey line) and $[\text{Zn}^{\text{II}}(5)]\cdot(\text{ClO}_4)_2$ (Figure 15, dark grey line) respectively, a clear opposite curve progression is seen, which is in contrast to the spectra of the corresponding ligands (see *experimental part F.9.2*, Figure 6). This is an unusual effect for ligand systems with two stereo centres of the same configuration, which form different geometric structures in combination with a zinc(II) metal. It might be caused by the varied bridging atom (oxygen or sulphur) in the ligand. The phenomenon of two non-

stereogenic atoms, like oxygen and sulphur, being responsible for a different geometry formation in the complex was already seen by *M. Seitz*, using a similar ligand system (Figure 14). But the CD spectra of the complexes **41/42** (see *experimental part F.9.2*, Figure 7) and $[\text{Zn}^{\text{II}}(\mathbf{1})]\cdot(\text{ClO}_4)_2$ (Figure 15, black line) show significant differences against one another and were not directly comparable.

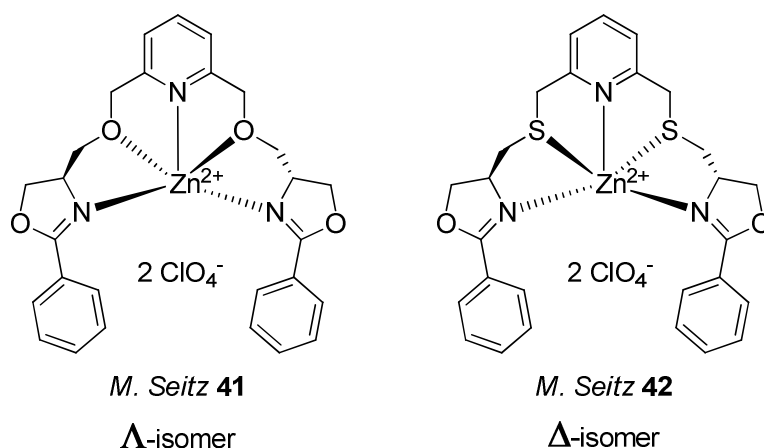


Figure 14. Two zinc(II) complexes – left ether bridged (*M. Seitz* **41**) and right thioether bridged (*M. Seitz* **42**).

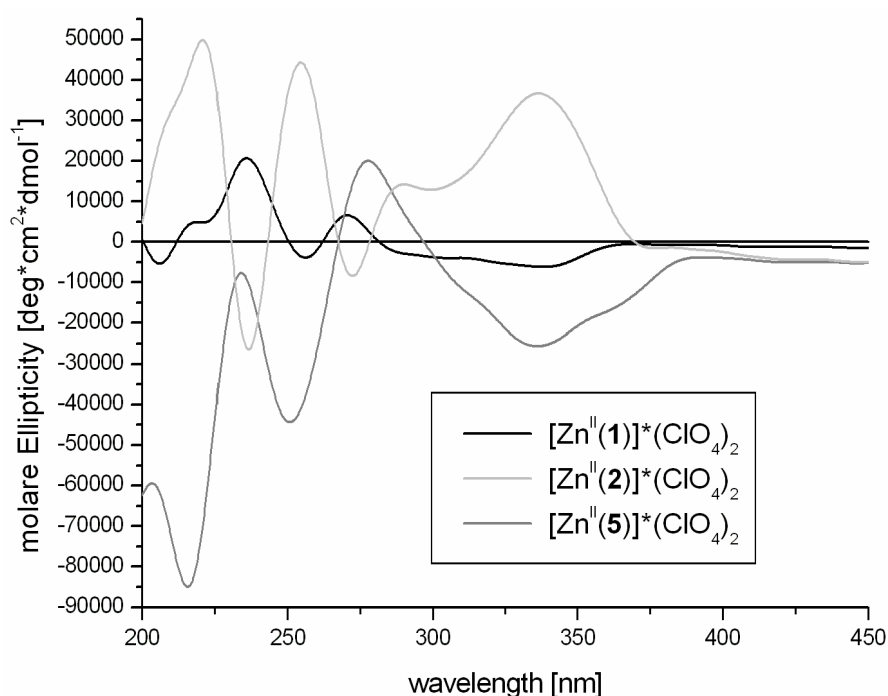


Figure 15. CD spectra of the complexes $[\text{Zn}^{\text{II}}(\mathbf{1/2})]\cdot(\text{ClO}_4)_2$ and $[\text{Zn}^{\text{II}}(\mathbf{5})]\cdot(\text{ClO}_4)_2$.

The unmethylated ether bridged complex $[\text{Zn}^{\text{II}}(\mathbf{1})]\cdot(\text{ClO}_4)_2$ (Figure 15, black line), with a different stereochemistry in comparison to the complexes $[\text{Zn}^{\text{II}}(\mathbf{2})]\cdot(\text{ClO}_4)_2$ and $[\text{Zn}^{\text{II}}(\mathbf{5})]\cdot(\text{ClO}_4)_2$, confirmed its ligand spectra in this point (see *experimental part F.9.2*,

Figure 6). Furthermore, its CD graph resembles more the curve of complex $[\text{Zn}^{\text{II}}(\mathbf{5})]\cdot(\text{ClO}_4)_2$ (thioether bridged) and exhibits an opposite curve progression with regard to complex $[\text{Zn}^{\text{II}}(\mathbf{2})]\cdot(\text{ClO}_4)_2$ (ether bridged). These untypical behaviours, where same stereo configurations in the ligands form different geometric isomers in the complexes, and that ether bridged complexes are not comparable with each other but behave similarly to thioether bridged complexes, led to the following proposal: The obtained information for the enantiopure crystallized zinc(II) complex isomer $[\text{Zn}^{\text{II}}((S,S)\text{-}\mathbf{4})]\cdot(\text{ClO}_4)_2$, was identified as a Δ -complex. On the basis of the probably oppositely formed geometry by different bridging atoms, complex $[\text{Zn}^{\text{II}}(\mathbf{1})]\cdot(\text{ClO}_4)_2$ was assumed to be a Λ -isomer. Corresponding to these assumptions, complex $[\text{Zn}^{\text{II}}(\mathbf{2})]\cdot(\text{ClO}_4)_2$ might have the Δ - and $[\text{Zn}^{\text{II}}(\mathbf{5})]\cdot(\text{ClO}_4)_2$ the Λ -geometry (Figure 16).

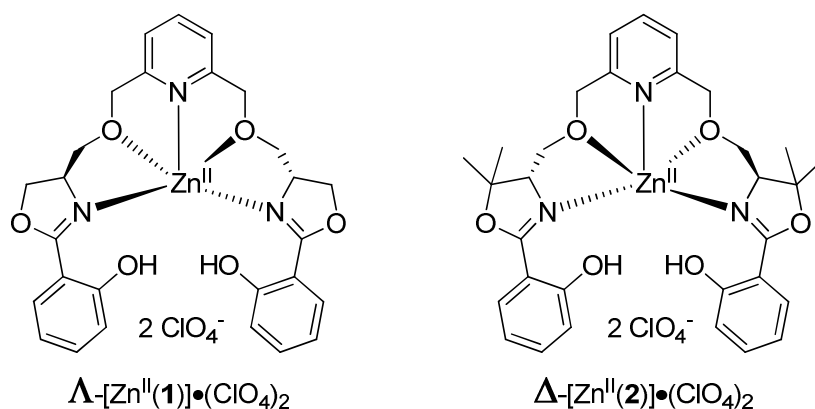


Figure 16. Proposed binding motif of the complexes $[\text{Zn}^{\text{II}}(\mathbf{1/2})]\cdot(\text{ClO}_4)_2$.

D.1.9 Summary

In conclusion, for all iron(III) complexes two different binding motifs have been suggested, depending on whether an ether or thioether bridged ligand is used, and whether tetradentate or pseudo-pentadentate chelation occurs. For the ruthenium based complexes two binding motifs were also assumed. In addition to this, the ligand seems to control the oxidation of Ru^{2+} to Ru^{3+} in the case of the ether bridged bis(oxazolines). The determination of the iron and ruthenium complex geometry was not possible due to the lack of X-ray structures, including a chiral ligand.

The crystal obtained in the zinc series allowed the identification of all complex isomers and confirmed all expectations with respect to reported literature.

Table 4. Summary of all structural geometries for the complexes obtained.

Entry	Salt	Ligand 1	Ligand 2	Ligand (\pm)-4/ (<i>meso</i>)-4	Ligand 5
1	$\text{Fe}(\text{ClO}_4)_2 \cdot 6\text{H}_2\text{O}$	Fe(III) tetra- dentate	Fe(III) tetra- dentate	Fe(III) pseudo- penta- dentate	Fe(III) pseudo- penta- dentate
2	$[\text{RuCl}_2(\text{benzene})_2]_2$	Ru(III) tetra- dentate	Ru(III) tetra- dentate	Ru(II) penta- dentate	Ru(II) penta- dentate
3	$\text{Zn}(\text{ClO}_4)_2 \cdot 6\text{H}_2\text{O}$	Λ (CD) penta- dentate	Δ (CD) penta- dentate	Δ (X-ray) penta- dentate	Λ (CD) penta- dentate

With regard to the aim of this work, to create a defined complex geometry including secondary pre-coordination functionalities, the obtained data led to a variety of results: For all observed iron(III) complexes, the postulated active intermediate stabilization is not possible on the basis of the changed binding situation. But for the zinc(II) complexes, the proposed binding motif of the bis(oxazolines) with the possibility for additional hydrogen bridge formation was confirmed.

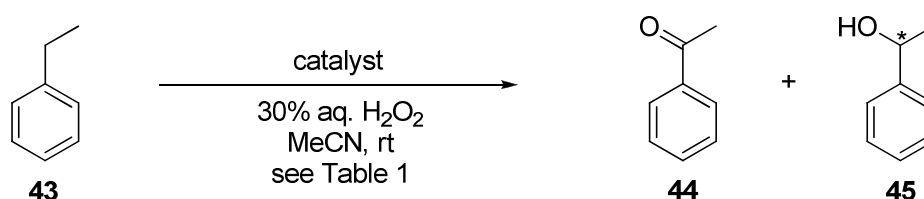
E. Main Part – Catalysis

E.1 Catalysis

E.1.1 Functionalization of Alkanes by C-H Bond Activation

The generation of ketones and alcohols from simple hydrocarbons is an important aim in organic chemistry, but the functionalization of non-activated C-H bonds by oxidation still requires drastic conditions and toxic metals.^{91,92} Many investigations have been devoted to develop new mild and efficient methods for oxidation reactions to functionalize saturated hydrocarbons. In the past, iron played only a minor role in catalytic approaches. However, iron has been the subject of increased interest in recent years due to its non-toxic and inexpensive nature.

Bolm and co-workers screened different iron-salts without addition of any ligand for reactivity with ethylbenzene (**43**) and reported an iron-catalyzed oxidation of alkylarenes by hydrogen peroxide.⁹³ The reactions were performed under ambient conditions (e.g. room temperature), using catalytic amounts of iron-salts and 30% aqueous H₂O₂ in acetonitrile (Scheme 1). The results indicated a rapid decomposition of hydrogen peroxide using Fe(OAc)₂ and Fe(acac)₂, therefore leading to no conversion of the starting material. However, Fe(ClO₄)₂•6H₂O (10 mol%) was able to oxidize ethylbenzene in 65% yield, with acetophenone (**44**) being the major product, and no significant decomposition of hydrogen peroxide was observed. In addition to this, carboxylic acids have been shown to be effective additives in iron-catalyzed oxidations,⁹⁴⁻⁹⁶ presumably by forming the corresponding peracid intermediates. Bolm and co-workers tested the addition of various carboxylic acids (e. g. acetic acid) under the same reaction conditions and obtained acetophenone as the only product at a similar conversion rate as before. The catalyst/substrate/H₂O₂/acid molar ratio of 1/10/50/2 has been employed.



Scheme 1. General oxidation of ethylbenzene.

Bouwman and co-workers⁴⁴ studied the catalytic effect of an iron complex containing a phenol-oxazoline ligand (\pm)-**46** (Figure 1, left), which has high similarity to the ligands described in this thesis (Figure 3). $\text{Fe}(\text{ClO}_4)_2 \cdot 6\text{H}_2\text{O}$ was used to form the catalytically active species with this ligand and the oxidation of ethylbenzene under ambient conditions was investigated. An excess of substrate with respect to hydrogen peroxide should reduce the ketone-formation and minimize the uncontrolled decomposition of H_2O_2 . A molar ratio of 1/1000/100 (catalyst/substrate/ H_2O_2) resulted in a 0.8/1 mixture of acetophenone and racemic 1-phenylethanol (**45**) with TONs of 8.8 and 11.0, respectively (Table 1, entry 2).

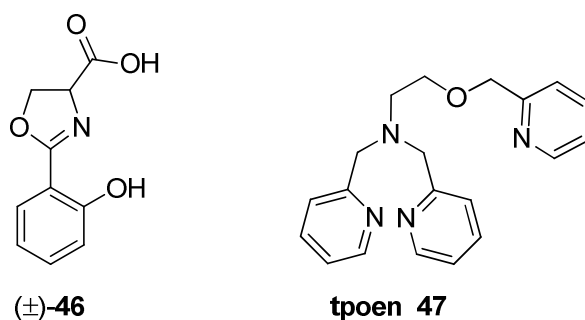


Figure 1. Phenol-oxazoline ligand (\pm)-**46** of Bouwman *et al.*⁴⁴ (left) and tpoen ligand **47** (= N-(2-pyridylmethoxyethyl)-N,N-bis(2-pyridylmethyl)amine) of Sun *et al.*⁹⁷ (right).

Sun and co-workers⁹⁷ investigated the catalytic properties of a multidentate N_4O ligand **47** (tpoen = N-(2-pyridyl-methoxyethyl)-N,N-bis(2-pyridylmethyl)amine) (Figure 1, right). Depending on the salt added, the corresponding complex is formed with different binding motifs. $\text{FeCl}_2 \cdot \text{H}_2\text{O}$ was used to generate a pentadentate complex **48**, $\text{FeCl}_3 \cdot 6\text{H}_2\text{O}$ to form a tridentate complex **49**, and $\text{Fe}(\text{ClO}_4)_2 \cdot 6\text{H}_2\text{O}$ was able to form a μ -oxo dinuclear iron complex **50** (Figure 2). The catalytic activity of the species formed was subsequently tested in the oxidation of ethylbenzene in acetonitrile, using a molar ratio of 1/1000/200 (catalyst/substrate/ H_2O_2) under a N_2 atmosphere at room temperature.

As outlined in Table 1, all three catalysts generated similar ratios of the products obtained, showing a slight preference for the ketone **44** (Table 1, entry 3-5). All TONs reported by Sun and co-workers are increased in comparison to those obtained by Bolm and Bouwman, which might be explained by the higher ratio of hydrogen peroxide used. Furthermore, it should be pointed out that the tridentate complex **49** achieved a TON of 17.2 for the ketone (Table 1, entry 4), a result which was improved by the pentadentate complex **48** (Table 1, entry 3). The highest reported TON so far was observed under these conditions with the dinuclear iron complex **50** (Table 1, entry 5).

Table 1. Comparison of reported oxidations of ethylbenzene.

Entry	Catalyst	TON ^d acetophenone 44	TON ^d phenylethanol 45	Ratio 44 / 45
1	Fe(ClO ₄) ₂ •6H ₂ O ^a	5.0	-	5.0 / 0
2	(HNet ₃) ₂ [Fe((±)- 46) ₂](ClO ₄) ^b	8.8	11.0	0.8 / 1
3	[Fe(47)Cl]PF ₆ ^c	22.7	15.7	1.4 / 1
4	Fe(47)Cl ₃ ^c	17.2	12.7	1.4 / 1
5	[Fe(47) ₂ (μ-O)](ClO ₄) ₄ ^c	26.2	16.4	1.6 / 1

^a reaction conditions: 1.0 mmol ethylbenzene, 0.1 mmol iron-salt, 0.2 mmol HOAc, 5.0 mmol H₂O₂, 5 mL acetonitrile, nitrobenzene (0.2 eq., internal standard) – 5 h / rt; ^b reaction conditions: 5.0 mmol ethylbenzene, 5 μmol iron-complexe, 0.5 mmol H₂O₂, 5 mL acetonitrile – 3 h / rt; ^c reaction conditions: 5.0 mmol ethylbenzene, 5 μmol iron-complexe, 1.0 mmol H₂O₂, 4 mL acetonitrile, 1,2-dichlorobenzene (internal standard) – 1.5 h / rt; ^d TON = turnover number of the product in mole product per mole catalyst.

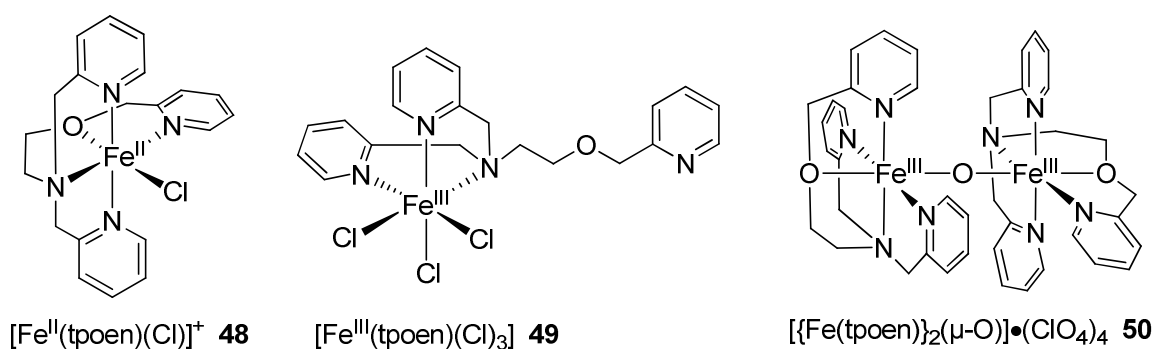


Figure 2. Three crystal structures of Sun and co-workers.⁹⁷

E.1.2 Oxidation of Ethylbenzene by Oxazoline / Bis(oxazoline) Complexes

To investigate the oxidation of ethylbenzene (Scheme 1) by oxazoline and bis(oxazoline) complexes, conditions were chosen on the basis of a number of reported protocols. Acetonitrile was envisioned to be a suitable solvent for all oxidation reactions because of the good solubility of the ligands, iron salts and the complexes formed by them. Furthermore, the substrate was added in a high excess as described by *Bouwman et al.* Two different iron-salts as well as three oxazoline and two bis(oxazoline) derivatives (Figure 3) were used to form the catalytically active species as 2:1- or 1:1-complexes. The molar ratio of catalyst/substrate/H₂O₂ was set to 1/100/50, 1/1000/100, or 1/1000/500. The effect of a carboxylic acid (HOAc) was also tested. All reactions were performed under ambient conditions and samples for GC-analysis were taken at a reaction time of 3 h, 5 h or 24 h.

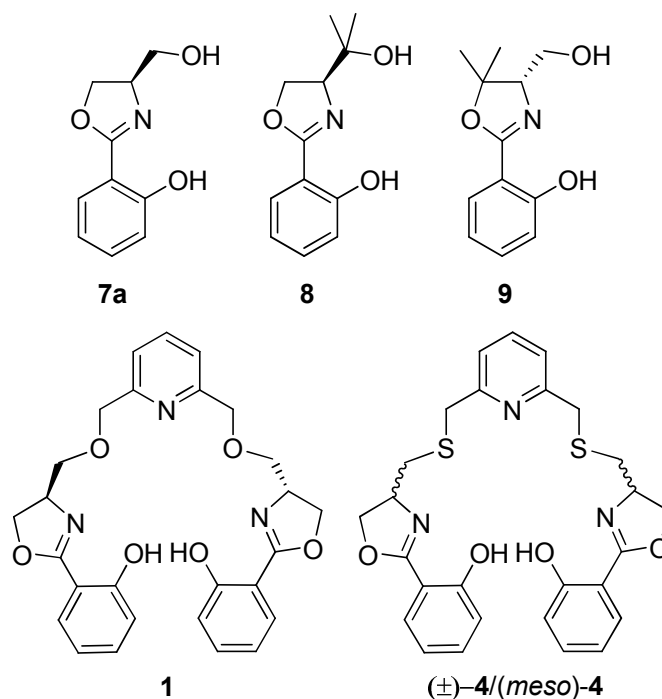


Figure 3. Oxazoline ligands **7a-9** and bis(oxazoline) ligands **1** and (±)-**4**/(*meso*)-**4** used for the catalysis.

In the first series of experiments the oxidation of ethylbenzene was performed using Fe(ClO₄)₂•6H₂O and Fe(OAc)₂. Table 2 summarizes the results obtained after 3 h reaction time. Higher TONs are seen for Fe(ClO₄)₂•6H₂O (Table 2, entry 1) in comparison to Fe(OAc)₂ (Table 2, entry 5) without addition of a ligand. These values show the same tendency reported by Bolm and co-workers,⁹³ but here acetophenone was not the only product which was obtained.

The best results for a 3 h reaction time were achieved by ligand **8** in combination with $\text{Fe}(\text{ClO}_4)_2 \cdot 6\text{H}_2\text{O}$ (Table 2, entry 3). A TON of 5.3 was obtained for the ketone and a ratio of **44** / **45** - 1.6 / 1 shows a slight preference for the ketone. An enantiomeric excess of 28%*ee* was determined for the chiral alcohol. The results for a 24 h reaction time are given in Table 3. Here the complex of ligand **8** with $\text{Fe}(\text{ClO}_4)_2 \cdot 6\text{H}_2\text{O}$ (Table 3, entry 3) afforded a TON of 10.8 for the ketone, which is comparable to the blank (ligand free) reaction for the same reaction time (Table 3, entry 1). Moreover, the selectivity of ligand **8** after 24 h was increased to a ratio of 2.3 / 1 towards the ketone (Table 3, entry 3), but at the same time the enantiomeric excess for the alcohol observed after 3 h had disappeared.

Table 2. Oxidation of ethylbenzene after 3 h. ^a

Entry	Salt	Ligand	TON acetophenone 44	TON phenylethanol 45	Ratio 44 / 45
1	$\text{Fe}(\text{ClO}_4)_2 \cdot 6\text{H}_2\text{O}$	-	7.9	7.5	1.0 / 1
2	$\text{Fe}(\text{ClO}_4)_2 \cdot 6\text{H}_2\text{O}$	7a	4.0	2.5	1.6 / 1
3	$\text{Fe}(\text{ClO}_4)_2 \cdot 6\text{H}_2\text{O}$	8	5.3	3.3 ^b	1.6 / 1
4	$\text{Fe}(\text{ClO}_4)_2 \cdot 6\text{H}_2\text{O}$	9	4.0	2.7	1.5 / 1
5	$\text{Fe}(\text{OAc})_2$	-	2.4	0.8	3.0 / 1
6	$\text{Fe}(\text{OAc})_2$	7a	3.2	1.7	1.9 / 1
7	$\text{Fe}(\text{OAc})_2$	8	3.0	1.3	2.3 / 1
8	$\text{Fe}(\text{OAc})_2$	9	3.0	1.4	2.1 / 1

^a reaction conditions: 10.0 mmol ethylbenzene, 0.01 mmol catalyst, 1.0 mmol H_2O_2 , 5 mL acetonitrile, bromobenzene (0.1 eq., internal standard) – 3 h / rt; ^b 28%*ee* determined by chiral GC.

Table 3. Oxidation of ethylbenzene after 24 h. ^a

Entry	Salt	Ligand	TON acetophenone 44	TON phenylethanol 45	Ratio 44 / 45
1	$\text{Fe}(\text{ClO}_4)_2 \cdot 6\text{H}_2\text{O}$	-	11.4	10.9	1.1 / 1
2	$\text{Fe}(\text{ClO}_4)_2 \cdot 6\text{H}_2\text{O}$	7a	5.2	3.0	1.8 / 1
3	$\text{Fe}(\text{ClO}_4)_2 \cdot 6\text{H}_2\text{O}$	8	10.8	4.8 ^b	2.3 / 1
4	$\text{Fe}(\text{ClO}_4)_2 \cdot 6\text{H}_2\text{O}$	9	6.9	5.0	1.4 / 1
5	$\text{Fe}(\text{OAc})_2$	-	3.0	1.0	3.1 / 1
6	$\text{Fe}(\text{OAc})_2$	7a	3.9	2.0	1.9 / 1
7	$\text{Fe}(\text{OAc})_2$	8	3.7	1.6	2.4 / 1
8	$\text{Fe}(\text{OAc})_2$	9	4.0	1.8	2.2 / 1

^a reaction conditions: 10.0 mmol ethylbenzene, 0.01 mmol catalyst, 1.0 mmol H_2O_2 , 5 mL acetonitrile, bromobenzene (0.1 eq., internal standard) – 24 h / rt; ^b 0%*ee* determined by chiral GC.

Due to the generally lower TONs for Fe(OAc)₂ in the oxidation of ethylbenzene, the focus for further investigations was shifted to the more promising Fe(ClO₄)₂•6H₂O complexes. The addition of a carboxylic acid (e.g. HOAc) and use of a higher amount of hydrogen peroxide was also explored in the next experiments. It was assumed that the rapid decomposition of H₂O₂ plays an important role for the observed low TON values and could be avoided by continuous addition of the oxidizing agent. The following 5 h and 24 h reactions were performed by a portion-wise addition of 1 mmol oxidant each hour during the first 5 h up to a total of 5 mmol hydrogen peroxide.

The results obtained after 5 h are shown in Table 4. The addition of acetic acid resulted in a higher blank value (TON 14.4 for the ketone) as well as in a better ratio of **44** / **45** - 2 / 1 (Table 4, entry 1-2). Furthermore, the continuous addition of five equivalents H₂O₂ with an elongated reaction time of 5 h improved all TONs (Table 4). Ligand **8** performed well under these conditions. A TON of 8.8 for the ketone and a selectivity of **44** / **45** - 2.2 / 1 was reached (Table 4, entry 6), while only 9%*ee* for the chiral alcohol was obtained. The corresponding complexes of the bis(oxazoline) ligands **1** and (±)-**4**/(*meso*)-**4** were also investigated, but they catalyzed the oxidation reaction less well in comparison to all the oxazolines **7a-9**. The complex of ligand **1** was able to form the ketone only with a TON of 5.0 (Table 4, entry 10), but the selectivity for the ketone is improved (2.8 / 1). While the addition of acetic acid resulted in slightly higher TONs for the oxazoline ligands **7a-9**, no detectable influence for the bis(oxazoline) catalysts was observed.

Table 4. Oxidation of ethylbenzene after 5 h.^a

Entry	Ligand	TON acetophenone 44	TON phenylethanol 45	Ratio 44 / 45
1	-	12.9	10.3	1.3 / 1
2	- ^b	14.4	7.1	2.0 / 1
3	7a	4.7	2.6	1.8 / 1
4	7a ^b	6.2	3.2	1.9 / 1
5	8	4.9	2.4	2.0 / 1
6	8 ^b	8.8	4.0 ^c	2.2 / 1
7	9	5.3	2.7	2.0 / 1
8	9 ^b	7.2	3.9	2.0 / 1
9	1	5.3	2.2	2.4 / 1
10	1 ^b	5.0	1.8	2.8 / 1
11	(±)- 4 /(<i>meso</i>)- 4	3.4	1.6	2.1 / 1
12	(±)- 4 /(<i>meso</i>)- 4 ^b	3.2	1.8	1.8 / 1

^a reaction conditions: 10.0 mmol ethylbenzene, 0.01 mmol catalyst, 5 x 1.0 mmol H₂O₂, 5 mL acetonitrile, bromobenzene (0.1 eq., internal standard) – 5 h / rt; ^b 0.2 mmol HOAc; ^c 9%*ee* determined by chiral GC.

A TON of 8.8 for the ketone obtained using ligand **8** after 5 h (Table 4, entry 6) is comparable with the results reported by Bouwman and co-workers (TON 8.8 for the ketone) (Table 1, entry 2).⁴⁴ In contrast to this, a ratio of 2.2 / 1 was observed, indicating a higher preference for the ketone, while *Bouwman et al.* achieved only a ratio of 0.8 / 1. The higher TONs of Sun and co-workers⁹⁷ were not reached using our catalytic system. Their three complexes catalyzed the oxidation reaction to a high degree (TON 17.2 – 26.2 for the ketone) (Table 1, entry 3-5), but the selectivity of their catalytic species is lower.

The data obtained from the 24 h-samples are summarized in Table 5 and indicate a further increase of the blank values (Table 5, entry 1-2) as well as a higher TON using ligand **8** (Table 5, entry 5-6). In addition to these improved results the enantiomeric excess of the alcohol was increased to 16% (Table 5, entry 6). Furthermore, after 24 h ligand **7a** afforded results quite similar to ligand **8** (Table 5, entry 4), but no enantiomeric excess could be detected. The best result for the bis(oxazoline) complexes was obtained with ligand **1** (Table 5, entry 10), but did not reach the TONs of ligand **7a** and **8**.

Table 5. Oxidation of ethylbenzene after 24 h. ^a

Entry	Ligand	TON acetophenone 44	TON phenylethanol 45	Ratio 44 / 45
1	-	15.0	8.4	1.8 / 1
2	- ^b	19.2	7.8	2.5 / 1
3	7a	10.0	8.8	1.1 / 1
4	7a ^b	11.7	4.2 ^c	2.8 / 1
5	8	8.00	2.9	2.7 / 1
6	8 ^b	11.6	4.5 ^d	2.6 / 1
7	9	9.2	3.9	2.3 / 1
8	9 ^b	14.1	6.2	2.3 / 1
9	1	6.2	2.6	2.4 / 1
10	1 ^b	7.8	3.1	2.5 / 1
11	(±)- 4 /(<i>meso</i>)- 4	4.0	1.8	2.2 / 1
12	(±)- 4 /(<i>meso</i>)- 4 ^b	3.5	1.6	2.1 / 1

^a reaction conditions: 10.0 mmol ethylbenzene, 0.01 mmol catalyst, 5 x 1.0 mmol H₂O₂, 5 mL acetonitrile, bromobenzene (0.1 eq., internal standard) – 24 h / rt; ^b 0.2 mmol HOAc; ^c 0%ee determined by chiral GC; ^d 16%ee determined by chiral GC.

Finally, an increase of the catalyst loading from 1 mol% to 10 mol% leads to the results shown in Table 6 and 7. In general, after 5 h as well as after 24 h, in all cases only very low TONs were observed. Even the blank values reached only TONs of 3.8 and 5.1 for the ketone after 5 h and 24 h, respectively (Table 6, entry 2, Table 7, entry 2). All complex-catalyzed

reactions showed TONs lower than 3.5 and the selectivity is in the same range as for the blank reactions.

Table 6. Oxidation of ethylbenzene after 5 h.^a

Entry	Ligand	TON acetophenone 44	TON phenylethanol 45	Ratio 44 / 45
1	-	3.3	1.9	1.7 / 1
2	- ^b	3.8	2.3	1.7 / 1
3	7a	0.9	0.8	1.0 / 1
4	7a ^b	1.1	1.0	1.0 / 1
5	8	1.6	1.0	1.6 / 1
6	8 ^b	2.7	1.7	1.6 / 1
7	9	2.0	1.3	1.5 / 1
8	9 ^b	2.1	1.4	1.5 / 1
9	1	1.1	0.9	1.2 / 1
10	1 ^b	1.3	0.6	2.2 / 1
11	(±)- 4 /(<i>meso</i>)- 4	0.5	0.5	1.0 / 1
12	(±)- 4 /(<i>meso</i>)- 4 ^b	0.6	0.6	1.0 / 1

^a reaction conditions: 10.0 mmol ethylbenzene, 0.1 mmol catalyst, 5 x 1.0 mmol H₂O₂, 5 mL acetonitrile, bromobenzene (0.1 eq., internal standard) – 5 h / rt; ^b 0.2 mmol HOAc.

Table 7. Oxidation of ethylbenzene after 24 h.^a

Entry	Ligand	TON acetophenone 44	TON phenylethanol 45	Ratio 44 / 45
1	-	3.9	2.2	1.8 / 1
2	- ^b	5.1	2.7	1.9 / 1
3	7a	1.0	0.9	1.1 / 1
4	7a ^b	1.0	0.9	1.1 / 1
5	8	2.1	1.5	1.5 / 1
6	8 ^b	3.3	2.2	1.5 / 1
7	9	2.6	1.6	1.6 / 1
8	9 ^b	2.9	1.8	1.6 / 1
3	1	0.9	0.5	1.8 / 1
4	1 ^b	1.3	0.7	2.0 / 1
5	(±)- 4 /(<i>meso</i>)- 4	0.2	0.4	0.5 / 1
6	(±)- 4 /(<i>meso</i>)- 4 ^b	0.3	0.4	0.8 / 1

^a reaction conditions: 10.0 mmol ethylbenzene, 0.1 mmol catalyst, 5 x 1.0 mmol H₂O₂, 5 mL acetonitrile, bromobenzene (0.1 eq., internal standard) – 24 h / rt; ^b 0.2 mmol HOAc.

E.1.3 Preparation of Optical Active Sulfoxides

Many sulfoxides are known to have high biological activity.⁹⁸ Their preparation involves the use of chiral auxiliaries or reagents in enantioselective oxidations of prochiral sulfides.⁹⁹ The utilization of chiral transition metal complexes in combination with an oxidizing agent is a powerful method to generate optically active sulfoxides. Recently Bolm and co-workers reported a highly selective catalytic process using iron^{96,100-103} (as one of the most inexpensive and user-friendly metals) in combination with Schiff bases (Figure 4) as chiral ligands, and very simple and mild reaction conditions.

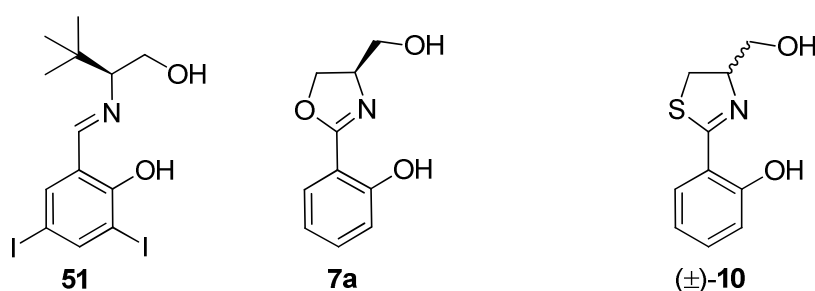
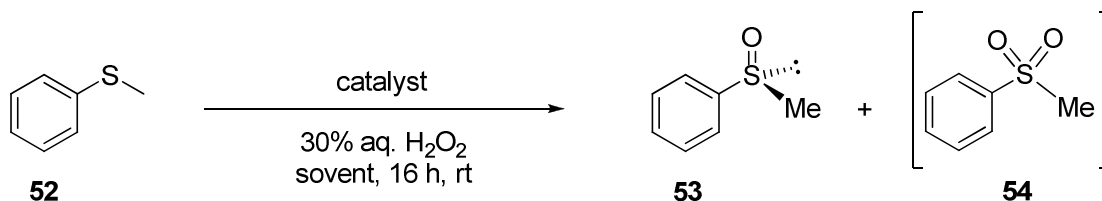


Figure 4. Schiff base ligand **51** used by Bolm *et al.* in comparison with oxazoline **7a** and thiazoline **10**.

The most successful Schiff base **51** (Figure 4), bearing iodine substituents in *para*- and *ortho*-positions to the hydroxyl group, generated promising *ee*-values in the oxidation of methyl phenyl sulfide (**52**) (Scheme 2), but only moderate yields (Table 8, entry 1).¹⁰⁰ This reaction was performed in dichloromethane at room temperature, using Fe(acac)₃ and 30% aqueous H₂O₂ as oxidant in a molar ratio of catalyst/substrate/H₂O₂ of 1/50/60.



Scheme 2. Oxidation of methyl phenyl sulfide by Bolm *et al.*

Further investigations revealed that the addition of various carboxylic acids and their lithium salts improved the yields as well as the enantiomeric excess. Table 8 shows an increase of the *ee*-value from 59% (Table 8, entry 1, no additive) to 77%*ee* (Table 8, entry 2,

addition of 4-methoxybenzoic acid) and to an excellent 90%*ee* (Table 8, entry 3, addition of lithium salt of 4-methoxybenzoic acid), while the low yield of 36% was nearly doubled to 63% (Table 8, entry 1-3). In all the oxidation reactions of methyl phenyl sulfide reported by Bolm and co-workers, no sulfone **54** as further oxidation product was observed.

Table 8. Comparison of reported oxidations of methyl phenyl sulfide by Bolm *et al.*^d

Entry	Ligand	Yield [%]	<i>ee</i> [%]
1	51 ^a	36	59
2	51 ^{a, b}	61	77
3	51 ^{a, c}	63	90

^a reaction conditions: 1.0 mmol methyl phenyl sulfide, 0.02 mmol Fe(acac)₃, 0.04 mmol Schiff base **51**, 1.2 mmol H₂O₂, 2 mL dichloromethane – 16 h / rt; ^b 0.01 mmol 4-methoxybenzoic acid; ^c 0.01 mmol lithium salt of 4-methoxybenzoic acid; ^d isolated yield, *ee*-values determined by chPLC.

E.1.4 Asymmetric Sulfide Oxidation

The high structural similarity between the Schiff base ligand **51** and oxazoline ligand **7a** (Figure 4) gave rise to speculation that they could also have comparable catalytic properties. It was assumed that on the basis of the comparable metal binding sites¹⁰⁴ the sulfide oxidation may also be successful using oxazoline complexes. Further evidence for the catalytic activity of oxazoline and bis(oxazoline) iron complexes is provided by the crystal structure of complex [Fe^{III}((*meso*)-**4**)_{ox}(H₂O)]•(ClO₄) (see *main part – bis(oxazoline) complex analysis D.1.2*, Figure 1), which resulted from a self oxidation reaction of the ligand. When the complex with Fe(ClO₄)₂•6H₂O was formed, one of the thioether bridges of the bis(oxazoline) ligand (*meso*)-**4** was oxidized by air into the corresponding sulfoxide. This self oxidation is promising for further investigations into the complexes potential as a catalyst for sulfide oxidations.

Applying the method reported by Bolm and co-workers,⁹⁶ oxazoline ligands **7a-9** and bis(oxazolines) **1** and (±)-**4**/(*meso*)-**4** were tested in combination with Fe(acac)₃ or Fe(ClO₄)₂•6H₂O in the oxidation of methyl phenyl sulfide. A 2:1 ratio of ligand to salt for oxazolines **7a-9** and a 1:1 ratio of ligand to salt for bis(oxazolines) **1** and (±)-**4**/(*meso*)-**4** were used (Scheme 2). Fe(acac)₃ and Fe(ClO₄)₂•6H₂O were explored in dichloromethane as solvent under ambient conditions over 16 h reaction time. Unfortunately, the first attempts of the sulfide oxidation resulted in only very low conversions. During the course of the reaction

(approximately 2 h after the addition of H₂O₂), a solid began to precipitate from the reaction mixture. It is assumed that the low solubility of the intermediate species might be a problem and is the reason for these disappointing results.

To overcome this solubility problem, a new solvent was chosen. The precipitation of the catalyst intermediate should be avoidable by using acetonitrile, a solvent which is known to be suitable for all oxazoline and bis(oxazoline) complexes as described above (see *main part – catalysis E.1.2*). In addition to this, Fe(OAc)₂ as a third salt was also tested and 4-methoxybenzoic acid was added to all reactions because of its reported positive effect.^{96,101} Furthermore, the thiazoline ligand (±)-**10** (Scheme 4) was also explored for its catalytic activity in the sulfide oxidation reaction.

The summarized results under these conditions are presented in Table 9-11. In general, the yields obtained for the Fe(acac)₃- (Table 10) and Fe(OAc)₂-based (Table 11) complexes reached only a maximum of 55% for the corresponding sulfoxide **53** and the determined *ee*-values were also extremely low. In contrast to this, Fe(ClO₄)₂•6H₂O-based complexes achieved the best yields of up to 73% by using ligand **8** (Table 9, entry 5), which are comparable to the results reported by Bolm and co-workers. Unfortunately, the *ee*-values did not exceed 23%.

Table 9. Oxidation of methyl phenyl sulfide.^{a, b}

Entry	Salt	Ligand	Ligand [mol%]	Sulfoxide 53 Yield [%] ^b	<i>ee</i> [%] ^c
1	Fe(ClO ₄) ₂ •6H ₂ O	-	-	26 / 10 ^d	-
2	Fe(ClO ₄) ₂ •6H ₂ O	1	2.0	57 / 28 ^d	14.5
3	Fe(ClO ₄) ₂ •6H ₂ O	(±)- 4 /(<i>meso</i>)- 4	2.0	36	1
4	Fe(ClO ₄) ₂ •6H ₂ O	7a	4.0	52	23
5	Fe(ClO ₄) ₂ •6H ₂ O	8	4.0	73	9
6	Fe(ClO ₄) ₂ •6H ₂ O	9	4.0	65	3.5
7	Fe(ClO ₄) ₂ •6H ₂ O	10	4.0	66	3

^a reaction conditions: 1.0 mmol methyl phenyl sulfide, 0.02 mmol catalyst, 1.2 mmol H₂O₂, 0.01 eq. 4-methoxybenzoic acid, 2.5 mL acetonitrile – 16 h / rt; ^b determined by ¹H-NMR; ^c *ee*-values determined by chPLC; ^d yield determined after complete solvent removal.

Table 10. Oxidation of methyl phenyl sulfide. ^a

Entry	Salt	Ligand	Ligand [mol%]	Sulfoxide 53 Yield [%]	<i>ee</i> [%]
1	Fe(acac) ₃	-	-	n.r. / 16 ^d	-
2	Fe(acac) ₃	1	2.0	41 / 20 ^d	3
3	Fe(acac) ₃	(±)- 4 /(<i>meso</i>)- 4	2.0	22	1
4	Fe(acac) ₃	7a	4.0	40	<1
5	Fe(acac) ₃	8	4.0	36	<1
6	Fe(acac) ₃	9	4.0	55	5.5
7	Fe(acac) ₃	10	4.0	37	3

^a reaction conditions: 1.0 mmol methyl phenyl sulfide, 0.02 mmol catalyst, 1.2 mmol H₂O₂, 0.01 eq. 4-methoxybenzoic acid, 2.5 mL acetonitrile – 16 h / rt; ^b determined by ¹H-NMR; ^c *ee*-values determined by chPLC, ^d yield determined after complete solvent removal.

Table 11. Oxidation of methyl phenyl sulfide. ^a

Entry	Salt	Ligand	Ligand [mol%]	Sulfoxide 53 Yield [%] ^b	<i>ee</i> [%] ^c
1	Fe(OAc) ₂	-	-	18	-
2	Fe(OAc) ₂	1	2.0	19	2
3	Fe(OAc) ₂	(±)- 4 /(<i>meso</i>)- 4	2.0	16	2
4	Fe(OAc) ₂	7a	4.0	37	4
5	Fe(OAc) ₂	8	4.0	43	<1
6	Fe(OAc) ₂	9	4.0	47	16.5
7	Fe(OAc) ₂	10	4.0	32	6

^a reaction conditions: 1.0 mmol methyl phenyl sulfide, 0.02 mmol catalyst, 1.2 mmol H₂O₂, 0.01 eq. 4-methoxybenzoic acid, 2.5 mL acetonitrile – 16 h / rt; ^b determined by ¹H-NMR; ^c *ee*-values determined by chPLC, ^d yield determined after complete solvent removal.

To prevent a possible source of error, based on the strong solvent excess in each sample, in four reactions (Table 9 and 10, entry 1 and 2) the solvent was completely removed. Because of this variation in the work-up, a reduced yield in each sample was detected, but the positive effect of the ligand was nevertheless observed.

In conclusion, for both oxidation reactions explored, the oxazoline ligands were able to generate better results compared to the bis(oxazoline) ligands. Ligand **8** in particular exhibited the best performance in all catalytic oxidations. All the results obtained were not able to match those already published, but do provide the basis for further investigations. Variations of substrates and reaction conditions are feasible.

F. Experimental Part

F.1 General

¹H NMR-Spectra were recorded on Bruker Avance 300, Bruker Avance 400, Bruker Avance 600, Varian Inova 600, Bruker DRX-400 with a H/C/P/F QNP gradient probe and Bruker Avance 500 with a dual carbon/proton CPDUL cryoprobe. The chemical shift δ is given in [ppm], calibration was set on chloroform-d₁ (7.26 ppm) or tetramethylsilane (0.00 ppm) as internal standard. The spectra were evaluated in 1st order and the coupling constants are given in Hertz [Hz]. The following abbreviations for the spin multiplicity were used: s = singlet, d = doublet, t = triplet, q = quartet, qt = quintet, m = multiplet, dt = doublet of a triplet, dd = double doublet, ddd = doublet of a double doublet, sept = septet. The used deuterated solvents are given separately.

¹³C NMR-Spectra were recorded on Bruker Avance 300, Bruker Avance 400, Bruker Avance 600, Varian Inova, Bruker DRX-400 with a H/C/P/F QNP gradient probe and Bruker Avance 500 with a dual carbon/proton CPDUL cryoprobe. The chemical shift δ is given in [ppm], calibration was set on chloroform-d₁ (77.16 ppm), or tetramethylsilane (0.00 ppm) as internal standard.

Melting points were measured on a Büchi SMP 20 in a silicon oil bath. The melting points are uncorrected.

Infrared-Spectra were recorded on a Bio-Rad Excalibur Series or Mattson Genesis Series FT-IR. Solid compounds were measured in KBr, liquid compounds as a neat film between NaCl-plates. The wave numbers are given in [cm⁻¹].

Massspectrometry was performed on Varian MAT 311A, Finnigan MAT 95, Thermoquest Finnigan TSQ 7000, Nermag quadrupoles, VG ZAB high-resolution double-focusing and VG Autospec-Q tandem hybrid with EBEqQ configuration. The percentage set in brackets gives the peak intensity related to the basic peak ($I = 100\%$). High resolution mass spectrometry (HRMS): The molecular formula was proven by the calculated precise mass.

Elemental analysis was prepared by the micro analytic section of the University of Regensburg using a Vario EL III or Mikro-Rapid CHN (Heraeus).

Optical rotation was measured at rt on a 241 MC Perkin-Elmer polarimeter at a wavelength of 589 nm (Na-D) in a 1 dm or 0.1 dm cell. The concentration is given in [g/100 ml].

X-ray analysis was performed by the crystallography laboratory of the University of Regensburg (STOE-IPDS, Stoe & Cie GmbH) and the crystallography laboratory of the University of Kansas.

Chiral HPLC was performed in the analytic department of the University of Regensburg or on a Kontron Instruments 325 System (HPLC 335 UV detector, $\lambda = 254$ nm, Chiracel OD/OD-H column (50x4.6 mm, 10 μ m, flow rate: 1 mL/min, 20 °C, *n*-heptane/ethanol 99:1).

Gaschromatography (GC) was measured in the analytic department of the University of Regensburg or on Fisons Instruments GC 8000 series (Data Jet Integrator, CP-chiralsil-DEX-CP column).

Thin layer chromatography (TLC) was prepared on TLC-aluminium sheets (Merck, silica gel 60 F₂₅₄, 0.2 mm). Detection in UV-light $\lambda = 254$ nm, staining with I₂, mostain, molybdatophosphoric-acid (5% in ethanol), KMnO₄ solution or vanillin-sulfuric acid.

Column chromatography was performed in glass columns (G2 or G3). As a stationary phase silica gel Merck-Geduran 60 (0.063-0.200 mm) or flash silica gel Merck 60 (0.040-0.063 mm) was used.

CD-spectra were measured on a JASCO model J-710/720 at the Institute of Bioanalytic and Sensoric of the University of Regensburg in the specified solvent. The background was subtracted to each spectrum and the absorption value is measured as molar ellipticity (deg•cm²•dmol⁻¹). The spectra were smoothed by adjacent averaging algorithm with Origin 6.0.

UV/Vis spectra were recorded on a Varian Cary BIO 50 UV/VIS/NIR spectrophotometer equipped with a jacketed cell holder using 1-cm cuvettes (quartz or glass) from Hellma

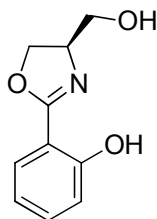
Solvents: Abs. solvents were prepared according to usual lab procedures or taken from the MB-SPS solvent purification system. Ethylacetate, hexanes (40-60 °C) and dichloromethane were purified by distillation before use. Further solvents and reagents were of p.a. quality.

Reactions with oxygen- and moisture sensitive reactants were performed in oven dried and in vacuo heated reaction flasks under a pre-dried inert gas (nitrogen or argon) atmosphere. For cooling to temperatures < -40 °C a cryostat Haake EK 90 or dry ice/*iso*-propanol mixture was used.

F.2 Abbreviations

α -KA	α -keto acid	L	ligand
abs	absolute	LAH	lithium aluminium hydride
acac	acetylacetonate	M	metal
bf	benzoylformate	Me	methyl
cat	catalytic	MeCN	acetonitrile
CD	circular dichroism	Mes	mesyl
CI	chemical ionization	min	minute
DCM	dichloromethane	MMOM	methane monooxygenase
DFO	desferrioxamine	MRT	5-methyltetrahydrofolate- homocystein methyltransferase
DFT	desferrithiocin	MS	molecular sieve
<i>dr</i>	diastereomeric ratio	nm	nano meters
DMA	N,N-dimethylacetamide	NMR	nuclear magnetic resonance
DMAP	N,N-dimethylamino pyridine	Nu	nucleophile
DMF	dimethyl formamide	OAc	acetate
<i>ee</i>	enantiomeric excess	OD	optical density
EE	eth	Ph	phenyl
eq	equivalents	PPL	porcine pancreas lipase enzyme
EI	electronic ionization	pyr	pyridine
Et	ethyl	RNR R2	ribonucleotide reductase type I
GC	gas-chromatograph	rt	room temperature
h	hour	TBDMS	<i>tert</i> -butyldimethylsilyl
HPLC	high pressure liquid Chromatography	TBAF	tetrabutylammonium fluoride
HR	hemerythrin	<i>t</i> Bu	<i>tert</i> -butyl
HRMS	high resolution mass Spectrometry	THF	tetrahydrofuran
ICE	iron clearing efficiency	TMS	trimethylsilyl
<i>i</i> Pr	<i>iso</i> -propyl	TP	tris(pyrazolyl)borate
IR	infra red	Ts	tosyl

F.3 Oxazoline and Thiazoline Ligands

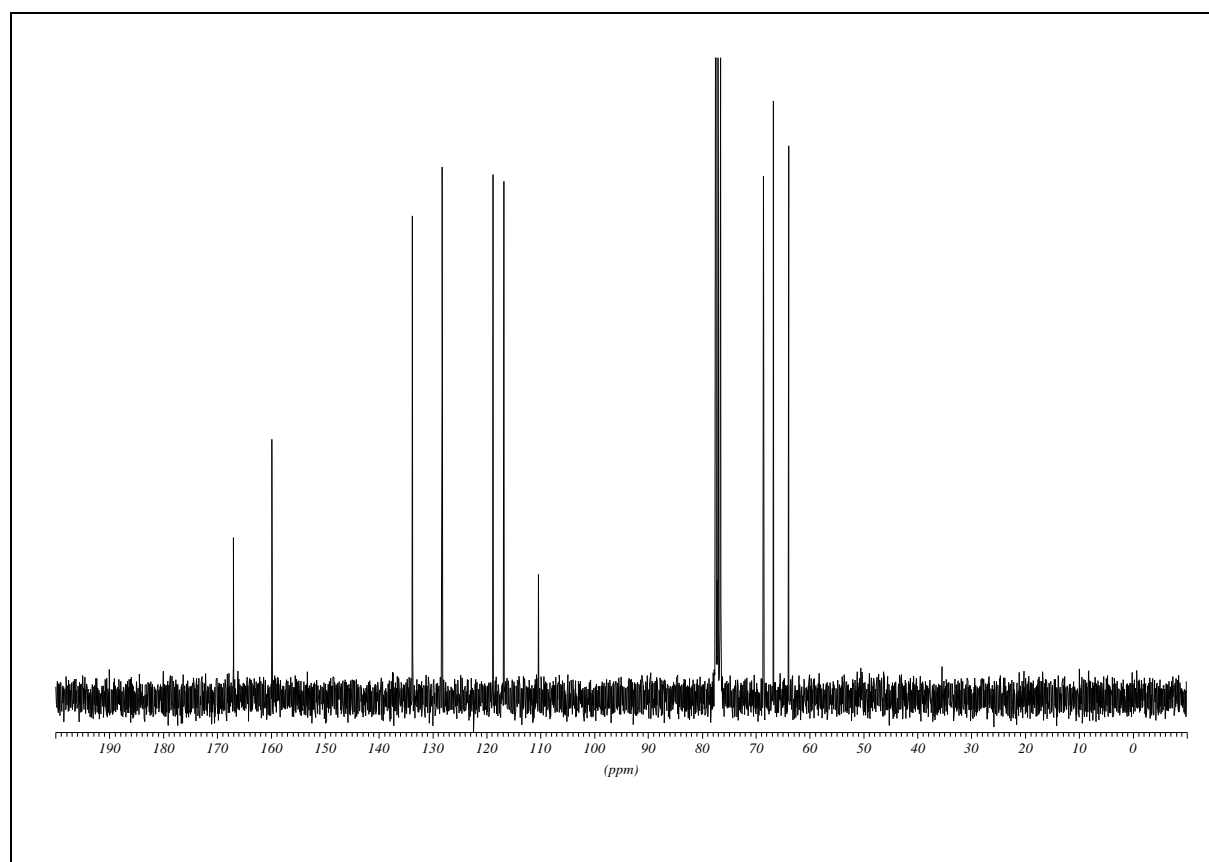
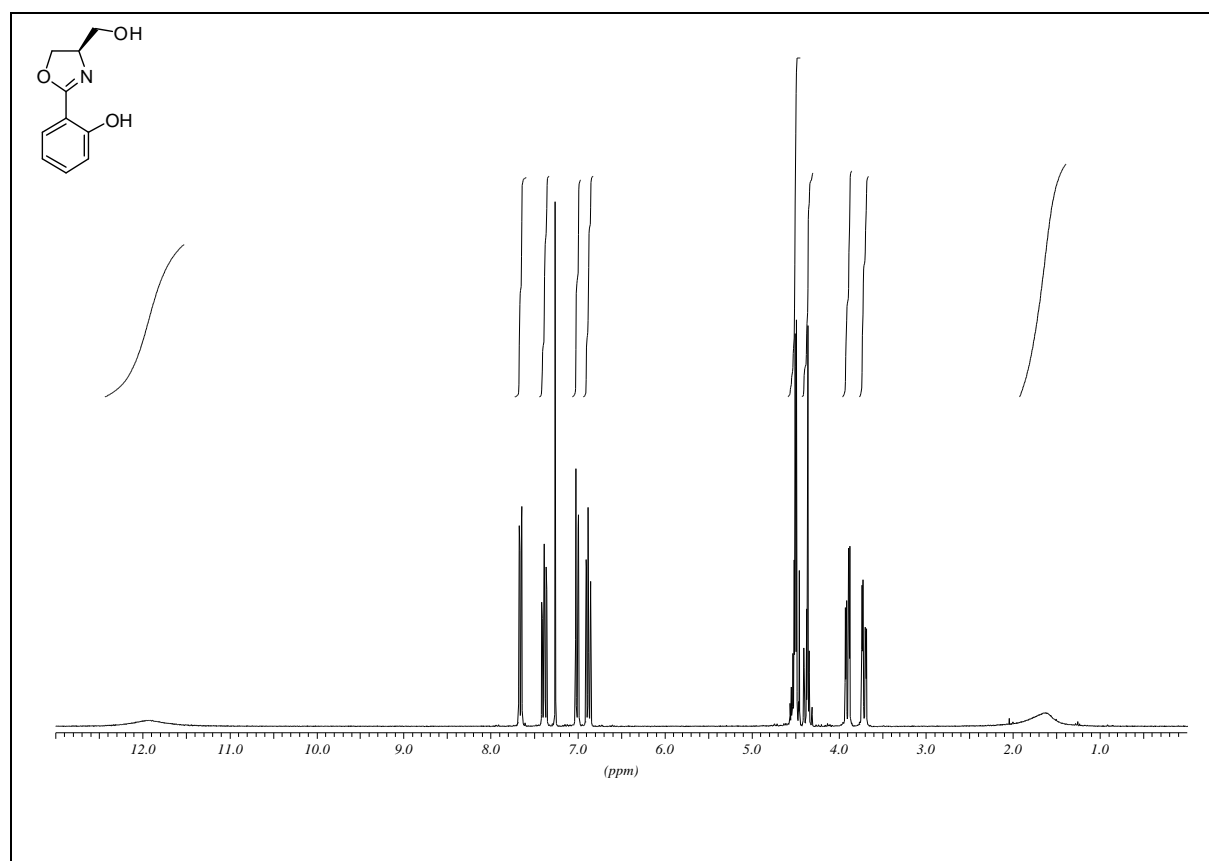


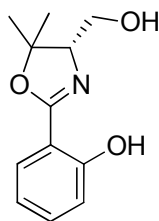
(*R*)-2-(4-(hydroxymethyl)-4,5-dihydrooxazol-2-yl)phenol (**7a**)

(*S*)-methyl-2-(2-hydroxyphenyl)-4,5-dihydrooxazole-4-carboxylate **16a** (8.09 g, 36.57 mmol, 1.0 equiv.) was dissolved in dry THF (100 mL) under N₂ and cooled to -30 °C. LiAlH₄ (1.80 g, 47.54 mmol, 1.3 equiv.) was added in portions and the mixture was stirred for 3.5 h at -30 °C. After addition of sat. aqueous KNa-tartrate-solution (200 mL) and Et₂O (200 mL) the mixture was continuously stirred over night at rt. The layers were separated and the aqueous layer was extracted with EtOAc (3 x 150 mL) and all combined organic layers were dried (Na₂SO₄). The solvent was evaporated under reduced pressure and the crude product was purified by flash column chromatography (SiO₂, hexanes/EtOAc 5:1 to 3:1 to EtOAc) to yield the product as slightly yellow solid (2.24 g, 11.61 mmol, 32%), which can be further recrystallized from Et₂O to afford a colourless solid.

R_f 0.14 (hexanes/EtOAc 5:1); m.p. 85 °C; $[\alpha]_D^{20} = +23.65$ (c = 0.99, EtOH); ¹H NMR (300 MHz, CDCl₃): δ 11.90 (bs, OH, 1H), 7.68-7.64 (m, CH_a, 1H), 7.43-7.33 (m, CH_a, 1H), 7.03-6.98 (m, CH_a, 1H), 6.91-6.84 (m, CH_a, 1H), 4.56-4.44 (m, CH₂-OH, 2H), 4.41-4.31 (m, CH, 1H), 3.90 (dd, *J* = 3.7, 11.4 Hz, CH-CH₂, 1H), 3.71 (dd, *J* = 11.4, 3.7 Hz, CH-CH₂, 1H); ¹³C NMR (75.5 MHz, CDCl₃): δ 167.0 (C_q), 159.8 (C_q), 133.8 (C_a), 128.3 (C_a), 118.8 (C_a), 116.8 (C_a), 110.4 (C_q), 68.6 (CH₂), 66.8 (CH), 64.0 (CH₂); IR (KBr): $\tilde{\nu}$ 3299, 2870, 1643, 1616, 1580, 1489, 1410, 1364, 1303, 1257, 1224, 1157, 1126, 1066, 1029, 982, 952, 860, 828, 788, 750 cm⁻¹; MS (CI, NH₃): *m/z* (%) = 194.1 (100, [MH]⁺); elemental analysis calcd (%) for C₁₀H₁₁NO₃ (256.1): C 62.17, H 5.74, N 7.25, found: C 62.08, H 6.21, N 7.23.

(R)-2-(4-(hydroxymethyl)-4,5-dihydrooxazol-2-yl)phenol (7a)



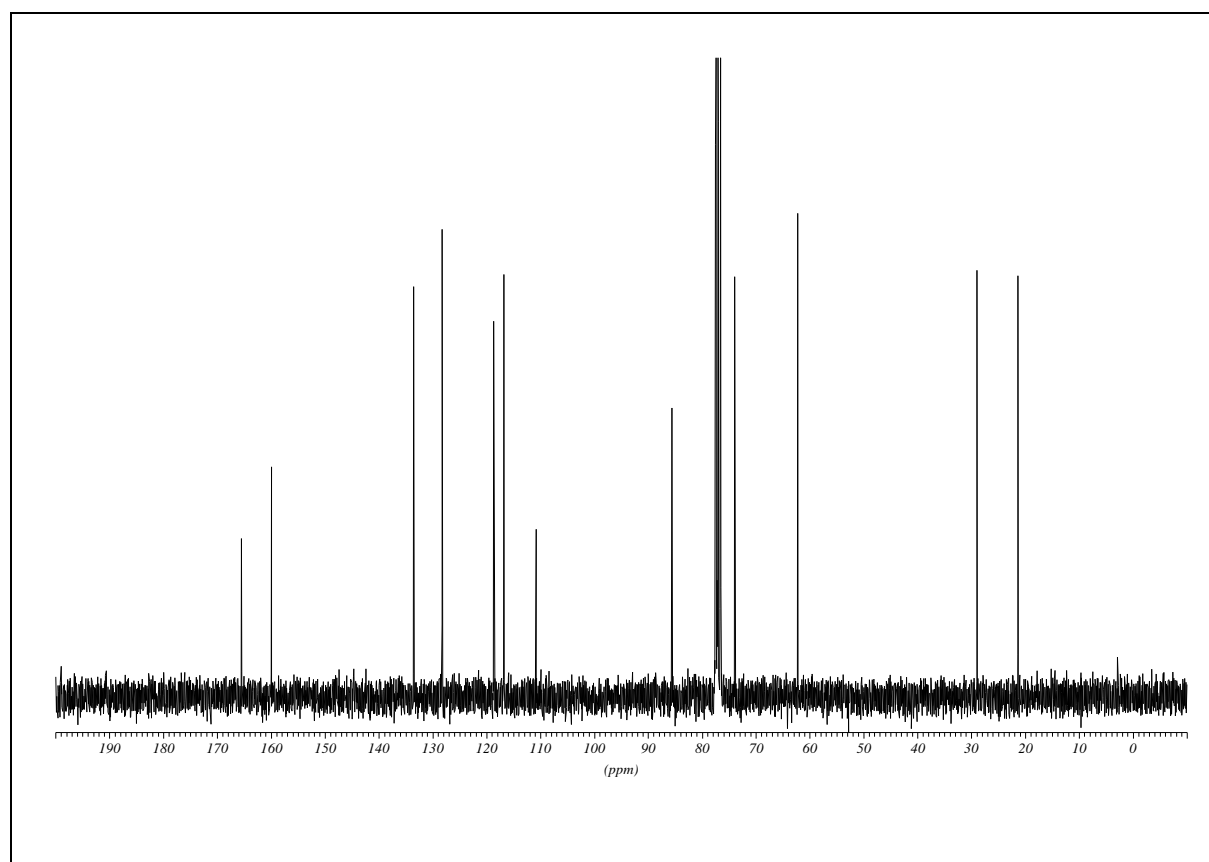
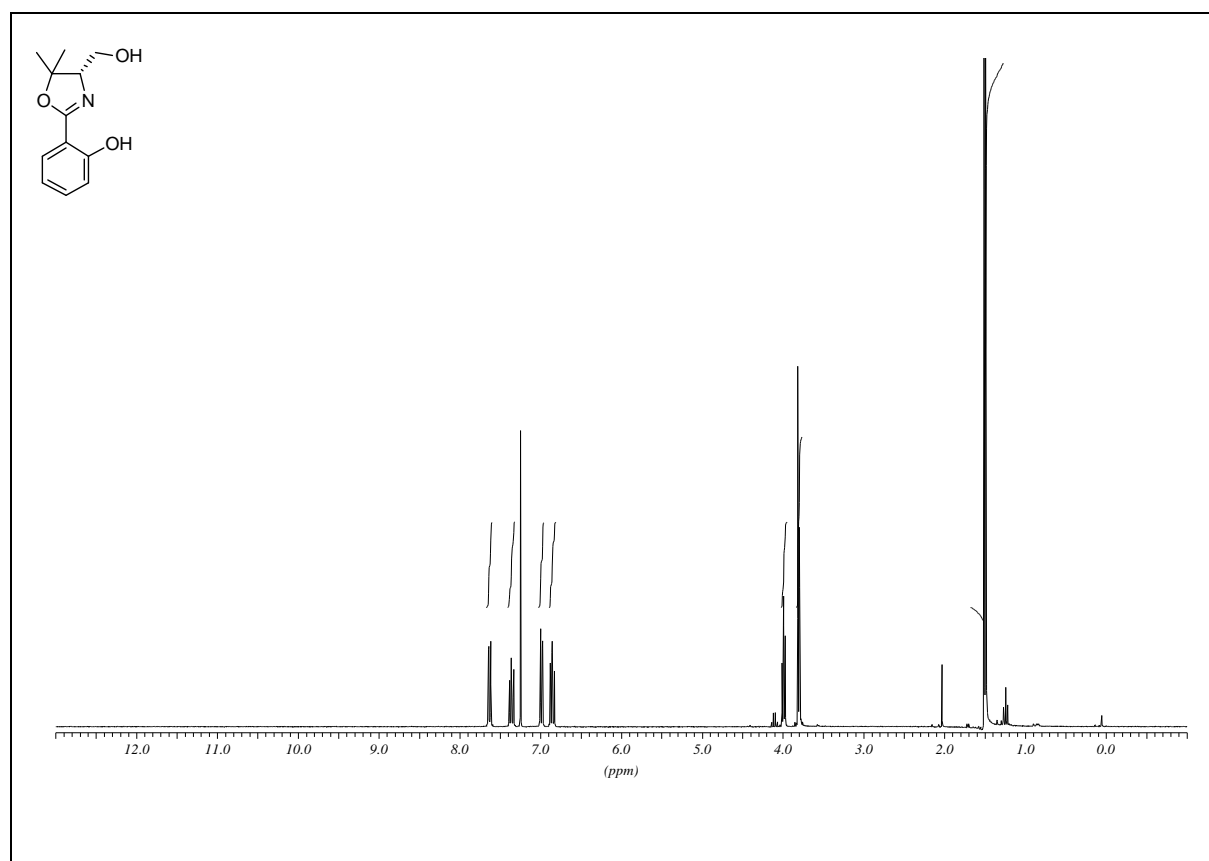


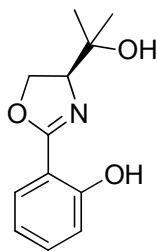
(S)-2-(4-(hydroxymethyl)-5,5-dimethyl-4,5-dihydrooxazol-2-yl)phenol (9)

(S)-2-(4-((*tert*-butyldimethylsilyloxy)methyl)-5,5-dimethyl-4,5-dihydrooxazol-2-yl)phenol **19** (2.75 g, 8.20 mmol, 1.0 equiv.) was dissolved in dry THF (50 mL), dry NEt₃ (115 μ L, 83 mg, 0.82 mmol, 0.1 equiv.) and TBAF (2.64 g, 8.36 mmol, 1.02 equiv.) were added at rt and the mixture was stirred for 20 h. The solvent was evaporated and the crude product was purified by column chromatography (SiO₂, hexanes/EtOAc 1:1) to yield the product as slightly orange oil (1.32 g, 5.97 mmol, 73%).

R_f 0.67 (hexanes/EtOAc 1:1); $[\alpha]_D^{20} = -33.39$ (c = 1.11, EtOH); ¹H NMR (300 MHz, CDCl₃): δ 7.67-7.60 (m, CH_a, 1H), 7.40-7.32 (m, CH_a, 1H), 7.02-6.96 (m, CH_a, 1H), 6.89-6.81 (m, CH_a, 1H), 3.99 (t, *J* = 5.6 Hz, CH, 1H), 3.82 (d, *J* = 6.0 Hz, CH₂, 2H), 1.51 (s, CH₃, 3H), 1.49 (s, CH₃, 3H); ¹³C NMR (75.5 MHz, CDCl₃): δ 165.5 (C_q), 160.0 (C_q), 133.5 (C_a), 128.3 (C_a), 118.7 (C_a), 116.8 (C_a), 110.9 (C_q), 85.6 (C_q), 73.9 (CH), 62.3 (CH₂), 29.0 (CH₃), 21.4 (CH₃); IR (film): $\tilde{\nu}$ 3425, 2975, 1633, 1491, 1365, 1307, 1256, 1153, 1127, 1074, 1037, 946, 893, 850, 801, 757, 692 cm⁻¹; MS (EI, 70 eV): *m/z* (%) = 121.1 (100, [C₇H₅O₂]⁺), 190.1 (38, [C₁₁H₁₂NO₂]⁺), 221.1 (52, [M]⁺); HRMS (EI, 70 eV): calcd for C₁₂H₁₅NO₃ [M]⁺ 221.1052, found 221.1055.

(S)-2-(4-(hydroxymethyl)-5,5-dimethyl-4,5-dihydrooxazol-2-yl)phenol (9)



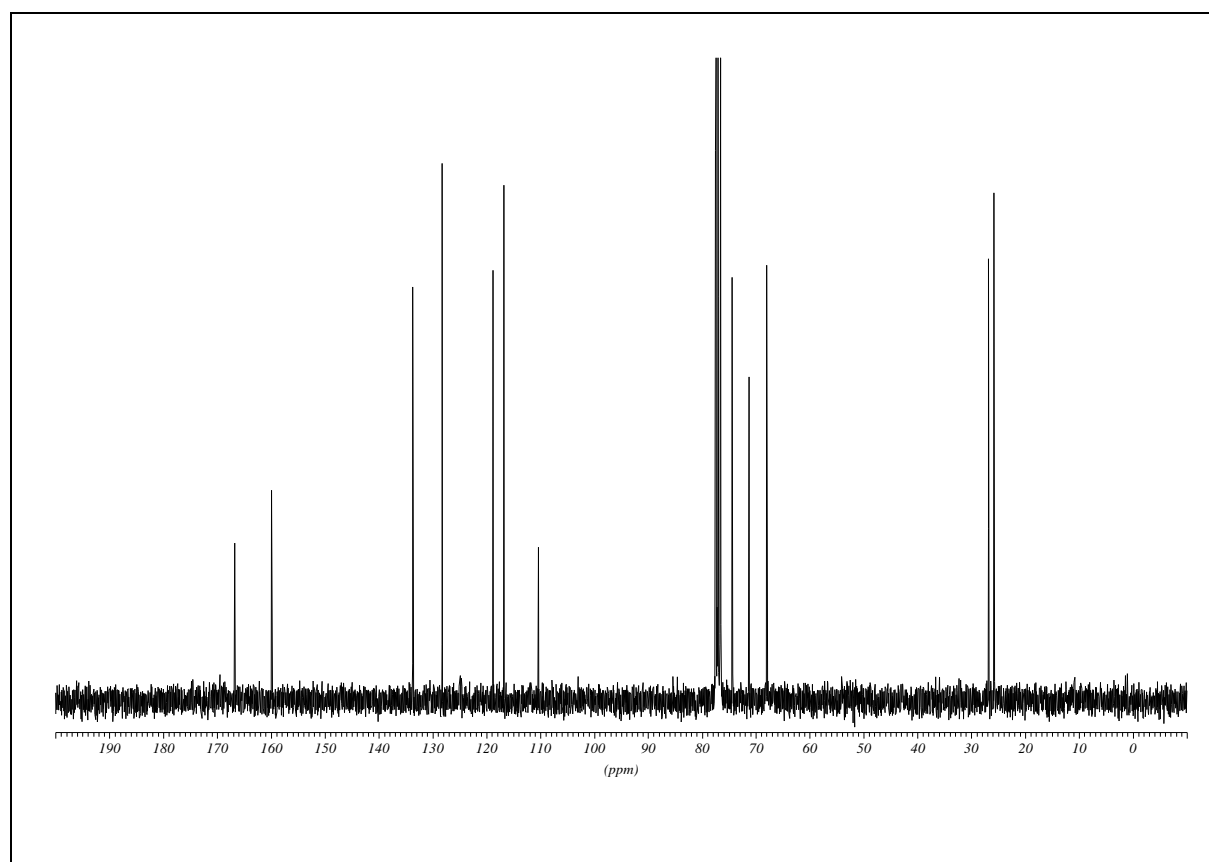
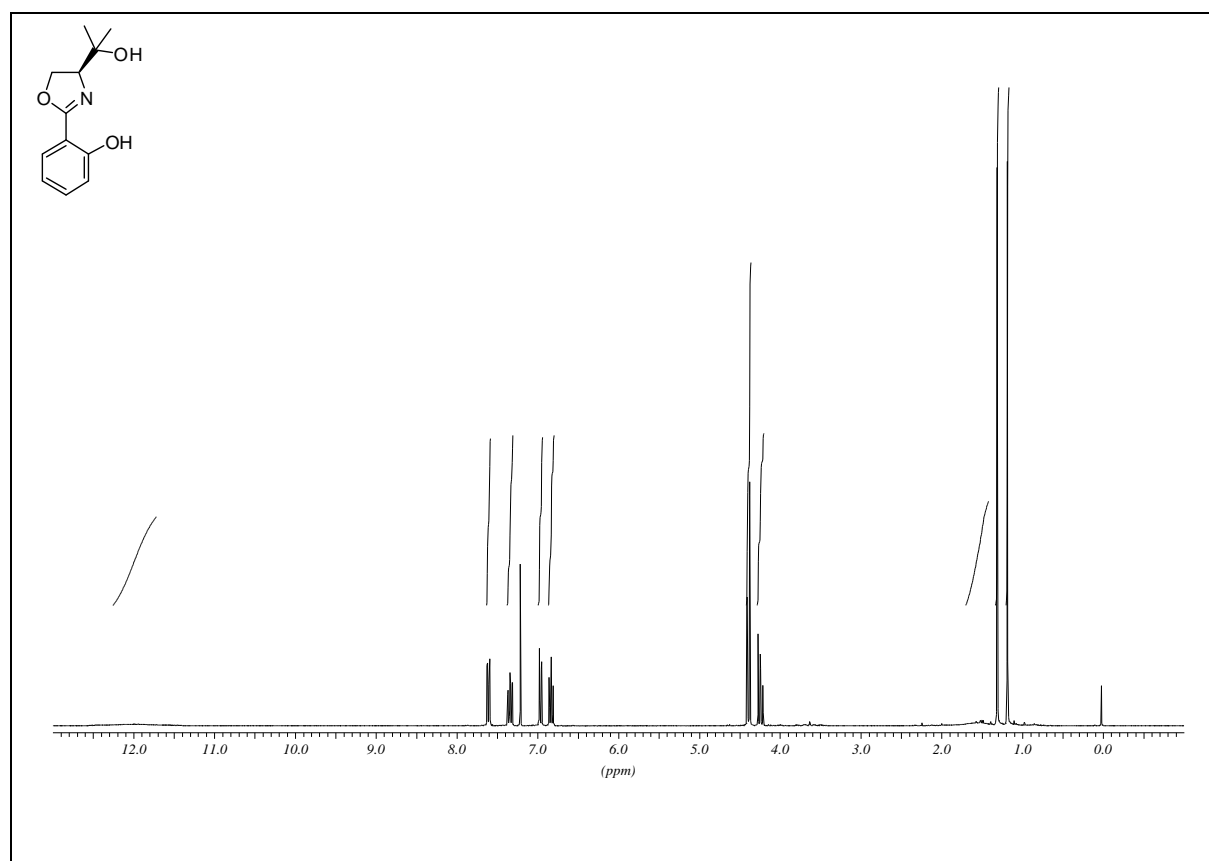


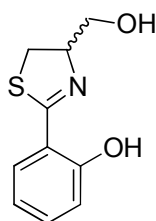
(S)-2-(4-(2-hydroxypropan-2-yl)-4,5-dihydrooxazol-2-yl)phenol (8)

(S)-methyl-2-(2-hydroxyphenyl)-4,5-dihydrooxazole-4-carboxylate **16a** (15.58 g, 70.43 mmol, 1.0 equiv.) was dissolved in dry Et₂O (300 mL) and cooled to 0 °C under N₂. A 3.0 M-solution of MeMgBr (69.50 mL, 208.5 mmol, 2.96 equiv.) was added dropwise. The mixture was stirred for 5 h at 0 °C. After addition of sat. NH₄Cl-solution (200 mL) stirring was continued until both layers were clear. After layer separation, the aqueous layer was extracted with Et₂O (5 x 100 mL) and the combined organic layers were dried (Na₂SO₄). The solvent was evaporated under reduced pressure and the crude product was purified by flash column chromatography (SiO₂, hexanes/EtOAc 3:1) to yield the product as yellow solid (10.90 g, 49.27 mmol, 70%).

R_f 0.49 (hexanes/EtOAc 3:1); m.p. 45 - 47 °C; $[\alpha]_D^{20} = -7.98$ (c = 1.02, EtOH); ¹H NMR (300 MHz, CDCl₃): δ 12.00 (bs, OH, 1H), 7.64-7.58 (m, CH_a, 1H), 7.38-7.30 (m, CH_a, 1H), 7.00-6.94 (m, CH_a, 1H), 6.87-6.80 (m, CH_a, 1H), 4.42-4.36 (m, CH₂, 2H), 4.38 (dd, J = 8.2 Hz, CH, 1H), 1.50 (bs, C(CH₃)₂-OH, 1H), 1.31 (s, CH₃, 3H), 1.19 (s, CH₃, 3H); ¹³C NMR (75.5 MHz, CDCl₃): δ 166.8 (C_q), 159.9 (C_q), 133.7 (C_a), 128.3 (C_a), 118.8 (C_a), 116.8 (C_a), 110.4 (C_q), 74.4 (CH), 71.3 (C_q), 68.0 (CH₂), 26.8 (CH₃), 25.8 (CH₃); IR (KBr): $\tilde{\nu}$ 3428, 3398, 2963, 1643, 1618, 1581, 1491, 1464, 1420, 1363, 1311, 1253, 1232, 1150, 1130, 1075, 1039, 955, 829, 793, 761 cm⁻¹; MS (EI, 70 eV): m/z (%) = 121.1 (100, [C₇H₅O₂⁺]), 221.2 (20, [M⁺]); HRMS (EI, 70 eV): calcd for C₁₂H₁₅NO₃ [M⁺] 221.1052, found 221.1051.

(S)-2-(4-(2-hydroxypropan-2-yl)-4,5-dihydrooxazol-2-yl)phenol (8)



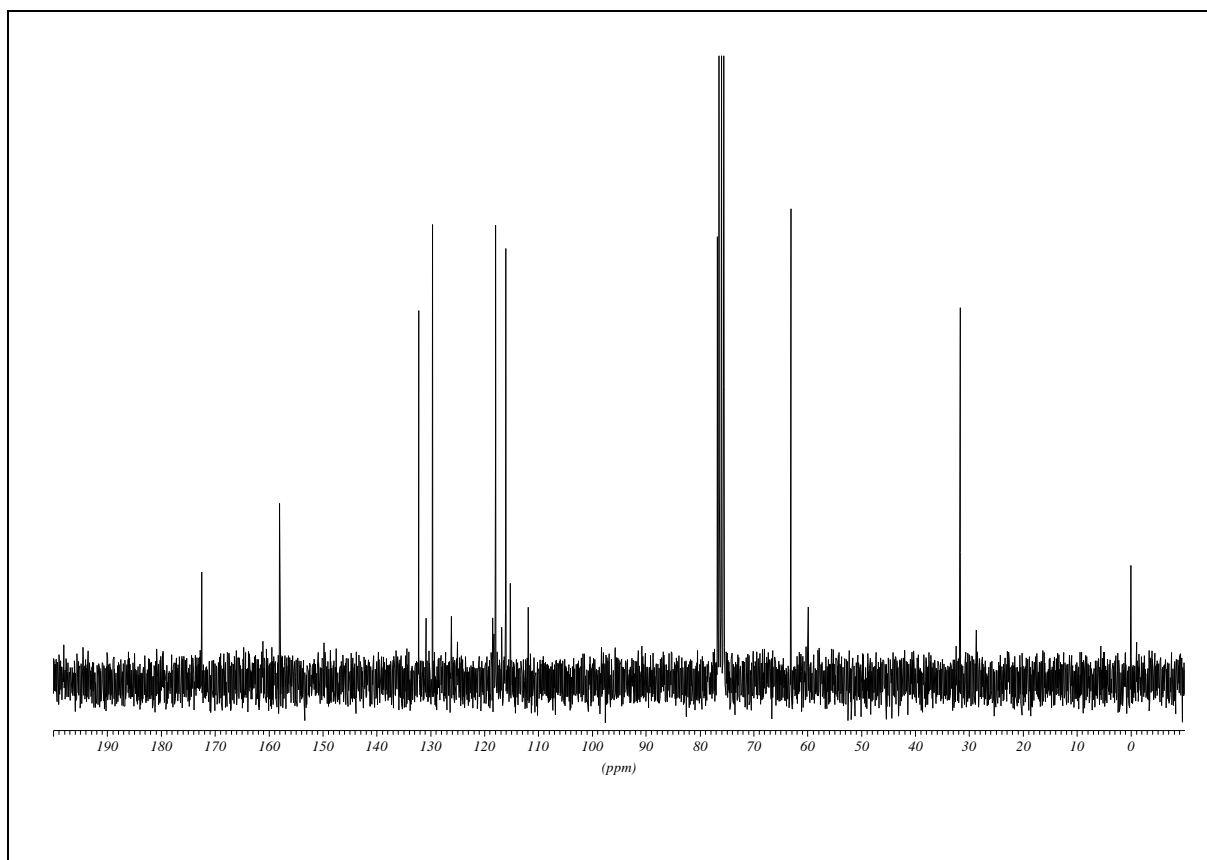
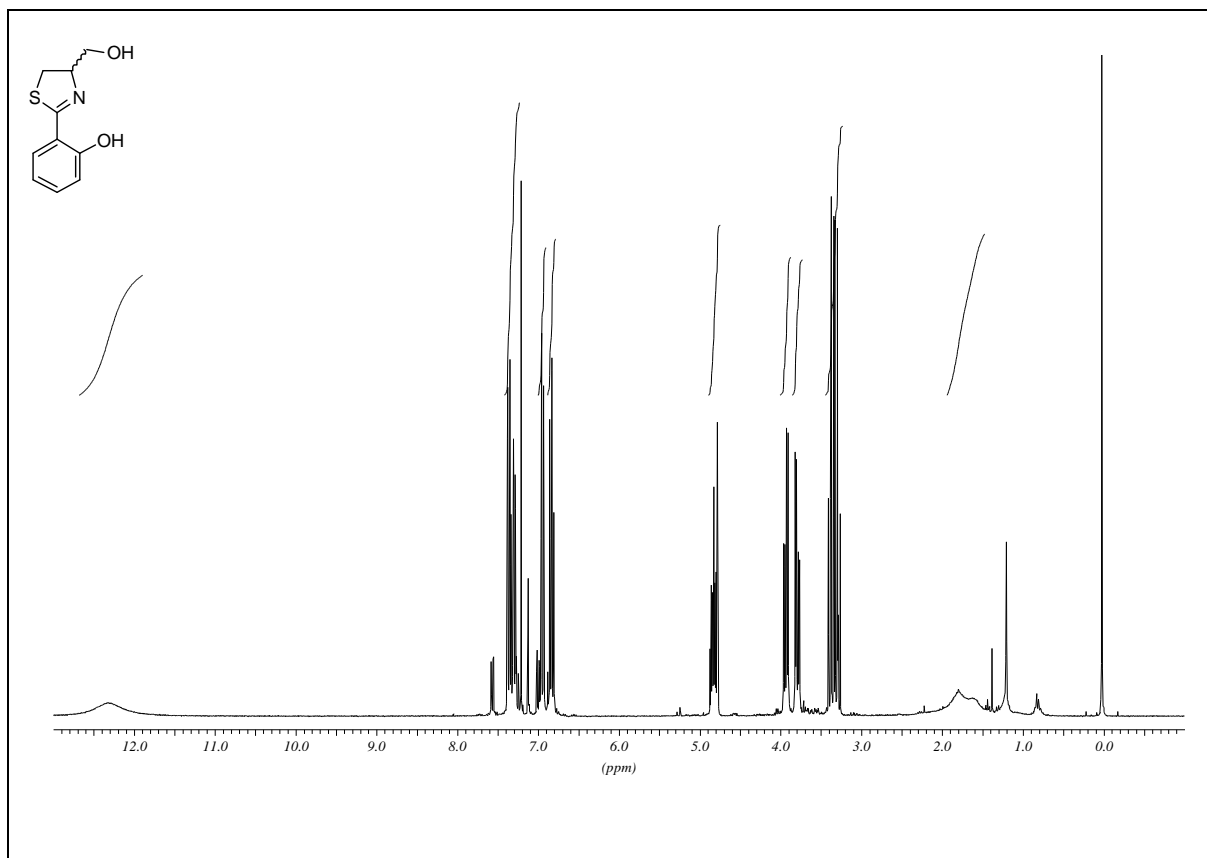


(±)-2-(4-(hydroxymethyl)-4,5-dihydrothiazol-2-yl)phenol (±)-(10)

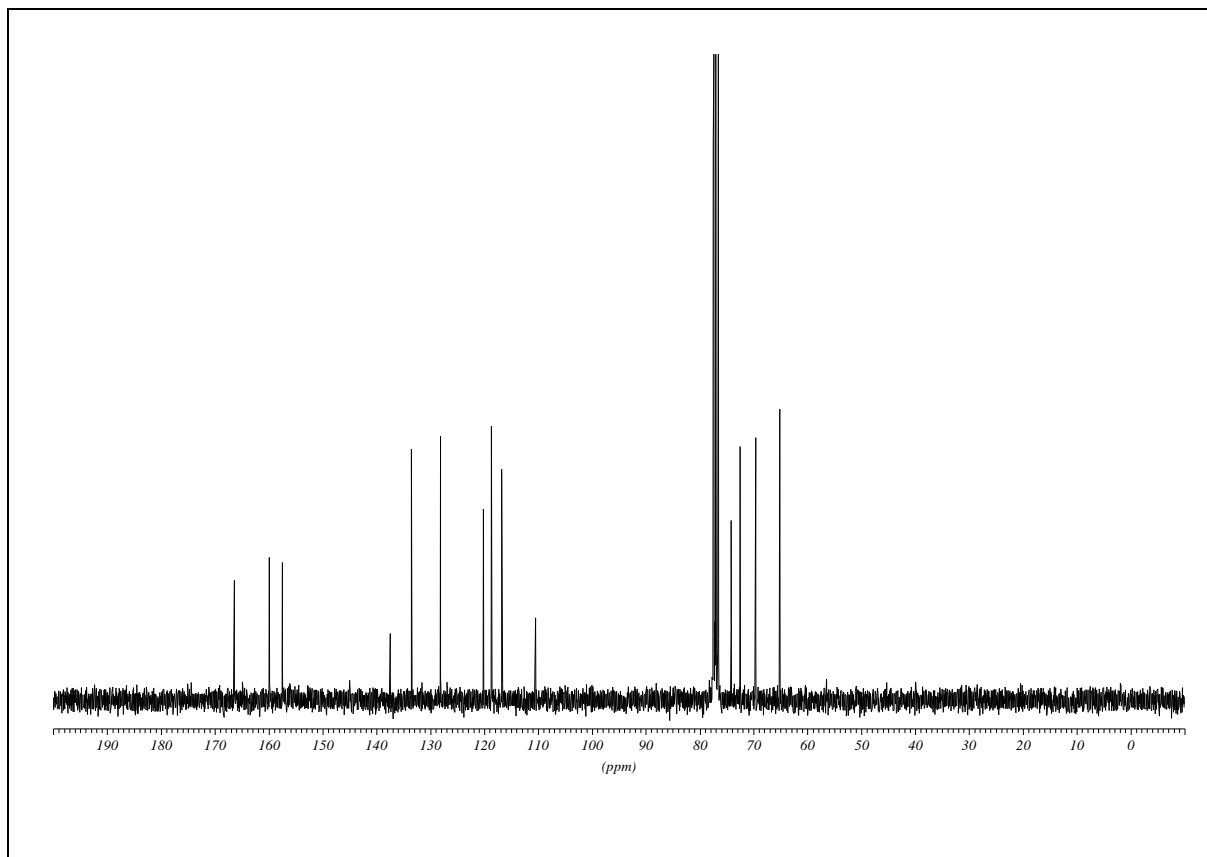
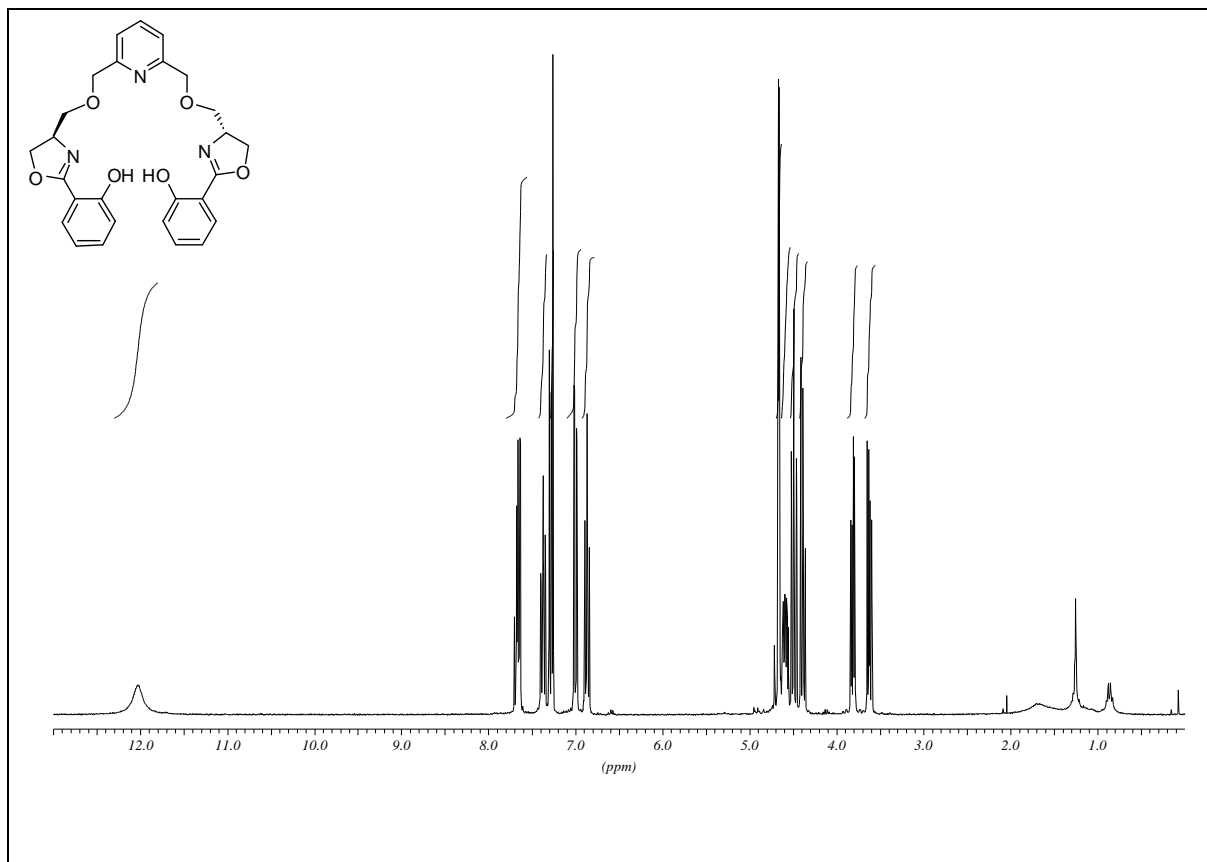
(*R*)-methyl-2-(2-hydroxyphenyl)-4,5-dihydrothiazole-4-carboxylate **21** (340 mg, 1.43 mmol, 1.0 equiv.) was dissolved in dry THF (15 mL). NaBH₄ (141 mg, 3.73 mmol, 2.6 equiv.) was added at once and the mixture started refluxing. MeOH (3 mL) was added over 15 min. and the solution was cooled down to 15 °C. H₂O (1 mL) was added and stirring was continued for 10 min., before additional H₂O (10 mL) was added. The layers were separated and the aqueous layer was extracted with Et₂O (3 x 20 mL) and all combined organic layers were washed with brine (30 mL) and dried (Na₂SO₄). The solvent was evaporated under reduced pressure and the crude product was purified by column chromatography (SiO₂, hexanes/EtOAc 2:1) to yield the product as yellow oil in racemic form (182 mg, 0.87 mmol, 61%).

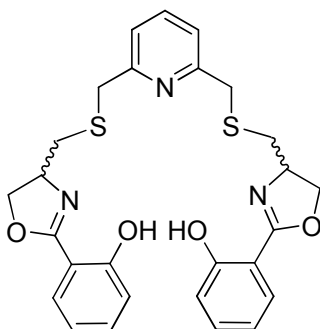
R_f 0.37 (hexanes/EtOAc 2:1); $[\alpha]_D^{20} = +1.38$ (*c* = 1.01, CHCl₃); ¹H NMR (300 MHz, CDCl₃): δ 12.3 (bs, OH, 1H), 7.39-7.27 (m, CH_a, 2H), 6.97-6.91 (m, CH_a, 1H), 6.87-6.80 (m, CH_a, 1H), 4.88-4.77 (m, CH, 1H), 3.94 (dd, *J* = 11.3, 5.2 Hz, CH₂-OH, 1H), 3.79 (dd, *J* = 11.3, 4.7 Hz, CH₂-OH, 1H), 3.38 (dd, *J* = 11.0, 8.8 Hz, CH-CH₂, 1H), 3.30 (dd, *J* = 11.0, 8.2 Hz, CH-CH₂, 1H); ¹³C NMR (75.5 MHz, CDCl₃): δ 172.5 (C_q), 158.0 (C_q), 132.2 (C_a), 129.7 (C_a), 118.5 (C_a), 116.1 (C_a), 111.9 (C_q), 76.7 (CH), 63.1 (CH₂), 31.7 (CH₂); IR (film): $\tilde{\nu}$ 3409, 2918, 2871, 1617, 1590, 1566, 1489, 1456, 1406, 1290, 1254, 1219, 1154, 1118, 1034, 953, 816, 749 cm⁻¹; MS (EI, 70 eV): *m/z* (%) = 178.1 (100, [M-CO₂H]), 209.1 (42, [M⁺]); HRMS (EI, 70 eV): calcd for C₁₀H₁₁NO₂S [M⁺] 209.0511, found 209.0511.

(±)-2-(4-(hydroxymethyl)-4,5-dihydrothiazol-2-yl)phenol (±)-(10)



2,2'-(4*R*,4'*R*)-4,4'-(pyridine-2,6-diylbis(methylene))bis(oxy)bis(methylene)bis(4,5-dihydrooxazole-4,2-diyl)diphenol (1)



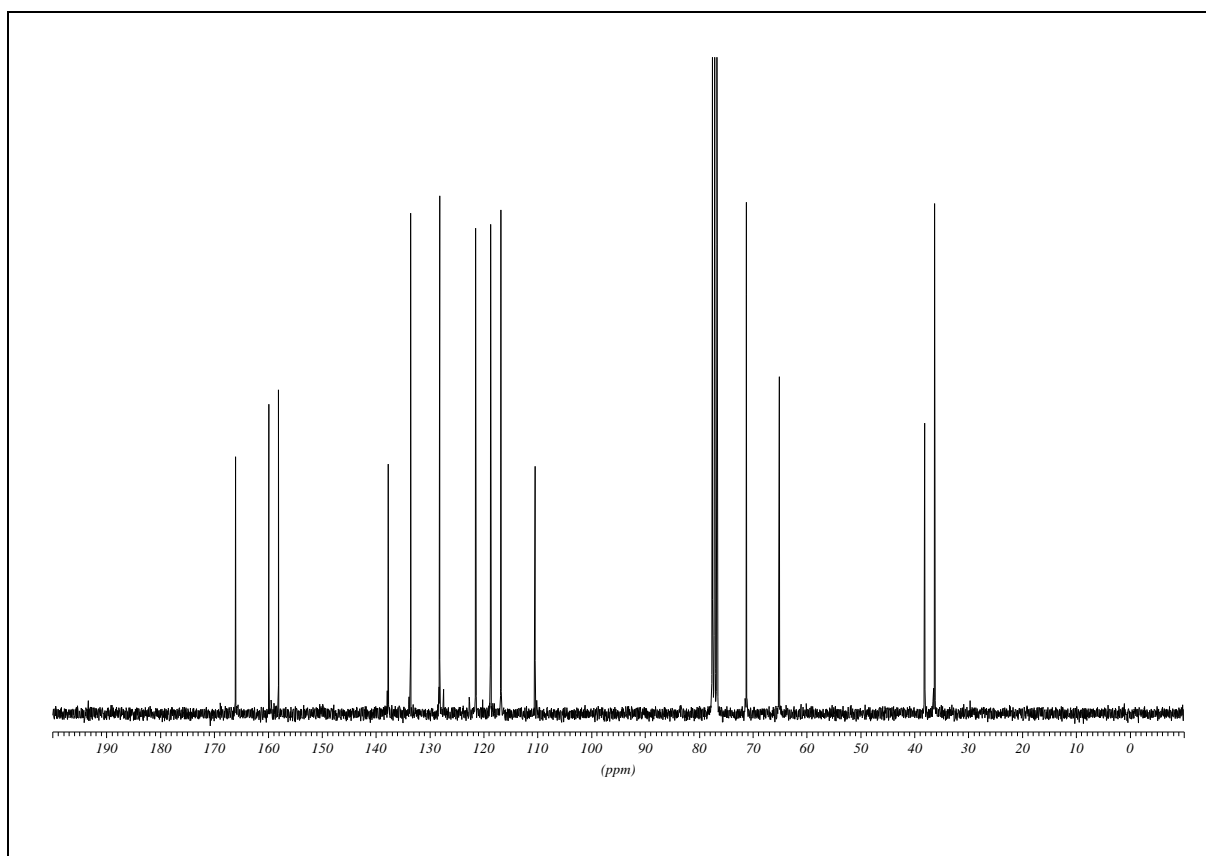
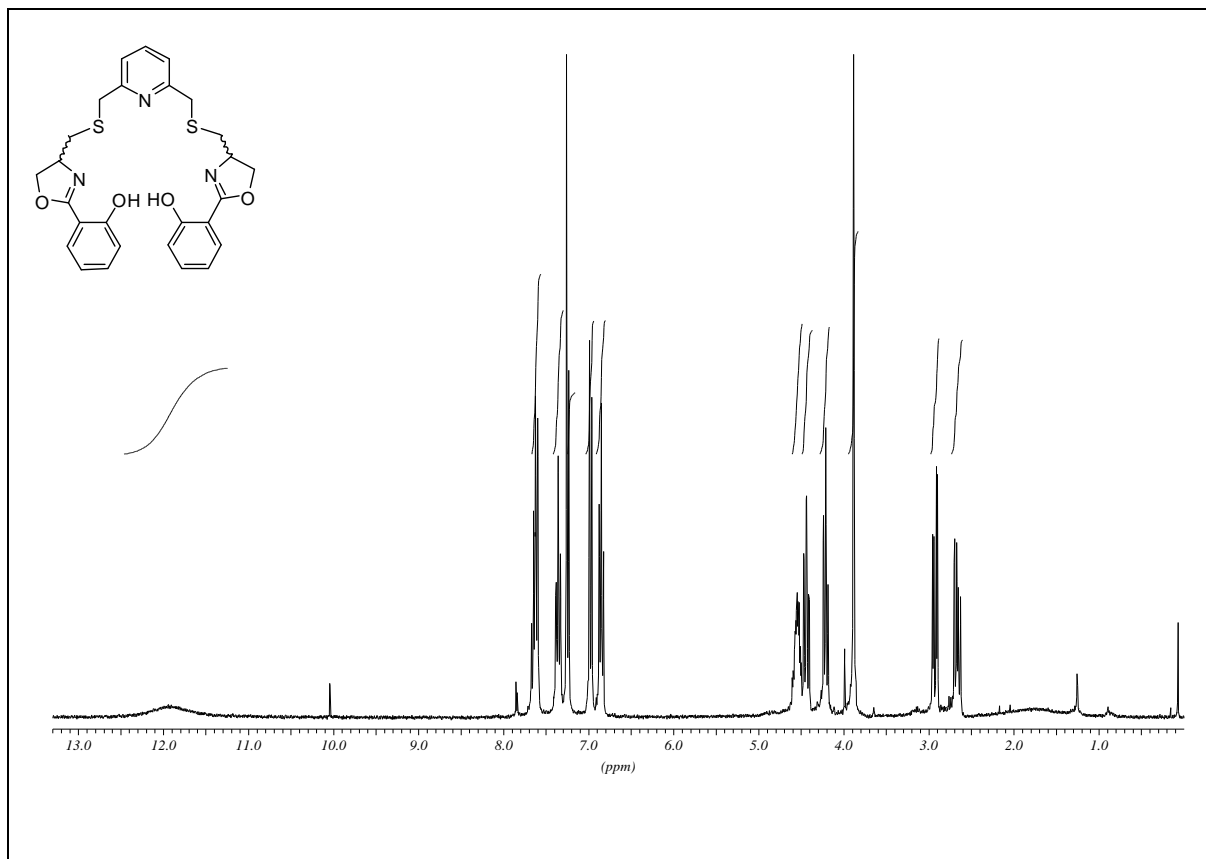


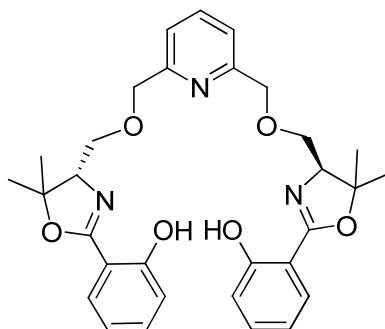
(±)-2,2'-(4,4'-(pyridine-2,6-diylbis(methylene))bis(sulfaneyl))bis(methylene)bis(4,5-dihydrooxazole-4,2-diyl)diphenol (±)-(4)

NaH (60% suspension in mineral oil) (70 mg, 1.75 mmol, 2.5 equiv.) was suspended in dry DMF (5 mL) under N₂ and cooled to 0 °C. 2,6-bis(mercaptomethyl)pyridine **27** (120 mg, 0.70 mmol, 1.0 equiv.) was added dropwise as a solution in dry DMF (3 mL) and the mixture was stirred until the evolution of hydrogen had ceased. (±)-2-(4-(bromomethyl)-4,5-dihydrooxazol-2-yl)phenol (±)-**28** (394 mg, 1.54 mmol, 2.2 equiv.) was dissolved in dry DMF (3 mL) and was also added dropwise. The ice-bath was removed and stirring was continued at 70 °C for 24 h. DMF was evaporated, water (10 mL) and CHCl₃ (20 mL) were added and the layers were separated. The aqueous layer was extracted with CHCl₃ (4 x 20 mL) and the combined organic layers were dried (Na₂SO₄). After removal of the solvent in vacuo, the residue was purified by column chromatography (SiO₂, hexanes/EtOAc 1:1) to yield the product as red oil in racemic form (285 mg, 0.546 mmol, 78%).

R_f 0.77 (hexanes/EtOAc 1:1); $[\alpha]_D^{20} = -0.69$ (c = 1.02, EtOH); ¹H NMR (300 MHz, CDCl₃): δ 12.00 (bs, OH, 2H), 7.64-7.58 (m, CH_a, 3H), 7.40-7.32 (m, CH_a, 3H), 7.23 (s, CH_a, 1H), 7.00-6.95 (m, CH_a, 2H), 6.88-6.81 (m, CH_a, 2H), 4.61-4.50 (m, CH, 2H), 4.48-4.38 (m, O-CH₂-CH, 2H), 4.25-4.18 (m, O-CH₂-CH, 2H), 3.89 (s, S-CH₂-C_a, 4H), 2.96 (dd, J = 13.3, 4.5 Hz, S-CH₂-CH, 2H), 2.66 (dd, J = 13.3, 7.8 Hz, S-CH₂-CH, 2H); ¹³C NMR (75.5 MHz, CDCl₃): δ 166.1 (C_q), 159.9 (C_q), 158.1 (C_q), 137.8 (C_a), 133.6 (C_a), 128.2 (C_a), 121.5 (C_a), 118.7 (C_a), 116.8 (C_a), 110.5 (C_q), 71.2 (CH₂), 65.1 (CH), 38.1 (CH₂), 36.4 (CH₂); IR (film): $\tilde{\nu}$ 3427, 2914, 1639, 1574, 1491, 1452, 1419, 1365, 1309, 1275, 1230, 1155, 1129, 1068, 1034, 958, 916, 825, 755, 684 cm⁻¹; MS (ESI): m/z (%) = 522.3 (100, [MH⁺]); elemental analysis calcd (%) for C₂₇H₂₇N₃O₄S₂ (521.65): C 62.17, H 5.22, N 8.06, S 12.29, found: C 61.92, H 5.07, N 7.83, S 12.11.

(±)-2,2'-(4,4'(pyridine-2,6-diylbis(methylene)))bis(sulfanediyl)bis(methylene)bis(4,5-dihydrooxazole-4,2-diyl)diphenol (±)-(4)



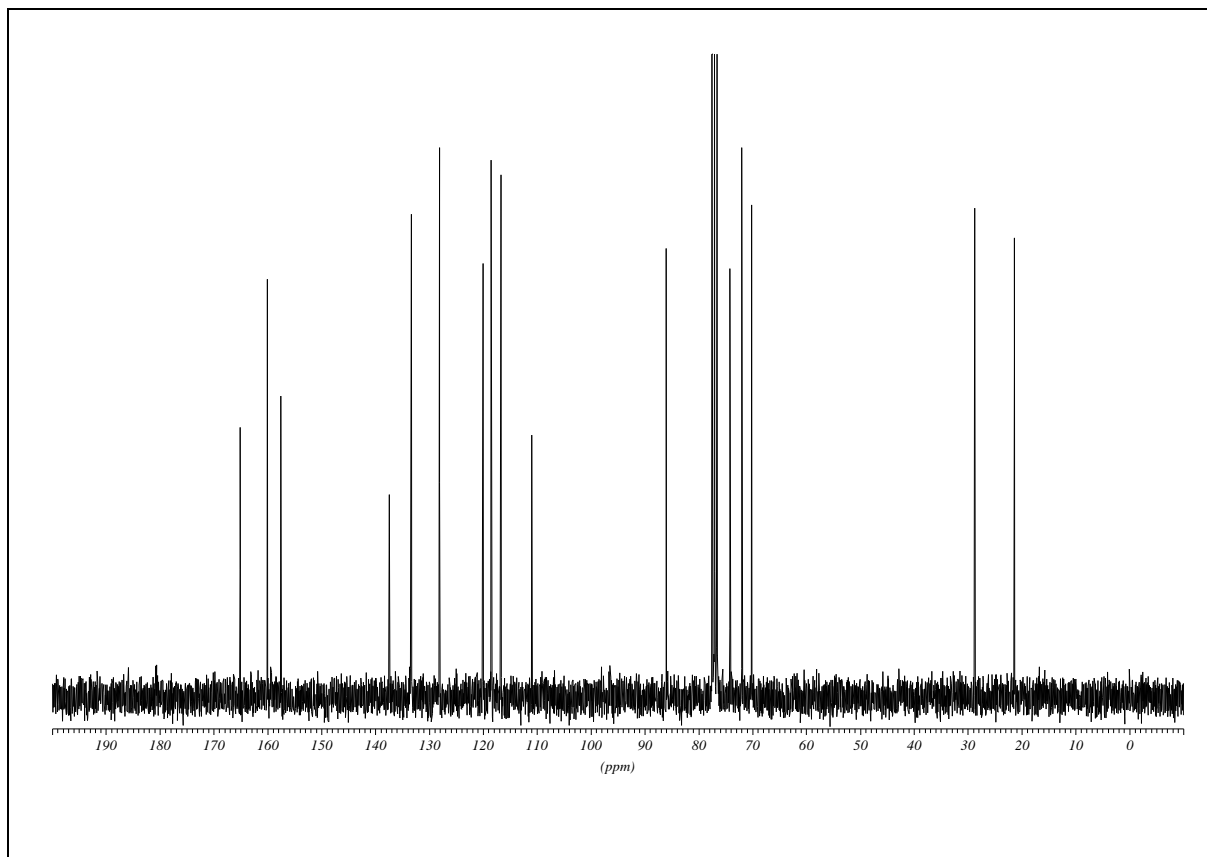
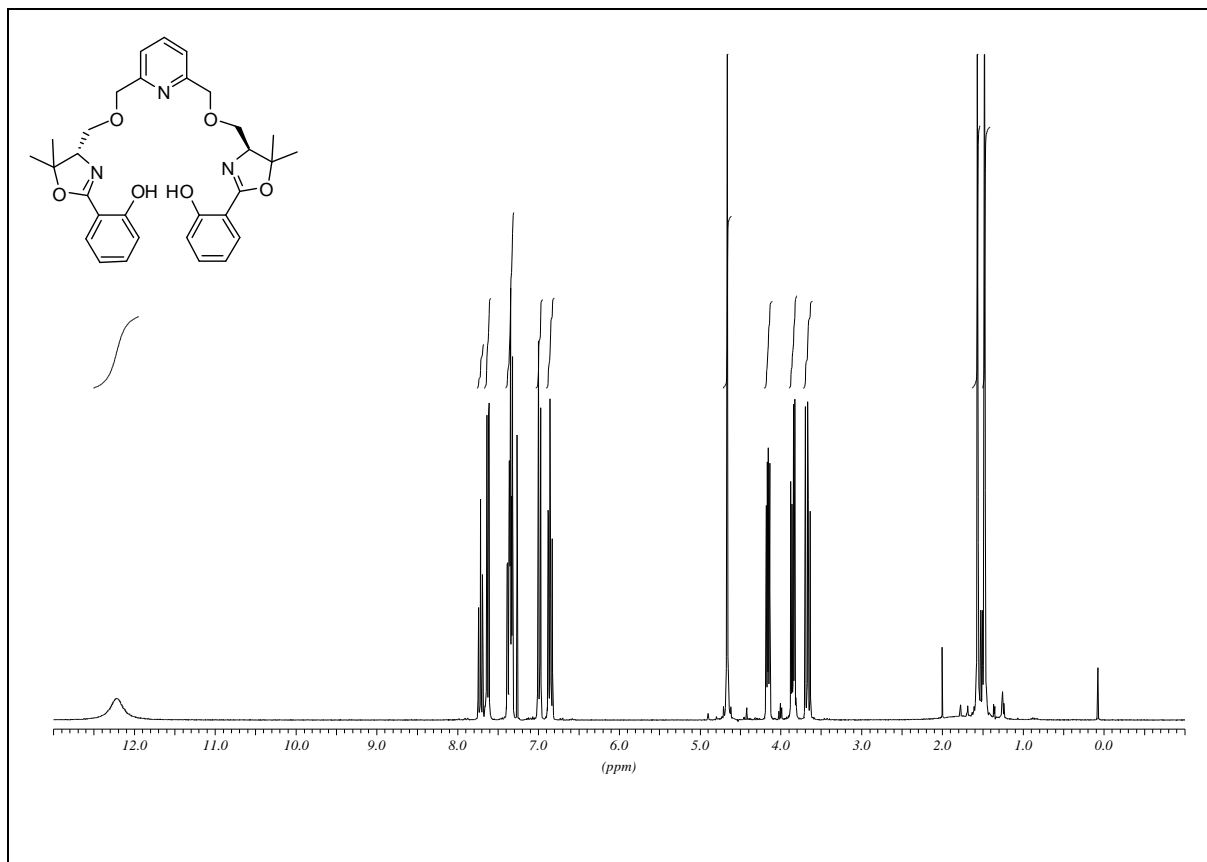


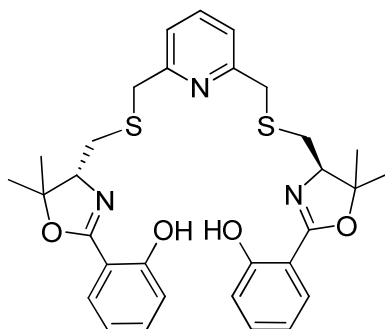
2,2'-(4*S*,4'*S*)-4,4'-(pyridine-2,6-diylbis(methylene))bis(oxy)bis(methylene)bis(5,5-dimethyl-4,5-dihydrooxazole-4,2-diyl)diphenol (2)

Under a N₂ atmosphere, (*S*)-2-(4-(hydroxymethyl)-5,5-dimethyl-4,5-dihydrooxazol-2-yl)-phenol **9** (300 mg, 1.36 mmol, 2.2 equiv.) was dissolved in dry DMF (15 mL) and cooled to 0 °C. NaH (60% suspension in mineral oil) (102 mg, 2.54 mmol, 4.1 equiv.) was added in portions and the mixture was stirred for 30 min. 2,6-bis(chloromethyl)pyridine **25** (109 mg, 0.62 mmol, 1.0 equiv.) was added as a solid and the ice-bath was removed. Stirring was continued at 70 °C for 72 h. DMF was evaporated, water (30 mL) and CHCl₃ (40 mL) were added and the layers were separated. The aqueous layer was extracted with CHCl₃ (5 x 40 mL) and the organic layer was dried (Na₂SO₄). After removal of the solvent in vacuo, the residue was purified by flash column chromatography (SiO₂, hexanes/EtOAc 2:1 to EtOAc to EtOAc/MeOH 1:4) and recrystallized from MeCN to yield the product as colourless solid (139 mg, 0.25 mmol, 40%).

R_f 0.49 (hexanes/EtOAc 2:1); m.p. 123 °C; $[\alpha]_D^{20} = -29.03$ (c = 1.03, CHCl₃); ¹H NMR (300 MHz, CDCl₃): δ 12.2 (bs, OH, 2H), 7.75-7.68 (m, CH_a, 1H), 7.65-7.59 (m, CH_a, 2H), 7.39-7.30 (m, CH_a, 4H), 7.02-6.95 (m, CH_a, 2H), 6.89-6.81 (m, CH_a, 2H), 4.66 (s, O-CH₂-C_a, 4 H), 4.18 (dd, *J* = 8.4, 4.8 Hz, O-CH₂-CH, 2H), 3.88 (dd, *J* = 9.9, 4.7 Hz, O-CH₂-CH, 2H), 3.70 (dd, *J* = 9.7, 8.4 Hz, CH, 2H), 1.57 (s, CH₃, 6H), 1.48 (s, CH₃, 6H); ¹³C NMR (75.5 MHz, CDCl₃): δ 165.1 (C_q), 160.0 (C_q), 157.6 (C_q), 137.4 (C_a), 133.3 (C_a), 128.1 (C_a), 120.1 (C_a), 118.5 (C_a), 116.8 (C_a), 111.0 (C_q), 86.0 (C_q), 74.2 (CH₂), 72.0 (CH), 70.2 (CH₂), 28.8 (CH₃), 21.4 (CH₃); IR (KBr): $\tilde{\nu}$ 2980, 2871, 1634, 1611, 1488, 1458, 1363, 1331, 1306, 1257, 1236, 1143, 1102, 1069, 1058, 1037, 933, 849, 749 cm⁻¹; MS (EI, 70 eV): *m/z* (%) = 121.0 (60, [C₇H₅O₂⁺]), 341.1 (100, [C₁₉H₂₁N₂O₄⁺]), 545.2 (22, [M⁺]); HRMS (EI, 70 eV): calcd for C₃₁H₃₅N₃O₆ [M⁺] 545.2526, found 545.2513.

2,2'-(4S,4'S)-4,4'-(pyridine-2,6-diylbis(methylene))bis(oxy)bis(methylene)bis(5,5-dimethyl-4,5-dihydrooxazole-4,2-diyl)diphenol (2)



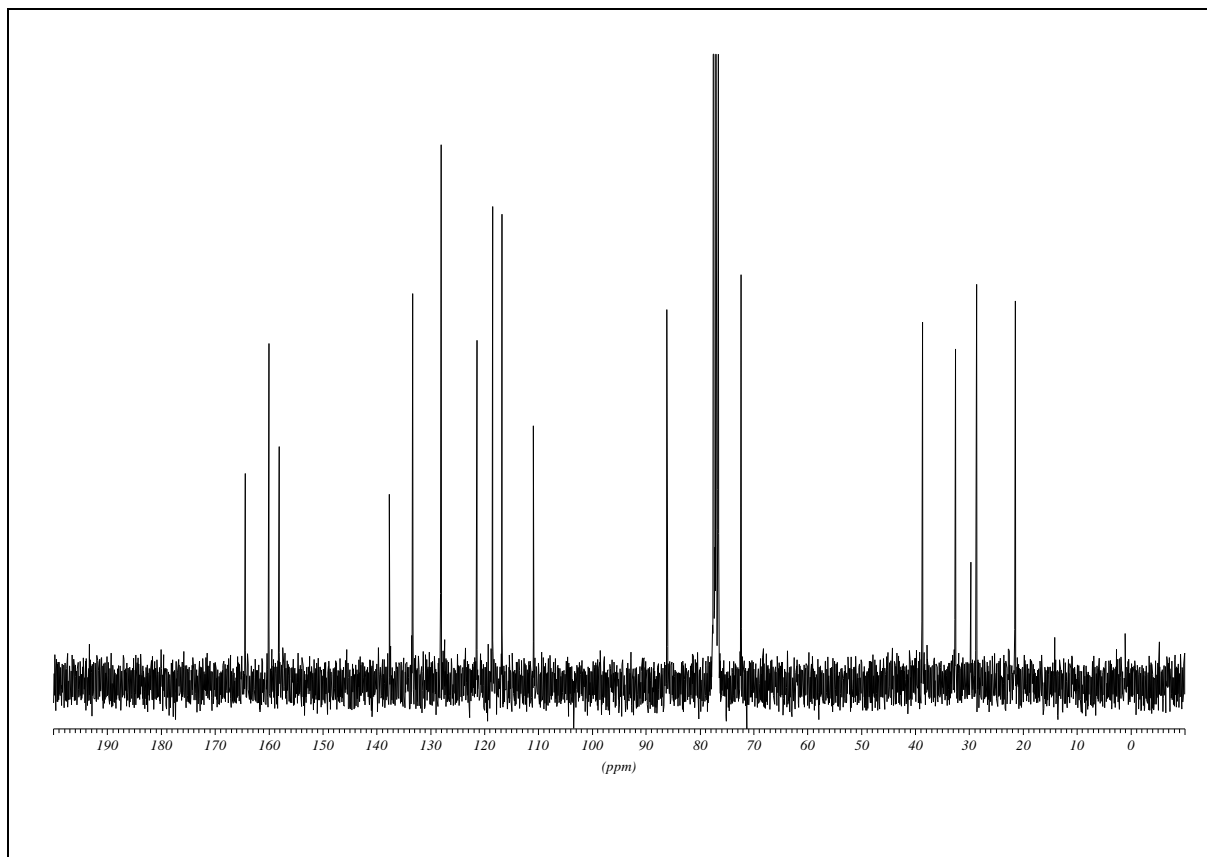
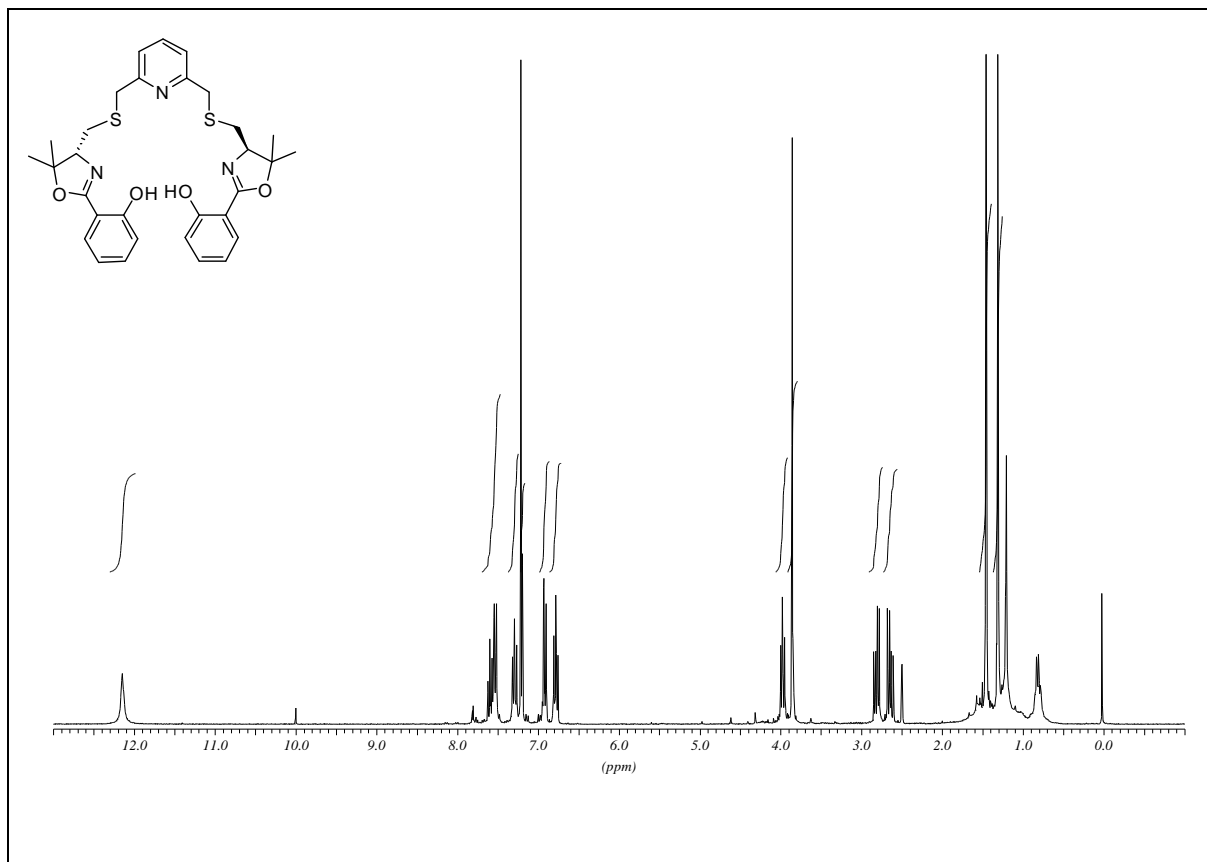


2,2'-(4*S*,4'*S*)-4,4'-(pyridine-2,6-diylbis(methylene))bis(sulfaneyl)bis(methylene)bis(5,5-dimethyl-4,5-dihydrooxazole-4,2-diyl)diphenol (5)

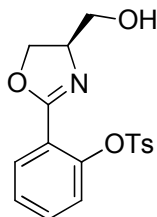
NaH (60% suspension in mineral oil) (46 mg, 1.15 mmol, 2.5 equiv.) was suspended in dry DMF (5 mL) under N₂ and cooled to 0 °C. 2,6-bis(mercaptomethyl)pyridine **27** (79 mg, 0.46 mmol, 1.0 equiv.) was added dropwise as a solution in dry DMF (3 mL) and the mixture was stirred until the evolution of hydrogen had ceased. (*R*)-2-(4-(bromomethyl)-5,5-dimethyl-4,5-dihydrooxazol-2-yl)phenol **30** (287 mg, 1.01 mmol, 2.2 equiv.) was dissolved in dry DMF (3 mL) and also added dropwise. The ice-bath was removed and stirring was continued at 75 °C for 90 h. DMF was evaporated, water (30 mL) and CHCl₃ (40 mL) were added and the layers were separated. The aqueous layer was extracted with CHCl₃ (4 x 20 mL) and the combined organic layers were dried (Na₂SO₄). After removal of the solvent in vacuo, the residue was purified by flash column chromatography (SiO₂, hexanes/EtOAc 2:1) to yield the product as red oil (205 mg, 0.36 mmol, 78%).

R_f 0.50 (hexanes/EtOAc 2:1); $[\alpha]_D^{20} = -3.47$ (*c* = 1.44, CHCl₃); ¹H NMR (300 MHz, CDCl₃): δ 12.15 (bs, OH, 2H), 7.67-7.50 (m, CH_a, 3H), 7.38-7.30 (m, CH_a, 2H), 7.28-7.33 (m, CH_a, 2H), 7.01-6.93 (m, CH_a, 2H), 6.88-6.78 (m, CH_a, 2H), 4.05 (dd, *J* = 8.0, 6.6 Hz, CH, 2H), 3.90 (s, S-CH₂-C_a, 4H), 2.87 (dd, *J* = 13.3, 6.5 Hz, S-CH₂-CH, 2H), 2.72 (dd, *J* = 13.2, 8.0 Hz, S-CH₂-CH, 2H), 1.50 (s, CH₃, 6H), 1.36 (s, CH₃, 6H); ¹³C NMR (75.5 MHz, CDCl₃): δ 164.4 (C_q), 160.0 (C_q), 158.2 (C_q), 137.6 (C_a), 133.3 (C_a), 128.1 (C_a), 121.4 (C_a), 118.5 (C_a), 116.8 (C_a), 110.9 (C_q), 86.1 (C_q), 72.4 (CH), 38.7 (CH₂), 32.6 (CH₂), 28.7 (CH₃), 21.5 (CH₃); IR (film): $\tilde{\nu}$ 3379, 2927, 1739, 1638, 1615, 1590, 1491, 1453, 1364, 1311, 1259, 1236, 1153, 1124, 755, cm⁻¹; MS (EI, 70 eV): *m/z* (%) = 204.2 (100, [C₁₂H₁₄NO₂⁺]), 374.3 (83, [C₁₉H₂₂N₂O₂S₂⁺]), 577.4 (30, [MH⁺]); HRMS (LSI, MeOH/Glycerin): calcd for C₃₁H₃₅N₃O₄S₂ [M⁺] 577.2069, found 577.2068.

2,2'-(4*S*,4'*S*)-4,4'-(pyridine-2,6-diylbis(methylene))bis(sulfanediyl)bis(methylene)bis(5,5-dimethyl-4,5-dihydrooxazole-4,2-diyl)diphenol (5)



F.5 Precursor for Oxazoline and Bis(oxazoline) Ligands

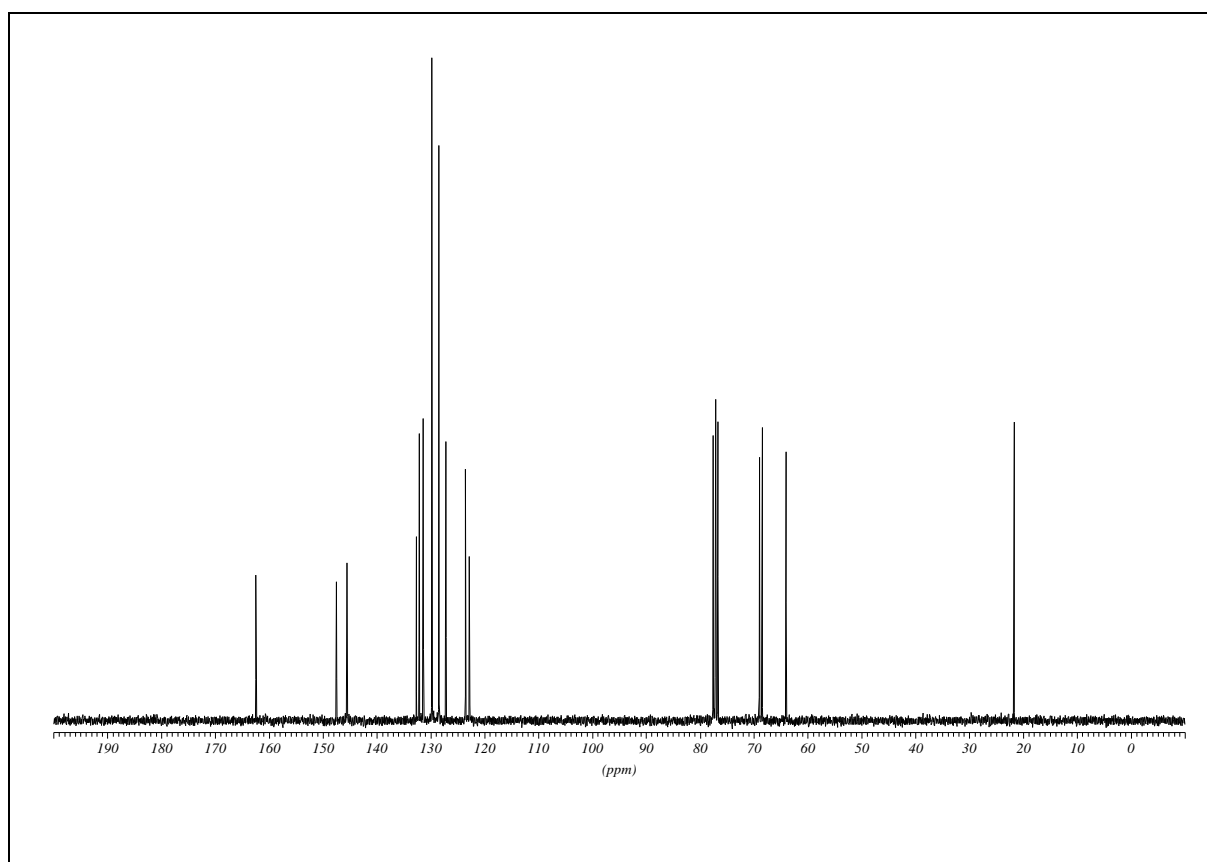
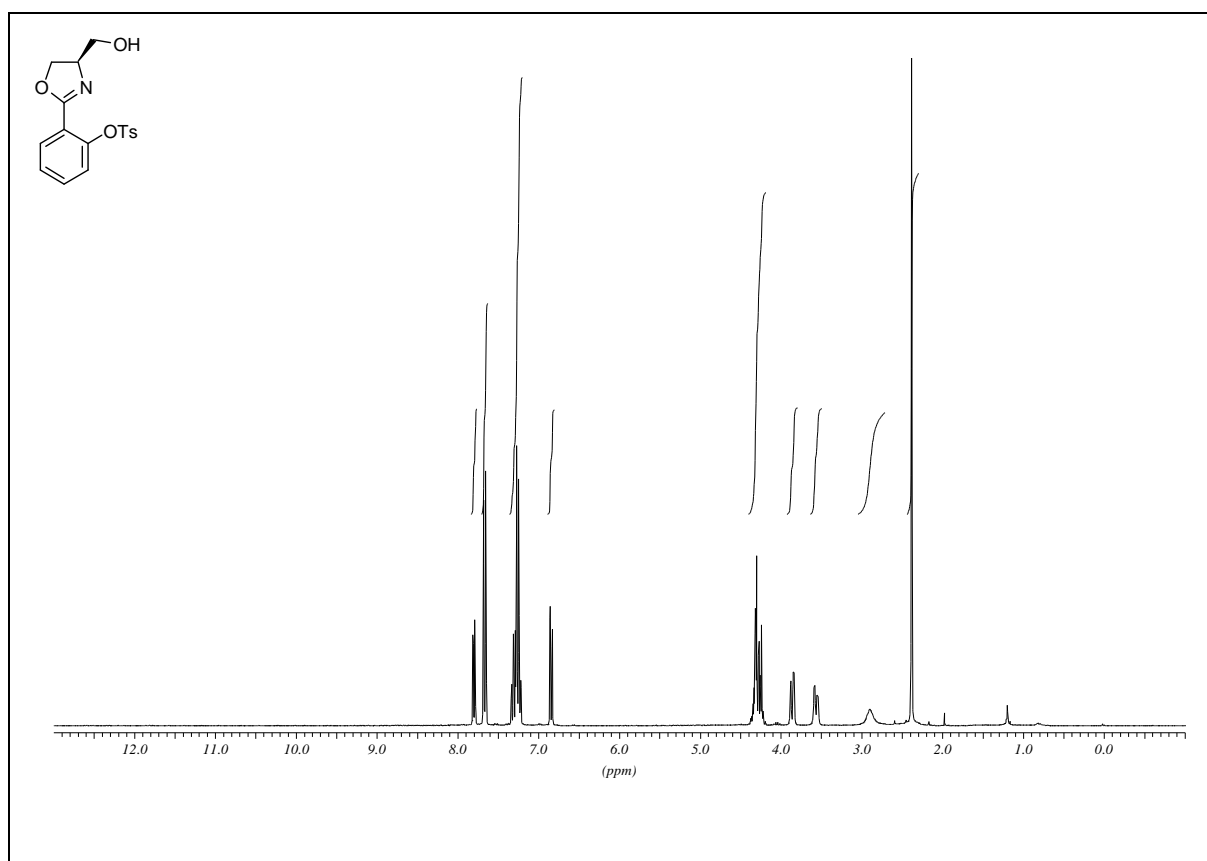


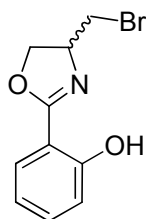
(S)-2-(2-(hydroxymethyl)-4,5-dihydrooxazol-4-yl)methyl-4-methylbenzenesulfonate (29b)

(*R*)-2-(4-(hydroxymethyl)-4,5-dihydrooxazol-2-yl)phenol **7a** (100 mg, 0.518 mmol, 1.0 equiv.) was dissolved in dry CH₂Cl₂ (3 mL) under nitrogen, dry NEt₃ (182 μ L, 131 mg, 1.294 mmol, 2.5 equiv.) was added and cooled to 0 °C. Fresh recrystallized tosyl chloride (109 mg, 0.569 mmol, 1.1 equiv.) was added in one portion and the mixture was stirred for 20 h at rt. The reaction mixture was washed with H₂O (1 mL) and then with sat. aqueous NaHCO₃ (1 mL). All combined organic layers were dried (Na₂SO₄). The solvent was evaporated under reduced pressure, and the crude product was purified by column chromatography (SiO₂, hexanes/EtOAc 1:1 to EtOAc) to afford the product as colourless solid (120 mg, 0.346 mmol, 67%).

R_f 0.35 (hexanes/EtOAc 1:1); m.p. 108 °C; $[\alpha]_D^{20} = +118.0$ ($c = 1.00$, CHCl₃); ¹H NMR (300 MHz, CDCl₃): δ 7.83-7.76 (m, CH_a, 1H), 7.71-7.62 (m, CH_a, 2H), 7.35-7.20 (m, CH_a, 4H), 6.88-6.81 (m, CH_a, 1H), 4.39-4.19 (m, CH/O_{Ts}-CH₂-CH, 3H), 3.86 (dd, $J = 11.5, 2.7$ Hz, O_{oxa}-CH₂-CH, 1H), 3.57 (dd, $J = 11.3, 2.7$ Hz, O_{oxa}-CH₂-CH, 1H), 2.90 (bs, OH, 1H), 2.38 (s, CH₃, 3H); ¹³C NMR (75.5 MHz, CDCl₃): δ 162.5 (C_q), 147.5 (C_q), 145.5 (C_q), 132.7 (C_q), 132.2 (C_a), 131.4 (C_a), 129.8 (C_a), 128.5 (C_a), 127.2 (C_a), 123.6 (C_a), 122.8 (C_q), 69.0 (CH₂), 68.5 (CH), 64.1 (CH₂), 21.7 (CH₃); IR (KBr): $\tilde{\nu}$ 2899, 1647, 1597, 1448, 1342, 1293, 1170, 1095, 1038, 962, 850, 815, 777, 729, 613, 562 cm⁻¹; MS (EI, 70 eV): m/z (%) = 91.1 (100, [C₇H₇⁺]), 316.1 (37, [C₁₇H₁₈NO₃S⁺]), 317.2 (39, [C₁₇H₁₉NO₃S⁺]), 347.2 (2, [M⁺]); HRMS (EI, 70 eV): calcd for C₁₇H₁₇NO₅S [M⁺] 347.0824, found 347.0824.

(S)-(2-(2-hydroxyphenyl)-4,5-dihydrooxazol-4-yl)methyl-4-methylbenzenesulfonate (29b)



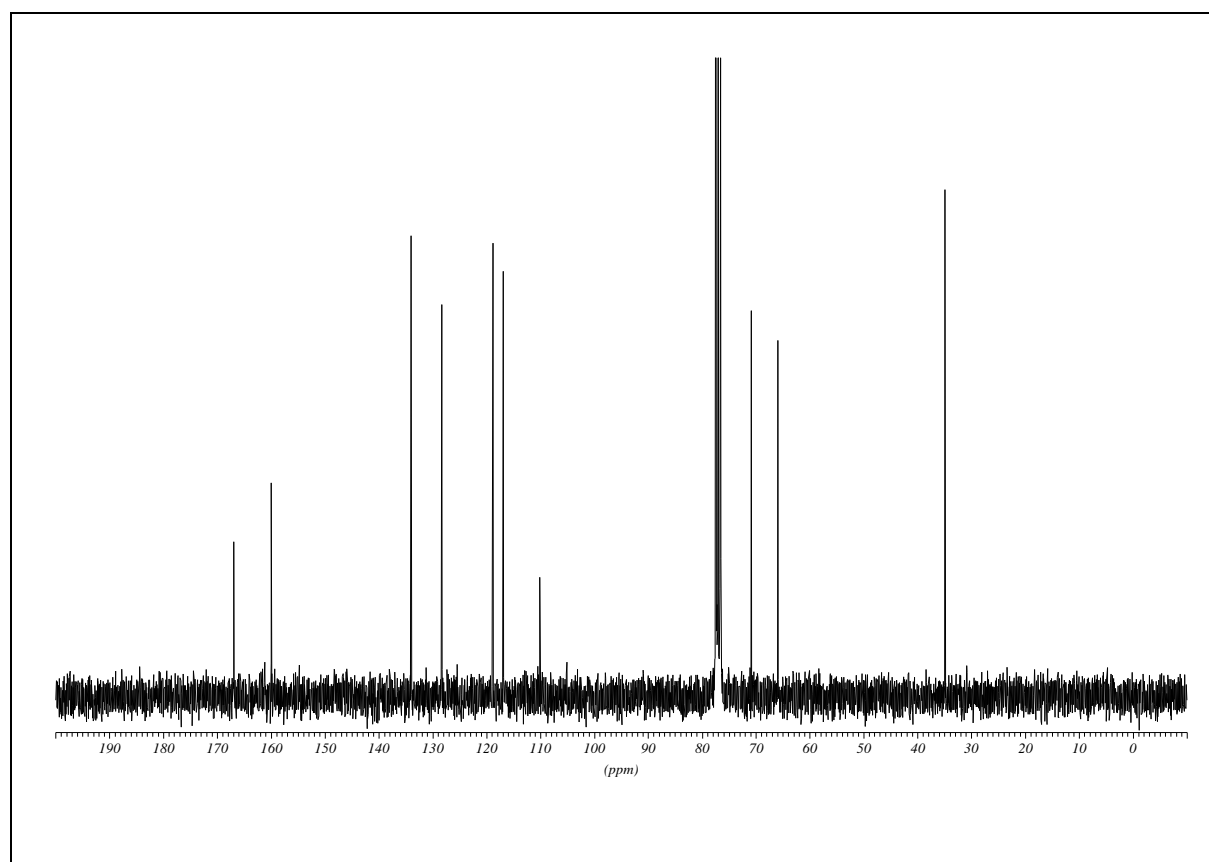
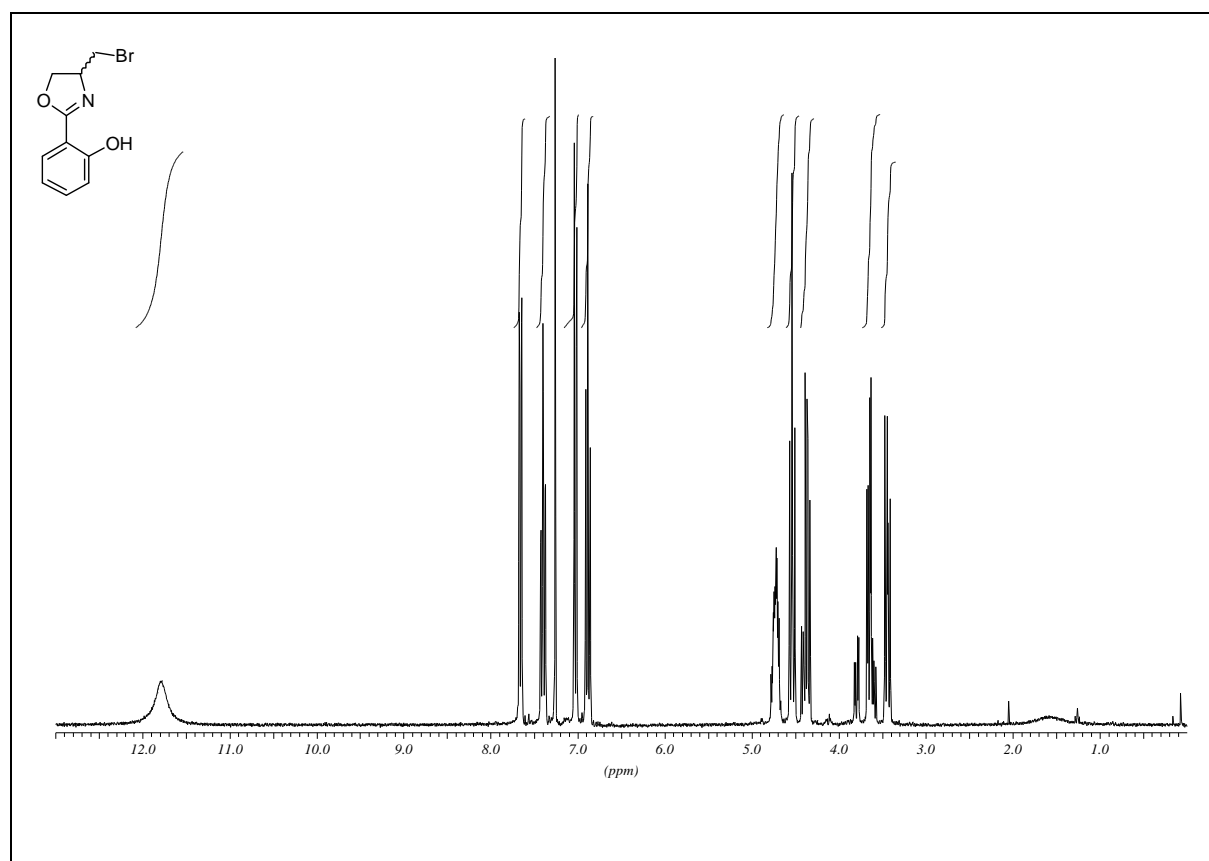


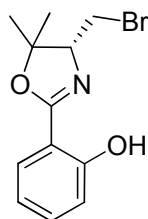
(±)-2-(4-(bromomethyl)-4,5-dihydrooxazol-2-yl)phenol (±)-(28)

(*R*)-2-(4-(hydroxymethyl)-4,5-dihydrooxazol-2-yl)phenol **7a** (0.502 g, 2.60 mmol, 1.0 equiv.) was dissolved in dry CH₂Cl₂ (20 mL) and cooled to 0 °C. CBr₄ (1.035 g, 3.12 mmol, 1.2 equiv.) was added in portions and the mixture was stirred for 15 min. Subsequently PPh₃ (0.818 g, 3.12 mmol, 1.2 equiv.) was added and the ice-bath was removed. Stirring was continued at rt for 20 h. Addition of brine (20 mL) followed and the layers were separated. The aqueous layer was extracted with CH₂Cl₂ (2 x 20 mL) and all combined organic layers were dried (Na₂SO₄). The solvent was evaporated under reduced pressure, and the crude product was purified by column chromatography (SiO₂, hexanes/EtOAc 4:1 to EtOAc) to afford the product as slightly pink solid in racemic form (0.447 g, 1.75 mmol, 67%).

R_f 0.73 (hexanes/EtOAc 4:1); m.p. 98 °C; $[\alpha]_D^{20} = -2.40$ (c = 1.04, EtOH); ¹H NMR (300 MHz, CDCl₃): δ 11.7 (bs, OH, 1H), 7.68-7.63 (m, CH_a, 1H), 7.43-7.36 (m, CH_a, 1H), 7.05-7.00 (m, CH_a, 1H), 6.92-6.85 (m, CH_a, 1H), 4.79-4.68 (m, CH, 1H), 4.54 (dd, *J* = 9.1, 9.1 Hz, O-CH₂-CH, 1H), 4.36 (dd, *J* = 8.8, 6.9 Hz, O-CH₂-CH, 1H), 3.65 (dd, *J* = 10.2, 3.8 Hz, Br-CH₂-CH, 1H), 3.44 (dd, *J* = 10.2, 7.7 Hz, Br-CH₂-CH, 1H); ¹³C NMR (75.5 MHz, CDCl₃): δ 167.0 (C_q), 160.0 (C_q), 134.0 (C_a), 128.3 (C_a), 118.9 (C_a), 116.9 (C_a), 110.1 (C_q), 70.9 (CH₂), 66.0 (CH), 34.9 (CH₂); IR (KBr): $\tilde{\nu}$ 2904, 1635, 1492, 1425, 1372, 1306, 1259, 1160, 1130, 1072, 1029, 964, 796, 757, 602 cm⁻¹; MS (CI, NH₃): *m/z* (%) = 256.0 (100, [MH]⁺_(79Br)), 258.0 (95, [MH]⁺_(81Br)); elemental analysis calcd (%) for C₁₀H₁₀BrNO₂ (256.1): C 46.90, H 3.94, N 5.47, found: C 47.06, H 4.14, N 5.37.

(±)-2-(4-(bromomethyl)-4,5-dihydrooxazol-2-yl)phenol (±)-(28)



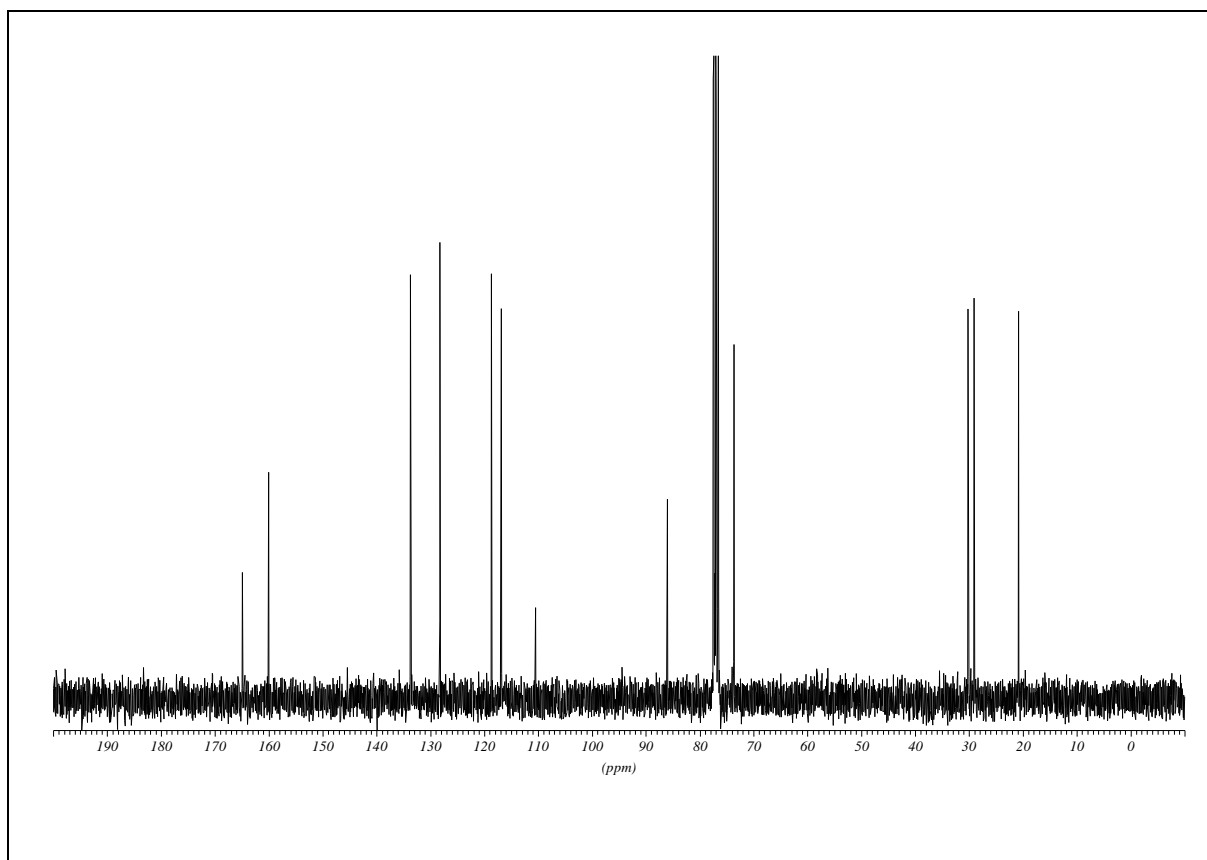
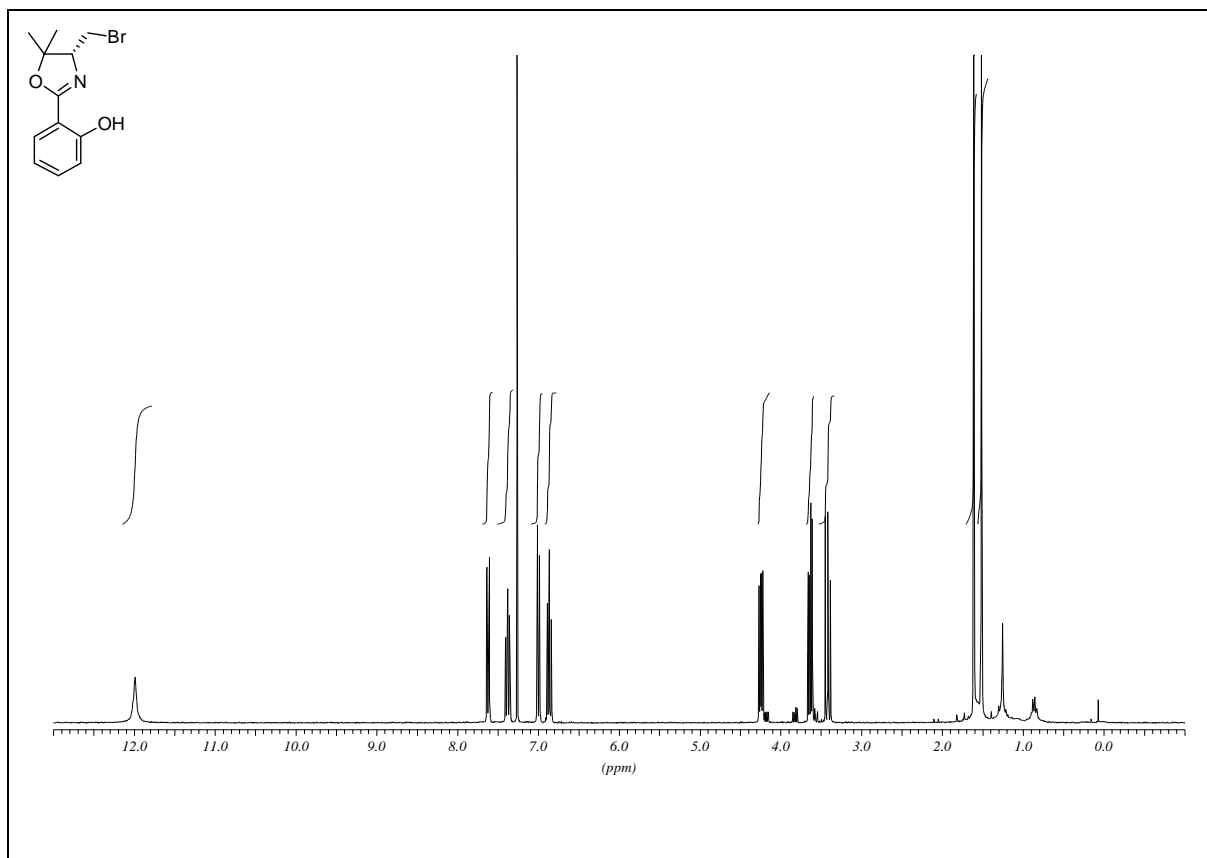


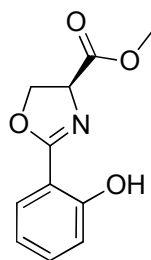
(*R*)-2-(4-(bromomethyl)-5,5-dimethyl-4,5-dihydrooxazol-2-yl)phenol (30)

(*S*)-2-(4-(hydroxymethyl)-5,5-dimethyl-4,5-dihydrooxazol-2-yl)phenol **9** (300 mg, 1.36 mmol, 1.0 equiv.) was dissolved in dry CH₂Cl₂ (15 mL) and cooled to 0 °C. CBr₄ (540 mg, 1.63 mmol, 1.2 equiv.) was added and the mixture was stirred for 10 min at 0 °C. After the addition of PPh₃ (428 mg, 1.63 mmol, 1.2 equiv.) the mixture was allowed to warm up to rt and stirred for 24 h. Addition of brine (15 mL) stopped the reaction and the layers were separated. The aqueous layer was extracted with CH₂Cl₂ (2 x 15 mL) and the combined organic layers were dried (Na₂SO₄). After removal of the solvent in vacuo, the residue was purified by column chromatography (SiO₂, hexanes/EtOAc 4:1) to yield the product as red oil (347.3 mg, 1.222 mmol, 90%).

R_f 0.82 (hexanes/EtOAc 4:1); $[\alpha]_D^{20} = -9.13$ ($c = 1.03$, EtOH); ¹H NMR (300 MHz, CDCl₃): δ 12.0 (bs, OH, 1H), 7.65-7.60 (m, CH_a, 1H), 7.41-7.34 (m, CH_a, 1H), 7.03-6.97 (m, CH_a, 1H), 6.90-6.82 (m, CH_a, 1H), 4.25 (dd, $J = 8.9, 5.1$ Hz, CH₂, 1H), 3.66 (dd, $J = 10.6, 5.1$ Hz, CH₂, 1H), 3.45 (dd, $J = 10.6, 8.9$ Hz, CH, 1H), 1.61 (s, CH₃, 3H), 1.52 (s, CH₃, 3H); ¹³C NMR (75.5 MHz, CDCl₃): δ 165.0 (C_q), 160.0 (C_q), 133.7 (C_a), 128.3 (C_a), 118.7 (C_a), 116.9 (C_a), 110.6 (C_q), 86.1 (C_q), 73.7 (CH), 30.2 (CH₂), 29.1 (CH₃), 20.9 (CH₃); IR (film): $\tilde{\nu}$ 2976, 2928, 1637, 1614, 1490, 1462, 1365, 1343, 1309, 1257, 1237, 1154, 1124, 1069, 1034, 960, 852, 756 cm⁻¹; MS (EI, 70 eV): m/z (%) = 92.1 (28, [CH₂Br⁺]), 121.1 (100, [C₇H₅O₂⁺]), 190.1 (22, [C₁₁H₁₂NO₂⁺]), 285.1 (23, [M⁺]); HRMS (EI, 70 eV): calcd for C₁₂H₁₄NO₂Br [M⁺] 283.0208, found 283.0203.

(R)-2-(4-(bromomethyl)-5,5-dimethyl-4,5-dihydrooxazol-2-yl)phenol (30)



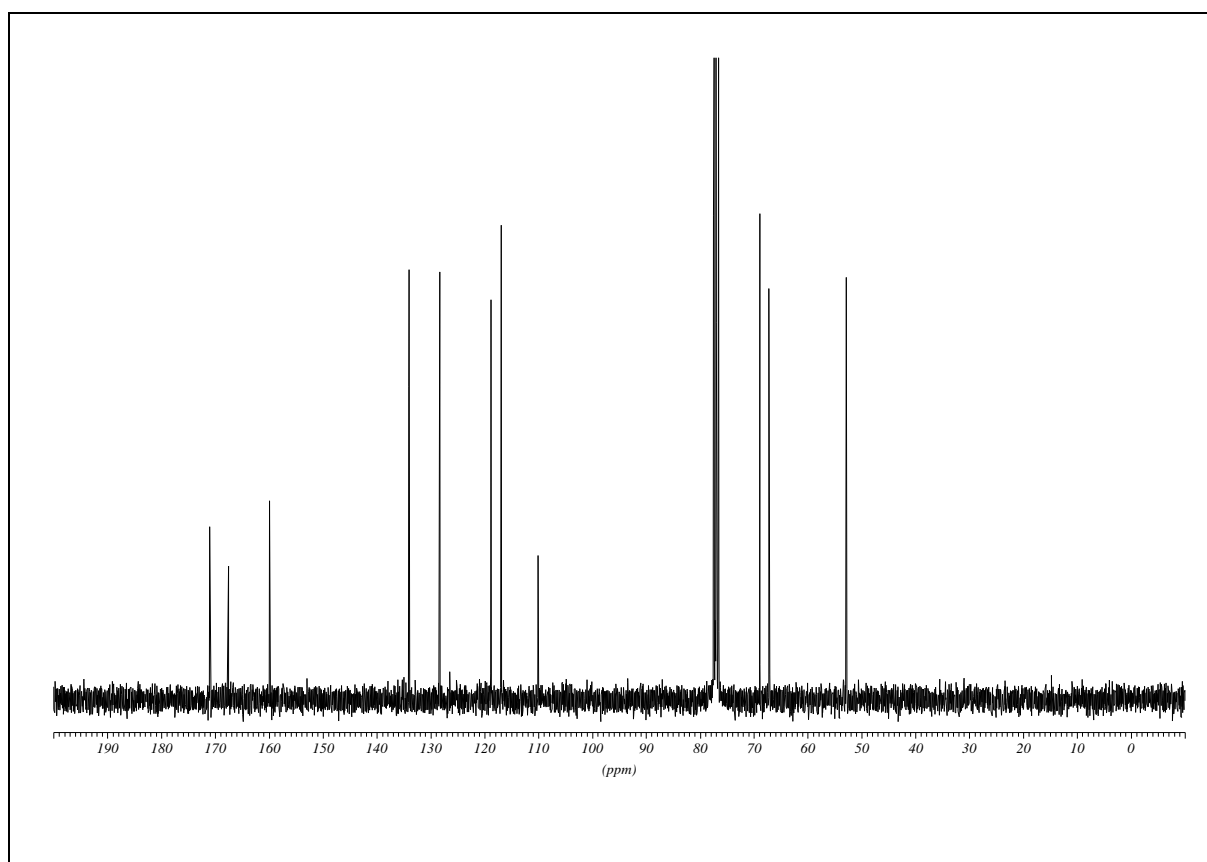
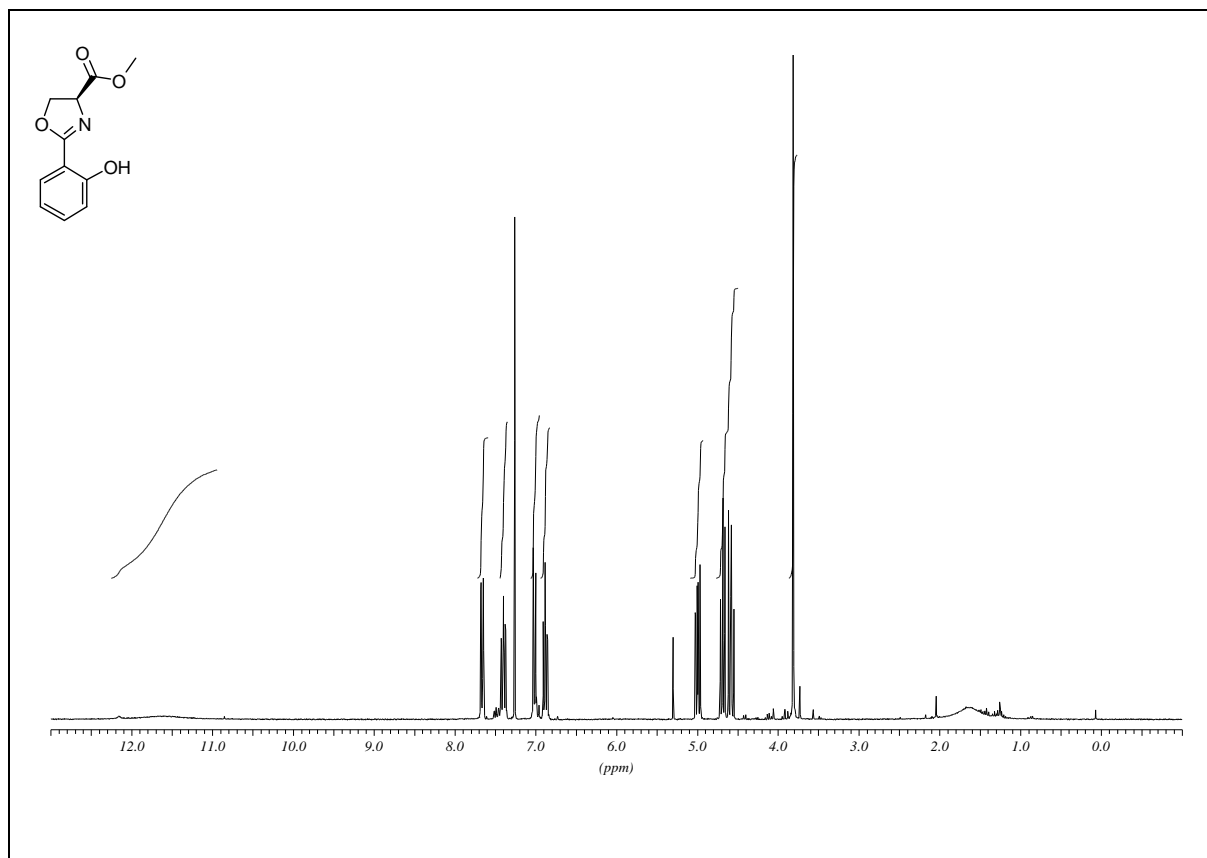


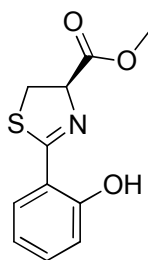
(S)-methyl-2-(2-hydroxyphenyl)-4,5-dihydrooxazole-4-carboxylate (16a)

Ethyl-2-hydroxybenzimidate **14** (33.43 g, 202.6 mmol, 1.0 equiv.) was dissolved in dry $\text{C}_2\text{H}_4\text{Cl}_2$ (300 mL) under N_2 and (S)-methyl-2-amino-3-hydroxypropanoate hydrochloride **15** (38.31 g, 243.1 mmol, 1.2 equiv.) was added to the solution. The reaction mixture was stirred under reflux for 60 h. After coming to rt the mixture was filtered and concentrated. Addition of Et_2O (100 mL), storing at 4 °C for some hours and a final filtration purified the product and afford a gold-brown oil (40.19 g, 181.7 mmol, 90%).

R_f 0.92 (EtOAc); $[\alpha]_D^{20} = +62.49$ ($c = 1.13$, EtOH); ^1H NMR (300 MHz, CDCl_3): δ 11.6 (bs, OH, 1H), 7.70-7.63 (m, CH_a , 1H), 7.44-7.35 (m, CH_a , 1H), 7.05-6.99 (m, CH_a , 1H), 6.92-6.84 (m, CH_a , 1H), 5.02 (dd, $J = 10.6, 7.6$ Hz, CH, 1H), 4.71 (dd, $J = 8.8, 7.4$ Hz, CH_2 , 1H), 4.61 (dd, $J = 10.4, 8.8$ Hz, CH_2 , 1H), 3.81 (s, CH_3 , 3H); ^{13}C NMR (75.5 MHz, CDCl_3): δ 171.0 (C_q), 167.6 (C_q), 159.9 (C_q), 134.0 (C_a), 128.4 (C_a), 118.9 (C_a), 117.0 (C_a), 110.1 (C_q), 68.9 (CH_2), 67.2 (CH), 52.9 (CH_3); IR (film): $\tilde{\nu}$ 2955, 1746, 1637, 1615, 1491, 1437, 1367, 1307, 1260, 1212, 1156, 1131, 1078, 968, 945, 830, 757 cm^{-1} ; MS (EI, 70 eV): m/z (%) = 162.0 (100, $[\text{C}_9\text{H}_8\text{NO}_2^+]$), 221.1 (57, $[\text{M}^+]$); HRMS (EI, 70 eV): calcd for $\text{C}_{11}\text{H}_{11}\text{NO}_4$ $[\text{M}^+]$ 221.0688, found 221.0689.

(S)-methyl-2-(2-hydroxyphenyl)-4,5-dihydrooxazole-4-carboxylate (16a)



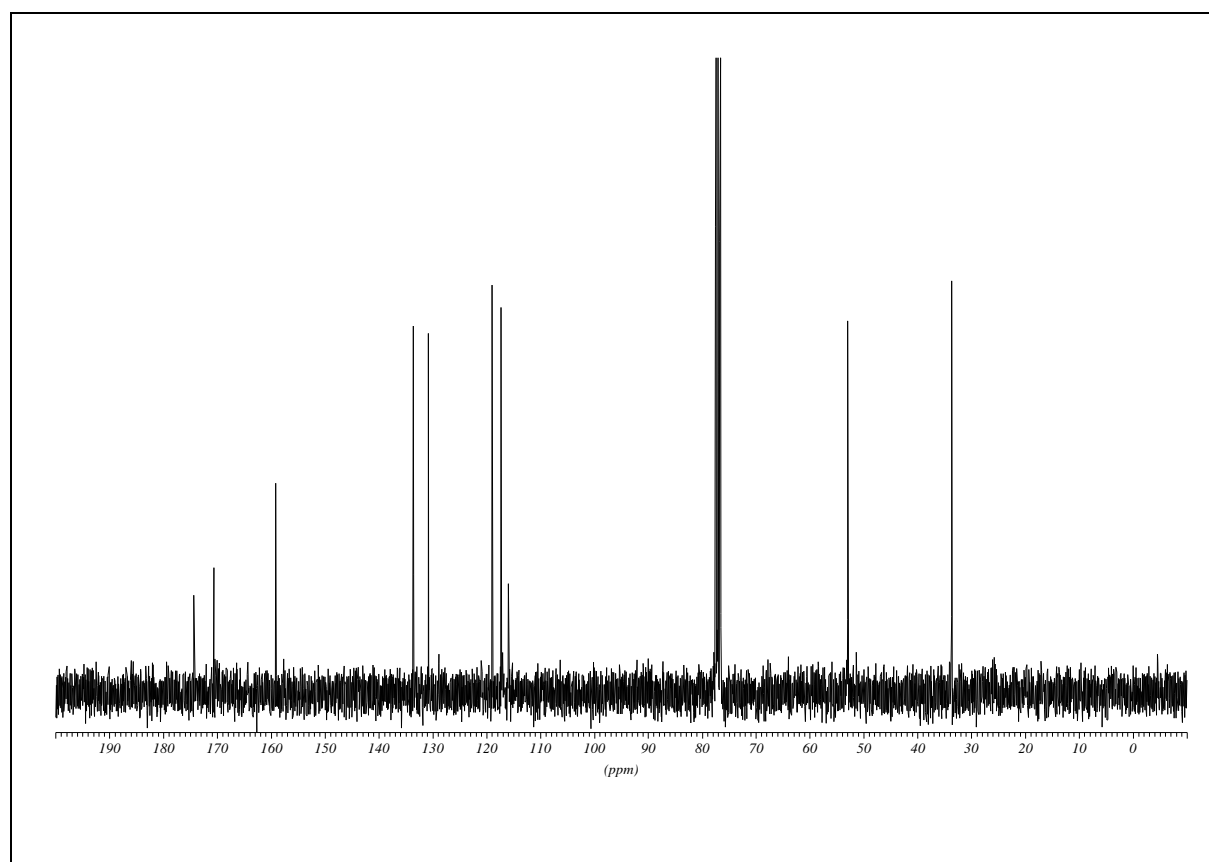
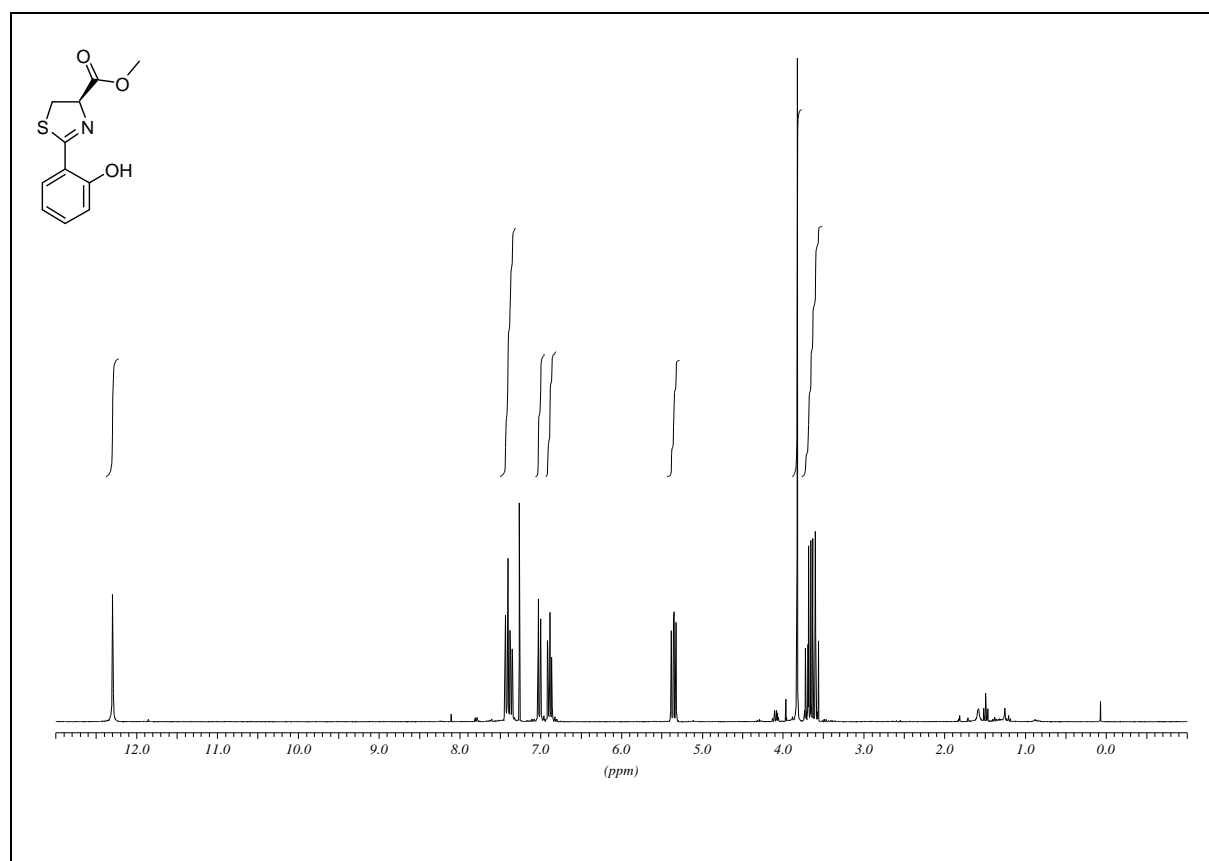


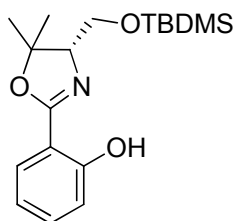
(R)-methyl-2-(2-hydroxyphenyl)-4,5-dihydrothiazole-4-carboxylate (21)

Ethyl-2-hydroxybenzimidate **14** (1.90 g, 11.52 mmol, 1.0 equiv.) was dissolved in dry $\text{C}_2\text{H}_4\text{Cl}_2$ (60 mL) under N_2 and (R)-methyl-2-amino-3-mercaptopropanoate hydrochloride (2.96 g, 17.28 mmol, 1.5 equiv.) was added to the solution. The reaction mixture was stirred under reflux for 48 h. After coming to rt the mixture was filtered and concentrated. For the further purification a column chromatography (SiO_2 , hexanes/EtOAc 4:1) was done and was obtained as the product as yellow oil (431 mg, 1.82 mmol, 16%).

R_f 0.43 (hexanes/EtOAc 4:1); $[\alpha]_D^{20} = -11.86$ ($c = 1.02$, EtOH); ^1H NMR (300 MHz, CDCl_3): δ 12.3 (s, OH, 1H), 7.45-7.34 (m, CH_a , 2H), 7.04-6.99 (m, CH_a , 1H), 6.92-6.85 (m, CH_a , 1H), 5.38 (dd, $J = 9.3, 8.0$ Hz, CH , 1H), 3.82 (s, CH_3 , 3H), 3.72 (dd, $J = 11.4, 8.1$ Hz, CH_2 , 1H), 3.63 (dd, $J = 11.3, 9.3$ Hz, CH_2 , 1H), ^{13}C NMR (75.5 MHz, CDCl_3): δ 174.3 (C_q), 170.6 (C_q), 159.2 (C_q), 133.6 (C_a), 130.8 (C_a), 118.9 (C_a), 117.3 (C_a), 116.0 (C_q), 76.7 (CH), 52.9 (CH_3), 33.7 (CH_2); IR (film): $\tilde{\nu}$ 2952, 1743, 1621, 1593, 1566, 1489, 1435, 1404, 1295, 1254, 1221, 1060, 951, 821, 753, cm^{-1} ; MS (EI, 70 eV): m/z (%) = 178.0 (100, $[\text{C}_9\text{H}_8\text{NOS}^+]$), 237.1 (45, $[\text{M}^+]$); HRMS (EI, 70 eV): calcd for $\text{C}_{11}\text{H}_{11}\text{NSO}_3$ $[\text{M}^+]$ 237.0460, found 237.0460.

(R)-methyl-2-(2-hydroxyphenyl)-4,5-dihydrothiazole-4-carboxylate (21)



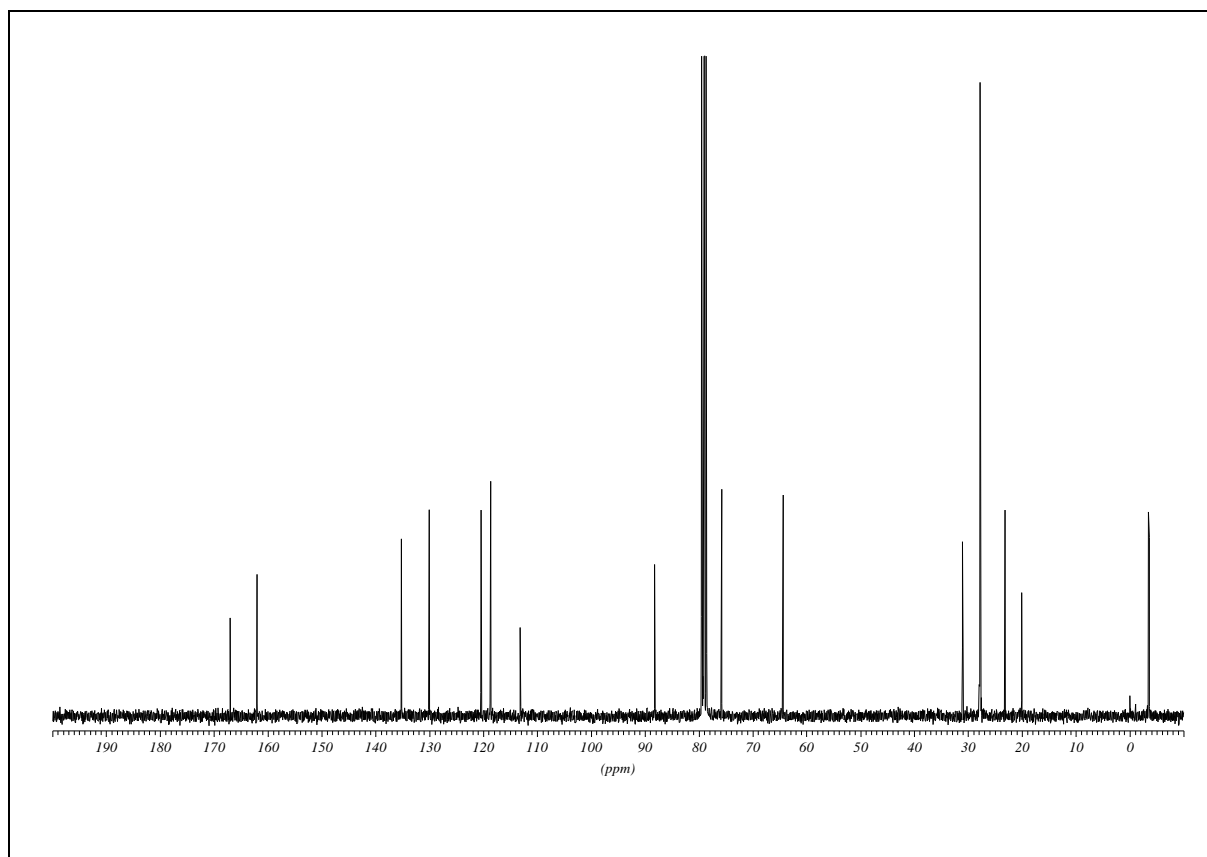
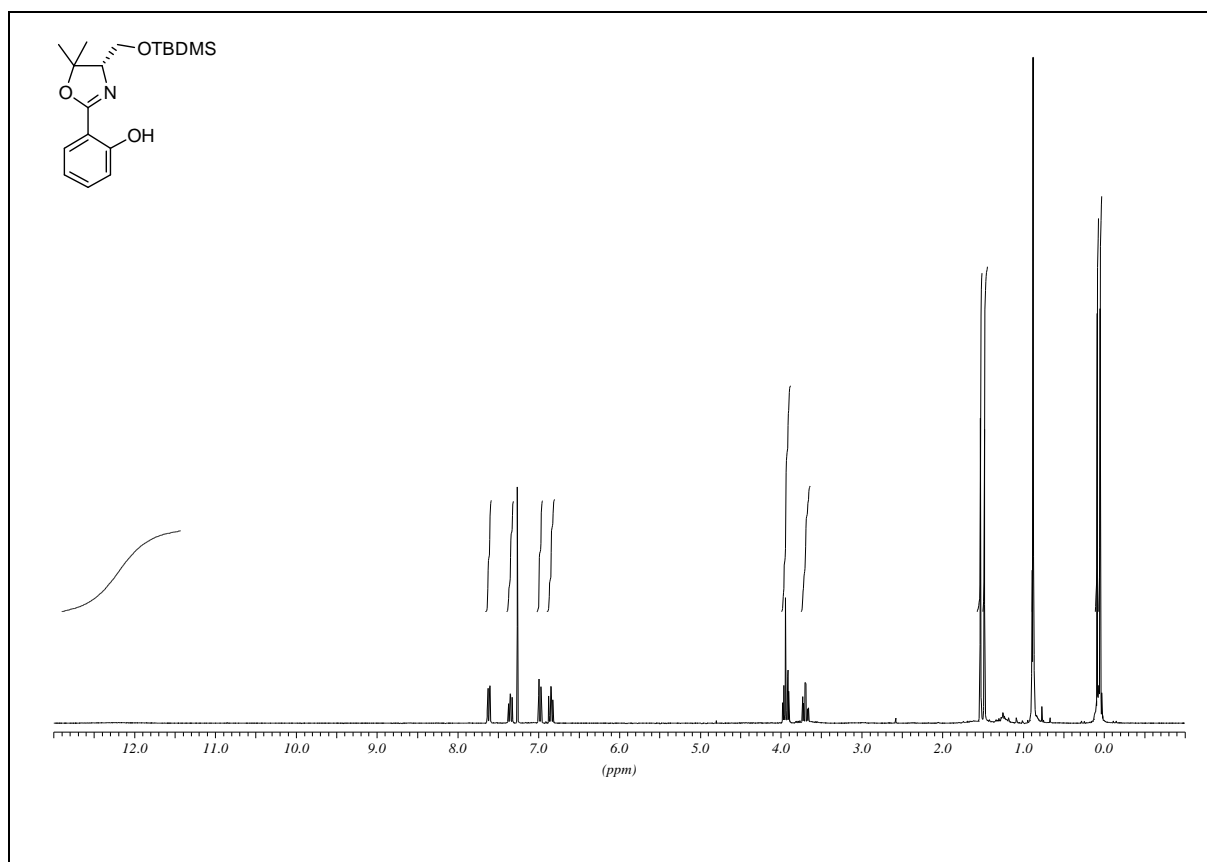


(S)-2-(4-((*tert*-butyldimethylsilyloxy)methyl)-5,5-dimethyl-4,5-dihydrooxazol-2-yl) phenol (19)

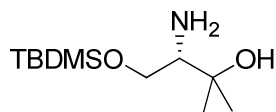
Under a N₂ atmosphere (*S*)-3-amino-4-(*tert*-butyldimethylsilyloxy)-2-methylbutan-2-ol **18** (6.35 g, 27.21 mmol, 1.5 equiv.) was dissolved in dry C₂H₄Cl₂ (50 mL) and ethyl-2-hydroxybenzimidate **14** (2.99 g, 18.14 mmol, 1.0 equiv.) was added in one portion. The mixture was refluxed for 4 d, filtered and evaporated. The crude product was purified by column chromatography (SiO₂, hexanes/EtOAc 4:1) to yield the product as red-brown oil (3.74 g, 11.15 mmol, 62%).

R_f 0.79 (hexanes/EtOAc 4:1); $[\alpha]_D^{20} = -9.80$ (c = 1.00, EtOH); ¹H NMR (300 MHz, CDCl₃): δ 12.2 (bs, OH, 1H), 7.65-7.59 (m, CH_a, 1H), 7.39-7.31 (m, CH_a, 1H), 7.01-6.95 (m, CH_a, 1H), 6.88-6.81 (m, CH_a, 1H), 3.99-3.89 (m, CH₂, 2H), 3.74-3.65 (m, CH, 1H), 1.53 (s, CH₃, 3H), 1.48 (s, CH₃, 3H), 0.88 (s, C-(CH₃)₃, 9H), 0.09 (s, Si-CH₃, 3H), 0.05 (s, Si-CH₃, 3H); ¹³C NMR (75.5 MHz, CDCl₃): δ 167.0 (C_q), 162.1 (C_q), 135.2 (C_a), 130.1 (C_a), 120.4 (C_a), 118.7 (C_a), 113.1 (C_q), 88.2 (C_q), 75.8 (CH), 64.4 (CH₂), 31.1 (CH₃), 27.9 (3 x CH₃), 23.2 (CH₃), 20.1 (C_q), -3.5 (CH₃), -3.6 (CH₃); IR (film): $\tilde{\nu}$ 2954, 2929, 2857, 1639, 1616, 1491, 1462, 1387, 1364, 1309, 1257, 1153, 1132, 1084, 837, 776, 755 cm⁻¹; MS (EI, 70 eV): *m/z* (%) = 278.2 (100, [C₁₄H₂₀NO₃Si⁺]), 335.2 (32, [M⁺]); HRMS (EI, 70 eV): calcd for C₁₈H₂₉NO₃Si [M⁺] 335.1917, found 335.1916.

(S)-2-(4-((*tert*-butyldimethylsilyloxy)methyl)-5,5-dimethyl-4,5-dihydrooxazol-2-yl)phenol
(19)



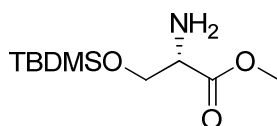
F.6 General precursor



(S)-3-amino-4-(*tert*-butyldimethylsilyloxy)-2-methylbutan-2-ol⁴⁸ (18)

(*S*)-methyl-2-amino-3-(*tert*-butyldimethylsilyloxy)propanoate **17** (7.05 g, 30.21 mmol, 1.0 equiv.) was dissolved in dry Et₂O (100 mL) and cooled under N₂ to 0 °C. A 3.0 M solution of MeMgBr (30.21 mL, 90.63 mmol, 3.0 equiv.) was added dropwise. The mixture was stirred for 2 h at 0 °C and was quenched with sat. NH₄Cl-solution (75 mL) and H₂O (25 mL). After separation, the aqueous layer was extracted with EtOAc (2 x 100 mL) and dried (Na₂SO₄). The crude product was obtained as a gold-brown gel (6.27 g, 26.86 mmol, 89%), which was pure enough to be used in further synthesis.

R_f 0.05 (hexanes/EtOAc 1:1; 0.1 % KMnO₄-stain); $[\alpha]_D^{20} = -10.00$ (c = 1.06, EtOH); ¹H NMR (300 MHz, CDCl₃): δ 3.78 (dd, *J* = 10.1, 4.3 Hz, CH₂, 1H), 3.68 (dd, *J* = 10.1, 6.6 Hz, CH₂, 1H), 2.72 (dd, *J* = 6.7, 4.2 Hz, CH, 1H), 2.31 (bs, NH₂, OH, 3H), 1.22 (s, CH₃, 3H), 1.19 (s, CH₃, 3H), 0.92 (s, C-(CH₃)₃, 9H), 0.10 (s, Si-(CH₃)₂, 6H); ¹³C NMR (75.5 MHz, CDCl₃): δ 71.3 (C_q), 65.0 (CH₂), 59.7 (CH), 27.8 (2 x CH₃), 25.7 (3 x CH₃), 18.2 (C_q), -5.5 (2 x CH₃); IR (film): $\tilde{\nu}$ 3373, 2955, 2929, 2884, 2857, 1675, 1579, 1467, 1386, 1362, 1256, 1090, 1005, 939, 836, 776, 756, 665 cm⁻¹; MS (CI): *m/z* (%) = 234.2 (100, [MH⁺]).

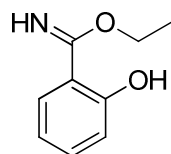


(S)-methyl-2-amino-3-(*tert*-butyldimethylsilyloxy)propanoate⁴⁸ (17)

(*S*)-methyl-2-amino-3-hydroxypropanoate hydrochloride **15** (10.5 g, 67.49 mmol, 1.0 equiv.) was suspended in CH₂Cl₂ (100 mL) at rt. NEt₃ (28.07 mL, 20.49 g, 202.5 mmol, 3.0 equiv.) and DMAP (0.825 g, 6.75 mmol, 0.1 equiv.) were added at once. Subsequently TBDMSCl (15.25 g, 101.2 mmol, 1.5 equiv.) was added slowly in portions. The mixture was stirred for

72 h at rt. H₂O (50 mL) was added to dissolve the precipitate and the layers were separated. The aqueous layer was extracted with CH₂Cl₂ (2 x 100 mL) and the combined organic layers were extracted with H₂O (2 x 100 mL) and finally dried (Na₂SO₄). The crude product was purified by distillation (100-135 °C, 0.1 mbar) to yield the product as colourless oil which immediately crystallized (11.25 g, 48.20 mmol, 71%).

$[\alpha]_D^{20} = +9.06$ (c = 1.07, EtOH); ¹H NMR (300 MHz, CDCl₃): δ 3.90 (dd, *J* = 4.4 Hz, CH₂, 1H), 3.79 (dd, *J* = 3.7, 9.7 Hz, CH₂, 1H), 3.69 (s, CH₃, 3H), 3.49 (t, *J* = 4.1 Hz CH, 1H), 1.82 (bs, NH₂, 2H), 0.83 (s, C(CH₃)₃, 9H), 0.01 (s, Si(CH₃)₂, 6H); ¹³C NMR (75.5 MHz, CDCl₃): δ 174.5 (C_q), 65.3 (CH₃), 56.5 (CH), 52.0 (CH₃), 25.7 (3 x CH₃), 18.2 (C_q), -5.4 (2 x CH₃); IR (film): $\tilde{\nu}$ 3387, 2953, 2930, 2885, 2857, 1745, 1600, 1463, 1436, 1361, 1256, 1105, 833, 777 cm⁻¹; MS (CI): *m/z* (%) = 116.0 (100, [C₆H₁₆Si⁺]), 176.0 (78, [M-C₄H₉⁺]), 234.2 (2, [MH⁺]).

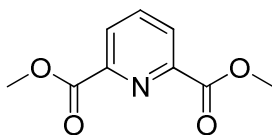


ethyl-2-hydroxybenzimidate (14)

2-Hydroxybenzonitrile **11** (25.0 g, 210.1 mmol, 1.0 equiv.) was dissolved in dry benzene (6 mL) and dry EtOH (14 mL), and the mixture was cooled to 0 °C. A stream of HCl gas was saturating the solution until more than 2.0 equiv. of HCl were in the flask. The product was given 14 days to precipitate at rt. The solid was suspended in CH₂Cl₂ (200 mL) and was completely dissolved by addition of saturated NaHCO₃-solution. A liquid-liquid extractor was used to transfer the product into the organic layer within 24 h. Subsequently the solvent was evaporated and afforded a slightly brown solid (33.43 g, 202.6 mmol, 96%), which was used without further purification.

m.p. 62 °C; ¹H NMR (300 MHz, CDCl₃): δ 14.00-13.50 (bs, OH, 1H), 7.83-7.77 (m, CH_a, 1H), 7.39-7.31 (m, CH_a, 1H), 7.01-6.95 (m, CH_a, 1H), 6.86-6.78 (m, CH_a, 1H), 4.08 (q, *J* = 7.0 Hz, CH₂, 2H), 1.49 (t, *J* = 7.0 Hz, CH₃, 3H); ¹³C NMR (75.5 MHz, CDCl₃): δ 165.7 (C_q), 161.1 (C_q), 133.2 (C_a), 127.8 (C_a), 118.0 (C_a), 117.3 (C_a), 114.5 (C_q), 60.1 (CH₂),

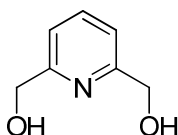
13.8 (CH₃); IR (KBr): $\tilde{\nu}$ 3307, 2982, 1639, 1598, 1500, 1465, 1408, 1375, 1352, 1269, 1153, 1093, 841, 756, 653 cm⁻¹; MS (EI, 70 eV): m/z (%) = 119.9 (100, [C₇H₅NO⁺]), 165.1 (38, [M⁺]); HRMS (EI, 70 eV): calcd for C₉H₁₁NO₂ [M⁺] 165.0790, found 165.0792.



dimethyl-pyridine-2,6-dicarboxylate (**23**)

2,6-pyridinedicarboxylic acid **22** (100.0 g, 598.4 mmol) was suspended in MeOH (700 mL) and treated cautiously with conc. H₂SO₄ (5 mL). The mixture was heated to reflux for 5 h. The product crystallized upon cooling to rt (3 days), then it was filtered and washed with MeOH (50 mL) and Et₂O (50 mL) and finally dried in vacuo to yield the product as colourless solid (105.6 g, 541.2 mmol, 90%).

¹H NMR (300 MHz, CDCl₃): δ 8.34 (d, J = 7.7 Hz, CH_a, 2H), 8.04 (t, J = 7.6 Hz, CH_a, 1H), 4.03 (s, CH₃, 6H).

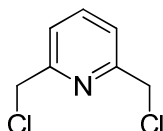


pyridine-2,6-diyl dimethanol (**24**)

Dimethyl-pyridine-2,6-dicarboxylate **23** (35.7 g, 183.0 mmol, 1.0 eq.) was dissolved in dry EtOH and cooled down at 0 °C. NaBH₄ (32.33 g, 854.6 mmol, 4.67 eq.) was added in portions and the mixture was stirred for 1 h at 0 °C. After removal of the ice bath the suspension stirred until exothermic reaction has stopped and in addition to that it stirred further 3 h at rt and 14 h under reflux. The solvent was evaporated and the residue was treated with acetone (120 mL) and refluxed for 1 h. Then the solvent was removed and sat. aqueous K₂CO₃-solution (120 mL) was added and refluxed again for 1 h. After a renew evaporation the suspension was treated with H₂O (500 mL) and CHCl₃ (500 mL) and filled in a liquid-liquid extractor to run

for 24 h. The obtained organic phase was evaporated and the product yields as colourless solid (24.47 g, 175.9 mmol, 96%).

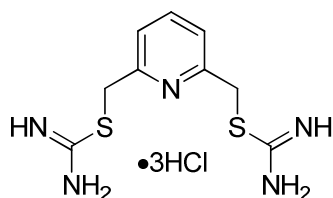
^1H NMR (300 MHz, DMSO- d_6): δ 7.78 (t, $J = 7.7$ Hz, CH_a , 1H), 7.31 (d, $J = 7.7$ Hz, CH_a , 2H), 5.36 (t, $J = 5.9$ Hz, OH, 2H), 4.52 (d, $J = 5.8$ Hz, CH_2 , 4H).



2,6-bis(chloromethyl)pyridine (25)

Pyridine-2,6-diylldimethanol **24** (22.24 g, 159.9 mmol, 1.0 eq.) was suspended in dry Et_2O (200 mL) and cooled down to 0 °C. SOCl_2 (25.52 mL, 41.85 g, 351.8 mmol, 2.2 eq.), diluted in Et_2O (10 mL), was slowly dropped into the mixture and stirred for further 1 h at 0 °C and 20 h at rt. The reaction mixture was filtered off, washed with Et_2O and dried in vacuo. The crude product was suspended in CH_2Cl_2 (200 mL) and sat. aqueous NaHCO_3 -solution (200 mL) was added in portion. After the development of gas has stopped, the phases were separated, the organic phase was extracted with CH_2Cl_2 (3 x 100 mL) and dried (Na_2SO_4). The product was obtained as colourless solid (25.38 g, 144.1 mmol, 90%).

^1H NMR (300 MHz, CDCl_3): δ 7.77 (t, $J = 7.8$ Hz, CH_a , 1H), 7.44 (d, $J = 7.7$ Hz, CH_a , 2H), 4.67 (s, CH_2 , 4H).

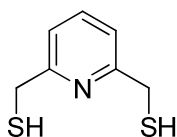


pyridine-2,6-diylbis(methylene)-dicarbamimidothioate-3-hydrochlorid (26)

2,6-bis(chloromethyl)pyridine **25** (22.41 g, 127.2 mmol, 1.0 eq.) was suspended in EtOH (325 mL) and thiourea (23.24 g, 305.3 mmol, 2.4 eq.) was added in portion. The mixture was

refluxed for 30 min and after cooling down to rt the precipitation was filtered off, washed with EtOH and Et₂O and dried in vacuo. The product was yielded as slightly brown solid (44.59 g, 122.2 mmol, 96%).

¹H NMR (300 MHz, D₂O): δ 7.76 (t, *J* = 7.8 Hz, CH_a, 1H), 7.34 (d, *J* = 8.0 Hz, CH_a, 2H), 4.40 (s, CH₂, 4H).



pyridine-2,6-diylbis(methanethiol) (**27**)

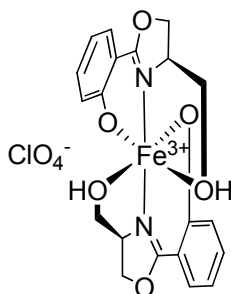
All steps were produced under nitrogen!

Pyridine-2,6-diylbis(methylene)-dicarbamimidothioate-3-hydrochlorid **26** (20.0 g, 54.8 mmol, 1.0 eq.) was dissolved in degassed H₂O (60 mL) and NaOH (12.1 g, 301.4 mmol, 5.5 eq.) was added at once. The reaction mixture was refluxed for 2 h. The solution was treated with degassed 2 N HCl until the value of the pH has reached 7. The neutral aqueous phase was extracted with degassed CHCl₃ (5 x 80 mL) and all organic phases were dried (Na₂SO₄). After evaporation the crude product was purified by distillation (0.1 mbar, 92 – 105 °C) to yield a colourless liquid (7.28 g, 42.5 mmol, 78%).

¹H NMR (300 MHz, CDCl₃): δ 7.63 (t, *J* = 7.7 Hz, CH_a, 1H), 7.21 (d, *J* = 7.7 Hz, CH_a, 2H), 3.82 (d, *J* = 8.0 Hz, CH₂, 4H), 2.01 (t, *J* = 8.1 Hz, OH, 2H).

F.7 Synthesized Complexes of Oxazoline Ligands

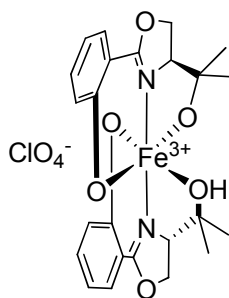
F.7.1 Iron Complexes



[Fe^{III}(7a)₂] • (ClO₄) • (HClO₄) • 4(H₂O) elemental analysis

Ligand **7a** (100 mg, 0.518 mmol, 2.0 eq.) and Fe(ClO₄)₂•6H₂O (94 mg, 0.259 mmol, 1.0 eq.) were dissolved separately in dry THF (each in 2 mL) and the ligand was transferred to the metal. The reaction mixture was stirred for 12 h at rt. The solvent was removed and the residue was dried in vacuo and stored at rt. The product was obtained as a dark purple solid (116 mg, 0.163 mmol, 63%). Recrystallization from acetonitrile / ethylacetate afforded purple needles which were suitable for X-Ray structure analysis.

MS (ESI, MeCN): m/z (%) = 193.9 (15, [LH⁺]), 440.0 (100, [L₂Fe³⁺-2H⁺]); elemental analysis calcd (%) for C₂₀H₂₉Cl₂FeN₂O₁₈ (711.0): C 33.73, H 4.10, N 3.93, found: C 33.94, H 3.98, N 3.76; IR (Diamond Single Reflection ATR System): $\tilde{\nu}$ 3409, 1608, 1587, 1542, 1507, 1474, 1441, 1398, 1329, 1316, 1247, 1080, 1062, 1030, 1001, 925, 853, 755, 618 cm⁻¹.

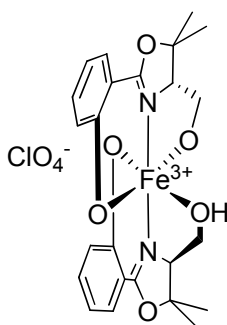


(proposed structure)

[Fe^{III}(8)₂] • (ClO₄) • (HClO₄) • 4(H₂O) • 2(THF) elemental analysis

Ligand **8** (100 mg, 0.452 mmol, 2.0 eq.) and Fe(ClO₄)₂•6H₂O (82 mg, 0.226 mmol, 1.0 eq.) were dissolved separately in dry THF (each in 4 mL) and the ligand was transferred to the metal. The reaction mixture was stirred over night at rt. The solvent was removed and the residue was dried in vacuo and stored at rt. The product was obtained as a dark purple solid (31 mg, 0.034 mmol, 15%).

MS (ESI, MeCN): m/z (%) = 222.0 (7, [LH⁺]), 496.2 (100, [L₂Fe³⁺-2H⁺]); elemental analysis calcd (%) for C₃₂H₅₃Cl₂FeN₂O₂₀ (911.2): C 42.12, H 5.85, N 3.07, found: C 41.87, H 5.79, N 2.93; IR (Diamond Single Reflection ATR System): $\tilde{\nu}$ 3322, 2979, 1612, 1543, 1472, 1439, 1391, 1326, 1246, 1085, 1031, 927, 851, 755, 666, 619 cm⁻¹.

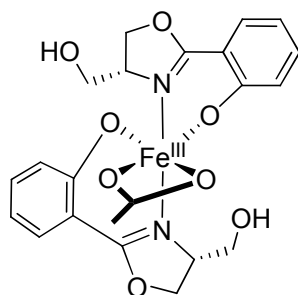


(proposed structure)

[Fe^{III}(9)₂] • (ClO₄) • (HClO₄) • 5(H₂O) • (THF) elemental analysis

Ligand **9** (100 mg, 0.452 mmol, 2.0 eq.) and Fe(ClO₄)₂•6H₂O (82 mg, 0.226 mmol, 1.0 eq.) were dissolved separately in dry THF (each in 2 mL) and the ligand was transferred to the metal. The reaction mixture was stirred over night at rt. The solvent was removed and the residue was dried in vacuo and stored at rt. The product was obtained as a dark purple solid (93 mg, 0.109 mmol, 48%).

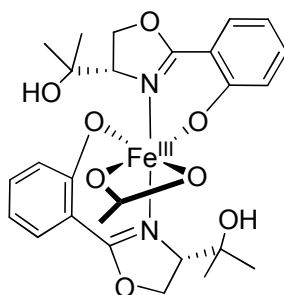
MS (ESI, MeCN): m/z (%) = 496.2 (100, [L₂Fe³⁺-2H⁺]); elemental analysis calcd (%) for C₂₈H₄₇Cl₂FeN₂O₂₀ (857.1): C 39.18, H 5.52, N 3.26, found: C 38.80, H 5.19, N 3.29; IR (Diamond Single Reflection ATR System): $\tilde{\nu}$ 3252, 2891, 1626, 1593, 1545, 1506, 1467, 1440, 1396, 1378, 1327, 1251, 1082, 1031, 925, 865, 754, 696, 619 cm⁻¹.



[Fe^{III}(7a)₂(OAc)] elemental analysis

Ligand **7a** (100 mg, 0.518 mmol, 2.0 eq.) and Fe(OAc)₂ (45 mg, 0.259 mmol, 1.0 eq.) were dissolved separately in DMA (each in 3 mL) and the ligand was transferred to the metal. The reaction mixture was stirred over night at rt. The solvent was removed, the residue was redissolved in Et₂O/THF/hexanes (1:1:5), filtered, dried in vacuo and stored at rt. The product was obtained as a dark orange-red solid (16 mg, 0.032 mmol, 12%). Recrystallization from THF / Et₂O afforded dark red needles which were suitable for X-Ray structure analysis.

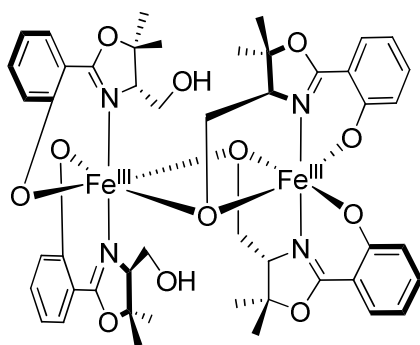
MS (ESI, MeCN): m/z (%) = 193.9 (23, [LH⁺]), 440.0 (100, [L₂Fe³⁺-2H⁺]); elemental analysis calcd (%) for C₂₂H₂₃FeN₂O₈ (499.1): C 52.92, H 4.64, N 5.61, found: C 53.35, H 5.06, N 6.14; IR (Diamond Single Reflection ATR System): $\tilde{\nu}$ 3342, 2932, 2880, 1606, 1584, 1547, 1471, 1441, 1390, 1328, 1243, 1156, 1076, 1030, 952, 848, 755, 688, 612 cm⁻¹.



[Fe^{III}(8)₂(OAc)] • (THF) elemental analysis

Ligand **8** (100 mg, 0.452 mmol, 2.0 eq.) and Fe(OAc)₂ (39 mg, 0.226 mmol, 1.0 eq.) were dissolved separately in DMA (each in 4 mL) and the ligand was transferred to the metal. The reaction mixture was stirred over night at rt. The solvent was removed and the residue was redissolved in Et₂O/THF (1:1), filtered, dried in vacuo and stored at rt. The product was obtained as a dark orange-red solid (126 mg, 0.201 mmol, 89%). Recrystallization from acetonitrile / ethylacetate afforded dark red needles which were suitable for X-Ray structure analysis.

MS (ESI, MeCN): m/z (%) = 222.0 (100, [LH⁺]), 496.2 (25, [L₂Fe³⁺-2H⁺]); elemental analysis calcd (%) for C₃₀H₃₉FeN₂O₉ (627.2): C 57.42, H 6.26, N 4.46, found: C 57.13, H 6.24, N 4.87; IR (Diamond Single Reflection ATR System): $\tilde{\nu}$ 3412, 2969, 2922, 1604, 1578, 1547, 1471, 1440, 1385, 1326, 1236, 1179, 1156, 1080, 1012, 942, 855, 808, 757, 689, 667, 623, 549 cm⁻¹.

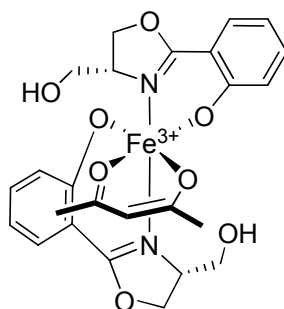


[Fe^{III}(9)₂]₂ crystal structure

[Fe^{III}(9)₂(OAc)] • (MeCN) • (H₂O) • (THF) elemental analysis

Ligand **9** (134 mg, 0.607 mmol, 2.0 eq.) and Fe(OAc)₂ (53 mg, 0.303 mmol, 1.0 eq.) were dissolved separately in DMA (each in 4 mL) and the ligand was transferred to the metal. The reaction mixture was stirred over night at rt. The solvent was removed and the residue was redissolved in Et₂O, filtered, dried in vacuo and stored at rt. The product was obtained as a dark orange-red solid (116 mg, 0.169 mmol, 56%). Recrystallization from acetonitrile / Et₂O afforded dark red needles which were suitable for X-Ray structure analysis.

MS (ESI, MeCN): *m/z* (%) = 222.0 (23, [LH⁺]), 496.2 (100, [L₂Fe³⁺-2H⁺]); elemental analysis calcd (%) for C₃₂H₄₄FeN₃O₁₀ (686.2): C 55.98, H 6.46, N 6.12, found: C 55.41, H 6.44, N 6.28; IR (Diamond Single Reflection ATR System): $\tilde{\nu}$ 3381, 2971, 2932, 1604, 1580, 1545, 1472, 1440, 1398, 1328, 1249, 1190, 1150, 1133, 1078, 1032, 955, 894, 869, 832, 755, 703, 688, 605 cm⁻¹.

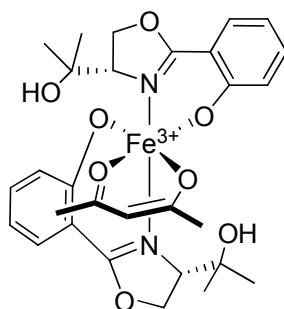


(proposed structure)

$[\text{Fe}^{\text{III}}(\mathbf{7a})_2(\text{acac})]$ elemental analysis

Ligand **7a** (100 mg, 0.518 mmol, 2.0 eq.) and $\text{Fe}(\text{acac})_3$ (92 mg, 0.259 mmol, 1.0 eq.) were dissolved separately in dry THF (each in 2 mL) and the ligand was transferred to the metal. The reaction mixture was stirred over night at rt. The solvent was removed and the residue was redissolved in Et_2O , filtered, dried in vacuo and stored at rt. The product was obtained as a blood-red solid (22 mg, 0.041 mmol, 16%).

MS (ESI, MeCN): m/z (%) = 193.9 (12, $[\text{LH}^+]$), 347.0 (53, $[\text{LFe}^{3+}-\text{H}^+(\text{acac})^-]$), 440.0 (100, $[\text{L}_2\text{Fe}^{3+}-2\text{H}^+]$); elemental analysis calcd (%) for $\text{C}_{25}\text{H}_{27}\text{FeN}_2\text{O}_8$ (539.1): C 55.67, H 5.05, N 5.19, found: C 55.85, H 5.26, N 4.69; IR (Diamond Single Reflection ATR System): $\tilde{\nu}$ 3351, 2936, 1607, 1582, 1549, 1523, 1480, 1442, 1389, 1373, 1327, 1242, 1152, 1075, 1034, 1020, 987, 966, 925, 861, 847, 758, 688, 665, 628, 555, 432 cm^{-1} .

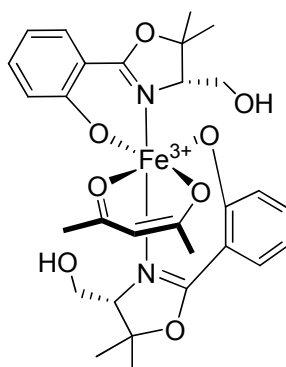


(proposed structure)

[Fe^{III}(8)₂(acac)] elemental analysis

Ligand **8** (100 mg, 0.452 mmol, 2.0 eq.) and Fe(acac)₃ (80 mg, 0.226 mmol, 1.0 eq.) were dissolved separately in dry THF (each in 2 mL) and the ligand was transferred to the metal. The reaction mixture was stirred over night at rt. The solvent was removed and the residue was redissolved in Et₂O/hexanes (1:5), filtered, dried in vacuo and stored at rt. The product was obtained as a blood-red solid (117 mg, 0.197 mmol, 87%).

MS (ESI, MeCN): m/z (%) = 222.0 (100, [LH⁺]), 375.0 (80, [LFe³⁺-H⁺+(acac)⁻]), 496.2 (37, [L₂Fe³⁺-2H⁺]); elemental analysis calcd (%) for C₂₉H₃₅FeN₂O₈ (595.2): C 58.50, H 5.92, N 4.70, found: C 58.15, H 6.49, N 3.99; IR (Diamond Single Reflection ATR System): $\tilde{\nu}$ 3407, 2970, 2927, 1641, 1605, 1572, 1519, 1473, 1441, 1360, 1259, 1234, 1154, 1076, 1018, 947, 927, 854, 755, 665, 611, 518 cm⁻¹.



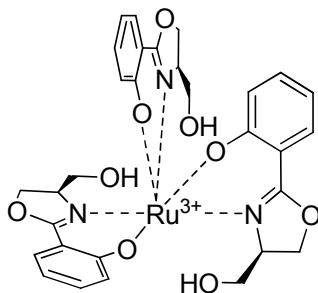
(proposed structure)

[Fe^{III}(**9**)₂(acac)] elemental analysis

Ligand **9** (100 mg, 0.452 mmol, 2.0 eq.) and Fe(acac)₃ (80 mg, 0.226 mmol, 1.0 eq.) were dissolved separately in dry THF (each in 2 mL) and the ligand was transferred to the metal. The reaction mixture was stirred over night at rt. The solvent was removed and the residue was redissolved in Et₂O/hexanes (1:6), filtered, dried in vacuo and stored at rt. The product was obtained as a blood-red solid (79 mg, 0.132 mmol, 58%).

MS (ESI, MeCN): m/z (%) = 222.0 (50, [LH⁺]), 375.1 (12, [LFe³⁺-H⁺+(acac)⁻]), 496.2 (100, [L₂Fe³⁺-2H⁺]); elemental analysis calcd (%) for C₂₉H₃₅FeN₂O₈ (595.2): C 58.50, H 5.92, N 4.70, found: C 58.27, H 6.33, N 4.63; IR (Diamond Single Reflection ATR System): $\tilde{\nu}$ 3433, 2964, 2929, 1606, 1577, 1545, 1520, 1472, 1441, 1367, 1332, 1251, 1150, 1133, 1079, 1021, 958, 927, 894, 835, 755, 707, 611, 537 cm⁻¹.

F.7.2 Ruthenium Complexes

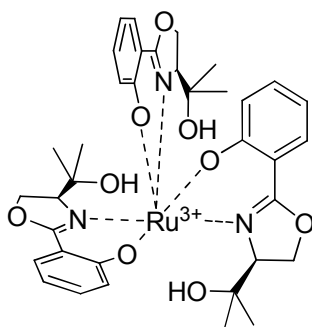


(proposed structures)

[Ru^{III}(**7a**)₃] • 2(EtOH) • (THF) elemental analysis

Ligand **7a** (100 mg, 0.518 mmol, 4.0 eq.) was dissolved in dry EtOH (2 mL) and was added to [RuCl₂(benzene)]₂ (65 mg, 0.130 mmol, 1.0 eq.), suspended in dry EtOH (2 mL). The reaction mixture was stirred under reflux for 48 h. The suspension was filtered through Celite and the solvent was removed in vacuo. The residue was redissolved in Et₂O/THF (1:1), filtered, dried in vacuo and stored at rt. The product was obtained as a dark purple solid (48 mg, 0.057 mmol, 44%).

MS (ESI, MeCN): m/z (%) = 194.0 (100, [LH⁺]), 486.1 (9, [L₂Ru³⁺-2H⁺]), 679.3 (30, [L₃Ru³⁺-2H⁺]); elemental analysis calcd (%) for C₃₈H₅₀N₃O₁₂Ru (842.2): C 54.21, H 5.99, N 4.99, found: C 54.16, H 5.89, N 5.83; IR (Diamond Single Reflection ATR System): $\tilde{\nu}$ 3300, 3065, 2972, 2931, 2873, 1605, 1587, 1541, 1476, 1437, 1391, 1369, 1323, 1303, 1238, 1157, 1079, 1036, 989, 955, 860, 843, 751 cm⁻¹.

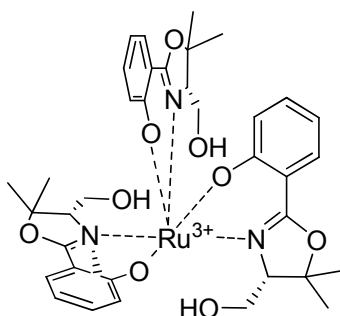


(proposed structures)

[Ru^{III}(**8**)₃] • (Et₂O) elemental analysis

Ligand **8** (100 mg, 0.452 mmol, 4.0 eq.) was dissolved in EtOH (2 mL) and was added to [RuCl₂(benzene)]₂ (57 mg, 0.113 mmol, 1.0 eq.), suspended in EtOH (2 mL). The reaction mixture was stirred under reflux for 48 h. The suspension was filtered through Celite and the solvent was removed in vacuo. The residue was redissolved in Et₂O/THF (1:1), filtered, dried in vacuo and stored at rt. The product was obtained as a dark purple solid (55 mg, 0.072 mmol, 64%).

MS (ESI, MeCN): m/z (%) = 222.0 (100, [LH⁺]), 542.2 (5, [L₂Ru³⁺-2H⁺]), 763.4 (4, [L₃Ru³⁺-2H⁺]); elemental analysis calcd (%) for C₄₀H₅₂N₃O₁₀Ru (836.3): C 57.47, H 6.27, N 5.03, found: C 57.75, H 6.56, N 5.07; IR (Diamond Single Reflection ATR System): $\tilde{\nu}$ 3355, 2971, 2923, 1605, 1541, 1470, 1435, 1366, 1324, 1232, 1154, 1131, 1075, 1037, 949, 855, 830, 751 cm⁻¹.



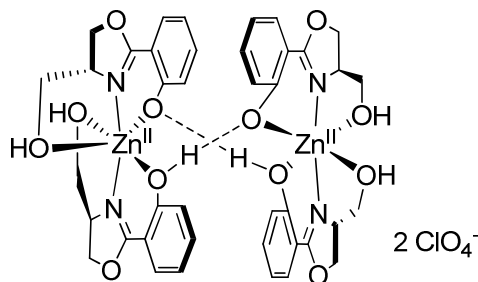
(proposed structures)

[Ru^{III}(**9**)₃] • 2(EtOH) elemental analysis

Ligand **9** (100 mg, 0.452 mmol, 4.0 eq.) was dissolved in EtOH (2 mL) and was added to [RuCl₂(benzene)]₂ (57 mg, 0.113 mmol, 1.0 eq.), suspended in EtOH (2 mL). The reaction mixture was stirred under reflux for 48 h. The suspension was filtered through Celite and the solvent was removed in vacuo. The residue was redissolved in Et₂O/THF (1:1), filtered, dried in vacuo and stored at rt. The product was obtained as a dark purple solid (50 mg, 0.059 mmol, 52%).

MS (ESI, MeCN): m/z (%) = 222.1 (100, [LH⁺]), 542.2 (6, [L₂Ru²⁺-2H⁺]), 763.4 (12, [L₃Ru³⁺-2H⁺]); elemental analysis calcd (%) for C₄₀H₅₄N₃O₁₁Ru (854.3): C 56.26, H 6.37, N 4.92, found: C 55.86, H 5.93, N 4.93; IR (Diamond Single Reflection ATR System): $\tilde{\nu}$ 3304, 2968, 2931, 1604, 1541, 1471, 1434, 1390, 1369, 1324, 1241, 1151, 1134, 1080, 1035, 958, 869, 832, 752 cm⁻¹.

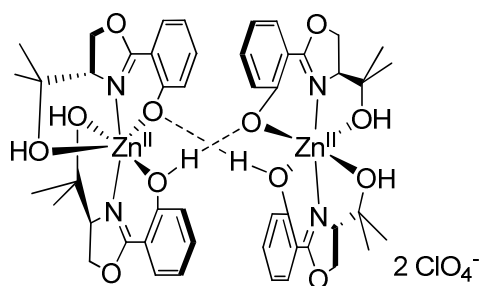
F.7.3 Zinc Complexes



[Zn^{II}(7a)₂] • (ClO₄) • (H₂O) elemental analysis

Ligand **7a** (50 mg, 0.259 mmol, 2.0 eq.) and Zn(ClO₄)₂•6H₂O (48 mg, 0.130 mmol, 1.0 eq.) were dissolved separately in THF (each in 2 mL) and the ligand was transferred to the metal. The reaction mixture was stirred over night at rt. The solvent was removed by pipette and the arising solid was washed with dry THF (3 x 3 mL), dried in vacuo and stored at rt. The product was obtained as a slightly orange oil (39 mg, 0.069 mmol, 53%). Recrystallization from THF / Et₂O afforded colourless crystals which were suitable for X-Ray structure analysis.

MS (ESI, MeCN): m/z (%) = 194.0 (100, [LH⁺]), 449.0 (35, [L₂Zn²⁺-2H⁺]); elemental analysis calcd (%) for C₂₀H₂₃ClN₂O₁₁Zn (566.0): C 42.27, H 4.08, N 4.93, found: C 42.79, H 4.07, N 5.37; IR (Diamond Single Reflection ATR System): $\tilde{\nu}$ 3482, 2904, 1613, 1556, 1475, 1388, 1322, 1235, 1147, 1061, 1040, 947, 927, 893, 836, 776, 751, 692, 659, 620, 573 cm⁻¹.

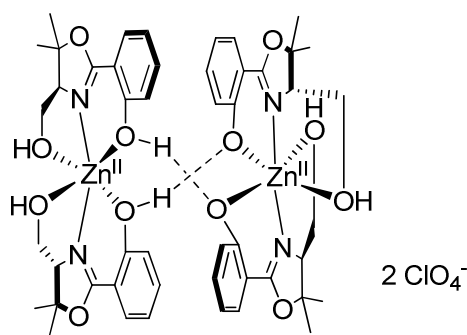


(proposed structure)

[Zn^{II}(8)₂] • (ClO₄) • 5(H₂O) elemental analysis

Ligand **8** (50 mg, 0.226 mmol, 2.0 eq.) and Zn(ClO₄)₂•6H₂O (42 mg, 0.113 mmol, 1.0 eq.) were dissolved separately in THF (each in 2 mL) and the ligand was transferred to the metal. The reaction mixture was stirred over night at rt. The solvent was removed and the arising solid was washed with dry THF (3 x 3 mL), dried in vacuo and stored at rt. The product was obtained as a slightly orange oil (65 mg, 0.094 mmol, 83%).

MS (ESI, MeCN): m/z (%) = 222.0 (57, [LH⁺]), 505.1 (100, [L₂Zn²⁺-H⁺]), 790.2 (22, [L₃Zn₂²⁺-3H⁺]); elemental analysis calcd (%) for C₂₄H₃₉ClN₂O₁₅Zn (694.1): C 41.39, H 5.64, N 4.02, found: C 41.27, H 5.19, N 3.97; IR (Diamond Single Reflection ATR System): $\tilde{\nu}$ 3461, 2979, 2939, 1626, 1555, 1477, 1383, 1317, 1240, 1067, 957, 932, 838, 753, 620 cm⁻¹.



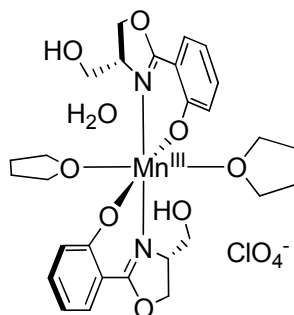
[Zn^{II}(9)₂] • (ClO₄) • 2(H₂O) elemental analysis

Ligand **9** (100 mg, 0.452 mmol, 2.0 eq.) and Zn(ClO₄)₂•6H₂O (84 mg, 0.226 mmol, 1.0 eq.) were dissolved separately in THF (each in 3 mL) and the ligand was transferred to the metal. The reaction mixture was stirred over night at rt. The solvent was removed by pipette and the arising solid was washed with dry THF (3 x 3 mL). Recrystallization from MeCN afforded the product as a colourless solid (49 mg, 0.077 mmol, 34%), which was dried in vacuo and stored at rt. Recrystallization from THF / Et₂O resulted in colourless crystals which were suitable for X-Ray structure analysis.

MS (ESI, MeCN): m/z (%) = 222.0 (23, [LH⁺]), 505.2 (24, [L₂Zn²⁺-H⁺])¹; elemental analysis calcd (%) for C₂₄H₃₃ClN₂O₁₂Zn (640.1): C 44.87, H 5.18, N 4.36, found: C 45.12, H 5.20, N 4.35; IR (Diamond Single Reflection ATR System): $\tilde{\nu}$ 3499, 2986, 1621, 1567, 1463, 1393, 1372, 1308, 1071, 1031, 964, 908, 857, 841, 777, 758, 696, 621 cm⁻¹.

¹ Massspectrometry shows an additional peak at 496.2 which indicates the presence of an iron complex. This might be caused by minimal amount of iron leaching from the injection needle (corrosion).

F.7.4 Manganese Complex



[Mn^{III}(7a)₂(THF)₂] • (ClO₄) crystal structure

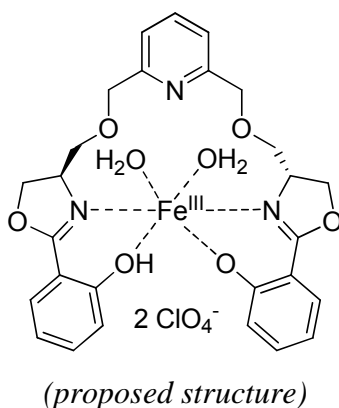
[Mn^{III}(7a)₂] • (ClO₄) • 4(H₂O) elemental analysis

Ligand **7a** (100 mg, 0.518 mmol, 2.0 eq.) and Mn(ClO₄)₂•6H₂O (94 mg, 0.259 mmol, 1.0 eq.) were dissolved separately in THF (each in 2 mL) and the ligand was transferred to the metal. The reaction mixture was stirred for 48 h at rt. The solvent was removed and the arising solid was washed with dry THF (3 x 3 mL), dried in vacuo and stored at rt. The product was obtained as a dark green solid (111 mg, 0.182 mmol, 70%). Recrystallization from Et₂O afforded colourless crystals which were suitable for X-Ray structure analysis.

MS (ESI, MeCN): m/z (%) = 194.0 (33, [LH⁺]), 439.1 (100, [L₂Mn³⁺-2H⁺]), 684 (13, [L₃Mn₂³⁺-5H⁺]); elemental analysis calcd (%) for C₂₀H₂₈ClMnN₂O₁₄ (610.1): C 39.33, H 4.62, N 4.59 found: C 39.94, H 4.10, N 4.51; IR (Diamond Single Reflection ATR System): $\tilde{\nu}$ 3481, 2952, 2896, 1604, 1583, 1546, 1480, 1442, 1406, 1325, 1246, 1086, 1032, 985, 928, 865, 750, 675, 619 cm⁻¹.

F.8 Synthesized Complexes of Bis(oxazoline) Ligands

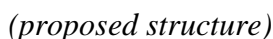
F.8.1 Iron Complexes

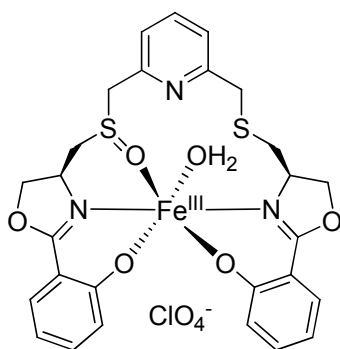


[Fe^{III}(1)(H₂O)₂] • 2(ClO₄) • (THF) elemental analysis

Ligand **1** (50 mg, 0.102 mmol, 1.0 eq.) and Fe(ClO₄)₂•6H₂O (37 mg, 0.102 mmol, 1.0 eq.) were dissolved separately in dry THF (each in 2 mL) and the ligand was transferred to the metal. The reaction mixture was stirred for 12 h at rt. The solvent was removed by pipette and the arising solid was washed with dry THF (3 x 3 mL), dried in vacuo and stored at rt. The product was obtained as a dark purple solid (85 mg, 0.099 mmol, 97%).

MS (ESI, MeCN): m/z (%) = 543.1 (100, [LFe³⁺-2H⁺]); elemental analysis calcd (%) for C₃₁H₃₈Cl₂FeN₃O₁₇ (850.1): C 43.73, H 4.50, N 4.94, found: C 43.21, H 4.23, N 5.21; IR (Diamond Single Reflection ATR System): $\tilde{\nu}$ 2975, 1604, 1579, 1545, 1475, 1441, 1393, 1332, 1247, 1064, 964, 930, 853, 757, 694, 666, 619 cm⁻¹.



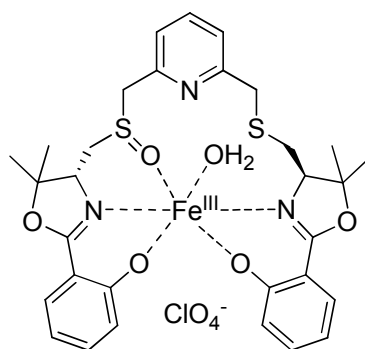


[Fe^{III}((*meso*)-4)_{ox}(H₂O)] • (ClO₄) crystal structure

[Fe^{III}((±)-4/(*meso*)-4)_{ox}(H₂O)] • (ClO₄) • (THF) • 4(H₂O) elemental analysis

Ligand (±)-4/(*meso*)-4 (50 mg, 0.096 mmol, 1.0 eq.) and Fe(ClO₄)₂•6H₂O (35 mg, 0.096 mmol, 1.0 eq.) were dissolved separately in dry THF (each in 2 mL) and the ligand was transferred to the metal. The reaction mixture was stirred for 4 h at rt. The solvent was removed by pipette and the arising solid was washed with dry THF (3 x 3 mL), dried in vacuo and stored at rt. The product was obtained as a dark violet solid (72 mg, 0.084 mmol, 88%). Recrystallization from acetonitrile / ethylacetate afforded violet needles which were suitable for X-Ray structure analysis.

MS (ESI, MeCN): m/z (%) = 575.0 (100, [LFe³⁺-2H⁺]), 591.0 (64, [LFe³⁺-2H⁺+O]); elemental analysis calcd (%) for C₃₁H₄₃ClFeN₃O₁₅S₂ (852.1): C 43.64, H 5.08, N 4.93, S 7.52, found: C 43.60, H 4.32, N 5.01, S 7.57; IR (Diamond Single Reflection ATR System): $\tilde{\nu}$ 2976, 1603, 1578, 1543, 1475, 1441, 1393, 1329, 1246, 1075, 963, 931, 856, 756, 692, 664, 619 cm⁻¹.



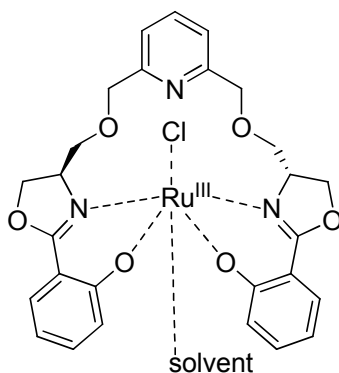
(proposed structure)

[Fe^{III}(5)_{ox}(H₂O)] • (ClO₄) • 4(H₂O) elemental analysis

Ligand **5** (40 mg, 0.069 mmol, 1.0 eq.) and Fe(ClO₄)₂•6H₂O (25 mg, 0.069 mmol, 1.0 eq.) were dissolved separately in dry THF (each in 2 mL) and the ligand was transferred to the metal. The reaction mixture was stirred over night at rt. The solvent was removed by pipette and the arising solid was washed with dry THF (3 x 3 mL), dried in vacuo and stored at rt. The product was obtained as a dark purple solid (24 mg, 0.029 mmol, 42%).

MS (ESI, MeCN): m/z (%) = 631.1 (100, [LFe³⁺-2H⁺]), 647.2 (7, [LFe³⁺-2H⁺+O]); elemental analysis calcd (%) for C₃₁H₄₃ClFeN₃O₁₄S₂ (836.1): C 44.48, H 5.18, N 5.02, S 7.66, found: C 44.82, H 4.90, N 4.59, S 7.03; IR (Diamond Single Reflection ATR System): $\tilde{\nu}$ 2975, 1603, 1575, 1542, 1473, 1439, 1393, 1329, 1255, 1074, 869, 756, 697, 619 cm⁻¹.

F.8.2 Ruthenium Complexes

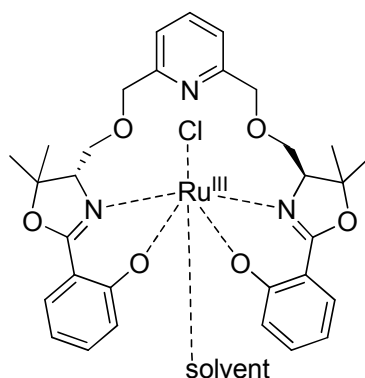


(proposed structure)

[Ru^{III}(1)(Cl)(solvent)] • 2(EtOH) elemental analysis

Ligand **1** (30 mg, 0.061 mmol, 2.0 eq.) was dissolved in dry EtOH (3 mL) and was added to [RuCl₂(benzene)]₂ (15.5 mg, 0.031 mmol, 1.0 eq.), suspended in dry EtOH (3 mL). The reaction mixture was refluxed for 16 h, the solvent was removed in vacuo and the residue was resuspended in CH₂Cl₂ (4 mL) and filtered through Celite. The solvent was removed in vacuo, the residue was dried and stored at rt. The product was obtained as a dark purple solid (18 mg, 0.025 mmol, 81%).

MS (ESI, MeCN): m/z (%) = 589.1 (40, [LRu³⁺-2H⁺]), 625.1 (100, [LRu³⁺-H⁺+Cl⁻]); elemental analysis calcd (%) for C₃₁H₃₇ClN₃O₈Ru (716.1): C 51.99, H 5.21, N 5.87, found: C 52.38, H 4.79, N 5.82; IR (Diamond Single Reflection ATR System): $\tilde{\nu}$ 3400, 3063, 2961, 2869, 1617, 1539, 1472, 1438, 1388, 1332, 1298, 1231, 1087, 1070, 1034, 847, 797, 753, 687 cm⁻¹.

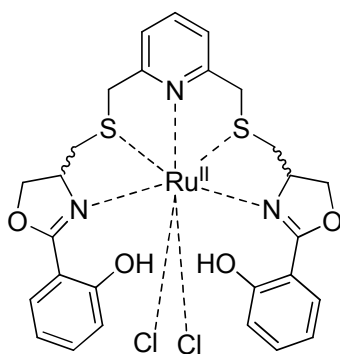


(proposed structure)

[Ru^{III}(2)(Cl)(solvent)] • 5(EtOH) • 2(H₂O) elemental analysis

Ligand **2** (50.0 mg, 0.092 mmol, 1.0 eq.) was dissolved in dry EtOH (3 mL) and was added to [RuCl₂(benzene)]₂ (23 mg, 0.046 mmol, 0.5 eq.), suspended in dry EtOH (3 mL). The reaction mixture was refluxed for 24 h and filtered. The solvent was removed in vacuo, the residue was dried and stored at rt. The product was obtained as a dark purple solid (70 mg, 0.074 mmol, 80%).

MS (LSIMS, MeOH/Glycerin): m/z (%) = 546.3 (100, [LH⁺]), 645.2 (20, [LRu³⁺-2H⁺]); elemental analysis calcd (%) for C₄₁H₆₇ClN₃O₁₃Ru (946.3): C 52.03, H 7.13, N 4.44, found: C 51.87, H 7.01, N 3.63; IR (Diamond Single Reflection ATR System): $\tilde{\nu}$ 3200, 2963, 2922, 2853, 1618, 1459, 1434, 1372, 1330, 1257, 1125, 1084, 1042, 795, 753, 684 cm⁻¹.

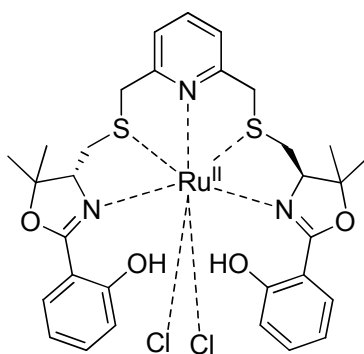


(proposed structure)

[Ru^{II}((±)-4/(*meso*)-4)(Cl)₂] • (EtOH) elemental analysis

Ligand (±)-4/(*meso*)-4 (150 mg, 0.288 mmol, 2.0 eq.) was dissolved in dry EtOH (3 mL) and was added to [RuCl₂(benzene)]₂ (71.9 mg, 0.143 mmol, 1.0 eq.), suspended in dry EtOH (3 mL). The reaction mixture was refluxed for 16 h, the solvent was removed in vacuo and the residue was resuspended in CH₂Cl₂ (4 mL) and filtered through Celite 535. The solvent was removed in vacuo, the residue was dried and stored at rt. The product was obtained as a dark green solid (79 mg, 0.107 mmol, 75%).

MS (ESI, MeCN): m/z (%) = 311.4 (68, [LRu²⁺]), 622.0 (100, [LRu²⁺-H⁺]), 658.0 (50, [LRu²⁺+Cl⁻]); elemental analysis calcd (%) for C₂₉H₃₃Cl₂N₃O₅RuS₂ (739.0): C 47.09, H 4.50, N 5.68, S 8.67, found: C 46.99, H 4.79, N 5.32, S 7.70; IR (Diamond Single Reflection ATR System): $\tilde{\nu}$ 3200, 3059, 2962, 1634, 1598, 1538, 1489, 1455, 1442, 1363, 1336, 1303, 1258, 1235, 1068, 1032, 933, 797, 751, 683, 662 cm⁻¹.



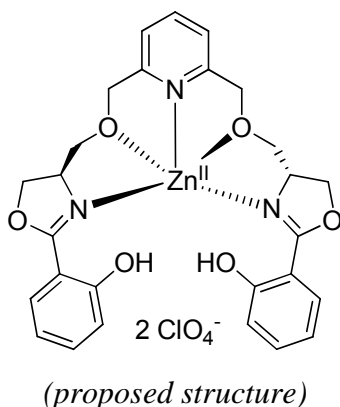
(proposed structure)

[Ru^{II}(5)(Cl)₂] • 3(EtOH) • 2(CH₂Cl₂) • (C₆H₆) • (H₂O) elemental analysis

Ligand **5** (35 mg, 0.061 mmol, 1.0 eq.) was dissolved in dry EtOH (2.5 mL) and was added to [RuCl₂(benzene)]₂ (51 mg, 0.102 mmol, 1.7 eq.), suspended in dry EtOH (2.5 mL). The reaction mixture was refluxed for 16 h, the solvent was removed in vacuo and the residue was resuspended in CH₂Cl₂ (4 mL) and filtered through Celite. The solvent was removed in vacuo, the residue was dried and stored at rt. The product was obtained as a dark green solid (45 mg, 0.039 mmol, 64%).

MS (ESI, MeCN): m/z (%) = 678.2 (100, [LRu²⁺-H⁺]), 714.2 (57, [LRu²⁺+Cl⁻]); elemental analysis calcd (%) for C₄₅H₆₅Cl₆N₃O₈RuS₂ (1151.1): C 46.84, H 5.68, N 3.64, S 5.56, found: C 46.38, H 5.88, N 3.26, S 5.24; IR (Diamond Single Reflection ATR System): $\tilde{\nu}$ 3355, 3190, 2922, 2852, 1719, 1633, 1606, 1526, 1492, 1458, 1391, 1375, 1334, 1289, 1259, 1243, 1148, 1123, 1074, 1031, 753 cm⁻¹.

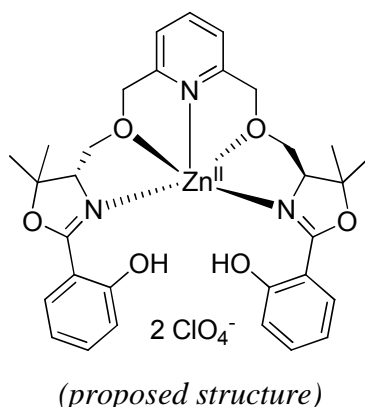
F.8.3 Zinc Complexes



[Zn^{II}(1)] • 2(ClO₄) • 2(THF) • (H₂O) elemental analysis

Ligand **1** (33 mg, 0.067 mmol, 1.0 eq.) and Zn(ClO₄)₂•6H₂O (25 mg, 0.067 mmol, 1.0 eq.) were dissolved separately in dry THF (each in 2 mL) and the ligand was transferred to the metal. The reaction mixture was stirred for 4 h at rt. The solvent was removed and the arising solid was washed with dry THF (3 x 3 mL), dried in vacuo and stored at rt. The product was obtained as a slightly pink solid (49 mg, 0.058 mmol, 87%).

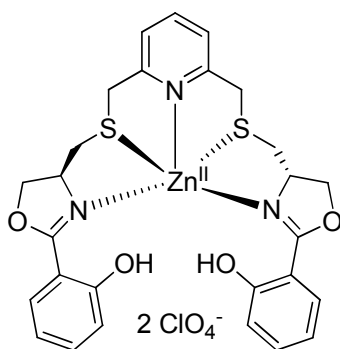
MS (ESI, MeCN): m/z (%) = 552.1 (7, [LZn²⁺-H⁺]), 570.1 (100, [LZn²⁺-H⁺+H₂O]); elemental analysis calcd (%) for C₃₁H₃₇Cl₂N₃O₁₆Zn (841.1): C 44.12, H 4.42, N 4.98, found: C 44.15, H 4.35, N 5.14; IR (Diamond Single Reflection ATR System): $\tilde{\nu}$ 3200, 2900, 1610, 1551, 1476, 1440, 1390, 1329, 1312, 1239, 1067, 963, 930, 840, 755, 697, 661, 620, 574 cm⁻¹.



[Zn^{II}(2)] • 2(ClO₄) • 2(THF) elemental analysis

Ligand **2** (37 mg, 0.068 mmol, 1.0 eq.) and Zn(ClO₄)₂•6H₂O (25 mg, 0.068 mmol, 1.0 eq.) were dissolved separately in dry THF (each in 2 mL) and the ligand was transferred to the metal. The reaction mixture was stirred for 4 h at rt. The solvent was removed and the arising solid was washed with dry THF (3 x 3 mL), dried in vacuo and stored at rt. The product was obtained as a colourless solid (17 mg, 0.019 mmol, 28%).

MS (LSIMS, MeOH/CH₂Cl₂/Glycerin): m/z (%) = 608.2 (100, [LZn²⁺-H⁺]); elemental analysis calcd (%) for C₃₉H₅₁Cl₂N₃O₁₆Zn (951.2): C 49.09, H 5.39, N 4.40, found: C 49.83, H 5.00, N 4.91; IR (Diamond Single Reflection ATR System): $\tilde{\nu}$ 2975, 2877, 1624, 1549, 1472, 1441, 1370, 1322, 1303, 1244, 1079, 967, 925, 859, 833, 763, 833, 622, 584 cm⁻¹.

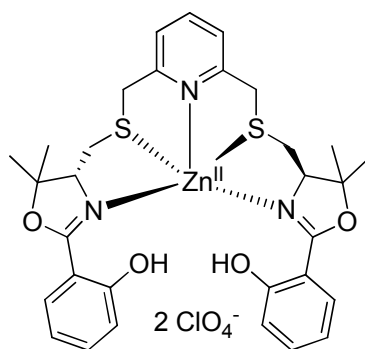


[Zn^{II}((*S,S*)-4)] • 2(ClO₄) crystal structure

[Zn^{II}((±)-4/(*meso*)-4)] • 2(ClO₄) • 2(THF) • 4(H₂O) elemental analysis

Ligand (±)-4/(*meso*)-4 (80 mg, 0.153 mmol, 1.0 eq.) and Zn(ClO₄)₂•6H₂O (71 mg, 0.192 mmol, 1.2 eq.) were dissolved separately in dry THF (each in 2 mL) and the ligand was transferred to the metal. The reaction mixture was stirred for 3 h at rt. The solvent was removed and the arising solid was washed with dry THF (3 x 3 mL), dried in vacuo and stored at rt. The product was obtained as a slightly yellow solid (116 mg, 0.116 mmol, 76%). Recrystallization from acetonitrile / ethylacetate afforded colourless needles which were suitable for X-Ray structure analysis.

MS (LSIMS, MeOH/Glycerin): m/z (%) = 522.3 (35, [LH⁺]), 584.1 (100, [LZn²⁺-H⁺]); elemental analysis calcd (%) for C₃₅H₅₁Cl₂N₃O₁₈S₂Zn (999.1): C 41.94, H 5.13, N 4.19, S 6.40, found: C 41.40, H 4.42, N 4.07, S 6.03; IR (Diamond Single Reflection ATR System): $\tilde{\nu}$ 2980, 1620, 1479, 1455, 1389, 1312, 1242, 1076, 1035, 993, 962, 919, 860, 839, 753, 691, 620, 578 cm⁻¹.



(proposed structure)

[Zn^{II}(5)] • 2(ClO₄) • (H₂O) elemental analysis

Ligand **5** (40 mg, 0.069 mmol, 1.0 eq.) and Zn(ClO₄)₂•6H₂O (26 mg, 0.069 mmol, 1.0 eq.) were dissolved separately in dry THF (each in 2 mL) and the ligand was transferred to the metal. The reaction mixture was stirred over night at rt. The solvent was removed by pipette and the arising solid was washed with dry THF (3 x 3 mL), dried in vacuo and stored at rt. The product was obtained as a yellow solid (22 mg, 0.026 mmol, 38%).

MS (ESI, MeCN): m/z (%) = 640.2 (100, [LZn²⁺-H⁺]); elemental analysis calcd (%) for C₃₁H₃₇Cl₂N₃O₁₃S₂Zn (857.0): C 43.29, H 4.34, N 4.89, S 7.46, found: C 43.78, H 4.47, N 4.67, S 7.33; IR (Diamond Single Reflection ATR System): $\tilde{\nu}$ 3200, 2982, 1618, 1590, 1557, 1476, 1440, 1377, 1313, 1242, 1077, 868, 929, 755, 700, 620, 579 cm⁻¹.

F.9 UV/Vis-Titrations

F.9.1 UV/Vis-Job`s Plot Titration

A stock solution of ligand **7a** (6.0 mM in MeCN) as well as $\text{Fe}(\text{ClO}_4)_2 \cdot 6\text{H}_2\text{O}$ (6.0 mM in MeCN) were used for preparing the samples. The allover concentration of the solutions, containing different ligand / salt ratios, is given with: $[\text{ligand}] + [\text{salt}] = 0.5 \text{ mM}$. Table 1 shows the different concentrations of the ligand and the salt in each sample and the resulting mole fraction values for ligand **7a**. The optical cell path length was for all measurements $d = 1 \text{ cm}$.

Table 1. Mole fraction for ligand **7a** and used concentrations.

Sample No.	Mole Fraction Ligand 7a	c_{Salt} [mM]	c_{Ligand} [mM]
1	0.1	0.45	0.05
2	0.25	0.375	0.125
3	0.375	0.3125	0.1875
4	0.5	0.25	0.25
5	0.625	0.1875	0.3125
6	0.675	0.1625	0.3375
7	0.875	0.0625	0.4375
8	0.995	0.0025	0.4975

F.9.2 UV/Vis-Equilibrium Constant Titration

All titrations were carried out in a solvent mixture of acetonitrile/H₂O (1:1), buffered with 0.053 M formic acid. The optical cell path length was for all measurements $d = 1$ cm. For all equilibrium titrations, FeCl₃•6H₂O was used as iron source.

Table 2. Forward titration of oxazoline **7a**.

No.	Ratio L/M	OD (530 nm)	OD (580 nm)	c _M [mM]	c _L [mM]
1	0.15	0.0463313	0.0397601	0.25	0.0375
2	0.60	0.189063	0.156025	0.25	0.15
3	1.05	0.312262	0.247508	0.25	0.2625
4	1.50	0.431260	0.330116	0.25	0.375
5	1.95	0.522818	0.385927	0.25	0.4875
6	2.40	0.612041	0.438692	0.25	0.6
7	2.85	0.701491	0.491547	0.25	0.7125
8	4.51	0.893168	0.589432	0.25	1.1275
9	11.3	1.11623	0.690552	0.25	2.825

Table 3. Reverse titration of oxazoline **7a**.

No.	Ratio M/L	OD (530 nm)	OD (580 nm)	c _M [mM]	c _L [mM]
1	0.16	0.0308677	0.0234003	0.02	0.125
2	0.64	0.0876823	0.0695113	0.08	0.125
3	1.12	0.115686	0.0940063	0.14	0.125
4	1.6	0.133199	0.110158	0.20	0.125
5	2.08	0.141174	0.117740	0.26	0.125
6	2.56	0.147343	0.123661	0.32	0.125
7	3.04	0.151961	0.128437	0.38	0.125
8	6.4	0.169025	0.146672	0.80	0.125
9	12	0.180968	0.160897	1.50	0.125

Table 4. Forward titration of thiazoline (\pm)-**10**.

No.	Ratio L/M	OD	OD	c_M [mM]	c_L [mM]
		(535 nm)	(580 nm)		
1	0.15	0.0147494	0.0126545	0.125	0.01875
2	0.60	0.0495793	0.0429302	0.125	0.075
3	1.05	0.0785201	0.0669466	0.125	0.13125
4	1.50	0.104655	0.0889260	0.125	0.1875
5	1.95	0.128978	0.108319	0.125	0.24375
6	2.40	0.148217	0.123307	0.125	0.3
7	2.85	0.166323	0.137165	0.125	0.35625
8	4.51	0.215077	0.172500	0.125	0.56375
9	11.3	0.317620	0.243837	0.125	1.4125

Table 5. Reverse titration of thiazoline (\pm)-**10**.

No.	Ratio M/L	OD	OD	c_M [mM]	c_L [mM]
		(535 nm)	(580 nm)		
1	0.16	0.0240740	0.0199488	0.02	0.125
2	0.64	0.0570581	0.0486704	0.08	0.125
3	1.12	0.0828912	0.0720409	0.14	0.125
4	1.6	0.0898935	0.0783712	0.20	0.125
5	2.08	0.0989253	0.0870519	0.26	0.125
6	2.56	0.102990	0.0906938	0.32	0.125
7	3.04	0.109526	0.0967431	0.38	0.125
8	6.4	0.173251	0.154841	0.80	0.125
9	12	0.141189	0.128324	1.50	0.125

F.9.2 General UV/Vis- and CD-Measurements

All complex, ligand and salt measurements were carried out in a 10^{-5} M solution (UV/Vis) or 10^{-4} M solution (CD) in acetonitrile at rt. The optical cell path length was for all measurements $d = 1$ cm (UV/Vis) or $d = 0.1$ cm (CD).

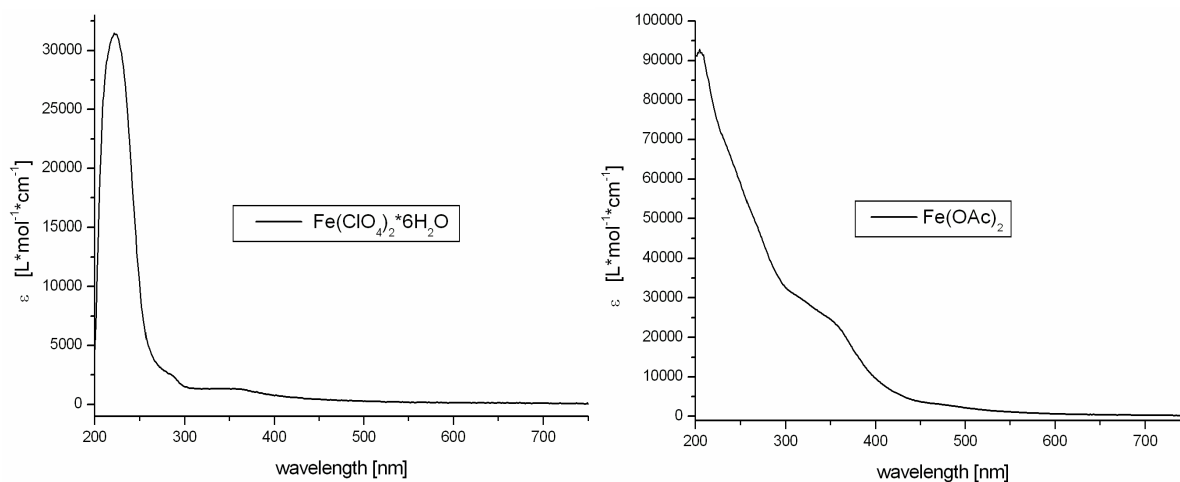


Figure 1. UV/Vis spectra of $\text{Fe}(\text{ClO}_4)_2 \cdot 6\text{H}_2\text{O}$ and $\text{Fe}(\text{OAc})_2$.

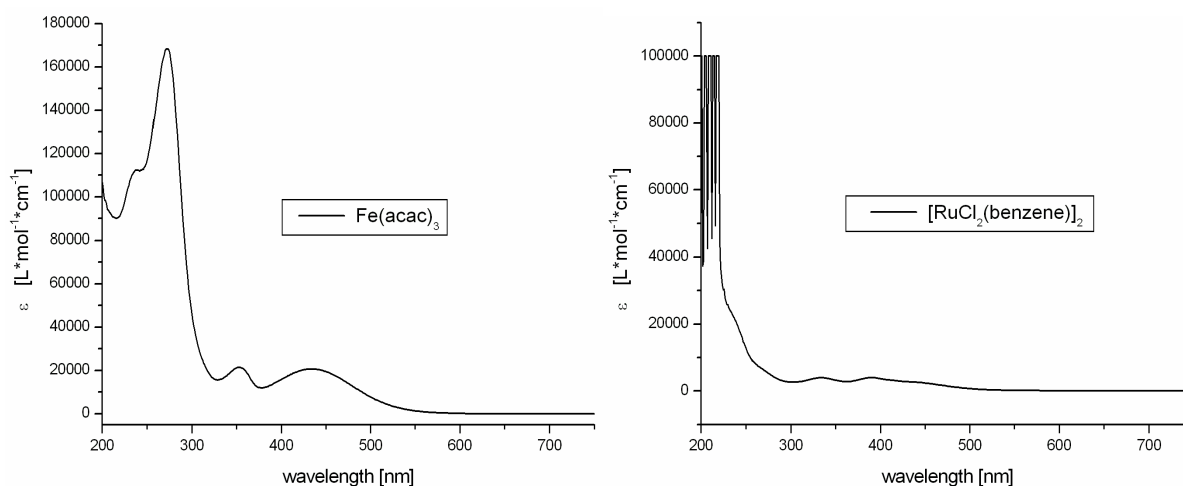


Figure 2. UV/Vis spectra of $\text{Fe}(\text{acac})_3$ and $[\text{RuCl}_2(\text{benzene})]_2$.

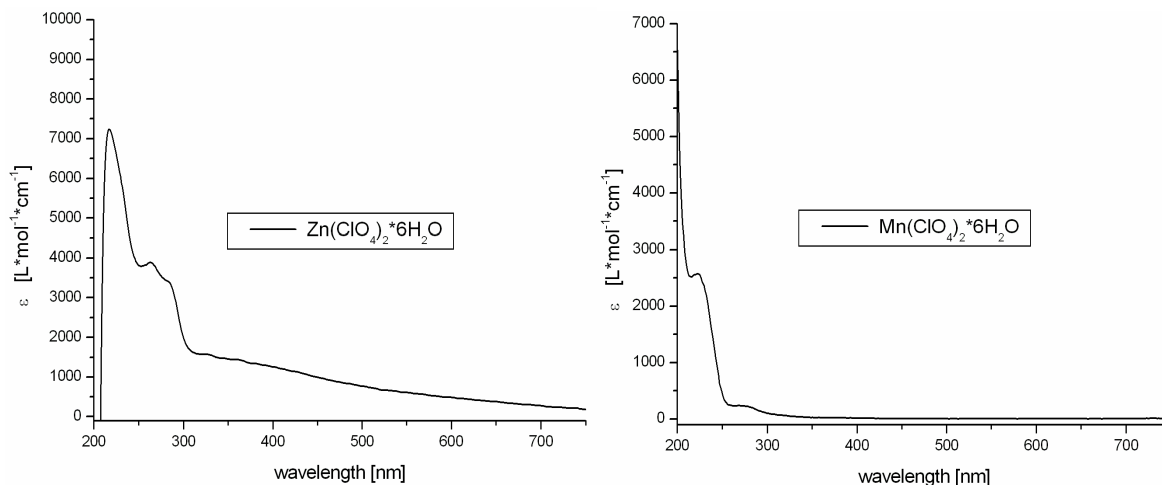


Figure 3. UV/Vis spectra of $\text{Zn}(\text{ClO}_4)_2 \cdot 6\text{H}_2\text{O}$ and $\text{Mn}(\text{ClO}_4)_2 \cdot 6\text{H}_2\text{O}$.

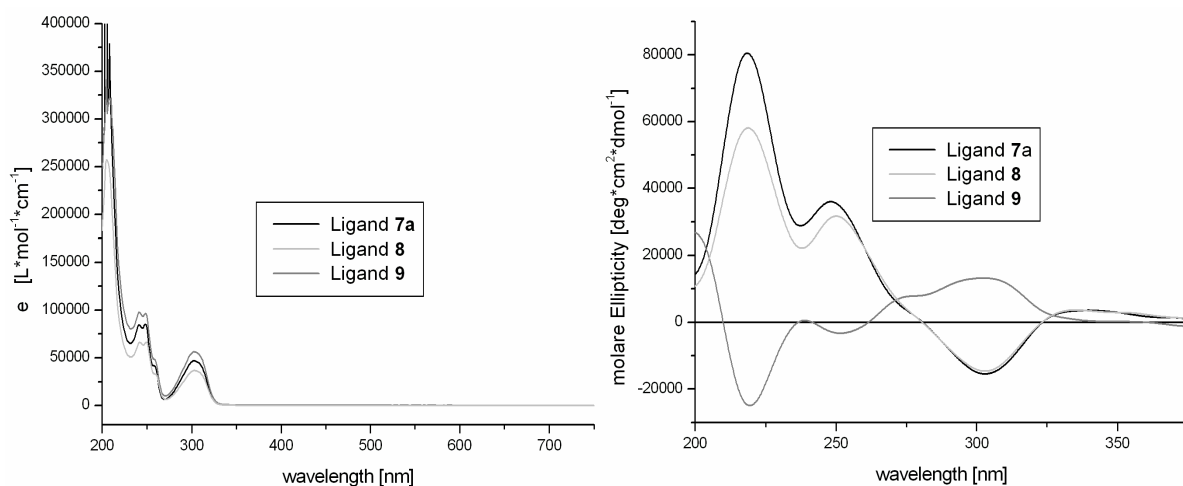


Figure 4. UV/Vis spectra (left) and CD spectra (right) of oxazoline ligands **7a-9**.

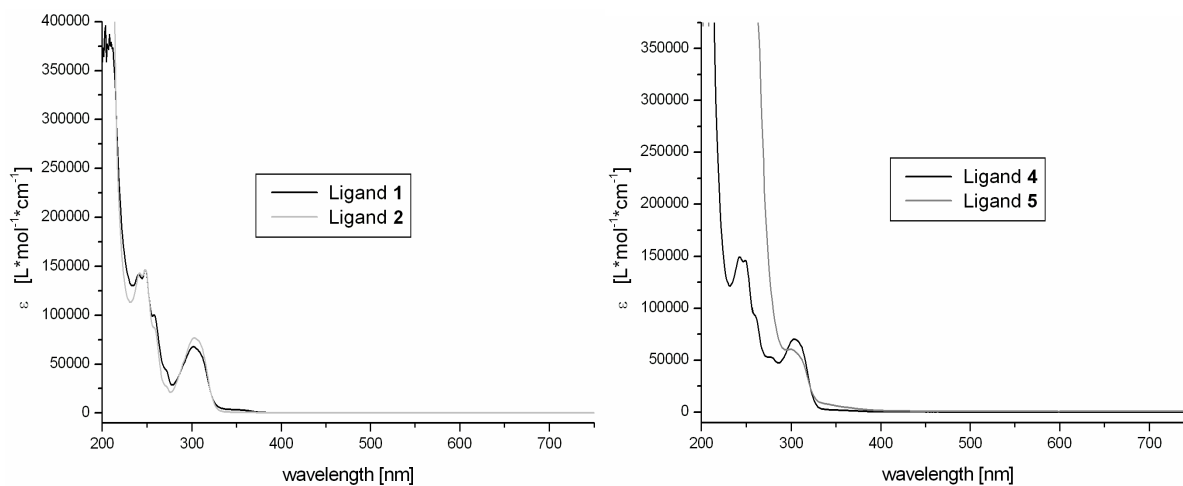


Figure 5. UV/Vis spectra of the bis(oxazoline) ligand **1** and **2** (left) as well as (\pm) -**4**/*meso*-**4** and **5** (right).

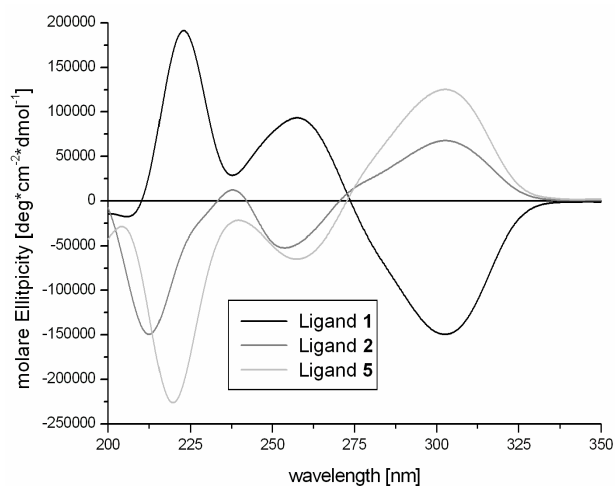


Figure 6. CD spectra of the bis(oxazoline) ligand **1**, **2** and **5**.

Table 6. General CD measurement conditions.

Wavelength range	200 – 750 nm
Resolution	0.2 nm
Bandwidth	1.0 nm
Sensitivity	50 mdeg
Response	2 sec
Accumulations	10
Speed	50 nm/min

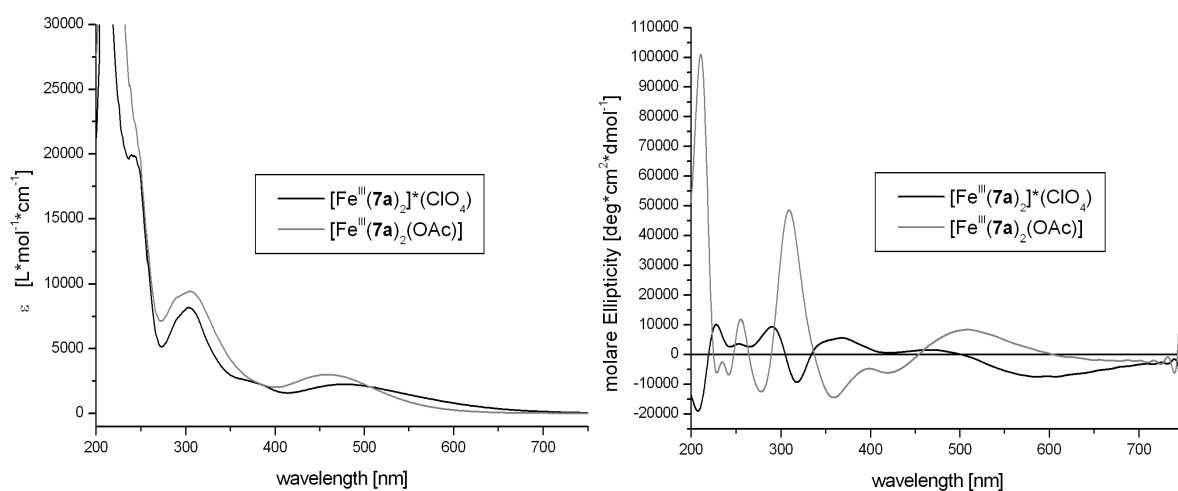


Figure 7. UV/Vis and CD spectra of $[Fe^{III}(7a)_2]^+(ClO_4)$ and $[Fe^{III}(7a)_2(OAc)]$.

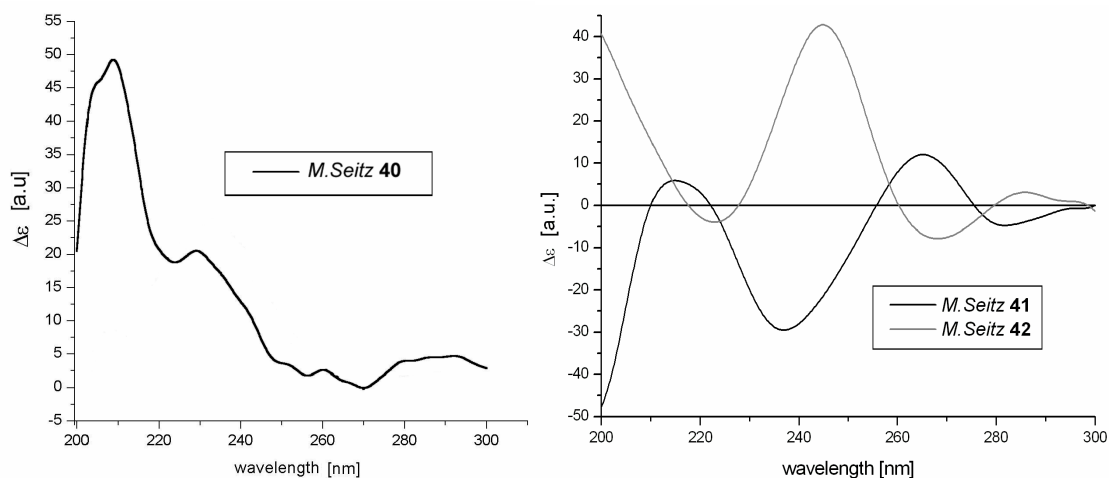


Figure 8. CD spectra of the complexes **40** (ruthenium), **41** (zinc) and **42** (zinc).

F.10 Catalysis Reactions

F.10.1 Oxidation of ethylbenzene

Ligand and salt were dissolved separately in acetonitrile (each in 2.5 mL). The ligand was then added to the salt and was stirred for 15 min at rt to form the complex (1 mol% or 10 mol%). The addition of HOAc (11.4 μ L, 12 mg, 0.20 mmol, 0.2 equiv.) followed and the reaction mixture was stirred for further 10 min. Ethylbenzene (1.22 mL, 1.06 g, 10.0 mmol, 10.0 equiv.). Bromobenzene (internal standard) (10.5 μ L, 16 mg, 0.100 mmol, 0.1 equiv.) and H₂O₂ (102 μ L, 113 mg, 1.0 mmol, 1.0 equiv.) was added. In the cases, for a total of 5 mmol H₂O₂, a portion-wise addition of 1 mmol oxidant each hour during the first 5 h was carried out. The reaction mixture was stirred at rt and after 3 h, 5 h or 24 h, samples for GC detection were taken. 0.1 mL reaction mixture was filtered through a plug of silica gel followed by a wash with 0.9 mL acetonitrile.

GC parameters:

- FISON GC 8130, Detektor FID 200 °C
- 200 °C injector
- column: J&W Scientific DBWAX; 30 m and 0.25 mm
- oven temperature: 130 °C / 4 min, 30 K / min to 180 °C, 180 °C / 4 min
- carrier gas helium
- retention time: 3.19 min (bromobenzene), 6.32 min (acetophenone) and 7.89 min (1-phenylethanol).

Chiral GC parameters:

- FISON GC 8000 series, Detektor FID 200 °C
- 200 °C injector
- column: CP-Chiracil-DEX-CP
- oven temperature: isotherm 100 °C
- carrier gas helium
- retention time: 10.28 min and 11.41 min ((\pm)-1-phenylethanol).

F.10.2 Oxidation of methyl phenyl sulfide

Ligand and salt were dissolved separately in dichloromethane or acetonitrile (each in 1.0 mL). The ligand was then added to the salt and the reaction mixture was stirred for 15 min at rt to form the complex (2 mol%). The complex mixture was then added to a suspension of 4-methoxybenzoic acid (1.5 mg, 0.01 mmol, 0.01 equiv.) in 0.5 mL dichloromethane or acetonitrile and was stirred for further 10 min. Methyl phenyl sulfide (118 μ L, 124 mg, 1.00 mmol 1.0 equiv.) and H₂O₂ (123 μ L, 136 mg, 1.2 mmol, 1.2 equiv.) was added. The catalysis reaction was stirred at rt for 16 h. Sat. NaSO₃-solution (5 mL) was added. After layer separation, the aqueous layer was extracted with dichloromethane (2 x 5 mL) and the combined organic layers were dried (Na₂SO₄). Subsequently the solvent was almost removed at reduced pressure (200 mbar, rt), and in comparison in a second series the solvent was completely removed under a high vacuum. In each case, the yield of the product was determined by ¹H NMR spectroscopy:

methyl phenyl sulfide:	(CH ₃) = 2.51 ppm (300MHz. CDCl ₃)
methyl phenyl sulfoxide:	(CH ₃) = 2.75 ppm (300MHz. CDCl ₃)
methyl phenyl sulfon:	(CH ₃) = 3.08 ppm (300MHz. CDCl ₃)

The enantiomeric excess of methyl phenyl sulfoxide was determined by chiral HPLC:

HPLC conditions:

- column: Daicel Chiralcel OD-H, 0.46 cm x 25 cm
- temperature: 15 °C
- eluent: *n*-Hexan / 2-propanol 90:10, 1.0 mL/min, isocratic
- retention time: 13.3 min and 16.8 min for enantiomers of the methyl phenyl sulfoxide

F.11 X-Ray Structure Data

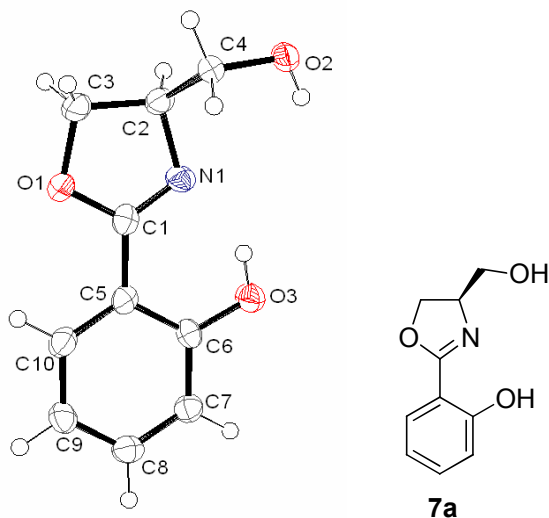


Table 7. Crystal data and structure refinement for (**7a**).

Crystal Data	
Empirical formula	C ₁₀ H ₁₁ N O ₃
Formula weight	193.20
Crystal size	0.42 x 0.06 x 0.03 mm
Crystal description	needle
Crystal colour	colourless
Crystal system	Monoclinic
Space group	C 2
Unit cell dimensions	a = 28.613(4) Å α = 90 deg. b = 4.6550(5) Å β = 99.358(16) deg. c = 14.035(2) Å γ = 90 deg.
Volume	1844.5(4) Å ³
Z. Calculated density	8. 1.391 Mg/m ³
Absorption coefficient	0.104 mm ⁻¹
F(000)	816
Data Collection	
Measurement device type	STOE-IPDS diffractometer
Measurement method	rotation
Temperature	123(1) K
Wavelength	0.71073 Å
Monochromator	graphite
Theta range for data collection	1.89 to 26.83 deg.
Index ranges	-36 ≤ h ≤ 36; -5 ≤ k ≤ 5; -17 ≤ l ≤ 17
Reflections collected / unique	10278 / 3938 [R(int) = 0.0849]
Reflections greater I > 2σ(I)	2147
Absorption correction	None
Refinement	
Refinement method	Full-matrix least-squares on F ²
Hydrogen treatment	:
Data / restraints / parameters	3938 / 1 / 253
Goodness-of-fit on F ²	0.730
Final R indices [I > 2σ(I)]	R1 = 0.0397. wR2 = 0.0516
R indices (all data)	R1 = 0.0959. wR2 = 0.0612
Absolute structure parameter	-0.4(12)
Largest diff. peak and hole	0.147 and -0.136 e.Å ⁻³

Table 8. Atomic coordinates ($\times 10^4$) and equivalent isotropic displacement parameters ($\text{\AA}^2 \times 10^3$).

Atom	x	y	z	U(eq)
O(1)	5352(1)	9428(5)	9080(1)	34(1)
O(2)	4823(1)	5395(5)	6101(1)	34(1)
O(3)	6411(1)	6643(5)	7506(1)	33(1)
N(1)	5537(1)	6575(6)	7880(2)	29(1)
C(1)	5678(1)	8362(7)	8555(2)	27(1)
C(2)	5015(1)	6208(7)	7834(2)	29(1)
C(3)	4906(1)	8035(8)	8692(2)	36(1)
C(4)	4757(1)	7287(7)	6868(2)	26(1)
C(5)	6163(1)	9459(7)	8799(2)	26(1)
C(6)	6507(1)	8500(7)	8250(2)	27(1)
C(7)	6969(1)	9565(7)	8473(2)	29(1)
C(8)	7087(1)	11501(7)	9207(2)	32(1)
C(9)	6751(1)	12477(7)	9755(2)	33(1)
C(10)	6294(1)	11403(7)	9540(2)	31(1)
O(4)	3153(1)	3294(5)	4775(1)	29(1)
O(5)	4317(1)	3885(4)	4371(1)	25(1)
O(6)	3988(1)	2982(5)	7538(1)	35(1)
N(2)	3791(1)	1340(5)	5724(2)	26(1)
C(11)	3436(1)	3050(7)	5641(2)	24(1)
C(12)	3796(1)	59(7)	4758(2)	29(1)
C(13)	3346(1)	1292(8)	4129(2)	32(1)
C(14)	4256(1)	876(7)	4393(2)	28(1)
C(15)	3315(1)	4855(7)	6430(2)	25(1)
C(16)	3603(1)	4733(7)	7343(2)	27(1)
C(17)	3501(1)	6472(8)	8089(2)	35(1)
C(18)	3112(1)	8290(8)	7924(2)	39(1)
C(19)	2817(1)	8372(7)	7031(2)	35(1)
C(20)	2923(1)	6661(6)	6286(2)	27(1)
H(1)	4658	9480	8469	44
H(2)	4796	6802	9186	44
H(3)	5114	5174	6097	40
H(4)	4415	7456	6895	31
H(5)	4877	9221	6739	31
H(6)	4937	4144	7928	34
H(7)	6128	6102	7452	40
H(8)	6064	12020	9913	37
H(9)	6833	13837	10258	39
H(10)	7402	12195	9348	38
H(11)	7203	8938	8112	34
H(12)	3426	2309	3558	38
H(13)	3116	-254	3908	38
H(14)	4430	4474	4926	30
H(15)	4529	8	4821	33
H(16)	4249	88	3736	33
H(17)	3770	-2079	4797	34
H(18)	4001	1914	7061	42
H(19)	2727	6726	5672	33
H(20)	2547	9585	6934	41
H(21)	3045	9500	8430	47
H(22)	3696	6417	8705	42

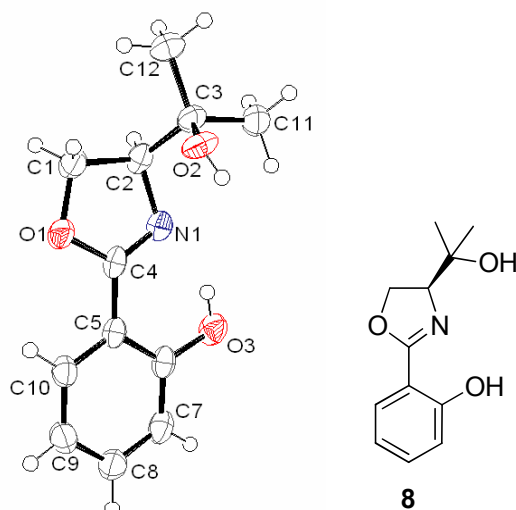


Table 9. Crystal data and structure refinement for **(8)**.

Crystal Data	
Empirical formula	C ₁₂ H ₁₅ N O ₃
Formula weight	221.25
Crystal size	0.44 x 0.28 x 0.08 mm
Crystal description	Rectangular
Crystal colour	Pale
Crystal system	Monoclinic
Space group	C 2
Unit cell dimensions	a = 20.7412(18) Å α = 90 deg. b = 14.1137(12) Å β = 101.928(2) deg. c = 8.1408(7) Å γ = 90 deg.
Volume	2331.6(3) Å ³
Z. Calculated density	8. 1.261 Mg/m ³
Absorption coefficient	0.091 mm ⁻¹
F(000)	944
Data Collection	
Measurement device type	CCD area detector
Measurement method	phi and omega scans
Temperature	153(2) K
Wavelength	0.71073 Å
Monochromator	graphite
Theta range for data collection	2.56 to 30.53 deg.
Index ranges	-29 ≤ h ≤ 29; -19 ≤ k ≤ 20; -11 ≤ l ≤ 11
Reflections collected / unique	14376 / 6837 [R(int) = 0.0394]
Reflections greater I>2σ(I)	5411
Absorption correction	:
Refinement	
Refinement method	Full-matrix least-squares on F ²
Hydrogen treatment	:
Data / restraints / parameters	6837 / 1 / 409
Goodness-of-fit on F ²	0.912
Final R indices [I>2σ(I)]	R1 = 0.0447. wR2 = 0.0841
R indices (all data)	R1 = 0.0569. wR2 = 0.0879
Absolute structure parameter	0.6(7)
Largest diff. peak and hole	0.298 and -0.191 e.Å ⁻³

Table 10. Atomic coordinates ($\times 10^4$) and equivalent isotropic displacement parameters ($\text{\AA}^2 \times 10^3$).

	x	y	z	U(eq)					
O(1)	2091(1)	4593(1)	2187(2)	41(1)	H(28)	1404(8)	5402(12)	-3950(20)	32(4)
O(2)	2099(1)	6848(1)	3997(2)	41(1)	H(29)	576(8)	6034(13)	-2730(20)	37(5)
O(3)	3958(1)	5541(1)	1722(2)	43(1)	H(30)	-190(9)	5045(13)	-1910(20)	37(5)
N(1)	2699(1)	5822(1)	1597(2)	32(1)	H(31A)	-1784(9)	488(13)	-1440(20)	39(5)
C(1)	1611(1)	5343(1)	1668(3)	39(1)	H(31B)	-2175(8)	574(12)	-3300(20)	37(5)
C(2)	2018(1)	6184(1)	1241(2)	34(1)	H(31C)	-2176(8)	1439(12)	-2040(20)	32(5)
C(3)	1947(1)	7078(1)	2247(2)	38(1)	H(32A)	-776(9)	4(13)	-2510(20)	39(5)
C(4)	2684(1)	4968(1)	2084(2)	32(1)	H(32B)	-1209(9)	75(13)	-4350(20)	35(4)
C(5)	3251(1)	4336(1)	2498(2)	31(1)	H(32C)	-548(10)	648(14)	-3960(20)	50(6)
C(6)	3866(1)	4650(1)	2231(2)	34(1)					
C(7)	4397(1)	4033(1)	2517(2)	40(1)					
C(8)	4334(1)	3137(1)	3126(3)	44(1)					
C(9)	3735(1)	2831(1)	3448(3)	44(1)					
C(10)	3203(1)	3427(1)	3133(2)	38(1)					
C(11)	2397(1)	7855(2)	1846(3)	51(1)					
C(12)	1227(1)	7410(2)	1868(3)	53(1)					
O(21)	-775(1)	3544(1)	-1409(2)	33(1)					
O(22)	-1566(1)	1862(1)	-4427(1)	33(1)					
O(23)	742(1)	2479(1)	-3527(1)	33(1)					
N(21)	-295(1)	2255(1)	-2259(2)	25(1)					
C(21)	-1199(1)	2759(1)	-1123(2)	32(1)					
C(22)	-865(1)	1872(1)	-1646(2)	25(1)					
C(23)	-1314(1)	1275(1)	-3001(2)	26(1)					
C(24)	-298(1)	3154(1)	-2089(2)	26(1)					
C(25)	181(1)	3796(1)	-2580(2)	28(1)					
C(26)	680(1)	3421(1)	-3317(2)	27(1)					
C(27)	1128(1)	4027(1)	-3842(2)	32(1)					
C(28)	1093(1)	4986(1)	-3593(2)	39(1)					
C(29)	610(1)	5364(1)	-2827(3)	42(1)					
C(30)	155(1)	4772(1)	-2348(2)	36(1)					
C(31)	-1918(1)	926(1)	-2386(2)	34(1)					
C(32)	-935(1)	445(1)	-3491(2)	36(1)					
H(1A)	1278(10)	5096(14)	670(30)	47(5)					
H(1B)	1426(9)	5463(13)	2640(20)	41(5)					
H(2)	1890(8)	6338(12)	20(20)	32(4)					
H(2O)	2474(11)	6822(17)	4300(30)	61(7)					
H(3O)	3600(11)	5809(16)	1580(30)	61(7)					
H(7)	4785(9)	4222(12)	2280(20)	31(4)					
H(8)	4707(9)	2729(14)	3320(20)	40(5)					
H(9)	3695(9)	2245(14)	3920(20)	42(5)					
H(10)	2779(9)	3233(12)	3400(20)	35(5)					
H(11A)	2865(10)	7643(13)	2110(20)	39(5)					
H(11B)	2282(11)	8022(16)	590(30)	67(7)					
H(11C)	2332(11)	8428(18)	2470(30)	73(7)					
H(12A)	938(11)	6908(17)	2080(30)	61(6)					
H(12B)	1071(11)	7551(15)	640(30)	65(6)					
H(12C)	1205(10)	8010(17)	2490(30)	57(6)					
H(21A)	-1612(8)	2897(11)	-1820(20)	25(4)					
H(21B)	-1219(8)	2779(13)	70(20)	38(5)					
H(22)	-706(7)	1451(11)	-750(20)	24(4)					
H(22O)	-1262(9)	1966(14)	-4880(20)	39(5)					
H(23O)	439(10)	2204(15)	-3270(30)	53(6)					
H(27)	1459(8)	3771(11)	-4330(20)	27(4)					

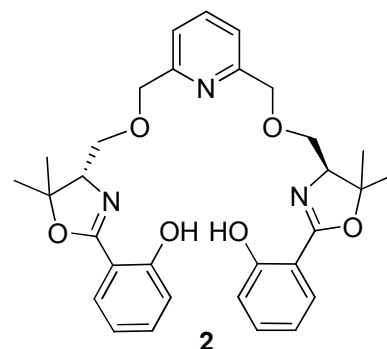
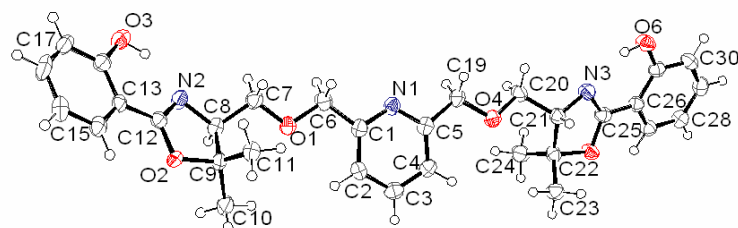


Table 11. Crystal data and structure refinement for (2).

Crystal Data	
Empirical formula	C ₃₁ H ₃₅ N ₃ O ₆
Formula weight	545.62
Crystal size	0.360 x 0.270 x 0.080 mm
Crystal description	prism
Crystal colour	translucent colourless
Crystal system	Monoclinic
Space group	P 2 ₁
Unit cell dimensions	a = 7.13738(17) Å alpha = 90 deg. b = 12.3186(2) Å beta = 90.701(2) deg. c = 15.9754(4) Å gamma = 90 deg.
Volume	1404.49(5) Å ³
Z. Calculated density	2.1290 Mg/m ³
Absorption coefficient	0.734 mm ⁻¹
F(000)	580
Data Collection	
Measurement device type	Oxford Diffraction Gemini Ultra
Measurement method	omega-scan
Temperature	123 K
Wavelength	1.54184 Å
Monochromator	graphite
Theta range for data collection	2.77 to 62.13 deg.
Index ranges	-8 ≤ h ≤ 7; -14 ≤ k ≤ 13; -18 ≤ l ≤ 15
Reflections collected / unique	4904 / 3355 [R(int) = 0.0210]
Reflections greater I > 2σ(I)	2793
Absorption correction	Semi-empirical from equivalents
Max. and min. transmission	1.00000 and 0.83170
Refinement	
Refinement method	Full-matrix least-squares on F ²
Hydrogen treatment	:
Data / restraints / parameters	3355 / 1 / 367
Goodness-of-fit on F ²	0.951
Final R indices [I > 2σ(I)]	R1 = 0.0338. wR2 = 0.0760
R indices (all data)	R1 = 0.0411. wR2 = 0.0779
Absolute structure parameter	-0.09(18)
Largest diff. peak and hole	0.165 and -0.167 e.Å ⁻³

Experimental Part

Table 12. Atomic coordinates ($\times 10^4$) and equivalent isotropic displacement parameters ($\text{\AA}^2 \times 10^3$).

Atom	x	y	z	U(eq)
O(1)	7250(2)	2313(1)	2485(1)	35(1)
O(2)	11092(2)	1991(1)	386(1)	31(1)
O(3)	13927(3)	4784(2)	1225(1)	47(1)
O(4)	-1263(2)	2007(1)	4738(1)	36(1)
O(5)	-5448(3)	666(1)	6403(1)	34(1)
O(6)	-7970(3)	3703(1)	6701(1)	41(1)
N(1)	3007(3)	2579(2)	3651(1)	32(1)
N(2)	11496(3)	3226(2)	1415(1)	34(1)
N(3)	-5326(3)	2449(2)	6090(1)	33(1)
C(1)	4323(3)	2091(2)	3195(2)	30(1)
C(2)	4292(4)	995(2)	3020(2)	33(1)
C(3)	2814(4)	384(2)	3317(2)	36(1)
C(4)	1431(4)	879(2)	3789(2)	34(1)
C(5)	1594(4)	1977(2)	3957(2)	31(1)
C(6)	5821(4)	2862(2)	2916(2)	37(1)
C(7)	8576(4)	3059(2)	2172(2)	36(1)
C(8)	10099(4)	2442(2)	1731(2)	32(1)
C(9)	9488(3)	1789(2)	951(2)	30(1)
C(10)	9378(4)	585(2)	1117(2)	41(1)
C(11)	7770(4)	2208(2)	505(2)	35(1)
C(12)	11945(3)	2892(2)	681(2)	28(1)
C(13)	13302(3)	3442(2)	153(2)	28(1)
C(14)	13655(3)	3081(2)	-657(2)	32(1)
C(15)	14873(4)	3637(2)	-1170(2)	42(1)
C(16)	15746(4)	4556(2)	-867(2)	46(1)
C(17)	15444(4)	4934(2)	-69(2)	41(1)
C(18)	14226(4)	4377(2)	450(2)	35(1)
C(19)	314(4)	2615(2)	4503(2)	38(1)
C(20)	-2320(4)	2556(2)	5350(2)	35(1)
C(21)	-4089(4)	1914(2)	5482(2)	31(1)
C(22)	-3835(4)	752(2)	5821(2)	30(1)
C(23)	-4083(4)	-102(2)	5152(2)	37(1)
C(24)	-2103(4)	565(2)	6352(2)	39(1)
C(25)	-6017(4)	1691(2)	6539(2)	31(1)
C(26)	-7496(4)	1853(2)	7156(2)	30(1)
C(27)	-8013(4)	1019(2)	7694(2)	33(1)
C(28)	-9488(4)	1149(2)	8236(2)	36(1)
C(29)	-10452(4)	2121(2)	8241(2)	38(1)
C(30)	-9935(4)	2963(2)	7729(2)	37(1)
C(31)	-8453(4)	2848(2)	7185(2)	32(1)
H(2)	5260	669	2705	39
H(3)	2745	-371	3198	43
H(3O)	13050(40)	4370(30)	1503(18)	56
H(4)	399	474	3992	41
H(6A)	5258	3420	2544	44
H(6B)	6368	3235	3410	44
H(6O)	-7030(40)	3520(20)	6375(18)	49
H(7A)	9124	3488	2638	44
H(7B)	7955	3566	1776	44
H(8)	10727	1941	2140	38
H(10A)	8483	448	1565	49
H(10B)	10617	315	1286	49
H(10C)	8961	210	606	49
H(11A)	7994	2953	316	42
H(11B)	6708	2199	888	42
H(11C)	7488	1745	21	42
H(14)	13051	2444	-860	39
H(15)	15104	3390	-1722	50
H(16)	16581	4940	-1218	55
H(17)	16064	5570	125	49
H(19A)	1008	2849	5012	45
H(19B)	-104	3275	4200	45
H(20A)	-2627	3299	5158	42
H(20B)	-1594	2608	5881	42
H(21)	-4776	1869	4934	38
H(23A)	-3170	18	4708	44
H(23B)	-5354	-56	4915	44
H(23C)	-3888	-823	5397	44
H(24A)	-2127	1045	6840	47
H(24B)	-987	720	6021	47
H(24C)	-2069	-193	6538	47
H(27)	-7344	352	7688	40
H(28)	-9835	577	8601	43
H(29)	-11487	2209	8603	45
H(30)	-10600	3630	7749	44

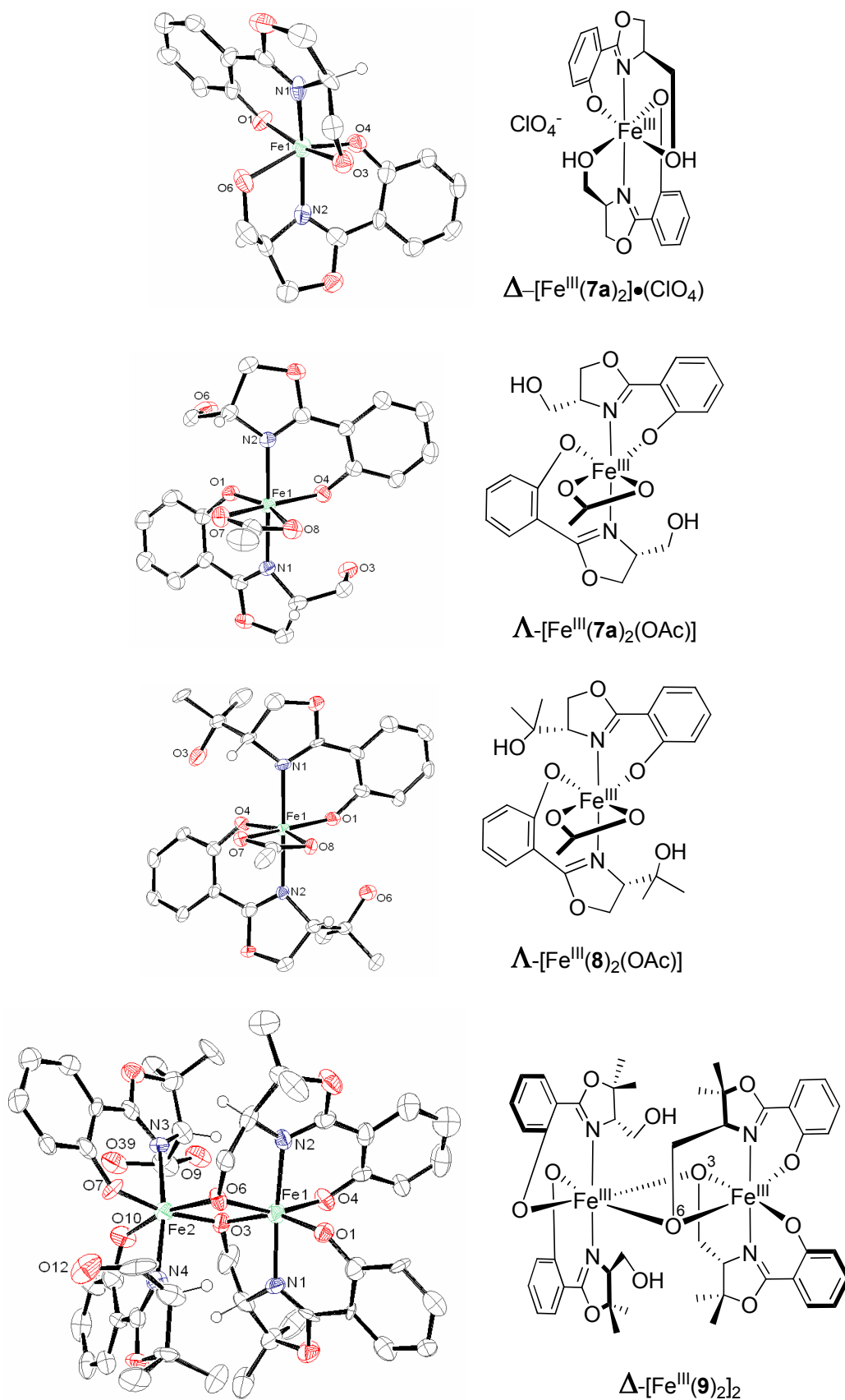


Figure 8. All iron(III) oxazoline complexes, [Fe^{III}(**7a**)₂](ClO₄), [Fe^{III}(**7a**)₂(OAc)], [Fe^{III}(**8**)₂(OAc)] and [Fe^{III}(**9**)₂]₂.

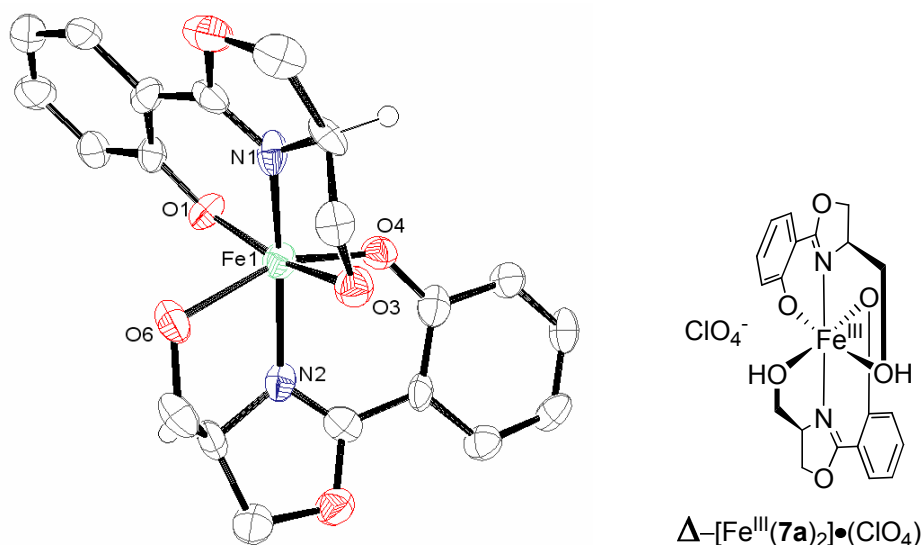


Table 13. Crystal data and structure refinement for [Fe^{III}(7a)₂]•(ClO₄).

Crystal Data	
Empirical formula	C ₂₀ H ₂₀ Fe N ₂ O ₆ , Cl O ₄
Formula weight	539.68
Crystal size	0.270 x 0.080 x 0.010 mm
Crystal description	needle
Crystal colour	purple
Crystal system	Orthorhombic
Space group	P 21 21 21
Unit cell dimensions	a = 6.3707(2) Å alpha = 90 deg. b = 11.7037(5) Å beta = 90 deg. c = 28.8800(9) Å gamma = 90 deg.
Volume	2153.32(13) Å ³
Z, Calculated density	4, 1.665 Mg/m ³
Absorption coefficient	7.326 mm ⁻¹
F(000)	1108
Data Collection	
Measurement device type	
Measurement method	
Temperature	123 K
Wavelength	1.54184 Å
Monochromator	graphite
Theta range for data collection	3.06 to 51.57 deg.
Index ranges	-6 ≤ h ≤ 4, -10 ≤ k ≤ 11, -27 ≤ l ≤ 29
Reflections collected / unique	4454 / 2137 [R(int) = 0.0825]
Reflections greater I > 2σ(I)	1631
Absorption correction	Semi-empirical from equivalents
Max. and min. transmission	1.00000 and 0.57176
Refinement	
Refinement method	Full-matrix least-squares on F ²
Hydrogen treatment	:
Data / restraints / parameters	2137 / 0 / 317
Goodness-of-fit on F ²	1.115
Final R indices [I > 2σ(I)]	R1 = 0.0625, wR2 = 0.1235
R indices (all data)	R1 = 0.0903, wR2 = 0.1362
Absolute structure parameter	-0.002(16)
Largest diff. peak and hole	0.553 and -0.505 e.Å ⁻³

Table 14. Atomic coordinates ($\times 10^4$) and equivalent isotropic displacement parameters ($\text{\AA}^2 \times 10^3$).

	x	y	z	U(eq)					
Fe(1)	2663(3)	1005(2)	3612(1)	33(1)	H(19)	-1351	-445	4147	44
O(1)	688(12)	1172(7)	3133(2)	35(3)	H(20A)	-1280	1030	4686	52
O(2)	3240(15)	4465(7)	3304(3)	48(4)	H(20B)	1222	926	4751	52
O(3)	4980(13)	1515(7)	4165(3)	38(3)					
O(4)	4735(13)	69(6)	3345(2)	35(3)					
O(5)	2226(14)	-1941(6)	4425(3)	44(3)					
O(6)	373(12)	1618(7)	4139(3)	41(3)					
N(1)	3577(15)	2605(8)	3472(3)	35(4)					
N(2)	1769(15)	-374(8)	3986(3)	33(4)					
C(1)	-190(19)	2096(11)	2965(4)	33(5)					
C(2)	-2090(20)	1950(11)	2705(4)	41(5)					
C(3)	-3100(20)	2867(12)	2514(4)	45(5)					
C(4)	-2320(20)	3957(13)	2558(3)	43(5)					
C(5)	-500(20)	4143(11)	2812(4)	44(5)					
C(6)	560(20)	3202(10)	3005(4)	32(5)					
C(7)	2500(20)	3404(11)	3273(4)	34(5)					
C(8)	5050(20)	4422(10)	3632(4)	45(5)					
C(9)	5381(18)	3140(9)	3711(4)	32(5)					
C(10)	5310(20)	2737(10)	4198(4)	35(5)					
C(11)	5640(19)	-891(11)	3478(4)	39(5)					
C(12)	7490(20)	-1247(9)	3269(4)	35(4)					
C(13)	8489(19)	-2235(11)	3385(4)	37(5)					
C(14)	7730(20)	-2906(10)	3746(4)	41(5)					
C(15)	5910(20)	-2601(10)	3967(4)	39(5)					
C(16)	4808(19)	-1597(10)	3842(4)	33(4)					
C(17)	2880(20)	-1267(11)	4074(4)	35(5)					
C(18)	430(20)	-1341(9)	4626(4)	43(5)					
C(19)	0(20)	-330(11)	4316(4)	37(5)					
C(20)	60(20)	857(10)	4526(4)	44(5)					
Cl(1)	204(6)	4645(3)	4615(1)	48(1)					
O(7)	255(16)	3533(7)	4802(3)	67(4)					
O(8)	-1693(16)	5099(10)	4552(4)	104(6)					
O(9)	2024(18)	5179(8)	4549(5)	105(6)					
O(10)	200(30)	4187(15)	4116(4)	58(7)					
O(10A)	200(30)	5200(16)	5117(6)	60(8)					
H(2)	-2648	1205	2665	50					
H(3)	-4366	2747	2348	54					
H(3A)	4923	1233	4432	45					
H(4)	-3026	4580	2416	51					
H(5)	23	4896	2855	53					
H(6)	406	2296	4235	49					
H(8A)	4702	4815	3926	54					
H(8B)	6310	4779	3495	54					
H(9)	6723	2891	3562	38					
H(10A)	6642	2908	4360	42					
H(10B)	4140	3106	4368	42					
H(12)	8080	-781	3034	42					
H(13)	9706	-2466	3219	45					
H(14)	8470	-3572	3839	49					
H(15)	5371	-3073	4207	47					
H(18A)	750	-1084	4944	51					
H(18B)	-815	-1850	4637	51					

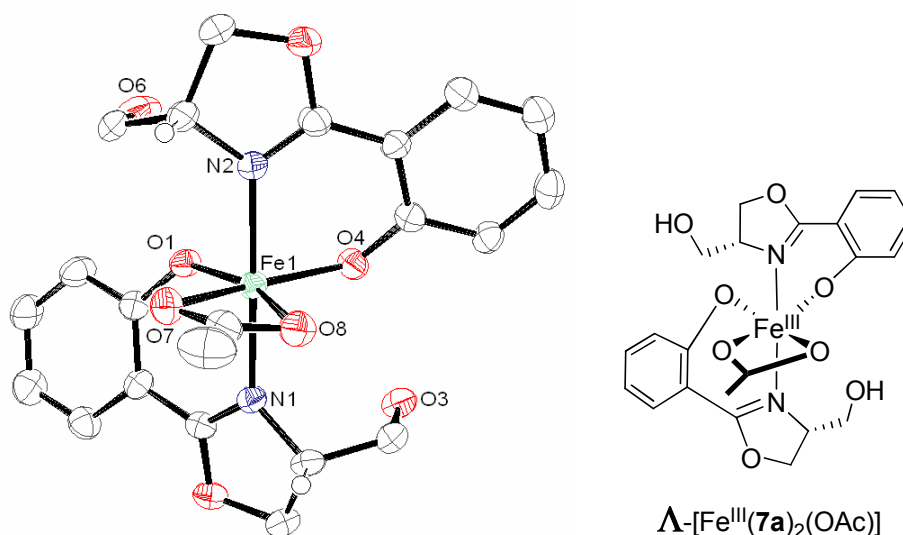


Table 15. Crystal data and structure refinement for [Fe^{III}(**7a**)₂(OAc)].

Crystal Data	
Empirical formula	C ₂₂ H ₂₃ Fe N ₂ O ₈
Formula weight	499.27
Crystal size	0.200 x 0.040 x 0.040 mm
Crystal description	rod
Crystal colour	brown to red
Crystal system	Monoclinic
Space group	C 2
Unit cell dimensions	a = 18.7581(5) Å alpha = 90 deg. b = 8.2252(2) Å beta = 91.301(2) deg. c = 15.2620(4) Å gamma = 90 deg.
Volume	2354.15(10) Å ³
Z, Calculated density	4, 1.409 Mg/m ³
Absorption coefficient	5.568 mm ⁻¹
F(000)	1036
Data Collection	
Measurement device type	Oxford Diffraction Gemini Ultra
Measurement method	omega-scan
Temperature	123 K
Wavelength	1.54184 Å
Monochromator	graphite
Theta range for data collection	4.72 to 62.28 deg.
Index ranges	-21 ≤ h ≤ 21, -9 ≤ k ≤ 9, 0 ≤ l ≤ 17
Reflections collected / unique	3621 / 3621 [R(int) = 0.0000]
Reflections greater I > 2σ(I)	2889
Absorption correction	Semi-empirical from equivalents
Max. and min. transmission	1.00000 and 0.48031
Refinement	
Refinement method	Full-matrix least-squares on F ²
Hydrogen treatment	:
Data / restraints / parameters	3621 / 1 / 304
Goodness-of-fit on F ²	0.964
Final R indices [I > 2σ(I)]	R1 = 0.0381, wR2 = 0.0860
R indices (all data)	R1 = 0.0489, wR2 = 0.0896
Absolute structure parameter	-0.026(4)
Largest diff. peak and hole	0.307 and -0.332 e.Å ⁻³

Experimental Part

Table 16. Atomic coordinates ($\times 10^4$) and equivalent isotropic displacement parameters ($\text{\AA}^2 \times 10^3$).

	x	y	z	U(eq)
Fe(1)	2995(1)	624(1)	2799(1)	25(1)
O(1)	2199(1)	-835(3)	2638(2)	29(1)
O(2)	1888(1)	833(4)	5190(2)	32(1)
O(3)	3736(2)	-872(4)	5009(2)	35(1)
O(4)	3766(1)	-773(3)	3148(2)	30(1)
O(5)	4045(1)	-479(4)	441(2)	39(1)
O(6)	2162(2)	-1650(5)	866(2)	53(1)
O(7)	2523(2)	2807(4)	2324(2)	38(1)
O(8)	3577(1)	2802(4)	2940(2)	35(1)
N(1)	2646(2)	945(4)	4078(2)	25(1)
N(2)	3323(2)	275(4)	1509(2)	28(1)
C(1)	1557(2)	-817(5)	2991(2)	28(1)
C(2)	989(2)	-1579(6)	2552(3)	41(2)
C(3)	313(2)	-1586(6)	2891(3)	43(2)
C(4)	186(2)	-866(6)	3693(3)	41(2)
C(5)	740(2)	-154(6)	4153(3)	36(2)
C(6)	1433(2)	-125(5)	3820(3)	28(1)
C(7)	2013(2)	603(6)	4340(2)	26(1)
C(8)	2567(2)	1323(5)	5593(3)	34(1)
C(9)	3057(2)	1633(5)	4831(3)	31(1)
C(10)	3788(2)	847(6)	4963(3)	35(1)
C(11)	4410(2)	-924(5)	2800(3)	27(1)
C(12)	5009(2)	-1270(5)	3343(3)	31(1)
C(13)	5664(2)	-1458(5)	2996(3)	39(2)
C(14)	5773(2)	-1325(6)	2099(3)	41(2)
C(15)	5206(2)	-964(6)	1570(3)	39(2)
C(16)	4513(2)	-759(5)	1897(3)	30(1)
C(17)	3931(2)	-307(5)	1306(3)	31(1)
C(18)	3389(2)	-52(6)	-19(3)	40(1)
C(19)	2929(2)	705(7)	686(2)	35(1)
C(20)	2167(2)	30(7)	678(3)	47(2)
C(21)	3087(2)	3593(5)	2537(3)	33(1)
C(22)	3172(3)	5323(6)	2326(3)	56(2)
H(2)	1069	-2103	2008	49
H(3)	-67	-2089	2573	52
H(3O)	3730(20)	-1180(60)	4490(30)	42
H(4)	-281	-866	3923	49
H(5)	653	329	4706	43
H(6O)	2160(30)	-1880(60)	1440(40)	63
H(8A)	2761	450	5976	40
H(8B)	2509	2322	5946	40
H(9)	3116	2831	4747	37
H(10A)	4096	1150	4470	42
H(10B)	4014	1263	5511	42
H(12)	4954	-1373	3958	37
H(13)	6060	-1686	3375	46
H(14)	6233	-1484	1865	49
H(15)	5276	-845	959	47
H(18A)	3157	-1029	-274	48
H(18B)	3479	736	-494	48
H(19)	2916	1913	614	42
H(20A)	1885	615	1119	56
H(20B)	1940	219	95	56
H(22A)	2799	5954	2611	67
H(22B)	3133	5474	1690	67
H(22C)	3642	5697	2538	67

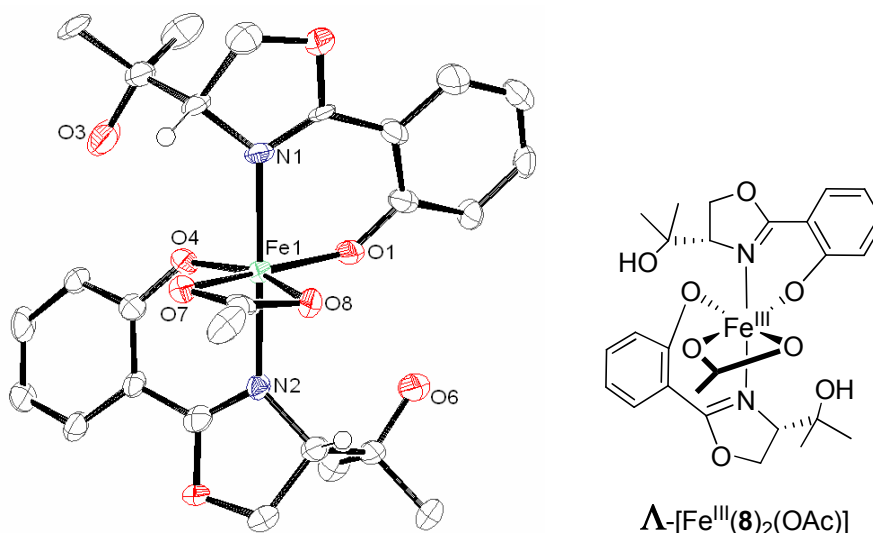


Table 17. Crystal data and structure refinement for [Fe^{III}(**8**)₂(OAc)].

Crystal Data	
Empirical formula	C ₂₆ H ₃₁ Fe N ₂ O ₈
Formula weight	555.38
Crystal size	0.070 x 0.060 x 0.030 mm
Crystal description	flat prism
Crystal colour	purple
Crystal system	Orthorhombic
Space group	P 21 21 21
Unit cell dimensions	a = 11.7914(3) Å α = 90 deg. b = 12.0459(3) Å β = 90 deg. c = 36.3297(12) Å γ = 90 deg.
Volume	5160.2(3) Å ³
Z, Calculated density	8, 1.430 Mg/m ³
Absorption coefficient	5.137 mm ⁻¹
F(000)	2328
Data Collection	
Measurement device type	Oxford Diffraction Gemini Ultra
Measurement method	omega-scan
Temperature	123 K
Wavelength	1.54178 Å
Monochromator	graphite
Theta range for data collection	3.87 to 51.45 deg.
Index ranges	-9 ≤ h ≤ 11, -10 ≤ k ≤ 12, -35 ≤ l ≤ 36
Reflections collected / unique	9296 / 4829 [R(int) = 0.0421]
Reflections greater I > 2σ(I)	3679
Absorption correction	Semi-empirical from equivalents
Max. and min. transmission	1.00000 and 0.82410
Refinement	
Refinement method	Full-matrix least-squares on F ²
Hydrogen treatment	:
Data / restraints / parameters	4829 / 0 / 677
Goodness-of-fit on F ²	0.971
Final R indices [I > 2σ(I)]	R1 = 0.0382, wR2 = 0.0766
R indices (all data)	R1 = 0.0574, wR2 = 0.0830
Absolute structure parameter	0.001(4)
Largest diff. peak and hole	0.335 and -0.219 e.Å ⁻³

Experimental Part

Table 18. Atomic coordinates ($\times 10^4$) and equivalent isotropic displacement parameters ($\text{\AA}^2 \times 10^3$).

	x	y	z	U(eq)					
Fe(1)	31(1)	5006(1)	417(1)	23(1)	C(51)	2521(6)	7918(4)	2728(2)	24(2)
O(1)	1062(3)	4264(3)	731(1)	29(2)	C(52)	2451(5)	8010(5)	3134(2)	36(2)
O(2)	-1028(3)	1658(3)	374(1)	32(2)	H(2A)	2850	3522	1043	34
O(3)	-3024(3)	4697(3)	608(1)	51(2)	H(3)	-2407	4867	709	62
O(4)	-1002(3)	5760(3)	732(1)	25(1)	H(3A)	3296	1691	1169	41
O(5)	1028(3)	8323(3)	292(1)	30(2)	H(4A)	2153	261	959	58
O(6)	3027(3)	5490(3)	713(1)	49(2)	H(5A)	477	664	661	55
O(7)	-814(3)	5398(3)	-81(1)	25(1)	H(6)	2387	5321	798	58
O(8)	820(3)	4573(3)	-92(1)	25(1)	H(8A)	-2665	1665	194	40
N(1)	-910(4)	3510(4)	415(1)	22(2)	H(8B)	-1764	1992	-122	40
N(2)	948(4)	6485(4)	399(1)	21(2)	H(9)	-2153	3758	26	30
C(1)	1332(5)	3204(5)	788(2)	26(3)	H(11A)	-2161	3065	989	57
C(2)	2350(5)	2945(5)	968(1)	28(2)	H(11B)	-2912	2087	817	57
C(3)	2623(5)	1859(5)	1037(2)	34(2)	H(11C)	-3507	3063	1045	57
C(4)	1940(6)	1012(5)	918(2)	48(3)	H(12A)	-4774	3537	514	43
C(5)	952(6)	1256(5)	739(2)	46(3)	H(12B)	-4228	2565	272	43
C(6)	620(5)	2339(4)	668(2)	29(2)	H(12C)	-4222	3815	123	43
C(7)	-444(5)	2564(5)	485(2)	23(2)	H(14A)	-2723	6566	1051	32
C(8)	-1952(5)	2069(5)	143(2)	33(3)	H(15A)	-3323	8412	1071	46
C(9)	-2054(5)	3295(4)	252(2)	25(2)	H(16A)	-2305	9768	750	44
C(10)	-3029(5)	3542(5)	526(2)	32(2)	H(17A)	-652	9336	463	39
C(11)	-2890(5)	2882(6)	874(2)	48(3)	H(20A)	2702	8314	155	35
C(12)	-4163(5)	3347(5)	343(2)	36(3)	H(20B)	1894	7822	-164	35
C(13)	-1311(5)	6822(5)	742(2)	25(2)	H(21)	2342	6166	69	32
C(14)	-2293(5)	7121(5)	929(1)	26(2)	H(23A)	4750	6673	638	46
C(15)	-2657(5)	8217(5)	939(2)	38(2)	H(23B)	4265	7560	350	46
C(16)	-2038(5)	9024(5)	754(2)	37(3)	H(23C)	4358	6279	237	46
C(17)	-1070(5)	8765(5)	582(2)	32(2)	H(24A)	1988	7209	1003	47
C(18)	-653(5)	7671(4)	571(2)	23(2)	H(24B)	2712	8158	804	47
C(19)	446(5)	7442(5)	421(2)	26(2)	H(24C)	3312	7335	1090	47
C(20)	2019(5)	7860(4)	106(2)	29(2)	H(26A)	622	4596	-770	45
C(21)	2143(5)	6703(4)	269(2)	26(2)	H(26B)	-127	5703	-767	45
C(22)	3005(5)	6595(4)	585(2)	29(2)	H(26C)	-731	4514	-750	45
C(23)	4201(5)	6795(5)	440(2)	38(2)	H(11)	4780	7548	1587	53
C(24)	2730(5)	7396(5)	899(2)	39(2)	H(14)	29	8077	1749	64
C(25)	-9(6)	4969(4)	-265(1)	22(2)	H(28A)	-312	6381	1439	31
C(26)	-66(5)	4944(5)	-673(1)	37(2)	H(29A)	-844	4560	1378	39
Fe(2)	2481(1)	7918(1)	2046(1)	25(1)	H(30A)	227	3144	1647	43
O(9)	1449(3)	7184(3)	1733(1)	28(1)	H(31A)	1885	3584	1948	42
O(10)	3535(3)	4628(3)	2144(1)	30(2)	H(34A)	5215	4654	2282	40
O(11)	5431(3)	7427(3)	1672(1)	44(2)	H(34B)	4404	5163	2597	40
O(12)	3461(3)	8739(3)	1732(1)	28(1)	H(35)	4852	6820	2344	33
O(13)	1449(3)	11211(3)	2232(1)	34(2)	H(37A)	4430	5589	1446	59
O(14)	-591(3)	8261(3)	1845(1)	54(2)	H(37B)	5296	4736	1633	59
O(15)	1733(3)	7451(3)	2551(1)	27(1)	H(37C)	5735	5584	1325	59
O(16)	3338(3)	8337(3)	2550(1)	26(1)	H(38A)	7227	6364	1774	57
N(3)	3445(4)	6460(4)	2031(1)	24(2)	H(38B)	6804	5433	2056	57
N(4)	1527(4)	9383(4)	2104(1)	26(2)	H(38C)	6810	6711	2177	57
C(27)	1169(5)	6110(5)	1714(1)	22(2)	H(40A)	5305	9544	1499	33
C(28)	158(5)	5816(5)	1539(1)	26(2)	H(41A)	5962	11342	1559	45
C(29)	-168(5)	4737(5)	1508(2)	32(2)	H(42A)	4896	12694	1871	44
C(30)	471(6)	3894(5)	1663(2)	36(3)	H(43A)	3161	12214	2116	40
C(31)	1452(6)	4159(5)	1837(2)	35(3)	H(46A)	-228	11196	2346	41
C(32)	1849(5)	5260(4)	1860(2)	25(2)	H(46B)	547	10735	2678	41
C(33)	2936(5)	5491(5)	2012(2)	23(2)	H(47)	203	9038	2457	34
C(34)	4528(5)	5106(5)	2328(2)	34(2)	H(49A)	-2296	9439	1928	50
C(35)	4637(5)	6263(4)	2152(2)	27(2)	H(49B)	-1774	10396	2182	50
C(36)	5472(5)	6327(5)	1827(2)	34(3)	H(49C)	-1814	9142	2327	50
C(37)	5210(6)	5485(5)	1532(2)	49(3)	H(50A)	362	9890	1495	59
C(38)	6688(5)	6197(5)	1971(2)	47(3)	H(50B)	-254	10903	1698	59
C(39)	3817(5)	9783(5)	1773(2)	28(3)	H(50C)	-974	10072	1446	59
C(40)	4861(5)	10080(5)	1625(1)	28(2)	H(52A)	3204	8175	3234	43
C(41)	5248(5)	11148(5)	1662(2)	37(2)	H(52B)	2177	7307	3237	43
C(42)	4616(6)	11958(5)	1847(2)	36(3)	H(52C)	1926	8608	3200	43
C(43)	3592(6)	11668(5)	1990(2)	34(3)					
C(44)	3151(5)	10597(5)	1957(2)	25(2)					
C(45)	2030(5)	10339(5)	2094(2)	29(3)					
C(46)	453(5)	10753(5)	2407(2)	34(3)					
C(47)	352(5)	9570(4)	2251(2)	28(2)					
C(48)	-553(5)	9405(5)	1946(2)	33(2)					
C(49)	-1711(5)	9614(5)	2110(2)	41(3)					
C(50)	-336(5)	10130(6)	1618(2)	49(3)					

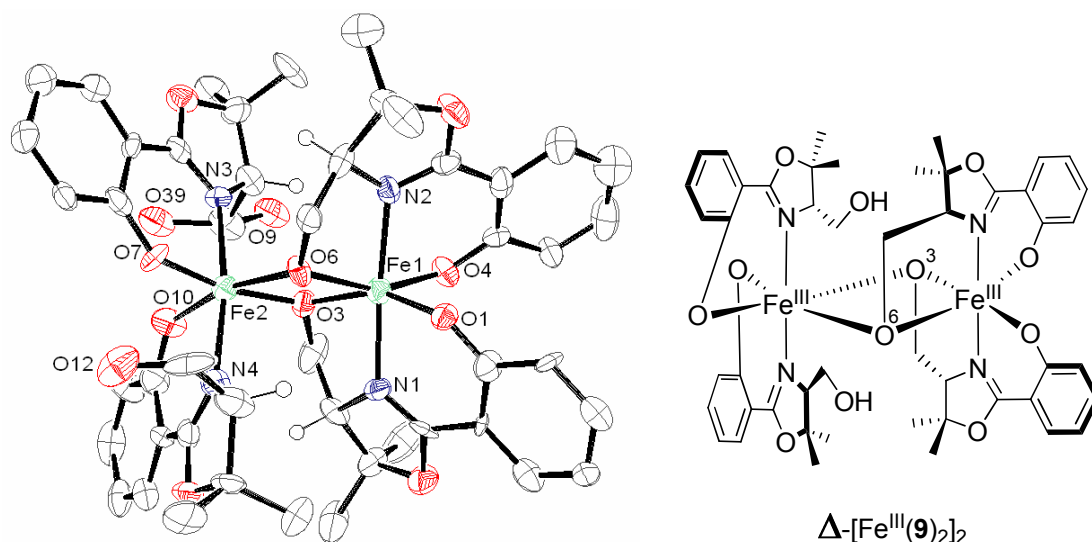


Table 19. Crystal data and structure refinement for [Fe^{III}(9)₂]₂.

Crystal Data	
Empirical formula	C ₄₈ H ₅₄ Fe ₂ N ₄ O ₁₂
Formula weight	990.65
Crystal size	0.050 x 0.020 x 0.020 mm
Crystal description	prism
Crystal colour	ruby-coloured
Crystal system	Monoclinic
Space group	P 21
Unit cell dimensions	a = 13.9286(2) Å alpha = 90 deg. b = 24.2175(3) Å beta = 92.3362(12) deg. c = 14.2035(2) Å gamma = 90 deg.
Volume	4787.08(11) Å ³
Z, Calculated density	4, 1.375 Mg/m ³
Absorption coefficient	5.405 mm ⁻¹
F(000)	2072
Data Collection	
Measurement device type	Oxford Diffraction Gemini Ultra
Measurement method	omega-scan
Temperature	123 K
Wavelength	1.54184 Å
Monochromator	graphite
Theta range for data collection	3.11 to 51.59 deg.
Index ranges	-14 ≤ h ≤ 14, -24 ≤ k ≤ 24, 0 ≤ l ≤ 14
Reflections collected / unique	8533 / 8533 [R(int) = 0.0000]
Reflections greater I > 2σ(I)	5626
Absorption correction	Semi-empirical from equivalents
Max. and min. transmission	1.00000 and 0.76099
Refinement	
Refinement method	Full-matrix least-squares on F ²
Hydrogen treatment	:
Data / restraints / parameters	8533 / 1 / 1219
Goodness-of-fit on F ²	0.966
Final R indices [I > 2σ(I)]	R1 = 0.0484, wR2 = 0.1088
R indices (all data)	R1 = 0.0764, wR2 = 0.1162
Absolute structure parameter	-0.012(5)
Largest diff. peak and hole	1.185 and -0.657 e.Å ⁻³

Experimental Part

Table 20. Atomic coordinates ($\times 10^4$) and equivalent isotropic displacement parameters ($\text{\AA}^2 \times 10^3$).

	x	y	z	U(eq)					
Fe(1)	6034(1)	8438(1)	9967(1)	31(1)	O(16)	-286(1)	8041(1)	4596(1)	43(1)
Fe(2)	7895(1)	8359(1)	8757(1)	32(1)	O(17)	497(1)	9447(1)	3056(2)	48(1)
O(1)	5866(1)	8679(1)	11274(1)	29(1)	O(18)	2478(1)	8172(1)	4329(1)	31(1)
O(2)	5139(2)	10079(1)	9608(2)	46(1)	O(19)	4222(1)	8424(1)	5592(1)	36(1)
O(3)	6457(1)	8514(1)	8624(1)	36(1)	O(20)	2512(2)	9767(1)	6358(2)	50(1)
O(4)	4665(1)	8293(1)	9742(1)	36(1)	O(21)	2528(3)	8743(2)	8081(3)	71(1)
O(5)	5732(1)	7012(1)	11506(2)	46(1)	O(22)	3284(2)	7756(1)	6917(1)	45(1)
O(6)	7456(1)	8255(1)	10076(1)	29(1)	O(23)	4134(2)	6466(1)	5156(1)	42(1)
O(7)	9176(1)	8090(1)	9026(1)	35(1)	O(24)	5498(2)	7593(1)	4571(2)	72(1)
O(8)	7880(1)	6690(1)	7751(1)	41(1)	N(5)	1049(2)	7091(1)	4568(2)	30(1)
O(10)	8119(2)	8630(1)	7492(1)	43(1)	N(6)	1005(2)	8760(1)	4032(2)	33(1)
O(11)	8859(1)	10031(1)	9133(1)	39(1)	N(7)	2505(2)	8840(1)	6170(2)	32(1)
O(12)	10302(2)	8952(1)	9919(2)	58(1)	N(8)	3584(2)	7325(1)	5155(2)	31(1)
O(39)	7557(3)	7707(2)	6247(3)	55(1)	C(51)	478(2)	7268(1)	2627(2)	35(1)
N(1)	5943(2)	9273(1)	9696(2)	34(1)	C(52)	222(2)	7290(1)	1663(2)	29(1)
N(2)	6075(2)	7603(1)	10362(2)	29(1)	C(53)	-132(2)	6834(1)	1190(2)	44(1)
N(3)	7602(2)	7570(1)	8215(2)	31(1)	C(54)	-279(2)	6348(1)	1660(2)	37(1)
N(4)	8385(2)	9148(1)	9213(2)	34(1)	C(55)	-64(2)	6309(2)	2619(2)	40(1)
C(1)	5386(2)	9097(1)	11589(2)	36(1)	C(56)	336(2)	6775(1)	3103(2)	24(1)
C(2)	5079(2)	9076(1)	12530(2)	28(1)	C(57)	581(2)	6733(1)	4091(2)	34(1)
C(3)	4624(2)	9500(1)	12932(2)	37(1)	C(58)	454(2)	6417(1)	5598(2)	39(1)
C(4)	4429(2)	9999(1)	12430(2)	39(1)	C(59)	1191(2)	6880(1)	5552(2)	41(1)
C(5)	4703(2)	10019(1)	11519(2)	39(1)	C(60)	1141(2)	7387(1)	6184(2)	46(1)
C(6)	5164(2)	9583(1)	11092(2)	25(1)	C(61)	-555(2)	6599(2)	5879(2)	51(1)
C(7)	5441(2)	9629(1)	10101(2)	29(1)	C(62)	805(3)	5896(2)	6126(2)	55(2)
C(8)	5342(2)	9941(1)	8616(2)	41(1)	C(63)	-909(2)	8323(1)	4139(2)	41(1)
C(9)	6052(2)	9467(1)	8720(2)	35(1)	C(64)	-1903(2)	8190(2)	4144(2)	50(1)
C(10)	5997(3)	8959(2)	8121(2)	53(1)	C(65)	-2560(2)	8507(2)	3643(2)	62(2)
C(11)	5831(3)	10456(2)	8232(3)	95(2)	C(66)	-2373(2)	8965(2)	3146(3)	56(1)
C(12)	4413(3)	9802(2)	8122(3)	76(2)	C(67)	-1434(2)	9113(2)	3129(2)	53(1)
C(13)	4110(2)	8010(1)	10289(2)	29(1)	C(68)	-699(2)	8814(2)	3606(3)	52(2)
C(14)	3135(2)	8160(1)	10323(2)	37(1)	C(69)	284(2)	9006(2)	3588(2)	44(1)
C(15)	2535(2)	7881(2)	10891(2)	58(1)	C(70)	1569(2)	9470(1)	3028(2)	40(1)
C(16)	2845(3)	7458(2)	11463(2)	59(1)	C(71)	1877(2)	9057(1)	3833(2)	35(1)
C(17)	3779(2)	7281(2)	11435(2)	48(1)	C(72)	2635(2)	8621(1)	3664(2)	35(1)
C(18)	4425(2)	7571(1)	10851(2)	37(1)	C(73)	1839(2)	10051(1)	3234(3)	62(1)
C(19)	5430(2)	7400(1)	10890(2)	32(1)	C(74)	1830(2)	9283(2)	2077(2)	54(1)
C(20)	6800(2)	6957(1)	11448(2)	40(1)	C(75)	4494(2)	8927(1)	5514(2)	26(1)
C(21)	7025(2)	7375(1)	10609(2)	38(1)	C(76)	5434(2)	9062(2)	5243(2)	45(1)
C(22)	7709(2)	7847(1)	10772(2)	32(1)	C(77)	5749(2)	9603(1)	5103(2)	38(1)
C(23)	7238(2)	7124(2)	12399(2)	55(1)	C(78)	5135(2)	10030(2)	5214(2)	46(1)
C(24)	7007(3)	6358(2)	11230(3)	69(2)	C(79)	4221(2)	9936(1)	5514(2)	38(1)
C(25)	9641(2)	7624(1)	8906(2)	34(1)	C(80)	3918(2)	9394(1)	5669(2)	27(1)
C(26)	10609(2)	7584(1)	9163(2)	31(1)	C(81)	2959(2)	9303(1)	6065(2)	35(1)
C(27)	11128(2)	7104(1)	9070(2)	37(1)	C(82)	1551(2)	9595(1)	6683(2)	42(1)
C(28)	10665(2)	6626(1)	8698(2)	40(1)	C(83)	1605(2)	8957(1)	6664(2)	39(1)
C(29)	9713(2)	6661(1)	8466(2)	37(1)	C(84)	1613(2)	8650(2)	7595(2)	49(1)
C(30)	9190(2)	7145(1)	8525(2)	26(1)	C(85)	801(2)	9837(2)	5981(2)	60(2)
C(31)	8216(2)	7157(1)	8173(2)	29(1)	C(86)	1464(2)	9870(2)	7632(2)	58(2)
C(32)	6827(2)	6770(1)	7542(3)	48(1)	C(87)	3465(2)	7247(1)	7220(2)	45(1)
C(33)	6710(2)	7397(1)	7675(2)	46(1)	C(88)	3451(2)	7149(2)	8198(2)	45(1)
C(34A)	6607(2)	7752(2)	6771(2)	50(1)	C(89)	3567(2)	6633(2)	8557(2)	58(1)
C(35)	6301(2)	6458(2)	8287(2)	59(1)	C(90)	3711(2)	6196(2)	7958(2)	59(2)
C(36)	6626(2)	6534(1)	6529(2)	51(1)	C(91)	3779(2)	6283(2)	6992(2)	47(1)
C(37)	8219(2)	9129(1)	7149(2)	43(1)	C(92)	3679(2)	6810(1)	6632(2)	33(1)
C(38)	8155(2)	9185(2)	6140(2)	54(2)	C(93)	3782(2)	6889(1)	5616(2)	25(1)
C(39)	8251(2)	9700(2)	5751(2)	55(1)	C(94)	4082(2)	6615(1)	4132(2)	32(1)
C(40)	8424(2)	10180(2)	6278(2)	45(1)	C(95)	3860(2)	7244(1)	4158(2)	35(1)
C(41)	8499(2)	10116(2)	7227(2)	45(1)	C(96)	4712(2)	7637(1)	3947(2)	47(1)
C(42)	8420(2)	9609(1)	7679(2)	33(1)	C(97)	3270(2)	6303(1)	3718(2)	42(1)
C(43)	8566(2)	9568(1)	8694(2)	34(1)	C(98)	5050(2)	6444(1)	3755(2)	38(1)
C(44)	8814(2)	9936(1)	10174(2)	49(1)	O(41)	554(4)	8730(2)	7862(4)	71(1)
C(45)	8688(3)	9290(1)	10205(2)	52(1)	C(84A)	1613(2)	8650(2)	7595(2)	49(1)
C(46)	9571(2)	8959(1)	10535(2)	54(2)	H(9)	6714	9624	8680	42
C(47)	7933(2)	10233(2)	10495(2)	52(1)	H(3)	4429	9466	13562	44
C(48)	9768(2)	10145(2)	10603(2)	53(1)	H(4)	4123	10303	12715	47
O(9)	5543(4)	7646(2)	6409(4)	55(1)	H(5)	4573	10344	11163	47
C(34)	6607(2)	7752(2)	6771(2)	50(1)	H(10A)	5317	8865	7968	64
Fe(3)	1074(1)	7931(1)	4349(1)	35(1)	H(10B)	6321	9025	7523	64
Fe(4)	2967(1)	8067(1)	5680(1)	36(1)	H(2)	5200	8750	12889	33
O(13)	865(1)	7709(1)	3025(1)	41(1)	H(39)	8196	9732	5085	66
O(14)	340(1)	6263(1)	4554(1)	38(1)	H(11C)	6478	10491	8525	114
O(15)	1567(1)	7832(1)	5717(1)	39(1)	H(12)	10765	9140	10141	70
					H(12A)	4132	9478	8419	91

Experimental Part

H(12B)	4522	9721	7459	91	H(24)	5389	7768	5067	86
H(12C)	3972	10116	8163	91	H(52)	295	7626	1330	35
H(14)	2894	8458	9948	44	H(61B)	-528	6721	6537	61
H(15)	1878	7985	10888	70	H(61C)	-1001	6288	5804	61
H(16)	2416	7287	11877	71	H(62A)	314	5607	6061	66
H(17)	3993	6971	11797	57	H(62B)	922	5982	6795	66
H(21)	7243	7155	10062	45	H(62C)	1402	5765	5860	66
H(22A)	7649	8000	11414	38	H(64)	-2112	7881	4494	60
H(22B)	8380	7722	10704	38	H(65)	-3212	8392	3647	74
H(23A)	6961	7477	12592	65	H(66)	-2866	9172	2827	67
H(11A)	5453	10784	8380	114	H(67)	-1267	9431	2780	64
H(11B)	5876	10423	7548	114	H(71)	2083	9274	4405	42
H(24A)	6684	6121	11677	82	H(72A)	2572	8483	3008	42
H(24B)	7702	6293	11284	82	H(72B)	3286	8778	3771	42
H(24C)	6770	6273	10587	82	H(73A)	1460	10297	2817	74
H(26)	10929	7901	9413	38	H(60B)	1489	7317	6794	55
H(27)	11791	7094	9255	44	H(61A)	-777	6905	5473	61
H(28)	11009	6292	8614	48	H(74A)	1580	8909	1964	65
H(29)	9387	6337	8253	45	H(74B)	2531	9280	2039	65
H(33)	6144	7467	8070	55	H(74C)	1551	9535	1600	65
H(34C)	6481	8142	6937	60	H(76)	5874	8769	5152	54
H(34D)	6063	7617	6364	60	H(77)	6390	9670	4930	46
H(35A)	6472	6066	8262	71	H(78)	5336	10396	5086	55
H(35B)	5607	6499	8171	71	H(79)	3800	10237	5614	46
H(35C)	6485	6606	8911	71	H(83)	1052	8818	6261	47
H(36A)	6923	6774	6068	61	H(84A)	1086	8786	7981	59
H(36B)	5931	6518	6394	61	H(84B)	1516	8250	7482	59
H(36C)	6897	6162	6490	61	H(85A)	922	10233	5901	72
H(38)	8049	8871	5749	65	H(85B)	158	9783	6219	72
H(39)	8018	7804	6609	66	H(85C)	845	9650	5372	72
H(40)	8486	10531	5988	54	H(86A)	1979	9738	8065	70
H(41)	8612	10435	7604	54	H(86B)	840	9778	7886	70
H(45)	8149	9200	10623	62	H(86C)	1515	10271	7559	70
H(46A)	9820	9113	11142	65	H(88)	3357	7450	8613	54
H(46B)	9371	8573	10651	65	H(89)	3550	6574	9217	69
H(47A)	7948	10618	10285	62	H(90)	3764	5832	8204	71
H(47B)	7923	10221	11185	62	H(91)	3894	5981	6584	56
H(47C)	7356	10052	10226	62	H(95)	3299	7329	3720	41
H(48A)	10298	9985	10260	64	H(96A)	4923	7558	3304	56
H(48B)	9829	10034	11266	64	H(96B)	4476	8022	3954	56
H(48C)	9791	10548	10557	64	H(97A)	3367	5908	3841	50
H(23B)	7935	7165	12354	65	H(97B)	3223	6367	3037	50
H(23C)	7102	6840	12865	65	H(97C)	2675	6424	4000	50
H(9)	5433	7821	5906	66	H(98A)	5570	6617	4135	46
H(34A)	7067	7633	6299	60	H(98B)	5085	6563	3098	46
H(34B)	6714	8148	6915	60	H(98C)	5115	6041	3791	46
H(21A)	2765	8440	8255	85	H(73B)	2524	10103	3129	74
H(53)	-275	6855	531	52	H(73C)	1711	10136	3892	74
H(54)	-530	6037	1326	45	H(41A)	230	8848	7392	85
H(55)	-182	5976	2948	48	H(84C)	2066	8818	8067	59
H(59)	1849	6717	5627	49	H(84D)	1773	8255	7517	59
H(60A)	463	7475	6309	55					

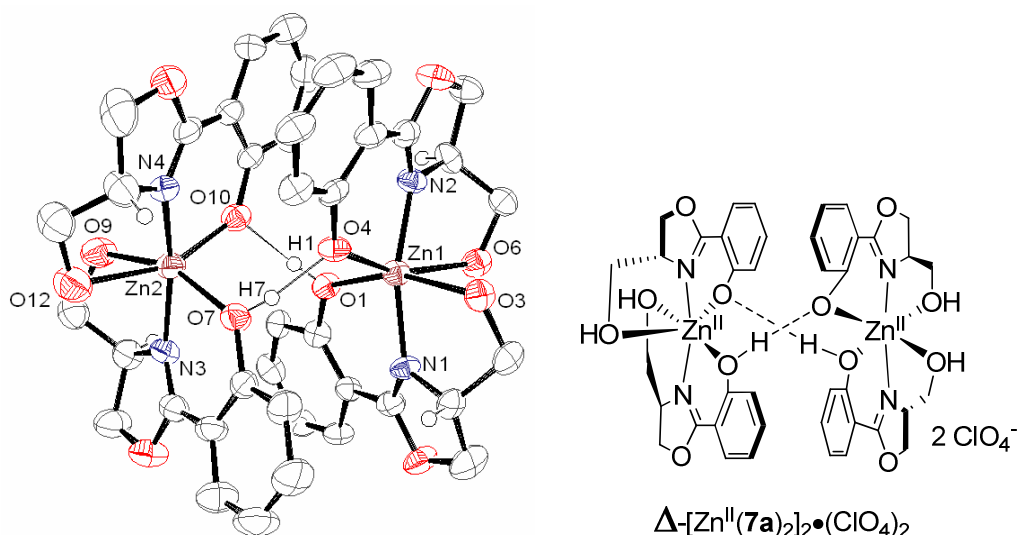


Table 21. Crystal data and structure refinement for [Zn^{II}(**7a**)₂]₂•(ClO₄)₂.

Crystal Data	
Empirical formula	2(C ₂₀ H ₂₁ N ₂ O ₆ Zn), 3(C ₄ H ₈ O), 2(Cl O ₄)
Formula weight	1317.34
Crystal size	0.28 x 0.20 x 0.14 mm
Crystal description	prism
Crystal colour	colourless
Crystal system	Monoclinic
Space group	P 21
Unit cell dimensions	a = 9.7188(3) Å alpha = 90 deg. b = 22.5542(5) Å beta = 101.576(4) deg. c = 13.3670(6) Å gamma = 90 deg.
Volume	2870.44(17) Å ³
Z, Calculated density	2, 1.524 Mg/m ³
Absorption coefficient	2.611 mm ⁻¹
F(000)	1369
Data Collection	
Measurement device type	Oxford Diffraction Gemini Ultra
Measurement method	omega-scan
Temperature	150 K
Wavelength	1.54178 Å
Monochromator	graphite
Theta range for data collection	3.90 to 58.93 deg.
Index ranges	-5 ≤ h ≤ 10, -25 ≤ k ≤ 24, -14 ≤ l ≤ 14
Reflections collected / unique	11212 / 6836 [R(int) = 0.0347]
Reflections greater I > 2σ(I)	5597
Absorption correction	Semi-empirical from equivalents
Max. and min. transmission	1.00000 and 0.41459
Refinement	
Refinement method	Full-matrix least-squares on F ²
Hydrogen treatment	:
Data / restraints / parameters	6836 / 1 / 757
Goodness-of-fit on F ²	0.957
Final R indices [I > 2σ(I)]	R1 = 0.0450, wR2 = 0.1076
R indices (all data)	R1 = 0.0544, wR2 = 0.1113
Absolute structure parameter	0.00(2)
Largest diff. peak and hole	0.644 and -0.553 e.Å ⁻³

Experimental Part

Table 22. Atomic coordinates ($\times 10^4$) and equivalent isotropic displacement parameters ($\text{\AA}^2 \times 10^3$).

	x	y	z	U(eq)					
Zn(1)	5585(1)	9300(1)	6864(1)	33(1)	O(14)	8428(7)	600(2)	2302(5)	82(2)
O(1)	7773(3)	9285(2)	7483(3)	33(1)	C(45)	7466(11)	1069(5)	2406(8)	98(4)
O(2)	6857(4)	10964(2)	6099(3)	46(1)	C(46)	7941(15)	1276(5)	3494(7)	121(6)
O(3)	3480(4)	9624(2)	6087(3)	39(1)	C(47)	9253(13)	981(7)	3897(8)	125(5)
O(4)	4929(3)	9178(2)	8200(3)	35(1)	C(48)	9684(10)	741(5)	2985(9)	98(4)
O(5)	4118(4)	7582(2)	6490(3)	47(1)	Cl(2)	2290(3)	2063(1)	5845(2)	92(1)
O(6)	5995(4)	9106(2)	5136(3)	41(1)	O(21)	3940(15)	2304(5)	6214(9)	74(5)
N(1)	5899(4)	10153(2)	6653(4)	32(2)	O(22)	2431(11)	1646(5)	6596(9)	142(6)
N(2)	5264(4)	8444(2)	6599(4)	33(2)	O(24)	2467(10)	1607(5)	5054(8)	92(5)
C(1)	8801(5)	9677(3)	7366(4)	34(2)	O(25)	1850(16)	2569(7)	6451(12)	125(8)
C(2)	10204(5)	9504(3)	7702(4)	34(2)	O(27)	1823(16)	2257(8)	4830(13)	154(9)
C(3)	11265(6)	9892(3)	7579(5)	43(2)	O(23)	3054(16)	2448(7)	5900(10)	64(7)
C(4)	10978(6)	10438(3)	7122(5)	46(2)	O(26)	692(14)	2122(7)	5724(11)	91(7)
C(5)	9572(6)	10605(3)	6777(4)	37(2)	Cl(1)	4522(2)	9955(1)	2853(1)	60(1)
C(6)	8477(5)	10224(2)	6896(4)	31(2)	O(15)	3534(8)	10385(4)	2971(4)	124(4)
C(7)	7034(6)	10428(3)	6564(4)	34(2)	O(16)	4727(6)	9985(3)	1831(4)	77(2)
C(8)	5334(6)	11037(3)	5722(6)	55(2)	O(17)	4015(6)	9394(3)	3030(5)	110(3)
C(9)	4680(6)	10537(3)	6254(5)	38(2)	O(18)	5814(5)	10029(3)	3573(4)	75(2)
C(10)	3610(6)	10166(3)	5550(5)	42(2)	H(1)	8065	9069	7993	40
C(11)	4108(5)	8750(2)	8433(4)	35(2)	H(2)	10424	9126	8009	41
C(12)	3476(6)	8818(3)	9275(5)	40(2)	H(3)	12216	9779	7816	52
C(13)	2574(7)	8397(3)	9527(5)	46(2)	H(3O)	3072	9369	5675	46
C(14)	2246(7)	7900(3)	8949(6)	54(3)	H(4)	11720	10697	7042	55
C(15)	2880(6)	7800(3)	8104(5)	50(2)	H(5)	9361	10980	6459	44
C(16)	3803(6)	8230(3)	7838(5)	36(2)	H(6O)	5919	9337	4635	49
C(17)	4444(6)	8103(3)	6971(4)	36(2)	H(8A)	5088	10993	4970	66
C(18)	4826(7)	7567(3)	5641(5)	45(2)	H(8B)	5013	11430	5912	66
C(19)	5662(6)	8144(3)	5718(4)	38(2)	H(9)	4271	10699	6827	45
C(20)	5320(6)	8551(3)	4808(4)	39(2)	H(10A)	2696	10374	5386	51
Zn(2)	8255(1)	9159(1)	10207(1)	41(1)	H(10B)	3929	10083	4905	51
O(7)	6536(4)	9730(2)	9519(3)	41(1)	H(12)	3673	9163	9687	48
O(8)	10098(5)	10816(2)	10240(4)	56(2)	H(13)	2174	8454	10112	56
O(9)	10357(4)	8903(2)	11012(4)	55(2)	H(14)	1592	7622	9115	65
O(10)	8352(4)	8638(2)	8972(3)	39(1)	H(15)	2690	7445	7716	59
O(11)	5867(5)	7716(2)	10748(3)	60(2)	H(18A)	4140	7546	4986	54
O(12)	8108(5)	9403(2)	11928(4)	62(2)	H(18B)	5461	7220	5692	54
N(3)	9369(5)	9884(2)	10081(4)	36(2)	H(19)	6691	8055	5872	46
N(4)	6966(5)	8567(2)	10600(4)	37(2)	H(20A)	5685	8387	4225	47
C(21)	6444(6)	10335(3)	9432(4)	37(2)	H(20B)	4292	8605	4596	47
C(22)	5136(7)	10598(3)	9104(5)	47(2)	H(7)	5979	9573	9029	49
C(23)	5027(8)	11206(3)	9030(6)	64(3)	H(9O)	9861	8836	11447	66
C(24)	6196(8)	11557(3)	9345(7)	70(3)	H(12O)	7565	9696	11805	74
C(25)	7496(8)	11304(3)	9667(6)	58(3)	H(22)	4319	10358	8933	56
C(26)	7628(6)	10687(3)	9705(5)	41(2)	H(23)	4144	11384	8761	76
C(27)	9042(6)	10432(3)	10014(4)	39(2)	H(24)	6101	11976	9339	84
C(28)	11370(7)	10481(3)	10597(6)	59(3)	H(25)	8303	11548	9862	70
C(29)	10907(6)	9834(3)	10401(5)	46(2)	H(28A)	11738	10552	11333	71
C(30)	11218(7)	9434(3)	11310(5)	53(2)	H(28B)	12103	10587	10211	71
C(31)	7934(6)	8079(3)	8787(4)	37(2)	H(29)	11316	9666	9833	55
C(32)	8286(6)	7783(3)	7946(5)	49(2)	H(30A)	12228	9330	11476	63
C(33)	7835(8)	7210(3)	7720(6)	62(3)	H(30B)	10960	9626	11912	63
C(34)	7000(8)	6908(3)	8279(6)	67(3)	H(32)	8837	7978	7533	59
C(35)	6644(7)	7190(3)	9097(5)	52(2)	H(33)	8105	7014	7160	74
C(36)	7090(6)	7770(3)	9376(5)	39(2)	H(34)	6685	6517	8100	79
C(37)	6667(6)	8041(3)	10236(5)	41(2)	H(35)	6077	6988	9489	63
C(38)	5651(8)	8070(4)	11629(6)	73(3)	H(38A)	6132	7887	12279	87
C(39)	6304(7)	8672(3)	11464(5)	55(3)	H(38B)	4639	8110	11635	87
C(40)	7386(7)	8916(3)	12329(5)	60(3)	H(39)	5536	8970	11267	66
O(54)	520(10)	8027(5)	2304(8)	69(3)	H(40A)	6928	9062	12880	71
C(50)	2039(13)	7870(5)	2878(8)	109(4)	H(40B)	8067	8603	12613	71
C(51)	1853(19)	7327(7)	2936(16)	232(9)	H(50A)	2757	7968	2474	130
C(52)	730(12)	7028(4)	2225(9)	102(4)	H(53A)	-886	7469	1416	152
C(53)	146(13)	7511(4)	1625(10)	127(5)	H(53B)	554	7547	1006	152
C(51A)	1853(19)	7327(7)	2936(16)	232(9)	H(50B)	2281	8060	3559	130
O(55)	1381(11)	7922(5)	1756(9)	69(3)	H(51A)	1703	7245	3633	280
C(50A)	2039(13)	7870(5)	2878(8)	109(4)	H(51B)	2745	7131	2876	280
C(52A)	730(12)	7028(4)	2225(9)	102(4)	H(52A)	1104	6725	1814	122
C(53A)	146(13)	7511(4)	1625(10)	127(5)	H(52B)	42	6842	2583	122
O(13)	1741(4)	8843(2)	4939(3)	49(2)	H(50C)	3045	7980	3028	130
C(41)	787(6)	9191(4)	4222(5)	53(2)	H(50D)	1526	8101	3317	130
C(42)	-404(6)	9327(3)	4755(5)	51(2)	H(51C)	1703	7245	3633	280
C(43)	-548(6)	8730(3)	5255(5)	49(2)	H(51D)	2745	7131	2876	280
C(44)	922(7)	8520(3)	5564(5)	56(2)	H(52C)	1104	6725	1814	122
					H(52D)	42	6842	2583	122

Experimental Part

H(53C)	-645	7689	1885	152
H(53D)	-178	7395	901	152
H(41A)	447	8967	3584	63
H(41B)	1242	9561	4055	63
H(42A)	-1272	9437	4265	61
H(42B)	-155	9646	5268	61
H(43A)	-992	8774	5855	59
H(43B)	-1113	8451	4765	59
H(44A)	1284	8602	6298	67
H(44B)	976	8088	5449	67
H(45A)	6489	920	2287	118
H(45B)	7524	1394	1919	118
H(46A)	8073	1711	3515	145
H(46B)	7231	1173	3903	145
H(47A)	9120	659	4373	150
H(47B)	9958	1264	4260	150
H(48A)	10272	383	3159	118
H(48B)	10226	1040	2682	118

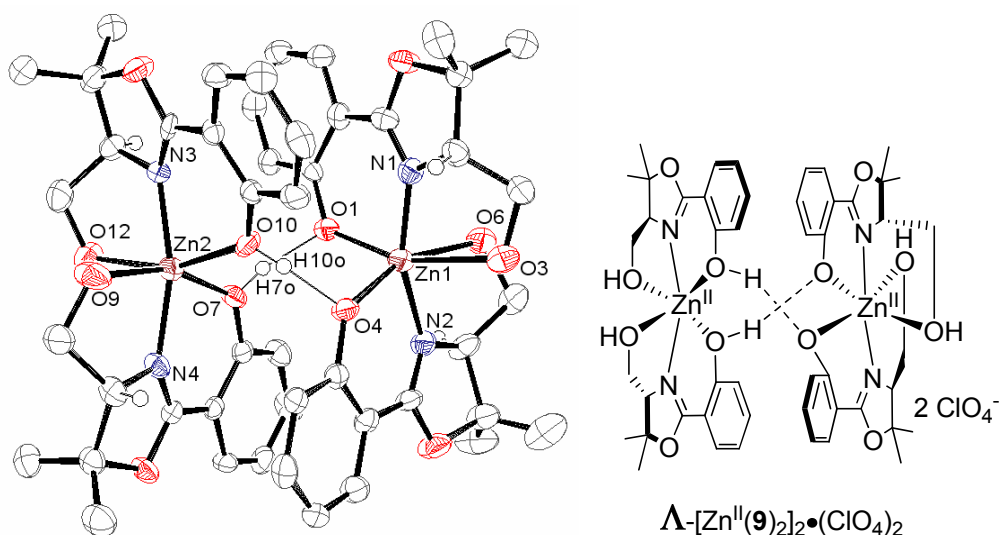


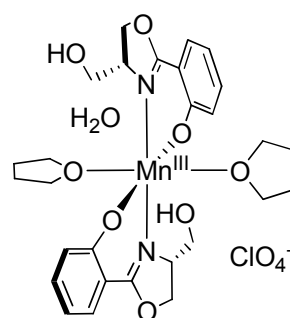
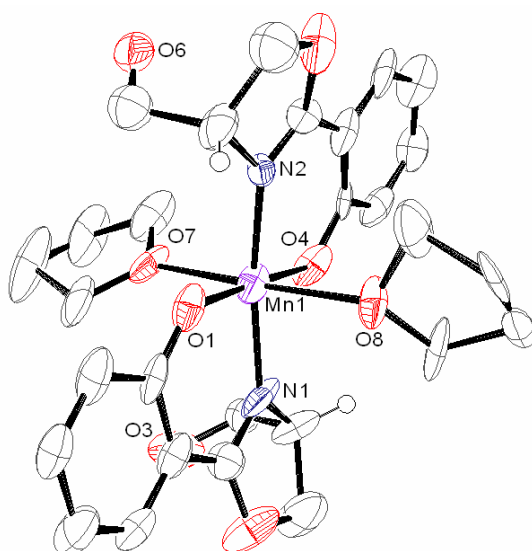
Table 23. Crystal data and structure refinement for [Zn^{II}(9)₂]₂•(ClO₄)₂.

Crystal Data	
Empirical formula	C ₂₄ H ₃₀ N ₂ O ₆ Zn, C ₂₄ H ₂₈ N ₂ O ₆ Zn, 2(Cl O ₄), 3(H ₂ O)
Formula weight	1266.67
Crystal size	0.19 x 0.17 x 0.08 mm
Crystal description	flat rod
Crystal colour	colourless
Crystal system	Orthorhombic
Space group	P 21 21 21
Unit cell dimensions	a = 14.0574(2) Å alpha = 90 deg. b = 18.0606(3) Å beta = 90 deg. c = 22.0306(2) Å gamma = 90 deg.
Volume	5593.24(13) Å ³
Z, Calculated density	4, 1.504 Mg/m ³
Absorption coefficient	2.653 mm ⁻¹
F(000)	2632
Data Collection	
Measurement device type	Oxford Diffraction Gemini Ultra
Measurement method	omega-scan
Temperature	150 K
Wavelength	1.54184 Å
Monochromator	graphite
Theta range for data collection	3.16 to 62.24 deg.
Index ranges	-16 ≤ h ≤ 15, -20 ≤ k ≤ 18, -25 ≤ l ≤ 25
Reflections collected / unique	24916 / 8633 [R(int) = 0.0395]
Reflections greater I > 2σ(I)	6409
Absorption correction	Semi-empirical from equivalents
Max. and min. transmission	1.00000 and 0.71596
Refinement	
Refinement method	Full-matrix least-squares on F ²
Hydrogen treatment	:
Data / restraints / parameters	8633 / 2 / 711
Goodness-of-fit on F ²	0.965
Final R indices [I > 2σ(I)]	R1 = 0.0478, wR2 = 0.1152
R indices (all data)	R1 = 0.0642, wR2 = 0.1211
Absolute structure parameter	-0.01(2)
Largest diff. peak and hole	1.371 and -0.406 e.Å ⁻³

Experimental Part

Table 24. Atomic coordinates ($\times 10^4$) and equivalent isotropic displacement parameters ($\text{\AA}^2 \times 10^3$).

	x	y	z	U(eq)					
Zn(2)	1074(1)	7500(1)	1461(1)	30(1)	O(56)	7865(12)	1478(10)	239(7)	79(5)
O(7)	449(3)	8510(2)	1180(2)	29(1)	Cl(1)	7588(1)	7950(1)	2590(1)	48(1)
O(8)	351(3)	7083(2)	-343(2)	32(1)	O(21)	8150(3)	8050(3)	3133(2)	60(2)
O(9)	1607(3)	6335(2)	1430(2)	53(2)	O(22)	7209(3)	7218(3)	2601(2)	57(2)
O(10)	2436(3)	7947(2)	1524(2)	31(1)	O(23)	8175(4)	8055(3)	2064(2)	61(2)
O(11)	1768(3)	7179(2)	3263(2)	37(1)	O(24)	6856(4)	8483(3)	2570(3)	88(3)
O(12)	-374(3)	7013(3)	1753(2)	39(1)	O(57)	7108(4)	9256(3)	3853(2)	77(2)
N(3)	1162(3)	7488(3)	2368(2)	25(1)	O(58)	7255(6)	9976(5)	1879(3)	134(3)
N(4)	915(3)	7212(2)	589(2)	28(2)	O(59)	2825(4)	5443(3)	1934(2)	77(2)
C(25)	6(4)	8703(3)	661(2)	27(2)	H(7O)	680(40)	8850(20)	1410(20)	35
C(26)	-443(4)	9381(3)	620(3)	36(2)	H(9)	1578	6055	1735	64
C(27)	-895(4)	9603(4)	84(3)	41(2)	H(10O)	2590(40)	8290(20)	1280(20)	37
C(28)	-903(4)	9137(3)	-409(3)	38(2)	H(12O)	-880(50)	7290(40)	1800(30)	46
C(29)	-477(4)	8454(3)	-379(2)	30(2)	H(26)	-445	9703	961	43
C(30)	-16(4)	8221(3)	150(2)	25(2)	H(27)	-1195	10074	60	49
C(31)	434(3)	7499(3)	155(2)	24(2)	H(28)	-1206	9288	-773	45
C(32)	1298(4)	6493(3)	391(2)	32(2)	H(29)	-496	8136	-722	36
C(33)	724(4)	6323(3)	-191(3)	33(2)	H(32)	1983	6555	281	38
C(34)	1226(5)	5963(4)	916(3)	48(3)	H(34A)	554	5826	990	57
C(35)	-120(4)	5828(4)	-97(3)	38(2)	H(34B)	1592	5507	831	57
C(36)	1335(5)	6099(4)	-724(3)	46(2)	H(35A)	-490	6005	251	46
C(37)	3119(4)	7798(3)	1928(2)	24(2)	H(35B)	98	5321	-19	46
C(38)	4068(4)	7897(3)	1773(2)	34(2)	H(35C)	-520	5834	-461	46
C(39)	4778(4)	7739(3)	2180(3)	36(2)	H(36A)	943	6078	-1092	55
C(40)	4564(4)	7486(4)	2753(2)	35(2)	H(36B)	1614	5611	-647	55
C(41)	3629(4)	7377(3)	2918(2)	33(2)	H(36C)	1845	6464	-780	55
C(42)	2888(3)	7535(3)	2512(2)	25(2)	H(38)	4228	8076	1381	41
C(43)	1898(4)	7408(3)	2701(2)	27(2)	H(39)	5424	7804	2065	44
C(44)	326(4)	7268(3)	2723(2)	30(2)	H(40)	5060	7387	3034	41
C(45)	737(4)	7001(4)	3336(2)	36(2)	H(41)	3485	7193	3311	39
C(46)	-237(4)	6716(4)	2350(3)	43(2)	H(44)	-77	7715	2797	35
C(47)	708(5)	6162(4)	3449(3)	41(2)	H(46A)	111	6241	2326	52
C(48)	396(4)	7449(4)	3868(2)	44(2)	H(46B)	-861	6623	2544	52
Zn(1)	2355(1)	9944(1)	1243(1)	33(1)	H(47A)	964	5902	3094	50
O(1)	1164(3)	9576(2)	1693(1)	30(1)	H(47B)	49	6006	3518	50
O(2)	3335(2)	9907(2)	3006(2)	35(1)	H(47C)	1093	6043	3806	50
O(3)	3967(3)	10468(3)	1058(2)	46(2)	H(48A)	741	7297	4234	53
O(4)	2671(3)	8957(2)	823(1)	30(1)	H(48B)	-287	7367	3927	53
O(5)	1577(3)	10401(2)	-526(2)	47(2)	H(48C)	513	7976	3790	53
O(6)	1972(3)	11306(2)	1380(2)	43(2)	H(2)	-408	9330	2220	36
N(1)	3046(3)	9910(3)	2013(2)	30(1)	H(3)	-766	9326	3233	43
N(2)	1888(3)	10313(3)	457(2)	32(2)	H(3O)	4310(50)	10780(40)	790(30)	56
C(1)	1000(4)	9573(3)	2296(2)	26(2)	H(4)	429	9553	3959	42
C(2)	82(4)	9428(3)	2506(3)	30(2)	H(5)	1969	9797	3644	40
C(3)	-133(4)	9423(3)	3106(3)	36(2)	H(6)	2264	11585	1622	52
C(4)	578(4)	9560(3)	3539(3)	35(2)	H(8)	4407	9540	1901	40
C(5)	1488(4)	9704(3)	3351(2)	34(2)	H(10A)	4072	11112	1791	48
C(6)	1720(4)	9715(3)	2729(2)	29(2)	H(10B)	5049	10701	1612	48
C(7)	2710(4)	9842(3)	2554(2)	31(2)	H(11A)	4619	10862	3397	48
C(8)	4089(4)	10001(4)	2049(2)	33(2)	H(11B)	4011	11209	2852	48
C(9)	4287(4)	10099(3)	2736(2)	30(2)	H(11C)	5118	11037	2760	48
C(10)	4349(5)	10644(4)	1636(2)	40(2)	H(12A)	5079	9605	3398	53
C(11)	4530(4)	10870(4)	2956(3)	40(2)	H(12B)	5576	9579	2745	53
C(12)	4971(4)	9531(4)	2963(3)	44(2)	H(12C)	4708	9035	2894	53
C(13)	2566(4)	8760(3)	237(2)	26(2)	H(14)	3171	7740	351	33
C(14)	2890(4)	8061(3)	60(2)	28(2)	H(15)	3011	7351	-654	41
C(15)	2802(4)	7832(3)	-540(2)	35(2)	H(16)	2347	8149	-1385	40
C(16)	2407(4)	8304(3)	-975(2)	34(2)	H(17)	1844	9306	-1100	42
C(17)	2111(4)	8987(3)	-803(2)	35(2)	H(20)	829	11080	530	48
C(18)	2184(4)	9241(3)	-199(2)	27(2)	H(22A)	2729	11610	644	53
C(19)	1901(4)	9988(4)	-60(2)	31(2)	H(22B)	1787	12101	749	53
C(20)	1505(5)	11077(4)	389(2)	40(2)	H(23A)	513	12002	-350	81
C(21)	1516(6)	11183(4)	-318(3)	48(2)	H(23B)	73	11191	-433	81
C(22)	2055(5)	11594(3)	773(3)	44(2)	H(23C)	632	11575	-981	81
C(23)	605(7)	11517(4)	-540(3)	67(3)	H(24A)	2956	11330	-377	81
C(24)	2390(6)	11564(4)	-550(3)	67(3)	H(24B)	2373	12087	-433	81
Cl(2)	6211(3)	1149(2)	237(1)	58(1)	H(24C)	2411	11526	-994	81
O(52)	6642(4)	572(4)	-118(3)	86(2)					
O(53)	6552(6)	969(5)	841(4)	123(3)					
O(54)	6492(6)	1802(5)	30(3)	123(3)					
O(55)	5177(6)	1189(5)	204(4)	76(3)					
Cl(3)	6990(4)	1139(3)	292(2)	46(2)					
O(52A)	6642(4)	572(4)	-118(3)	86(2)					
O(53A)	6552(6)	969(5)	841(4)	123(3)					
O(54A)	6492(6)	1802(5)	30(3)	123(3)					



trans-[Mn^{III}(**7a**)₂(THF)₂]•(ClO₄)

Table 25. Crystal data and structure refinement for [Mn^{III}(**7a**)₂(THF)₂]•(ClO₄)

Crystal Data	
Empirical formula	C ₂₈ H ₃₄ Mn N ₂ O ₈ , Cl O ₄
Formula weight	680.96
Crystal size	0.330 x 0.080 x 0.080 mm
Crystal description	rod
Crystal colour	moss-green to turquoise
Crystal system	Trigonal
Space group	P 31
Unit cell dimensions	a = 21.0613(2) Å alpha = 90 deg. b = 21.0613(2) Å beta = 90 deg. c = 17.70770(10) Å gamma = 120 deg.
Volume	6802.42(10) Å ³
Z, Calculated density	9, 1.496 Mg/m ³
Absorption coefficient	4.945 mm ⁻¹
F(000)	3186
Data Collection	
Measurement device type	Oxford Diffraction Gemini Ultra
Measurement method	omega-scan
Temperature	123 K
Wavelength	1.54184 Å
Monochromator	graphite
Theta range for data collection	3.48 to 51.63 deg.
Index ranges	-21 ≤ h ≤ 21, -21 ≤ k ≤ 15, -17 ≤ l ≤ 17
Reflections collected / unique	26572 / 9735 [R(int) = 0.0344]
Reflections greater I > 2σ(I)	7678
Absorption correction	Semi-empirical from equivalents
Max. and min. transmission	1.00000 and 0.54397
Refinement	
Refinement method	Full-matrix least-squares on F ²
Hydrogen treatment	:
Data / restraints / parameters	9735 / 1 / 1005
Goodness-of-fit on F ²	1.050
Final R indices [I > 2σ(I)]	R1 = 0.0939, wR2 = 0.1764
R indices (all data)	R1 = 0.1125, wR2 = 0.1845
Absolute structure parameter	0.053(5)
Largest diff. peak and hole	0.808 and -0.831 e.Å ⁻³

Experimental Part

Table 26. Atomic coordinates ($\times 10^4$) and equivalent isotropic displacement parameters ($\text{\AA}^2 \times 10^3$).

	x	y	z	U(eq)					
Mn(1)	-4481(1)	1144(1)	2024(1)	39(1)	C(52)	71(3)	603(4)	-1948(5)	75(3)
O(1)	-5226(2)	1090(2)	1409(3)	41(1)	C(53)	-1546(3)	2370(3)	-918(4)	42(2)
O(2)	-3897(2)	706(2)	-56(3)	65(2)	C(54)	-2094(3)	2585(3)	-1225(4)	50(2)
O(3)	-2669(2)	2221(3)	551(3)	65(2)	C(55)	-2782(3)	1841(3)	-1347(4)	52(2)
O(4)	-3728(2)	1189(2)	2611(3)	44(1)	C(56)	-2484(3)	1369(3)	-1618(4)	40(2)
O(5)	-5366(2)	924(2)	4169(3)	68(2)	Mn(3)	2194(1)	-2278(1)	-822(1)	13(1)
O(6)	-5140(2)	2369(2)	3490(3)	68(1)	O(17)	1451(2)	-2987(2)	-214(2)	18(1)
O(7)	-3870(2)	2354(2)	1954(3)	50(1)	O(18)	2825(2)	-1319(2)	1295(2)	36(1)
O(8)	-5104(2)	-124(2)	2144(3)	49(1)	O(19)	4016(2)	-1639(2)	623(2)	47(1)
N(1)	-4008(3)	991(3)	1129(3)	53(2)	O(20)	2937(2)	-1585(2)	-1411(2)	18(1)
N(2)	-4999(2)	1146(2)	2937(3)	34(1)	O(21)	1248(2)	-2896(2)	-2924(2)	25(1)
C(1)	-5340(3)	1041(3)	661(4)	39(2)	O(22)	1436(2)	-4174(2)	-2306(2)	53(1)
C(2)	-5904(3)	1111(3)	377(4)	54(2)	O(23)	1620(2)	-1589(2)	-889(2)	40(1)
C(3)	-6045(3)	1061(3)	-377(4)	50(2)	O(24)	2761(2)	-2911(2)	-803(2)	31(1)
C(4)	-5618(4)	940(4)	-876(5)	66(3)	N(5)	2720(2)	-1685(2)	85(2)	22(1)
C(5)	-5031(3)	892(3)	-605(4)	46(2)	N(6)	1628(2)	-2789(2)	-1733(2)	21(1)
C(6)	-4883(3)	929(3)	161(4)	41(2)	C(57)	1354(3)	-3036(3)	546(3)	22(1)
C(7)	-4245(3)	910(3)	397(4)	42(2)	C(58)	733(3)	-3681(3)	817(3)	28(2)
C(8)	-3313(4)	680(4)	352(4)	78(3)	C(59)	621(3)	-3772(3)	1589(3)	39(2)
C(9)	-3274(3)	1030(4)	1135(4)	59(2)	C(60)	1111(3)	-3199(3)	2089(4)	35(2)
C(10)	-2631(3)	1836(3)	1148(4)	42(2)	C(61)	1672(3)	-2605(3)	1828(3)	33(2)
C(11)	-3652(3)	1199(3)	3378(3)	27(2)	C(62)	1820(3)	-2491(3)	1051(3)	25(2)
C(12)	-3003(3)	1281(3)	3645(4)	48(2)	C(63)	2450(3)	-1835(3)	763(3)	27(2)
C(13)	-2885(3)	1258(3)	4417(4)	48(2)	C(64)	3415(3)	-687(3)	878(3)	30(2)
C(14)	-3431(4)	1160(4)	4918(5)	63(3)	C(65)	3437(3)	-1017(3)	114(3)	22(1)
C(15)	-4087(3)	1080(3)	4618(5)	51(2)	C(66)	4036(3)	-1174(3)	1(3)	45(2)
C(16)	-4212(3)	1110(3)	3857(4)	45(2)	C(67)	3010(2)	-1518(3)	-2154(3)	20(2)
C(17)	-4869(3)	1086(3)	3636(4)	36(2)	C(68)	3675(3)	-951(3)	-2469(3)	24(1)
C(18)	-5994(4)	842(4)	3743(4)	68(2)	C(69)	3775(3)	-851(3)	-3231(3)	31(2)
C(19)	-5733(3)	1142(3)	2939(4)	54(2)	C(70)	3228(3)	-1249(3)	-3725(3)	35(2)
C(20)	-5555(4)	1936(4)	2848(4)	57(2)	C(71)	2569(3)	-1807(3)	-3467(3)	28(2)
C(21)	-3836(4)	2786(3)	1341(5)	68(2)	C(72)	2477(3)	-1909(3)	-2670(3)	23(2)
C(22)	-3393(4)	3572(4)	1589(7)	103(4)	C(73)	1807(3)	-2516(3)	-2412(3)	25(1)
C(23)	-2905(4)	3539(4)	2207(6)	89(4)	C(74)	588(3)	-3452(3)	-2512(3)	36(2)
C(24)	-3365(4)	2813(4)	2547(5)	70(3)	C(75)	912(3)	-3488(3)	-1741(3)	24(1)
C(25)	-5736(4)	-523(4)	2750(4)	70(3)	C(76)	1045(3)	-4128(3)	-1668(3)	33(2)
C(26)	-5984(4)	-1331(3)	2541(3)	49(2)	C(77)	1976(3)	-817(3)	-768(5)	60(2)
C(27)	-5261(4)	-1305(3)	2403(4)	65(3)	C(78)	1529(3)	-520(4)	-1123(4)	52(2)
C(28)	-4763(3)	-545(3)	2052(5)	61(2)	C(79)	789(3)	-1199(3)	-1285(5)	64(2)
Mn(2)	-1070(1)	1120(1)	-1325(1)	41(1)	C(80)	1017(3)	-1747(3)	-1433(4)	52(2)
O(9)	-1777(2)	383(2)	-696(3)	53(1)	C(81)	2778(3)	-3350(3)	-167(3)	33(2)
O(10)	-514(2)	2127(2)	776(3)	63(2)	C(82)	3225(3)	-3684(3)	-438(4)	55(2)
O(11)	780(3)	1939(3)	239(3)	76(2)	C(83)	3715(4)	-3179(4)	-1078(4)	76(3)
O(12)	-357(2)	1840(2)	-1930(3)	46(1)	C(84)	3256(3)	-2901(3)	-1410(3)	28(2)
O(13)	-2000(2)	410(2)	-3408(3)	57(1)	Cl(1)	-1225(1)	4269(1)	344(1)	70(1)
O(14)	-1673(2)	-735(2)	-2743(3)	66(2)	O(25)	-830(4)	4727(4)	846(5)	268(4)
O(15)	-409(3)	562(2)	-1309(3)	70(2)	O(26)	-1918(3)	4138(4)	133(5)	162(3)
O(16)	-1762(2)	1688(2)	-1286(2)	47(1)	O(27)	-1249(3)	3633(3)	428(4)	133(3)
N(3)	-567(2)	1713(2)	-395(3)	44(2)	O(28)	-754(3)	4479(5)	-333(3)	168(3)
N(4)	-1611(2)	575(2)	-2225(3)	32(1)	Cl(2)	-4565(1)	-2267(1)	843(1)	59(1)
C(29)	-1897(4)	324(4)	61(4)	62(2)	O(29)	-4078(3)	-2077(3)	1443(3)	90(2)
C(30)	-2415(3)	-337(4)	301(4)	53(2)	O(30)	-5250(3)	-2830(3)	1008(4)	108(2)
C(31)	-2561(4)	-444(3)	1032(5)	60(3)	O(31)	-4233(2)	-2377(3)	225(3)	100(2)
C(32)	-2133(4)	134(4)	1600(5)	66(2)	O(32)	-4660(3)	-1684(3)	563(3)	122(2)
C(33)	-1577(3)	782(3)	1278(4)	42(2)	Cl(3)	-929(1)	-2113(1)	-2913(2)	81(1)
C(34)	-1416(3)	906(3)	563(4)	38(2)	O(33)	-745(5)	-2335(4)	-2307(4)	159(3)
C(35)	-825(3)	1595(3)	264(4)	37(2)	O(34)	-410(4)	-1393(3)	-3114(6)	177(4)
C(36)	45(4)	2745(4)	344(5)	72(3)	O(35)	-1224(4)	-2576(4)	-3591(4)	125(3)
C(37)	116(3)	2444(3)	-395(4)	47(2)	O(36)	-1612(4)	-2049(5)	-2765(5)	155(3)
C(38)	759(3)	2300(4)	-412(5)	74(3)	H(2)	-6204	1196	713	64
C(39)	-283(3)	1937(3)	-2671(3)	35(2)	H(3)	-6443	1110	-559	61
C(40)	349(3)	2528(3)	-2980(5)	62(3)	H(4)	-5727	890	-1401	79
C(41)	440(3)	2686(3)	-3735(4)	54(2)	H(5)	-4719	833	-951	55
C(42)	-78(3)	2195(4)	-4213(4)	58(2)	H(8A)	-2841	961	81	93
C(43)	-707(3)	1617(3)	-3973(4)	49(2)	H(8B)	-3424	167	411	93
C(44)	-813(3)	1436(3)	-3191(4)	47(2)	H(9)	-3236	735	1556	71
C(45)	-1506(3)	802(3)	-2911(4)	47(2)	H(10A)	-2647	2074	1624	50
C(46)	-2595(3)	-134(4)	-3001(4)	50(2)	H(10B)	-2159	1839	1133	50
C(47)	-2321(3)	-165(3)	-2257(4)	45(2)	H(12)	-2628	1355	3298	58
C(48)	-2123(4)	-758(3)	-2084(4)	62(2)	H(13)	-2437	1309	4596	58
C(49)	-400(4)	135(4)	-702(5)	69(3)	H(14)	-3366	1147	5448	75
C(50)	-50(4)	-270(4)	-899(8)	165(5)	H(15)	-4467	1000	4961	61
C(51)	466(4)	202(4)	-1556(7)	131(5)	H(18A)	-6203	1117	3991	81
					H(18B)	-6379	318	3719	81

Experimental Part

H(19)	-6076	813	2541	65	H(80A)	1193	-1704	-1959	63
H(20A)	-5269	2145	2380	69	H(80B)	601	-2250	-1355	63
H(20B)	-6016	1950	2805	69	H(81A)	2276	-3737	-31	39
H(21A)	-4336	2671	1191	81	H(81B)	3010	-3036	280	39
H(21B)	-3601	2694	904	81	H(82A)	2901	-4188	-629	66
H(22A)	-3096	3891	1167	124	H(82B)	3528	-3705	-22	66
H(22B)	-3711	3753	1790	124	H(83A)	4180	-2773	-876	92
H(23A)	-2772	3933	2584	107	H(83B)	3827	-3457	-1454	92
H(23B)	-2451	3583	1991	107	H(84A)	2964	-3217	-1836	33
H(24A)	-3059	2606	2721	84	H(84B)	3568	-2396	-1600	33
H(24B)	-3640	2847	2984	84					
H(25A)	-5548	-403	3273	84					
H(25B)	-6135	-409	2678	84					
H(26A)	-6258	-1668	2961	60					
H(26B)	-6294	-1487	2082	60					
H(27A)	-5326	-1699	2052	78					
H(27B)	-5051	-1359	2882	78					
H(28A)	-4279	-304	2305	73					
H(28B)	-4688	-596	1508	73					
H(30)	-2674	-725	-49	64					
H(31)	-2950	-904	1199	72					
H(32)	-2227	70	2127	79					
H(33)	-1287	1171	1616	50					
H(36A)	519	2978	618	87					
H(36B)	-104	3118	263	87					
H(37)	131	2754	-829	56					
H(38A)	714	1999	-860	89					
H(38B)	1223	2773	-457	89					
H(40)	735	2836	-2647	75					
H(41)	850	3122	-3918	65					
H(42)	9	2264	-4741	70					
H(43)	-1082	1329	-4326	59					
H(46A)	-2795	-614	-3259	60					
H(46B)	-2989	-10	-2959	60					
H(47)	-2668	-177	-1864	54					
H(48A)	-1838	-647	-1609	74					
H(48B)	-2570	-1246	-2038	74					
H(49A)	-909	-209	-541	83					
H(49B)	-139	459	-269	83					
H(50A)	-409	-771	-1072	198					
H(50B)	234	-303	-470	198					
H(51A)	532	-114	-1925	156					
H(51B)	953	568	-1357	156					
H(52A)	426	1115	-2089	90					
H(52B)	-217	332	-2397	90					
H(53A)	-1036	2741	-1050	51					
H(53B)	-1586	2309	-362	51					
H(54A)	-2183	2884	-854	60					
H(54B)	-1919	2860	-1704	60					
H(55A)	-3059	1650	-871	62					
H(55B)	-3106	1874	-1731	62					
H(56A)	-2797	857	-1447	48					
H(56B)	-2455	1376	-2176	48					
H(58)	401	-4043	476	34					
H(59)	223	-4210	1787	47					
H(60A)	1024	-3253	2617	42					
H(61A)	1991	-2239	2174	39					
H(64A)	3891	-488	1144	36					
H(64B)	3295	-292	814	36					
H(65)	3461	-679	-295	26					
H(66A)	4513	-712	-7	54					
H(66B)	3973	-1429	-487	54					
H(68)	4060	-633	-2140	29					
H(69)	4241	-492	-3418	37					
H(70)	3299	-1143	-4250	42					
H(71)	2189	-2114	-3806	34					
H(74A)	357	-3932	-2772	44					
H(74B)	221	-3292	-2453	44					
H(75)	593	-3494	-1320	28					
H(76A)	1330	-4070	-1203	39					
H(76B)	569	-4588	-1623	39					
H(77A)	2472	-578	-995	71					
H(77B)	2029	-712	-220	71					
H(78A)	1474	-185	-772	62					
H(78B)	1761	-252	-1595	62					
H(79A)	456	-1338	-844	76					
H(79B)	548	-1128	-1730	76					

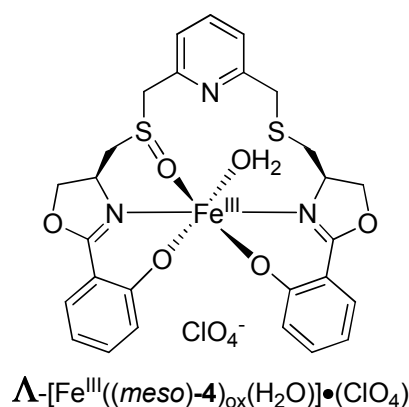
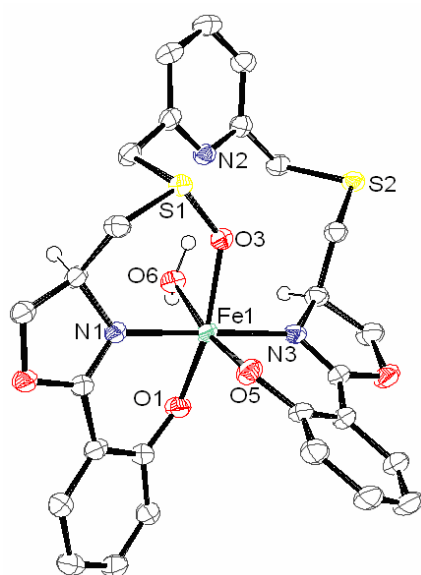


Table 27. Crystal data and structure refinement for [Fe^{III}((*meso*)-4)_{ox}(H₂O)]•(ClO₄).

Crystal Data	
Empirical formula	C ₂₇ H ₂₇ Fe N ₃ O ₆ S ₂ , Cl O ₄
Formula weight	708.96
Crystal size	0.35 x 0.27 x 0.13 mm
Crystal description	flat prism
Crystal colour	dark red
Crystal system	Monoclinic
Space group	P 2 ₁ /n
Unit cell dimensions	a = 9.7199(9) Å alpha = 90 deg. b = 26.575(2) Å beta = 112.697(11) deg. c = 12.0604(13) Å gamma = 90 deg.
Volume	2874.0(5) Å ³
Z, Calculated density	4, 1.638 Mg/m ³
Absorption coefficient	0.827 mm ⁻¹
F(000)	1460
Data Collection	
Measurement device type	STOE-IPDS diffractometer
Measurement method	rotation
Temperature	123(1) K
Wavelength	0.71073 Å
Monochromator	graphite
Theta range for data collection	1.98 to 25.84 deg.
Index ranges	-11 ≤ h ≤ 11 -32 ≤ k ≤ 32 -14 ≤ l ≤ 14
Reflections collected / unique	30411 / 5525 [R(int) = 0.0915]
Reflections greater I > 2σ(I)	4060
Absorption correction	Analytical
Max. and min. transmission	0.8851 and 0.7616
Refinement	
Refinement method	Full-matrix least-squares on F ²
Hydrogen treatment	:
Data / restraints / parameters	5525 / 0 / 405
Goodness-of-fit on F ²	0.940
Final R indices [I > 2σ(I)]	R1 = 0.0398, wR2 = 0.0948
R indices (all data)	R1 = 0.0581, wR2 = 0.1006
Absolute structure parameter	.
Largest diff. peak and hole	0.715 and -0.461 e.Å ⁻³

Experimental Part

Table 28. Atomic coordinates ($\times 10^4$) and equivalent isotropic displacement parameters ($\text{\AA}^2 \times 10^3$).

	x	y	z	U(eq)					
Fe(2)	7125(1)	1249(1)	138(1)	21(1)	H(11B)	6286	-477	-1413	32
S(1)	7781(1)	241(1)	-1245(1)	23(1)	H(13)	7972	-1159	-499	36
S(2)	11393(1)	212(1)	3751(1)	24(1)	H(14)	9634	-1553	1248	39
O(1)	5814(2)	1671(1)	579(2)	27(1)	H(15)	10481	-1104	3071	34
O(2)	3179(2)	1336(1)	-3039(2)	28(1)	H(17A)	9962	-404	4216	32
O(3)	8214(2)	657(1)	-305(2)	23(1)	H(17B)	8916	53	3516	32
O(4)	10700(3)	1895(1)	3059(2)	35(1)	H(18A)	11479	840	2430	29
O(5)	7925(2)	1738(1)	-615(2)	29(1)	H(18B)	10028	498	1809	29
O(6)	6554(3)	653(1)	1066(2)	26(1)	H(19)	8910	920	3067	30
N(1)	5273(3)	1116(1)	-1476(2)	23(1)	H(20A)	10090	1554	4314	42
N(2)	8235(3)	-253(1)	1395(2)	24(1)	H(20B)	11604	1329	4262	42
N(3)	8983(3)	1394(1)	1734(2)	24(1)	H(23)	10848	2731	2337	40
C(1)	4744(3)	1973(1)	-109(2)	25(1)	H(24)	10897	3350	967	48
C(2)	4323(4)	2392(1)	411(3)	29(1)	H(25)	9693	3206	-1084	45
C(3)	3278(4)	2730(1)	-276(3)	34(1)	H(26)	8367	2468	-1805	40
C(4)	2557(4)	2667(1)	-1524(3)	34(1)	H(27)	6330(50)	724(17)	1520(40)	49(13)
C(5)	2879(4)	2246(1)	-2049(3)	30(1)	H(28)	7190(50)	386(18)	1250(30)	55(12)
C(6)	3946(3)	1893(1)	-1363(2)	24(1)					
C(7)	4205(3)	1439(1)	-1928(2)	23(1)					
C(8)	3724(4)	894(1)	-3466(2)	28(1)					
C(9)	4926(3)	680(1)	-2322(2)	24(1)					
C(10)	6273(3)	489(1)	-2546(2)	25(1)					
C(11)	6762(3)	-232(1)	-756(2)	27(1)					
C(12)	7812(3)	-504(1)	338(2)	25(1)					
C(13)	8307(4)	-990(1)	253(3)	30(1)					
C(14)	9294(4)	-1220(1)	1280(3)	32(1)					
C(15)	9782(4)	-956(1)	2358(3)	29(1)					
C(16)	9229(3)	-469(1)	2383(2)	25(1)					
C(17)	9736(4)	-170(1)	3529(2)	27(1)					
C(18)	10642(3)	674(1)	2562(2)	24(1)					
C(19)	9688(3)	1078(1)	2829(2)	25(1)					
C(20)	10601(4)	1462(1)	3774(3)	35(1)					
C(21)	9675(3)	1825(1)	1942(3)	27(1)					
C(22)	9547(3)	2222(1)	1078(3)	28(1)					
C(23)	10339(4)	2677(1)	1499(3)	34(1)					
C(24)	10375(4)	3043(1)	686(3)	40(1)					
C(25)	9647(4)	2959(1)	-531(3)	37(1)					
C(26)	8847(4)	2519(1)	-963(3)	33(1)					
C(27)	8740(3)	2148(1)	-170(3)	28(1)					
Cl(2)	6074(1)	767(1)	3898(1)	24(1)					
O(7)	6599(3)	295(1)	3610(2)	35(1)					
O(8)	7196(3)	990(1)	4924(2)	51(1)					
O(9)	5739(3)	1097(1)	2872(2)	41(1)					
O(10)	4754(3)	688(1)	4120(3)	52(1)					
H(2)	4774	2439	1256	35					
H(3)	3038	3013	98	40					
H(4)	1861	2910	-1998	41					
H(5)	2369	2193	-2888	35					
H(8A)	4152	990	-4060	34					
H(8B)	2913	647	-3838	34					
H(9)	4495	400	-2006	29					
H(10A)	6667	768	-2880	30					
H(10B)	5935	221	-3164	30					
H(11A)	5967	-66	-566	32					

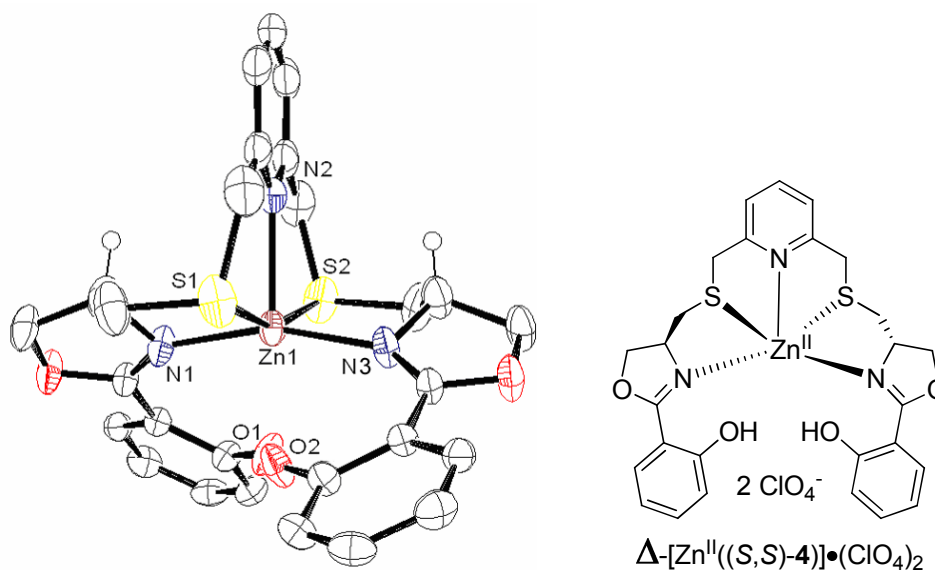


Table 29. Crystal data and structure refinement for [Zn^{II}((S,S)-4)]•(ClO₄)₂.

Crystal Data	
Empirical formula	C ₂₇ H ₂₇ N ₃ O ₄ S ₂ Zn, 2(Cl O ₄)
Formula weight	785.95
Crystal size	0.27 x 0.19 x 0.11 mm
Crystal description	prism
Crystal colour	leicht rosa
Crystal system	Monoclinic
Space group	C 2/c
Unit cell dimensions	a = 14.4742(12) Å alpha = 90 deg. b = 12.9006(12) Å beta = 110.552(9) deg. c = 17.5248(14) Å gamma = 90 deg.
Volume	3064.1(5) Å ³
Z, Calculated density	4, 1.704 Mg/m ³
Absorption coefficient	1.182 mm ⁻¹
F(000)	1608
Data Collection	
Measurement device type	STOE-IPDS diffractometer
Measurement method	rotation
Temperature	123(1) K
Wavelength	0.71073 Å
Monochromator	graphite
Theta range for data collection	2.18 to 26.84 deg.
Index ranges	-18 ≤ h ≤ 18 -16 ≤ k ≤ 16 -22 ≤ l ≤ 22
Reflections collected / unique	16916 / 3275 [R(int) = 0.0463]
Reflections greater I > 2σ(I)	2560
Absorption correction	Analytical
Max. and min. transmission	0.9022 and 0.7618
Refinement	
Refinement method	Full-matrix least-squares on F ²
Hydrogen treatment	:
Data / restraints / parameters	3275 / 0 / 215
Goodness-of-fit on F ²	1.041
Final R indices [I > 2σ(I)]	R1 = 0.0663, wR2 = 0.1647
R indices (all data)	R1 = 0.0824, wR2 = 0.1734
Absolute structure parameter	.
Largest diff. peak and hole	1.344 and -0.817 e.Å ⁻³

Table 30. Atomic coordinates ($\times 10^4$) and equivalent isotropic displacement parameters ($\text{\AA}^2 \times 10^3$).

	x	y	z	U(eq)
Zn(1)	0	1309(1)	7500	29(1)
S(1)	-627(1)	952(1)	5966(1)	46(1)
O(1)	-77(2)	3053(3)	8218(2)	41(1)
O(2)	-2919(2)	1935(3)	7353(2)	42(1)
N(1)	-1425(3)	1561(3)	7309(2)	34(1)
N(2)	0	-435(4)	7500	35(2)
C(1)	-639(3)	3149(3)	8690(2)	30(1)
C(2)	-326(4)	3711(4)	9417(3)	35(1)
C(3)	-935(4)	3816(3)	9872(3)	37(1)
C(4)	-1862(4)	3361(4)	9609(3)	38(1)
C(5)	-2173(3)	2792(3)	8895(3)	31(1)
C(6)	-1570(3)	2666(3)	8425(2)	26(1)
C(7)	-1934(3)	2037(4)	7676(2)	30(1)
C(8)	-3131(3)	1314(5)	6610(3)	44(1)
C(9)	-2101(4)	908(5)	6646(3)	45(2)
C(10)	-1910(4)	1046(5)	5877(3)	53(2)
C(11)	-308(4)	-408(5)	6015(3)	51(2)
C(12)	-161(3)	-975(4)	6801(3)	41(2)
C(13)	-172(4)	-2054(5)	6788(4)	56(2)
C(14)	0	-2591(7)	7500	65(3)
Cl(1)	7180(1)	9605(1)	8588(1)	52(1)
O(3)	7362(5)	9449(4)	7877(3)	81(2)
O(4)	7056(9)	8714(6)	8959(4)	190(5)
O(5)	6214(5)	10109(11)	8356(5)	175(6)
O(6)	7876(3)	10281(3)	9126(2)	53(1)
H(1)	406	3458	8387	50
H(2)	309	4025	9600	43
H(3)	-716	4201	10366	44
H(4)	-2281	3440	9918	45
H(5)	-2807	2479	8719	37
H(8A)	-3440	1744	6118	53
H(8B)	-3578	730	6604	53
H(9)	-2024	162	6812	53
H(10A)	-2162	1734	5648	63
H(10B)	-2290	516	5483	63
H(11A)	-833	-769	5574	62
H(11B)	308	-473	5894	62
H(13)	-298	-2416	6290	67
H(14)	0	-3327	7500	77

G. References

- (1) Williams, R. J. P. *Coord. Chem. Rev.* **2001**, 216-217, 583-595.
- (2) Wood, J. M. *Naturwissenschaften* **1975**, 62, 357-64.
- (3) Kraatz, H.-B.; Metzler-Nolte, N. *Concepts and Models in Bioinorganic Chemistry*; WILEY-VCH GmbH & Co. KGaA: Weinheim, 2006.
- (4) Battersby, A. R. *Pure Appl. Chem.* **1993**, 65, 1113-22.
- (5) Kadish, K. M.; Smith, K. M.; Guillard, R. *The Porphyrin Handbook*; Elsevier Science: Oxford, 2000.
- (6) Kadish, K. M.; Smith, K. M.; Guillard, R. *The Porphyrin Handbook*; Elsevier Science: Oxford, 2003.
- (7) Denisov, I. G.; Makris, T. M.; Sligar, S. G.; Schlichting, I. *Chem. Rev.* **2005**, 105, 2253-2277.
- (8) Collman, J. P.; Fu, L. *Acc. Chem. Res.* **1999**, 32, 455-463.
- (9) Messerschmidt, A.; Huber, R.; Poulos, T.; Wieghardt, K. *Handbook of Metalloproteins*; J. Wiley & Sons: Chichester, UK, 2001; Vol. 1.
- (10) Eschenmoser, A. *Angew. Chem.* **1988**, 100, 5-40.
- (11) Krauss, G. *Biochemistry of Signal Transduction and Regulation*; 2nd ed.; Wiley-VCH GmbH: Weinheim, 2001.
- (12) Lodish, H.; Berk, A.; Zipursky, S. L.; Matsudaira, P.; Baltimore, D.; Darnell, J. E. *Molecular Cell Biology*; 4th ed.; W. H. Freeman and Company: New York, 2000.
- (13) Rees, D. C.; Howard, J. B. *Science* **2003**, 300, 929-931.
- (14) Beinert, H.; Holm, R. H.; Munck, E. *Science* **1997**, 277, 653-659.
- (15) Bian, S.; Cowan, J. A. *Coord. Chem. Rev.* **1999**, 190-192, 1049-1066.
- (16) Orme-Johnson, W. H. *Annu. Rev. Biochem* **1973**, 42, 159-204.
- (17) Shan, X.; Que, L. *J. Inorg. Biochem.* **2006**, 100, 421-433.
- (18) Koehntop, K. D.; Emerson, J. P.; Que, L., Jr. *J. Biol. Inorg. Chem.* **2005**, 10, 87-93.
- (19) Solomon, E. I.; Brunold, T. C.; Davis, M. I.; Kemsley, J. N.; Lee, S.-K.; Lehnert, N.; Neese, F.; Skulan, A. J.; Yang, Y.-S.; Zhou, J. *Chem. Rev.* **2000**, 100, 235-349.
- (20) Solomon, E. I.; Decker, A.; Lehnert, N. *PNAS* **2003**, 100, 3589-3594.
- (21) Costas, M.; Mehn, M. P.; Jensen, M. P.; Que, L., Jr. *Chem. Rev.* **2004**, 104, 939-986.
- (22) Kryatov, S. V.; Rybak-Akimova, E. V.; Schindler, S. *Chem. Rev.* **2005**, 105, 2175-2226.

References

- (23) Mehn, M. P.; Fujisawa, K.; Hegg, E. L.; Que, L., Jr. *J. Am. Chem. Soc.* **2003**, *125*, 7828-7842.
- (24) Merckx, M.; Kopp, D. A.; Sazinsky, M. H.; Blazyk, J. L.; Muller, J.; Lippard, S. J. *Angew. Chem. Int. Ed.* **2001**, *40*, 2782-2807.
- (25) Stenkamp, R. E.; Sieker, L. C.; Jensen, L. H. *J. Am. Chem. Soc.* **1984**, *106*, 618-22.
- (26) Stenkamp, R. E. *Chem. Rev.* **1994**, *94*, 715-26.
- (27) Wallar, B. J.; Lipscomb, J. D. *Chem. Rev.* **1996**, *96*, 2625-2657.
- (28) Stubbe, J. *Curr. Opin. Chem. Biol.* **2003**, *7*, 183-188.
- (29) Fontecave, M.; Menage, S.; Duboc-Toia, C. *Coord. Chem. Rev.* **1998**, *178-180*, 1555-1572.
- (30) Tolman, W. B.; Que, L., Jr. *J. Chem. Soc., Dalton Trans.* **2002**, 653-660.
- (31) Rohde, J.-U.; In, J.-H.; Lim, M. H.; Brennessel, W. W.; Bukowski, M. R.; Stubna, A.; Muenck, E.; Nam, W.; Que, L., Jr. *Science* **2003**, *299*, 1037-1039.
- (32) Klinker, E. J.; Kaizer, J.; Brennessel, W. W.; Woodrum, N. L.; Cramer, C. J.; Que, L., Jr. *Angew. Chem. Int. Ed.* **2005**, *44*, 3690-3694.
- (33) Lim, M. H.; Rohde, J.-U.; Stubna, A.; Bukowski, M. R.; Costas, M.; Ho, R. Y. N.; Munck, E.; Nam, W.; Que, L., Jr. *PNAS* **2003**, *100*, 3665-3670.
- (34) Jensen, M. P.; Costas, M.; Ho, R. Y. N.; Kaizer, J.; Payeras, A. M.; Muenck, E.; Que, L., Jr.; Rohde, J.-U.; Stubna, A. *J. Am. Chem. Soc.* **2005**, *127*, 10512-10525.
- (35) Rohde, J.-U.; Torelli, S.; Shan, X.; Lim, M. H.; Klinker, E. J.; Kaizer, J.; Chen, K.; Nam, W.; Que, L., Jr. *J. Am. Chem. Soc.* **2004**, *126*, 16750-16761.
- (36) Brown, C. A.; Remar, G. J.; Musselman, R. L.; Solomon, E. I. *Inorg. Chem.* **1995**, *34*, 688-717.
- (37) Wieghardt, K.; Pohl, K.; Gebert, W. *Angew. Chem.* **1983**, *95*, 739-40.
- (38) Armstrong, W. H.; Lippard, S. J. *J. Am. Chem. Soc.* **1983**, *105*, 4837-8.
- (39) Kim, K.; Lippard, S. J. *J. Am. Chem. Soc.* **1996**, *118*, 4914-15.
- (40) Que, L., Jr.; Dong, Y. *Acc. Chem. Res.* **1996**, *29*, 190-6.
- (41) Hsu, H.-F.; Dong, Y.; Shu, L.; Young, V. G., Jr.; Que, L., Jr. *J. Am. Chem. Soc.* **1999**, *121*, 5230-5237.
- (42) Seitz, M. PhD, University of Regensburg, 2004.
- (43) Kaiser, A. PhD, University of Regensburg, 2004.
- (44) Godbole, M. D.; Puig, M. P.; Tanase, S.; Kooijman, H.; Spek, A. L.; Bouwman, E. *Inorg. Chim. Acta* **2007**, *360*, 1954-1960.

-
- (45) Seitz, M.; Kaiser, A.; Tereshchenko, A.; Geiger, C.; Uematsu, Y.; Reiser, O. *Tetrahedron* **2006**, *62*, 9973-9980.
 - (46) Estimated by weight.
 - (47) Meyers, A. I.; Schmidt, W.; McKennon, M. J. *Synthesis* **1993**, 250-62.
 - (48) Novachek, K. A.; Myers, A. I. *Tetrahedron Lett.* **1996**, *37*, 1743-6.
 - (49) Zunnundzhanov, A.; Bessonova, I. A.; Abdullaev, N. D.; Ogai, D. K. *Chem. Nat. Compd.* **1988**, *23*.
 - (50) Zamri, A.; Abdallah, M. A. *Tetrahedron* **2000**, *56*, 9397.
 - (51) Rinehart, K. L.; Staley, A. L.; Wilson, S. R.; Ankenbauer, R. G.; Cox, C. D. *J. Org. Chem.* **1995**, *60*, 2786-91.
 - (52) Appel, R. *Angew. Chem.* **1975**, *87*, 863-74.
 - (53) Christen, H. R.; Vögtle, F. *Organische Chemie - Von den Grundlagen zur Forschung*; Otto Salle Verlag GmbH & Co. / Sauerländer AG: Frankfurt am Main / Aarau, 1992; Vol. 1.
 - (54) Frump, J. A. *Chem. Rev.* **1971**, *71*, 483-506.
 - (55) Cox, P. A. *The Elements on Earth*; Oxford University Press: Oxford, 1995.
 - (56) Bergeron, R. J.; Wiegand, J.; McManis, J. S.; Weimar, W. R.; Park, J.-H.; Eiler-McManis, E.; Bergeron, J.; Brittenham, G. M. *J. Med. Chem.* **2005**, *48*, 821-831.
 - (57) Ponka, P. J. *Trace Elem. Exp. Med.* **2003**, *16*, 201-217.
 - (58) Ponka, P. J. *Trace Elem. Exp. Med.* **2000**, *13*, 73-83.
 - (59) Hollemann, A. F.; Wiberg, E. *Lehrbuch der Anorganischen Chemie*; Walter de Gruyter: Berlin New York, 1995; Vol. 101.
 - (60) Bergeron, R. J.; Wiegand, J.; Weimar, W. R.; McManis, J. S.; Smith, R. E.; Abboud, K. A. *Chirality* **2003**, *15*, 593-599.
 - (61) Graf, E.; Mahoney, J. R.; Bryant, R. G.; Eaton, J. W. *J. Biol. Chem.* **1984**, *259*, 3620-4.
 - (62) Halliwell, B. *Nutr. Rev.* **1994**, *52*, 253-65.
 - (63) Halliwell, B. *Lancet* **1994**, *344*, 721-4.
 - (64) Olivieri, N. F.; Brittenham, G. M. *Blood* **1997**, *89*, 739-61.
 - (65) Giardina, P. J.; Grady, R. W. *Semin. Hematol.* **2001**, *38*, 360-6.
 - (66) Naegeli, H. U.; Zaehner, H. *Helv. Chim. Acta* **1980**, *63*, 1400-6.
 - (67) Anderegg, G.; Raeber, M. *J. Chem. Soc., Chem. Commun.* **1990**, 1194-6.
 - (68) Hahn, F. E.; McMurry, T. J.; Hugi, A.; Raymond, K. N. *J. Am. Chem. Soc.* **1990**, *112*, 1854-60.
-

- (69) Bergeron, R. J.; Wiegand, J.; Dionis, J. B.; Egli-Karmakka, M.; Frei, J.; Huxley-Tencer, A.; Peter, H. H. *J. Med. Chem.* **1991**, *34*, 2072-8.
- (70) Bergeron, R. J.; Streiff, R. R.; Wiegand, J.; Vinson, J. R.; Luchetta, G.; Evans, K. M.; Peter, H.; Jenny, H. B. *Ann. N. Y. Acad. Sci.* **1990**, *612*, 378-93.
- (71) Bergeron, R. J.; Streiff, R. R.; Creary, E. A.; Daniels, R. D., Jr.; King, W.; Luchetta, G.; Wiegand, J.; Moerker, T.; Peter, H. H. *Blood* **1993**, *81*, 2166-73.
- (72) Bergeron, R. J.; Wiegand, J.; McManis, J. S.; Bharti, N. *J. Med. Chem.* **2006**, *49*, 7032-7043.
- (73) Bergeron, R. J.; Wiegand, J.; McManis, J. S.; Vinson, J. R. T.; Yao, H.; Bharti, N.; Rocca, J. R. *J. Med. Chem.* **2006**, *49*, 2772-2783.
- (74) Tanase, S.; Bouwman, E.; Long, G. J.; Shahin, A. M.; Mills, A. M.; Spek, A. L.; Reedijk, J. *Eur. J. Inorg. Chem.* **2004**, 4572-4578.
- (75) Gaber, B. P.; Miskowski, V.; Spiro, T. G. *J. Am. Chem. Soc.* **1974**, *96*, 6868-73.
- (76) Ainscough, E. W.; Brodie, A. M.; Plowman, J. E.; Brown, K. L.; Addison, A. W.; Gainsford, A. R. *Inorg. Chem.* **1980**, *19*, 3655-63.
- (77) Bergeron, R. J.; Liu, C. Z.; McManis, J. S.; Xia, M. X. B.; Algee, S. E.; Wiegand, J. *J. Med. Chem.* **1994**, *37*, 1411-17.
- (78) Bergeron, R. J.; Wiegand, J.; Weimar, W. R.; Vinson, J. R. T.; Bussenius, J.; Yao, G. W.; McManis, J. S. *J. Med. Chem.* **1999**, *42*, 95-108.
- (79) Tseng, C.-F.; Burger, A.; Mislin, G. L. A.; Schalk, I. J.; Yu, S. S. F.; Chan, S. I.; Abdallah, M. A. *J. Biol. Inorg. Chem.* **2006**, *11*, 419-432.
- (80) Sreerama, S. G.; Mukhopadhyay, A.; Pal, S. *Inorg. Chem. Commun.* **2006**, *9*, 1083-1086.
- (81) Langemann, K.; Heineke, D.; Rupprecht, S.; Raymond, K. N. *Inorg. Chem.* **1996**, *35*, 5663-5673.
- (82) Godbole, M. D.; Roubeau, O.; Mills, A. M.; Kooijman, H.; Spek, A. L.; Bouwman, E. *Inorg. Chem.* **2006**, *45*, 6713-6722.
- (83) Stubna, A.; Jo, D.-H.; Costas, M.; Brenessel, W. W.; Andres, H.; Bominaar, E. L.; Muenck, E.; Que, L., Jr. *Inorg. Chem.* **2004**, *43*, 3067-3079.
- (84) Bennett, M. A.; Smith, A. K. *J. Chem. Soc. Dalton Trans.* **1974**, 233-41.
- (85) Bag, N.; Lahiri, G. K.; Bhattacharya, S.; Falvello, L. R.; Chakravorty, A. *Inorg. Chem.* **1988**, *27*, 4396-402.
- (86) Steiner, T. *Angew. Chem. Int. Ed.* **2002**, *41*, 48-76.
- (87) Moriuchi, T.; Nishiyama, M.; Hirao, T. *Eur. J. Inorg. Chem.* **2002**, 447-451.

- (88) Tong, Y.-P.; Zheng, S.-L.; Chen, X.-M. *J. Mol. Struct.* **2007**, 826, 104-112.
- (89) Godbole, M. D.; Hotze, A. C. G.; Hage, R.; Mills, A. M.; Kooijman, H.; Spek, A. L.; Bouwman, E. *Inorg. Chem.* **2005**, 44, 9253-9266.
- (90) Seitz, M.; Kaiser, A.; Powell, D. R.; Borovik, A. S.; Reiser, O. *Adv. Synth. Catal.* **2004**, 346, 737-741.
- (91) Baucherel, X.; Gonsalvi, L.; Arends, I. W. C. E.; Ellwood, S.; Sheldon, R. A. *Adv. Synth. Catal.* **2004**, 346, 286-296.
- (92) Shilov, A. E.; Shul'pin, G. B. *Chem. Rev.* **1997**, 97, 2879-2932.
- (93) Pavan, C.; Legros, J.; Bolm, C. *Adv. Synth. Catal.* **2005**, 347, 703-705.
- (94) Lane, B. S.; Burgess, K. *Chem. Rev.* **2003**, 103, 2457-2473.
- (95) White, M. C.; Doyle, A. G.; Jacobsen, E. N. *J. Am. Chem. Soc.* **2001**, 123, 7194-7195.
- (96) Legros, J.; Bolm, C. *Angew. Chem. Int. Ed.* **2004**, 43, 4225-4228.
- (97) Li, F.; Wang, M.; Ma, C.; Gao, A.; Chen, H.; Sun, L. *Dalton Transactions* **2006**, 2427-2434.
- (98) Kalir, A.; Kalir, H. H. *Chemistry of Sulphur-Containing Functional Groups* **1993**, 957-73.
- (99) Bolm, C. *Coord. Chem. Rev.* **2003**, 237, 245-256.
- (100) Legros, J.; Bolm, C. *Angew. Chem. Int. Ed.* **2003**, 42, 5487-5489.
- (101) Legros, J.; Bolm, C. *Chem. Eur. J.* **2005**, 11, 1086-1092.
- (102) Korte, A.; Legros, J.; Bolm, C. *Synlett* **2004**, 2397-2399.
- (103) Bolm, C.; Legros, J.; Le Paih, J.; Zani, L. *Chem. Rev.* **2004**, 104, 6217-6254.
- (104) No structure analysis of the Schiff base complexed with iron is published until now.

H. Curriculum Vitae

Caroline A. Schall

Personal Data

Address	Lieblstr. 51 93059 Regensburg, Germany
Phone	+ 49 - 941 - 2068349
E-mail	caroline.schall@chemie.uni-regensburg.de
Born	June 12 th 1977, Schwandorf, Germany
Nationality	German

Education

11/2007	Final defense <i>“Chiral Oxazoline and Bis(oxazoline) Ligands – New biomimetic Models for Iron containing nonheme Proteins and their Application in Catalysis”</i>
03/2006 - 05/2006	Exchange program: University of Kansas, Lawrence, USA Research in the group of Prof. A.S. Borovik <i>(Bioinorganic Chemistry)</i>
Since 08/2004	PhD thesis in the research group of Prof. Dr. O. Reiser University of Regensburg, Germany (<i>Organic Chemistry</i>)
01/2004 - 07/2004	Research in the group of Prof. Dr. R. Andreesen University of Regensburg, Germany (<i>Heamatology/Oncology</i>) supervisor Prof. Dr. S. Elz <i>“Investigations on human regulatory T cells”</i>
12/2003	Diploma in Chemistry - University of Regensburg, Germany (master degree in chemistry)
03/2003 - 11/2003	Diploma thesis in the research group of Prof. Dr. S. Elz University of Regensburg, Germany (<i>Pharmacology/Physiology</i>) <i>“Regulation of Cyclooxygenase-2 depending on Angiotensin-II in cultured mesangial cells of the rat”</i>

Curriculum Vitae

04/2001 - 02/2003	Study of Chemistry, University of Regensburg, Germany
08/2000 - 03/2001	Study of Chemistry and Biochemistry, University of Aberdeen, Scotland
01/2001 - 03/2001	Research project in the group of Dr. J. Feldmann University of Aberdeen, Scotland (Organic Chemistry) “ <i>Synthesis of arsenic sugars</i> “
08/2000	Intermediate exam - University of Regensburg, Germany
04/1999 - 08/2000	Student of general Chemistry, University of Regensburg, Germany
10/1996 - 03/1999	Student of Technological Chemistry Georg-Simon-Ohm Fachhochschule, Nürnberg, Germany
09/1994 - 07/1996	Fachoberschule, Schwandorf, Germany (high school graduation)

Professional Experience

09/2005	EU-Project ASIA-Link Medicinal Chemistry , Shanghai, China “ <i>Sommerschool Medicinal Chemistry</i> ”
07/2002 - 10/2002	Internship in the department of Prof. Dr. D. Männel (Tumor Immunology), University of Regensburg, Germany “ <i>Cell culture training</i> ”
08/2001 - 10/2001	Summer Research Internship at BAYER AG , Pharma Research, Wuppertal, Germany
05/2001 - 07/2001	Internship in the department of Prof. Dr. S. Elz, (Pharmaceutical & Medicinal Chemistry I) University of Regensburg, Germany “ <i>Ligand-Receptor-Effects on guinea pig trachea</i> ”
03/2000 - 04/2000	Internship at the Max-Planck-Institut of Immunobiology Research group of Prof. Dr. A. Kispert (Development Biology), Freiburg, Germany “ <i>Characterization of sFRP-2 Gen in mouse</i> ”
12/1998	Workshop at Roche Diagnostics , Nürnberg, Germany “ <i>Basic techniques of enzymatic analysis</i> ”
07/1998 - 08/1998	Internship at Bayerische Landesanstalt für Bodenkultur und Pflanzenbau, (Gene analysis in plants), Freising, Germany
09/1997	Internship at Bayerisches Landesamt für Umweltschutz, (Environmental analytical chemistry), Schwandorf, Germany

Presentations

- 1) *“Pentadentate Bis(oxazoline) Ligands: A Promising Model for C-H-Activation”* Caroline Wagner, M. Seitz, A. Kaiser, Oliver Reiser; DFG 1118 – “Sekundäre Wechselwirkungen als Steuerungsprinzip zur gerichteten Funktionalisierung reaktionsträger Substrate” 2006, Schleiden, Germany
- 2) *“Pentadentate Bis(oxazoline) Ligands: A Promising Model for C-H Activation”* Caroline Wagner, M. Seitz, A. Kaiser, Oliver Reiser; Summerschool Medicinal Chemistry 2005, Shanghai, China
- 3) *“Metallkomplexe neuer Bis(oxazolin)liganden als Katalysatoren für die Oxidation von Kohlenwasserstoffen”* A. Kaiser, M. Seitz, Caroline Wagner, A. Tereshenko, Oliver Reiser; DFG meeting, 2005, Germany
- 4) *“Iron(II) metal complexes with pentadentate bis(oxazolines)”* Caroline Wagner, M. Seitz, A. Kaiser, Oliver Reiser; Workshop on biomimetic metal mediated oxidative transformations 2005, Marburg, Germany
- 5) *“In vitro expanded CD4⁺CD25^{high} cells retain regulatory T cell characteristics”* Caroline Wagner, B. Piseshka, R. Eder, A. Havasi, P. Hoffmann, M. Edinger; Heamatology/Oncology department meeting 2004, Hirschberg, Germany

Scholarships

06/2006 – 08/2006	RISE DAAD student exchange tutor
08/2000 - 03/2001	ERASMUS/SOKRATES student exchange program

I. Acknowledgement

Für das Gelingen dieser Arbeit möchte ich mich bei folgenden Personen bedanken:

Herrn Prof. Dr. O. Reiser für die Bereitstellung des Themas und die Ermöglichung meines Auslandsaufenthaltes an der University of Kansas, USA.

Herrn Prof. Dr. A. Borovik für die freundliche Aufnahme in seiner Arbeitsgruppe und allen Kollegen in Kansas für ihre hilfsbereite Unterstützung und eine tolle Zeit.

Herrn Prof. Dr. R. Winter für die Benutzung seiner Laborgeräte sowie für seine Diskussionsbereitschaft.

Herrn Dr. Zabel und Frau Stempfhuber für die Vermessung meiner zahlreichen Kristallstrukturen sowie ihre stete Hilfsbereitschaft.

Herr Dr. Rudi Vasold für seinen starken Einsatz in der Untersuchung meiner Substanzen durch GC und HPLC Analytik, sowie zahlreichen informative Gespräche über die Geheimnisse des GC Analytik.

Herrn Dr. Burgemeister, Herrn Kastner, Frau Schramm und Frau Stühler für die stete und freundliche Unterstützung in allen NMR-Problemen.

Herrn Kiermaier und Herrn Söllner für ihre freundliche Zusammenarbeit und ständige Hilfsbereitschaft in der massenspektroskopischen Analyse meiner Substanzen.

Frau W. Krutina und Frau B. Baumann für Ihre freundliche Art und schnelle Durchführung meiner Elementaranalysen.

Herrn Dr. Peter Kreitmeier für seine überdurchschnittliche Hilfestellung bei allen Problemen rund ums Labor und die Chemie, sowie für nette Frühstückskaffeerunden.

Acknowledgement

Frau Rotermund und Frau Ohli für ihre ebenfalls überdurchschnittliche Hilfsbereitschaft in jeder Lebenslage.

Andrea Roithmaier, Georg Adolin, Klaus Döring und Robert Tomahogh für eine sehr angenehme und überaus hilfsbereite Zusammenarbeit, sowie für unsere netten Frühstückskaffeerunden.

Dominic Laventine, Markus Hager und Dr. Kirsten Zeitler für ihre wertvolle Hilfestellung beim Korrekturlesen dieser Arbeit.

Max und Steve, für ihre enorme Unterstützung während ihres Praktikums in meinem Labor.

Allen jetzigen und ehemaligen Mitgliedern der Arbeitsgruppe Reiser für zahllose Grillfestl, Kuchengelage und Pläusche.

Last but not least,

Ganz besonderer Dank gebührt meiner Familie, die immer an mich geglaubt und mir den nötigen Halt für meine Ziele gegeben hat.

Bei meiner Schwester Julia möchte ich mich für ihre aufmunternden Worte bedanken. Du schaffst das auch!

Letztendlich möchte ich mich bei meinem Liebsten, Andy, bedanken, der meine Gedanken auch ohne Worte kennt, der Nachts die gleichen Träume träumt und der mich spüren lässt, jemand ganz besonderen zu sein. Dafür Liebe ich Ihn über alles. Danke mein Schatz!